Stability of Superconducting Rutherford Cables

for accelerator magnets

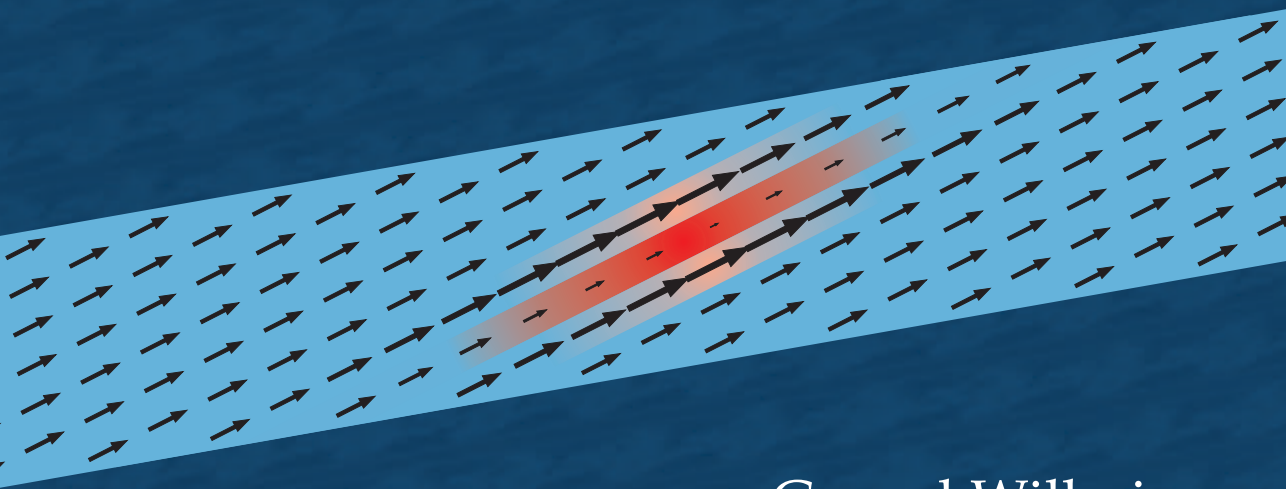

Gerard Willering

STABILITY OF SUPERCONDUCTING RUTHERFORD CABLES

FOR ACCELERATOR MAGNETS

Ph.D. Committee:

Dr. L. Bottura	CERN, Geneva
Prof. dr. ir. H.J.M. ter Brake	University of Twente
Prof. dr. ir. B. van Eijk	University of Twente
Prof. dr. ir. J.W.M. Hilgenkamp	University of Twente
Prof. dr. ir. H.H.J. ten Kate	University of Twente
Prof. dr. J.J. Smit	University of Delft
Prof. dr. G. van der Steenhoven	University of Twente
Prof. dr. J.J.W. van der Vegt	University of Twente
Dr. ir. A. Verweij	CERN, Geneva

G.P. Willering
Stability of Superconducting Rutherford Cables for Accelerator Magnets
Ph.D. thesis, University of Twente, The Netherlands

ISBN: 978-90-365-2817-7

Printed by PrintPartner Ipskamp, The Netherlands

STABILITY OF SUPERCONDUCTING RUTHERFORD CABLES

FOR ACCELERATOR MAGNETS

PROEFSCHRIFT

ter verkrijging van
de graad van doctor aan de Universiteit Twente,
op gezag van de rector magnificus,
prof. dr. H. Brinksma,
volgens besluit van het College voor Promoties
in het openbaar te verdedigen
op woensdag 27 mei 2009 om 15:00 uur.

door

Geert Pieter Willering
geboren op 25 oktober 1978
te Kampen

Dit proefschrift is goedgekeurd door de promotor en assistent-promotor

prof. dr. ir. H.H.J. ten Kate
dr. ir. A.P. Verweij

Preface

The work described in this thesis results from an extensive collaboration between the special chair for Industrial Application of Superconductors in the Low Temperature Division at the University of Twente and the Magnets, Superconductors and Cryostats group at CERN. The research has been carried out at CERN as well as at the University of Twente and it is funded by both institutes.

Part of the cable samples were prepared by GSI in the frame of research collaboration on cable stability.

I am very grateful to the members of these groups for giving me the opportunity to perform the research, for their interest and useful discussions.

University of Twente
Enschede - The Netherlands

Contents

Preface **i**

1 Introduction **1**
1.1 Superconducting accelerator magnets 2
1.2 Superconductivity 8
1.3 Practical superconductors 8
1.3.1 Strands 9
1.3.2 Cables 10
1.4 Quench and recovery 14
1.5 Scope of the thesis 17

2 Superconductor Stability **21**
2.1 Sources of heat 22
2.1.1 Steady state loss 23
2.1.2 Conductor motion 24
2.1.3 Epoxy cracking 26
2.1.4 Transient beam loss 27
2.2 Definition of stability 27
2.2.1 Single wires 27
2.2.2 Cables 32
2.2.3 Magnets 34
2.3 Modeling cable stability 36
2.3.1 Analytical approach 38
2.3.2 Numerical approach 40
2.3.3 Electrodynamic and thermal cable simulation model CUDI . 40
2.3.4 Limitations of simulations with CUDI 43
2.4 Cable stability regimes 44
2.4.1 Transversal normal zone propagation 46
2.4.2 Criteria 48
2.4.3 Transition current and stability regimes 52
2.4.4 Quench and recovery of a local normal zone 52
2.5 Cable geometry 54
2.5.1 Cross contact surfaces 56

2.5.2 Adjacent contact surfaces . . . 57
2.5.3 Helium contact surface . . . 58
2.5.4 Void size . . . 59
2.6 Conclusion . . . 61

3 Advanced Measurement Techniques 63
3.1 Experiment . . . 64
3.1.1 FRESCA cable test facility . . . 64
3.1.2 Cable sample . . . 65
3.1.3 Sample holder . . . 66
3.1.4 Sample insert . . . 67
3.1.5 Representativity of the measurements . . . 67
3.2 Heat deposition . . . 69
3.2.1 Heaters . . . 69
3.2.2 Heater production . . . 71
3.2.3 Effective heat flow into a strand . . . 73
3.3 MQE measurement . . . 75
3.4 Local self-field measurement . . . 76
3.4.1 Hall probe signals for $E_p <$ MQE . . . 77
3.4.2 Hall probe signals for $E_p >$ MQE . . . 80
3.4.3 Hall probe signals in case of non-uniform transport current distribution . . . 81
3.5 Strand voltages . . . 82
3.6 Conclusion . . . 86

4 Interstrand Contacts Affecting Stability 87
4.1 Interstrand contacts . . . 88
4.1.1 Non-cored cable . . . 89
4.1.2 Cored cable . . . 93
4.1.3 Soldered cable . . . 94
4.1.4 Interstrand electrical resistance . . . 95
4.1.5 Interstrand thermal conductance . . . 97
4.2 Current and heat distribution . . . 99
4.2.1 Current redistribution paths . . . 99
4.2.2 Primary and secondary current redistribution paths . . . 103
4.2.3 Interstrand heat diffusion . . . 104
4.3 Influence of R_a and R_c on stability . . . 105
4.4 Influence of interstrand thermal conductance on stability . . . 110
4.5 Conclusion . . . 113

5 Helium Cooling Affecting Stability 115
5.1 Introduction . . . 116
5.2 Helium as a coolant . . . 117
5.2.1 Superfluid Helium . . . 118
5.2.2 Liquid Helium . . . 124

5.2.3 Supercritical Helium . . . 129
5.3 Influence of superfluid helium on stability . . . 131
5.4 Influence of liquid helium on stability . . . 136
5.5 Influence of supercritical helium on stability . . . 140
5.6 Conclusion . . . 143

6 Experiment and Simulation 145
6.1 Introduction . . . 146
6.2 Fitting of calculated to measured MQE . . . 149
6.3 Local voltage and self-field . . . 153
6.4 Validation of CUDI . . . 156
6.5 Sample LHC 01 - A . . . 157
6.6 Sample LHC 01 - B . . . 160
6.7 Sample LHC 01 - C . . . 163
6.8 Samples LHC 01 - D and E . . . 165
6.9 Sample LHC 01 - F . . . 167
6.10 SIS 300 dipole samples . . . 169
6.11 Conclusion . . . 173

7 Impact of cable design on magnet stability 175
7.1 Stability of cables in magnets. . . . 176
7.1.1 Heat deposition volumes . . . 176
7.1.2 Quench energy levels in LHC dipole magnets . . . 177
7.1.3 Quench energy levels in SIS 300 quadrupole magnets . . . 182
7.2 Effect of non-uniform current distribution on stability . . . 185
7.3 Core versus highly resistive coating . . . 188
7.4 Improvement of edge stability . . . 191
7.4.1 Local reduction of the interstrand thermal conductance . . . 192
7.4.2 Local removal of the insulation at the thin edge . . . 194
7.5 Stability of mixed strand cables . . . 196
7.6 Conclusion . . . 200

8 Conclusion and recommendations 203
8.1 Cable stability mechanisms . . . 204
8.2 Measuring cable stability . . . 205
8.3 Modeling cable stability . . . 206
8.4 Improving cable stability . . . 207
8.5 Cable stability in a magnet . . . 208
8.6 Recommendations . . . 210

Nomenclature 221

Samenvatting (Summary in Dutch) 225

Dankwoord - Acknowledgements 229

Chapter 1

Introduction

After the discovery of superconductivity in the beginning of the 20^{th} century the understanding of the phenomenon has grown. Practical conductors are produced for various magnet applications. Although the number of superconducting materials is high, only a few can be used in high-field and high-current density applications. This thesis deals with cable stability, with the focus on application in accelerator magnets.

In this chapter a brief overview of the existing and near future accelerators and their superconducting magnets is presented. The most recent superconducting accelerator, the LHC *and the near future superconducting accelerator* SIS *300 are described.*

The phenomenon of superconductivity is shortly discussed and practical superconductors are introduced with an emphasis on strands and cables. Different types of cables are presented and the relevance of this thesis for in particular the Rutherford type of cable is discussed.

The terms quench and recovery are introduced. The importance of research on stability is illustrated by the large number of training quenches in the LHC *main dipole magnets.*

1.1 Superconducting accelerator magnets

In High Energy Physics the interaction of elementary particles is being studied. Many particle accelerators have been constructed to accelerate particles and collide them at high energy. Synchrotron accelerators provide a circular track with RF-cavities to accelerate bunches of particles each cycle.

Synchrotron accelerators require dipole magnets to bend the particle beam and keep it in its circular track. Quadrupole magnets are used to focus and defocus the beam and higher-order magnets correct field distortions and chromaticity. The collision energy depends on the magnetic field in the aperture of the dipole B_a (T) and the bending radius of the dipole magnets r_d (km) following $E \approx 0.3 B_a r_d$ (TeV). The limitation in the track circumference is strongly dictated by the amount of material and the costs involved. In normal conducting magnets iron is applied to enhance the electromagnetic field produced with copper windings. The magnetic field in iron saturates at about 2 T, therefore the needed amount of copper windings and the costs involved increase strongly for higher field magnets. A more economic way to produce high field magnets is with the use of superconducting magnets.

The first accelerator built with superconducting magnets is the Tevatron at Fermilab, completed in 1983, with a dipole field up to 4.4 T. With the proven success of a superconducting accelerator other projects started. It was followed by the successful construction of HERA at DESY in 1991 and RHIC at BNL in 1997.

The most recent superconducting accelerator, the Large Hadron Collider (LHC) at CERN, Geneva, Switzerland [1] has started operation with a first beam in September 2008. It is the largest system with a circumference of 27 km and the highest design operation magnetic dipole field of 8.33 T. A typical operation cycle incorporates a dipole field sweep from injection field of 0.54 T to the nominal field of 8.33 T in about 1200 s. Given the ramp rate of 0.007 T/s, the LHC main dipoles can be characterized as slow ramping magnets. The nominal magnetic field is maintained for up to 12 hours, before the field is ramped down. In the case of a quench in a coil, the magnets that are connected in series are discharged rapidly in about 100 s, with a maximum discharge rate of -0.084 T/s.

The design of a new accelerator complex is currently prepared at GSI - Darmstadt, Germany with two accelerators in one ring, the heavy ion synchrotrons SIS 100 and SIS 300. The SIS 100 dipoles are ramped at about 4 T/s to a field of 1.9 T and with a cycle time of about 1 s [2, 3]. The SIS 300 dipoles are ramped at about 1 T/s to a field of 4.5 T, with a cycle time of about 20 s [3]. The main dipole magnets of both accelerators can be characterized as fast ramping magnets.

All four existing accelerators exhibiting superconducting magnets are based on NbTi conductor. The design of near future accelerators mostly rely on the proven NbTi technology, while Nb_3Sn is under investigation for more powerful accelerators and special magnets in existing accelerators.

A list of the current and future superconducting accelerators is given in table 1.1. The scheme in figure 1.1 illustrates the main characteristics of accelerator systems. In this thesis the research is focused on two specific designs of accelerator

magnets: the LHC main dipole magnet and the SIS 300 main quadrupole magnet. The choice represents the extremes of three characteristics:

1. The most recent and the near future accelerators are covered, designed with the most recent technology.
2. The LHC is a slow ramping system with a field sweep rate of 7 mT/s. The SIS 300 is a fast ramping system with a field sweep rate of 1 T/s.
3. The LHC is the only superconducting accelerator with magnets cooled with superfluid helium, operating at 1.9 K. The SIS 300 is cooled with supercritical helium at 4.5 K, therefore representing many other systems.

Table 1.1: Magnetic field characteristics of superconducting accelerator magnets.

Institute	Accelerator	Magnet type	B_a T	Field-sweep rate Ts^{-1}	Field gradient T/m
Fermilab	Tevatron	dipole	4.4	0.010	-
Fermilab	Tevatron	quadrupole	-	-	76
DESY	HERA	dipole	4.68	0.004	-
DESY	HERA	quadrupole	-	-	91
BNL	RHIC	dipole	3.45	0.042	-
BNL	RHIC	quadrupole	-	-	72
CERN	LHC	dipole	8.33	0.007	-
CERN	LHC	quadrupole	-	-	223
GSI	SIS 100*	dipole	1.9	4	-
GSI	SIS 100*	quadrupole	-	-	27
GSI	SIS 300*	dipole	4.5	1	-
GSI	SIS 300*	quadrupole	-	-	45

* model magnets, system is not yet contracted

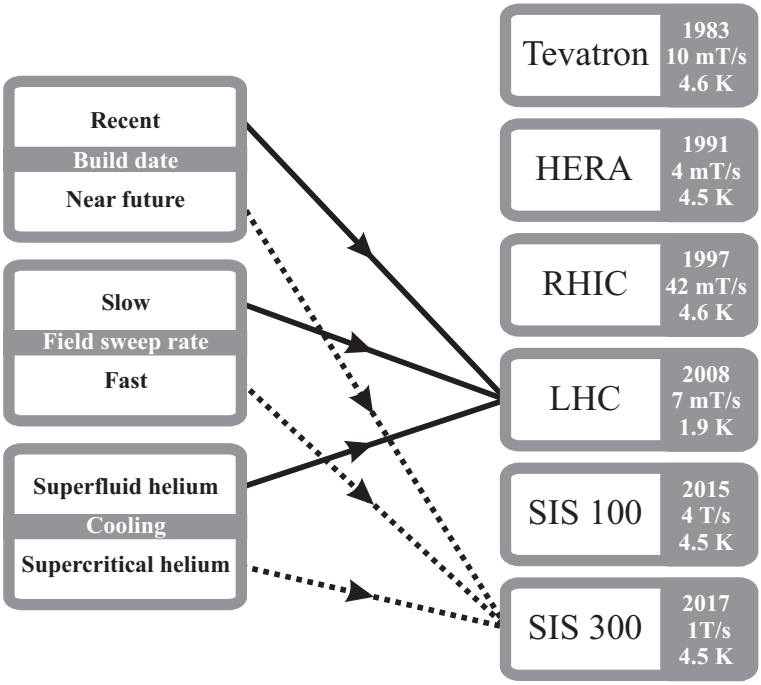

Figure 1.1: Schematic of the representativity of the LHC and SIS 300 accelerators for superconducting accelerator magnets.

The differences between the systems demand a specific investigation of cable stability for each magnet. Cable stability proves to be strongly case dependent, with a strong influence of variation in helium cooling, operation temperature and interstrand resistance requirements.

Pure dipole and quadrupole fields are produced by a current distribution given with overlapping circles and ellipses, respectively, see figure 1.2. In $\cos\theta$ accelerator dipole magnets, the field in the aperture is controlled by the current through a large number of turns of a cable.

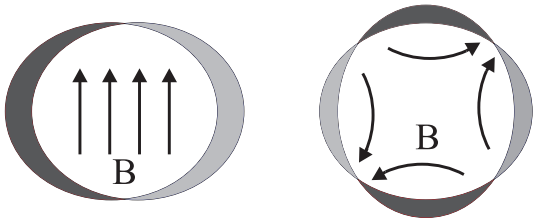

Figure 1.2: Ideal current distribution for generating a pure dipole and quadrupole magnetic field. The arrows show the magnetic field direction with uniform current density in one direction in the light gray area and in the opposite direction in the dark area.

The perfect magnetic field proves to be impossible to obtain and therefore it is approached by one or two layers of superconducting cable. Magnetic field homogeneity is optimized with the use of spacers between the blocks of conductors. In figure 1.3a the cables in one quadrant of the cross-section of an LHC dipole magnet are shown. The shading shows the intensity of the magnetic field in the conductor. LHC dipoles consist of two layers: The outer layer with 25 turns of LHC type 02 cable, numbered from 1 to 25 and the inner layer with 15 turns of LHC type 01 cable, numbered from 26 to 40. The magnetic field map shows that the highest average magnetic field and the highest maximum magnetic field in the conductor are in turn 40. The magnetic field on each conductor throughout the cross-section of the magnets is inhomogeneous. To prevent magnetic field errors and achieve good current distribution, the possible current paths in the conductor need to be fully transposed. Therefore the cables need to consist of fully transposed strands.

In figure 1.3b the magnetic field in the turns of one octant of the current SIS 300 dipole design is shown. The quadrupole is designed with one layer of cables. At the design magnetic field gradient in the aperture of 45 T/m, the maximum field in the conductor is 3.6 T in turn 20.

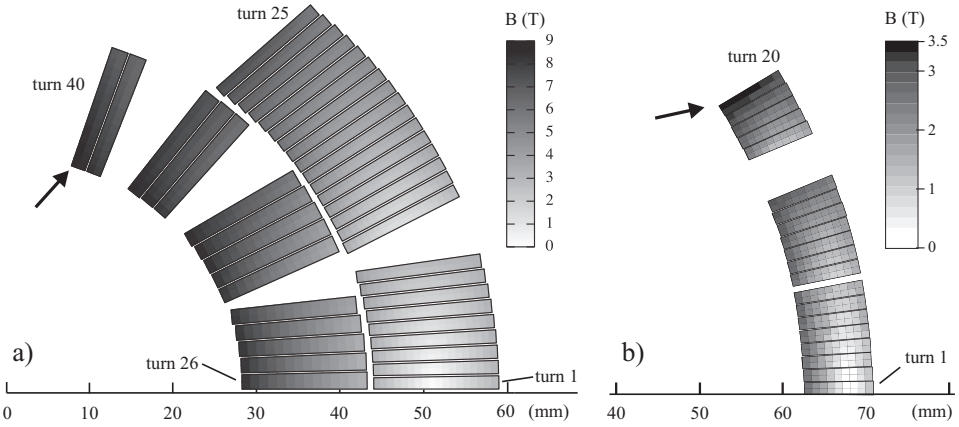

Figure 1.3: a) The magnetic field in the cables of one quadrant of an LHC dipole magnet with a central field of 8.33 T. The winding is divided in two layers consisting of two different cables. b) The magnetic field in one octant of the current SIS 300 quadrupole design with an aperature gradient of 45 T/m. The arrows indicate the positions with the highest magnetic field.

The coils of a magnet need a force restraining system. In figure 1.4a the cross-section of the 15 m long LHC dipole magnet is shown. It consists of a twin aperture guiding two bundles of proton beams in opposite direction. Therefore the magnetic field in the apertures is opposite. The superconducting coils are surrounded by non-magnetic support collars, which provide a part of the prestress and define the geometry of the coils. The iron yoke shields the exterior against the internal field and enhances the central field in the aperture. The outer cylinder, having a diameter of 57 cm, provides structural rigidity of the cold mass. To cool the cold mass, the system is filled with liquid helium. The temperature is further reduced to 1.9 K by using a heat exchanger. In the heat exchanger tube, the helium temperature is controlled by keeping the helium at vapor pressure. Between the cold mass and the vacuum vessel, a vacuum is produced to prevent heat leak through conduction. The diameter of the vacuum vessel is 91 cm. The multilayer superinsulation reduces heat exchange by radiation between the warm and cold parts of the system.

In figure 1.4b, the inner part of the cross-section of the most recent design of the 8 m long SIS 300 quadrupole magnet is shown. The shrinking cylinder is 34 cm in diameter. The SIS magnets are cooled with forced flow of supercritical helium, therefore the cooling system is different from LHC magnets.

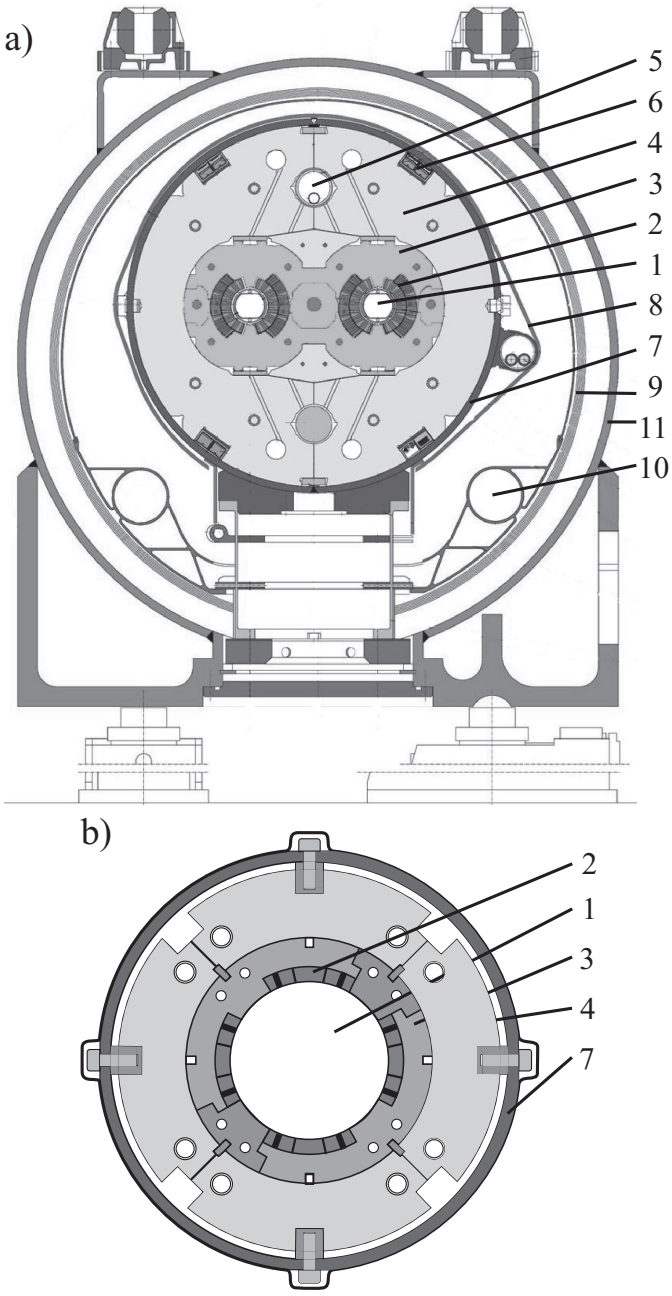

Figure 1.4: Cross-section of a) the LHC main dipoles and b) the designed SIS main quadrupole.

1. Beam pipe
2. Superconducting coils
3. Stainless steel collars
4. Iron yoke
5. Heat exchanger
6. Busbars
7. Shrinking cylinder
8. Superinsulation
9. Thermal shield
10. Gaseous helium pipe
11. Vacuum vessel

1.2 Superconductivity

Superconducting materials have been used in many applications since the discovery of the superconductivity of Mercury in 1911. Superconductors only exhibit zero electrical resistance below a critical surface, dependent on temperature, current density and magnetic field.

So-called type II superconductors are capable of carrying high-current density at high-magnetic fields. Since the 1950's the most commonly used materials are NbTi and Nb_3Sn. The main magnets of all existing and near future accelerator systems are constructed with NbTi conductor. NbTi and Nb_3Sn magnets are cooled with helium as a cryogenic at temperatures from 1.8 to 5 K. In 1985 superconductivity in complex compounds with cuprate layers was discovered with high critical temperatures, permitting cooling with fluid nitrogen at 77 K. The difference in the usable cryogen has led to a division of superconductors in low-temperature superconductors (LTS) and high-temperature superconductors (HTS). More recently the superconducting properties of MgB_2 are discovered and with a critical operation temperature of 39 K, it can be regarded as an intermediate temperature superconductor.

1.3 Practical superconductors

Superconductors in high-magnetic field applications, like accelerator magnets, require high current density at high-magnetic field. Large magnets cannot be built from wires made of pure superconductor, due to the intrinsic instability of a superconductor: the normal resistivity of superconductors, above the critical temperature T_c, is several orders of magnitude higher than the resistivity of Cu. When the temperature in a superconductor carrying high current density exceeds the critical temperature T_c, the resistivity increases strongly and Joule heating melts the superconductor a short time later. To prevent the superconductor from overheating at $T > T_c$, superconducting filaments are incorporated in a normal metal with low electrical resistivity.

Pure and large superconductors are vulnerable to heat generation caused by flux jumps. Flux jumps are prevented by the use of thin filaments in the order of a few tens of μm. To reduced the magnetic field errors, for accelerator magnets the filament size is further reduced to a few μm.

In accelerators at injection field, the field errors and energy loss are mainly determined by the filament magnetization. Filament magnetization or loss is reduced by the use of fine filaments [4]. The magnetization of filaments is linearly related to the filament diameter d_f and can be described by

$$M = \lambda \mu_0 \frac{2}{3\pi} J_c d_f \quad [Am^{-1}], \tag{1.1}$$

with λ the filling factor, μ_0 the permeability of vacuum, J_c the critical current density.

Technically, to fulfill the requirements for carrying high current densities, the superconducting material is incorporated in a good conducting matrix with many filaments; the strand.

In section 1.3.1 the design of superconducting strands is described. In section 1.3.2 five designs of superconducting cables and the relevance of this thesis for each design are discussed.

1.3.1 Strands

The volume of a superconducting strand contains superconducting filaments in a normal conducting matrix, typically Cu. Due to the requirements of thin and twisted filaments, the production takes many steps. The production of NbTi strands starts with hexagonal shaped Cu tube, in which a NbTi rod is inserted. The production process involves extrusion, rolling, drawing, stacking and re-stacking. Finally a cylindrical wire with a diameter in the order of 1 mm is produced. In figure 1.5, the cross-section of an LHC 01 strand is shown. It is made in a double stack process with in total about 8900 filaments stacked in a hexagonal structure.

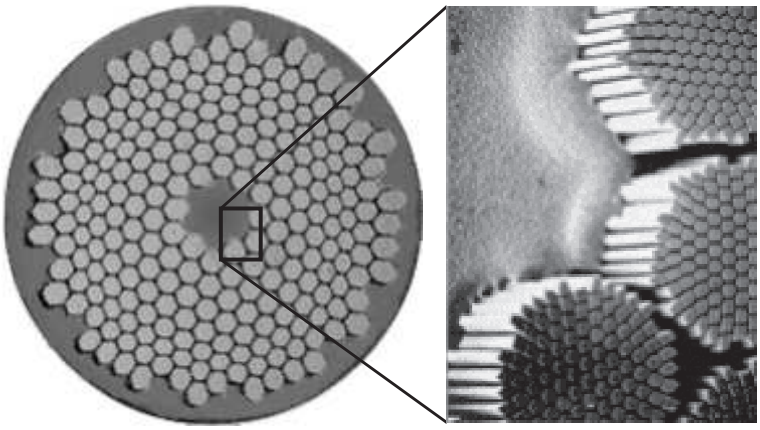

Figure 1.5: Cross-section of a superconducting strand with about 8900 filaments in a double stack pattern. Filament bundles are stacked in a hexagonal structure as is visible in the enlarged section.

The experiment and simulations presented in this thesis are performed on cables composed of three strand designs, LHC 01, LHC 02 and SIS 300 strands.

- LHC 01 strands are part of the LHC cable in the inner layer of the main dipole magnets.
- LHC 02 strands are part of the LHC cable in the outer layer of the main dipole magnets and both layers of the LHC main quadrupole magnets [1]. They are also a subject in the experimental stability research program for the main dipole and quadrupole magnets of the SIS 300 accelerator.
- SIS 300 strands are part of the design of the main dipole and quadrupole magnets of the SIS 300 accelerator [5].

The main specifications are listed in table 1.2.

Table 1.2: Specification of the strands of the LHC main dipole inner layer cable (LHC 01) and outer layer cable (LHC 02) [1] and the SIS 300 cable. These wires are used as reference-wires throughout this thesis.

Parameter	LHC 01	LHC 02	SIS 300
Diameter (mm)	1.065	0.825	0.825
Copper to superconductor ratio	1.65	1.95	1.40
Filament diameter (μm)	7.0	6.0	3.5
Number of filaments	$\approx$ 8900	$\approx$ 6500	*
RRR	$\geq$ 150	$\geq$ 150	*
Filament twist pitch after cabling (mm)	18	15	4 - 5
Critical current at 10 T, 1.9 K(A)	$\geq$ 515	-	-
Critical current at 9 T, 1.9 K (A)	-	$\geq$ 380	-
Critical current density at 5 T, 4.2 K (Amm^{-2})	-	-	2700
Coating material	$Sn_{0.95}Ag_{0.05}$	$Sn_{0.95}Ag_{0.05}$	*

* The design is not yet finalized

1.3.2 Cables

Most applications with high-field or high-current density require conductor with fully transposed current paths to ensure low AC-loss and homogeneous current density. In applications like accelerator magnets, fusion magnets, high-current transport cables, transformers and motors, multiple cable designs are used. The structure of five cable designs is shown in figure 1.6 and discussed.

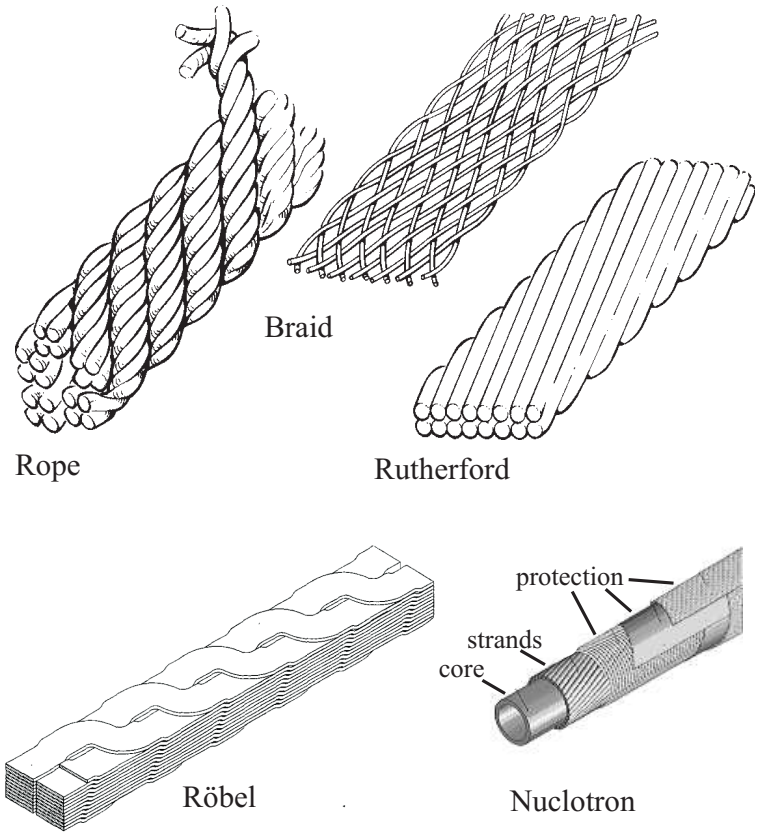

Figure 1.6: Different types of design for superconducting cables.

- **Rutherford**-type cable design is used in all current accelerator magnets and in the SIS 300 design. It is a favorite design for high-field accelerator type superconducting magnets for several reasons. It allows the highest current densities due to a very high packing factor. The good stacking possibilities and the mechanically stable structure of the Rutherford cable provide a good base for application in magnets. The research in this thesis is focused on Rutherford type cables.
- **Rope**-type cables exist of multistage twisted strands and and are mainly applied in Cable-in-Conduit-Conductor (CICC). For example; cables for the ITER coils incorporate more than thousand strands and have a sufficient void fraction to allow forced supercritical helium flow through the cable. It is not used for accelerators as it lacks the advantages of the Rutherford cable.
- **Braid**-type cables are, relative to the Rutherford type cable, more vulnerable to force applied on the broad surface of the cable. Magnets containing high

Table 1.3: Survey of the geometry of Rutherford-type cables of existing and future accelerator dipole magnets.

Accelerator	Specification	Cable type	Nr. of strands	Width or diam. mm	Av. height mm	Strand coating
RHIC		Rutherford	30	9.7	1.17	none
LHC	LHC 01	Rutherford	28	15.1	1.90	SnAg
	LHC 02	Rutherford	36	15.1	1.48	SnAg
HERA	inner layer	Rutherford	24	10	1.48	SnAg
	outer layer	Rutherford	24	10	1.48	SnAg
Tevatron		Rutherford	23	7.8	1.26	zebra
SIS 100		Nuclotron	23-38	7.4 - 8.3	-	*
SIS 300	dipole	Rutherford	36	15.1	1.48	*
	quadrupole	Rutherford	19	8.45	1.48	*

*The design is not finalized yet.

current density combined with high field need high parallel and transversal pressures to counteract against the Lorentz force. Rutherford cables have shown better stability against thermal disturbances and a better mechanical stability over braid cables and are therefore more favorable to apply [6].

- **Nuclotron**-type cables consist of spiraling strands around a tube. A Nuclotron cable can be cooled by a forced forced flow of helium through the central tube. In some designs a helical structure is used to provide the strands with direct helium cooling too. Nuclotron cables and Rutherford cables are closely related as the latter can be considered as a flattened Nuclotron cable. The Nuclotron cable is used in the design propositions for the SIS 100 magnets [3].

- **Röbel**-type cables are composed of a flat conductor with meander geometry. Röbel cables are thought to be feasible for HTS tape cables for application in superconducting transformers and second generation fusion reactors [7]. The Röbel cable consists of ribbon or tape conductors and the structure is roughly comparable to the Rutherford cable with round conductor. The design is mainly useful for HTS tape conductor. Therefore the material characteristics are very different from the conductors that are under investigation in this thesis and no quantitative statements can be given.

Rutherford cables exhibit the most profitable characteristics for superconducting accelerator magnets. Therefore Rutherford cables are used in the existing and near future accelerator magnets, except for the SIS 100 design, which is featuring Nuclotron type cables [2]. The research in this thesis is focused on the stability of Rutherford cables. An overview of the cable specifications in the current and near future accelerator magnets is given in table 1.3.

The experimental set-up was initially designed to perform the reception tests of the Rutherford cables for the LHC magnets. Special sample holders are designed for the stability experiments.

The simulation model CUDI is specially designed to investigate the effect of time varying current distribution in Rutherford cables. For the research to cable stability a thermal model is added. All thermodynamic and electrodynamic behavior can now be simulated with CUDI. A more detailed description of CUDI is given in section 2.3.3.

For cable stability against short local heat disturbances, small time scales are involved of a few tens of ms. Fast current redistribution proves to be very important in providing improved cable stability. It is proven that the primary current redistribution is into parallel strands, due to its low inductive current paths.

In general, current redistribution is a main issue for cable stability and therefore cables that provide parallel current paths and interconnections between strands will have corresponding thermodynamic and electrodynamic behavior. Therefore the qualitative description of cable stability is useful too for other cables with parallel strands.

Nuclotron cables can be modeled with the same network model of nodes that describes the adjacent contacts in the Rutherford cable. In CUDI the cross contacts between strands can be ignored and therefore it provides the possibility to simulate Nuclotron cables as well. However, the geometry of nuclotron cables is different from the geometry of Rutherford cables and therefore current redistribution paths exhibit different inductance. Since the main current redistribution is into the neighboring parallel strands it is assumed that the variation is too small to give large errors.

The network of interconnecting nodes describing the Röbel type cable structure is similar to the network of the Rutherford type cable. The conductor type and the contacts between the conductors are different from the conductor and contacts in the Rutherford cable. The Röbel type cable is not investigated in this thesis, but the cable stability mechanisms described here may be relevant.

The strands in a Braid type cable alternate their paths between both layers of the cable and provide semi-parallel paths. The relevance of the cable stability research on Rutherford cables for cable stability of Braid type cables is hard to estimate.

Rope type cables have a complex structure of strands. Parallel current paths exist, but the total structure and the type of application is very different from the Rutherford cable type. Although some similarity is present, the results of this thesis are not extrapolated to Rope type cables.

Table 1.4: Characteristics of the reference cables used throughout this thesis.

	LHC 01	LHC 02	SIS 300 dipole	SIS 300 quadrupole**	model cable
Cable type	Rutherford	Rutherford	Rutherford	Rutherford	Rutherford
Cable width (mm)	15.1	15.1	15.1	8.25	9.7
Cable av. thickness (mm)	1.9	1.48	1.48	1.48	1.9
Keystone angle (°)	1.25	0.90	0.90	0.90	1.25
Strand type	LHC 01	LHC 02*	LHC 02*	LHC 02	LHC 01
# strands	28	36	36	19	18
Strand diameter (mm)	1.065	0.825	0.825	0.825	1.065
Twist pitch strands (mm)	100	110	110	110	64
Strand coating	various	AgSn	AgSn	various	various
Core	none	none	25 μm SS	various	various

* In the stability experiments and simulations the cables are composed of LHC 02 strands, while the design uses SIS 300 strands.
** In simulations an 18 strand cable is used as CUDI requires an even number of strands.

Throughout this thesis, 5 types of Rutherford cables are used for stability investigated, consisting of three types of strand, see section 1.3.1. The characteristics of the reference cables are listed in table 1.4.

For systematic parameter variation study in chapters 4 and 5, a model cable is specified, comprising LHC 01 strands. The design is based on the LHC 01 cable, but to reduce the simulation time the number of strands is reduced to 18 strands.

Measurements and simulations presented in chapter 6 have been performed on LHC 01 cables and SIS 300 dipole cables. The LHC 01 dipole cable is designed for the inner turns of the LHC main dipole magnets and the LHC quadrupole magnets and it consists of 28 LHC 01 strands. The strands for the final design of the SIS 300 cable were not finished before the stability research, therefore the SIS 300 dipole cable referred to in this thesis is based on the LHC 02 outer cable produced with 36 LHC 02 strands.

The simulations performed in chapter 7 quantify the stability of cables in the LHC main dipole magnets and cables in the SIS 300 main quadrupole magnets. Therefore the used cables are of the type: LHC 01, LHC 02 and SIS 300 quadrupole.

1.4 Quench and recovery

The high-current density of superconducting wires and cables gives high expectations for high-field superconducting magnets. However, most superconducting magnets tend to suffer from repetitive quenches before the full current density is reached. A quench is defined as the sudden and irreversible transition of the superconductor into the normal-conducting state. The global temperature increase in the cable requires re-cooling to normal operation temperature before normal operation can be resumed.

Normally a training behavior is observed, whereby the quench magnetic field improves after consecutive current test cycles of the magnet. In general, the number

of training quenches that are needed to reach the design current increases with the length and bore size of the magnet [8]. Since magnet training is very expensive and time consuming, it is necessary to reduce the number of training quenches as much as possible.

The magnets of the current superconducting accelerators have shown to train with an average number of quenches of 0.5 for the HERA magnets to 4 for the Tevatron magnets [9]. Magnet training is a major issue in large scale magnet systems as for example the most recent and largest system, the LHC. The 1232 LHC main dipole magnets have been tested and trained prior to installation in the ring, with an average training number of 0.9 quenches per dipole, to reach the design current and magnetic field of 8.33 T [10]. The 128 magnets that performed the worst were tested again after a full thermal cycle and for this second test an average training number of 0.3 quenches per magnet was needed.

After a thermal cycle, storage and transport, the dipole magnets were installed in eight sections, each comprising 154 dipoles in series. During the commissioning of the accelerator system, one octant is trained up 7.9 T. Extrapolation of the quench field during this retraining, see figure 1.7, suggest that about 160 training quenches are needed before the design field of 8.33 T [11] is reached.

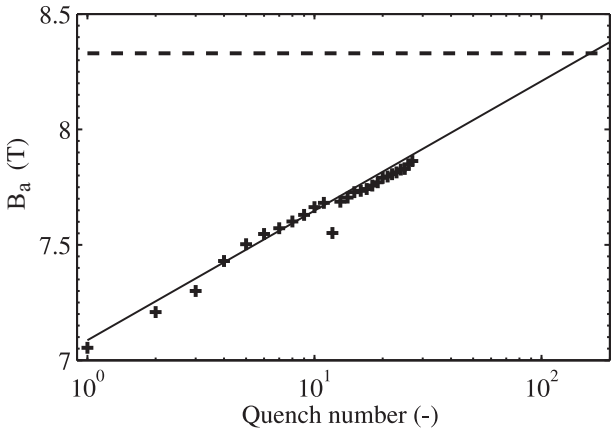

Figure 1.7: The aperture magnetic field as a function of the consecutive quench number in one octant of the LHC main magnet ring, consisting of 154 dipole magnets [11]. Each cross indicates a quench in one dipole, the line shows an exponential extrapolation. The dashed line shows the design magnetic field of 8.33 T.

The increase in the number of quenches as function of the increase in quench field seem to depend exponentially on the magnetic field, see figure 1.7. Three important characteristics for cable stability change strongly as a function of magnetic field as well. The temperature margin T_m decreases strongly for increased magnetic field. The normalized current $i = I/I_c$ increases more than linear with increasing magnetic field and the Joule heating in the case of a normal zone in

the cable increases quadratically with the current and hence the magnetic field. The three characteristics are shown in figure 1.8 for that part of the LHC 01 cable subject to the highest magnetic field, i.e. turn 40 in figure 1.3, as a function of the central aperture magnetic field B_a.

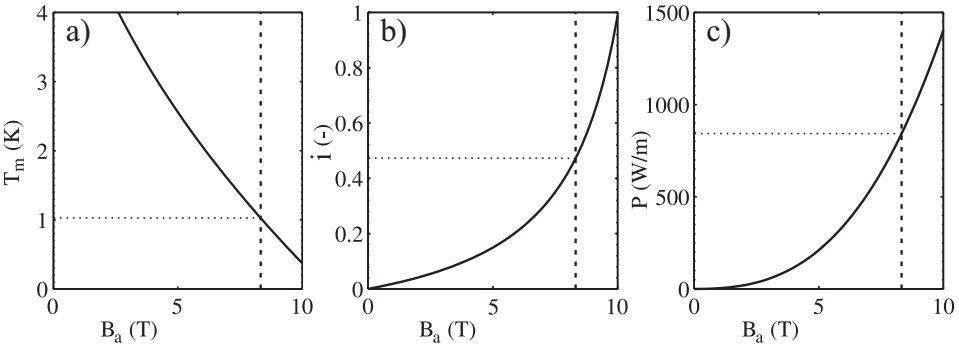

Figure 1.8: Three characteristic values of the LHC 01 cable in the highest field position as a function of the central aperture field, with a) the temperature margin, b) normalized current and c) the heating power per meter of cable when the full cable exhibits normal resistance at 10 K. The dashed line indicates the design field of 8.33 T.

A reasonable temperature margin of the superconductor is necessary for stable operation, therefore the practical working magnetic field is considerably lower than the conductor limit. For instance the 15 meter long LHC main dipole magnets are designed to operate at 86 % on the load line, which is state of the art performance for slow ramping magnets [1]. The temperature margin of the conductor at the highest magnetic field position is 1.5 K.

Instability of a superconductor is dominated by the increase of the resistance in a superconductor with orders of magnitude for a small temperature change of tenths of K. The thermal runaway process leading to a quench is visualized in figure 1.9a. A source of heat with an energy as small as a few to tens of μJ can create a normal conducting zone in a strand. This event can cause a quench in a full magnet and the extraction of the magnetic field. The total energy of the magnet at nominal field, in the order of 10 MJ for an LHC dipole magnet, heats up the magnet. After such an event the cool down of the magnet takes a few hours and operation of the accelerator is halted. This is a very costly process and causes additional down-time for the physics experiments. Therefore it is important to build magnets as stable as possible.

One possibility for recovery from a local normal zone in a magnet is the reduction of Joule heating. In cables this is possible if a part of the strands remain superconducting while others are locally normal. Current redistribution is forced by the resistance of the normal conducting zone and the current in the normal

conducting zones is reduced. Joule heating is reduced and the normal zone can cool-down to the superconducting state again, see the visualization in figure 1.9b. The goal of research on cable stability is to describe the mechanisms involved in the recovery process and to implement possible changes in cable design that can improve the recovery process.

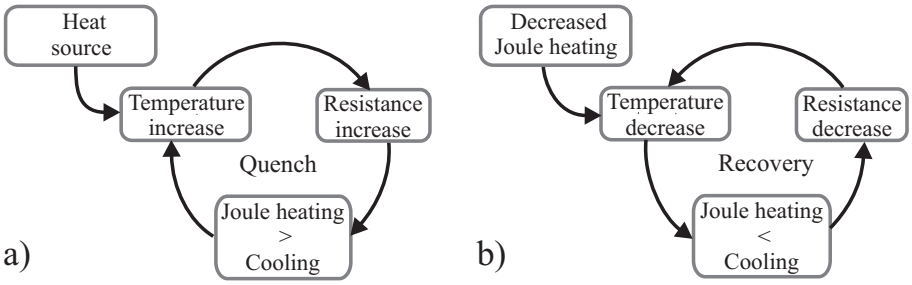

Figure 1.9: a) Scheme illustrating the mechanism leading to a quench. b) Scheme illustrating the mechanism of recovery from a local normal zone.

1.5 Scope of the thesis

The ultimate goal of this thesis is to provide the tools for predicting and optimizing the stability of superconducting cables. The maximum operational magnetic field of magnets in an accelerator system is determined by its training quench behavior. Crucial is the smallest amount of heat that can quench a conductor in a magnet, the Minimum Quench Energy (MQE). In the worst case, the MQE is equal to the energy needed to raise the temperature of a single strand to above T_c over a length of a few mm. Minimum Quench Energies involved are in the order of a few μJ.

In a real magnet, the magnetic field along the conductor, but also local cooling conditions, mechanical pressure and the magnetic field gradients are very different from the conditions in a cable test station. Thus it is very hard to mimic magnet operation conditions in experiments. Therefore the strategy is to use the advanced simulation model CUDI to perform parameter studies for finding optimum conditions and to validate CUDI by systematic comparison with test cases. After validation the magnet specific parameters and geometry are used as input in CUDI to provide the MQE curves and to investigate the possible improvements of stability.

In figure 1.10 the structure of this thesis is shown. The arrows show the flow of information and the connection between the chapters. The parts of the chapters that overlap with the gray area rely on simulations with CUDI.

The thesis is structured along the following chapters:

- In chapter 2 the sources of heat in an accelerator magnet are briefly discussed. The theory of superconductor stability is described for strands, cables and magnets. The network model CUDI is introduced and used to identify the

mechanisms of cable stability. The characteristics of cable stability are discussed and a definition of cable stability regimes is given.

- In chapter 3 the experimental details for stability measurements are given. It includes a description of the experimental set-up, the heaters, the measurement procedure, local self-field measurements and local voltage measurements. The cable geometry is investigated and the interstrand contact surface, helium contact surface and the helium volume are determined across the cable. The cable geometry is described and volumes and surface areas across the cable width are obtained.

- In chapter 4 the interstrand contacts are investigated. A wide variety of strand coatings is present, which determines the interstrand electrical resistances and the interstrand thermal contact as well. The influence of both parameters on cable stability is examined with CUDI.

- In chapter 5 the effect of local cooling conditions by helium on the cable stability is investigated. Literature provides a theoretical base for heat flow and heat flow limits of helium to small volumes for superfluid He II, liquid He I and supercritical helium. The influence of variation in helium cooling parameters for the three helium phases is examined with CUDI as well.

- In chapter 6 the measurement results for a variety of cable samples are presented. The model CUDI is used to simulate the measurement data with the parameters obtained in the previous chapters. By varying the parameters of interest a best fit of the measurement data is obtained. A stepwise scheme for obtaining the best fit parameters for a specific sample is given. The reliability of results obtained with CUDI is discussed.

- In chapter 7 the impact of cable design on magnets regarding stability is investigated for a few cases using CUDI.
  - The MQE curves for three turns in an LHC dipole magnet and one turn in an SIS 300 quadrupole magnet are investigated.
  - The effect of non-uniform current distribution on cable stability is shown for the LHC dipole and SIS 300 quadrupole magnet.
  - The choice between a cored cable and a highly resistive coating for the SIS 300 quadrupole magnets is discussed.
  - Cable edge stability is investigated with options for improvement.
  - The influence of mixed strands on cable stability is discussed.

The research on cable stability and the quantification of MQE levels in the superconducting cable are essential for the reduction of magnet quenches by optimizing the cable properties.

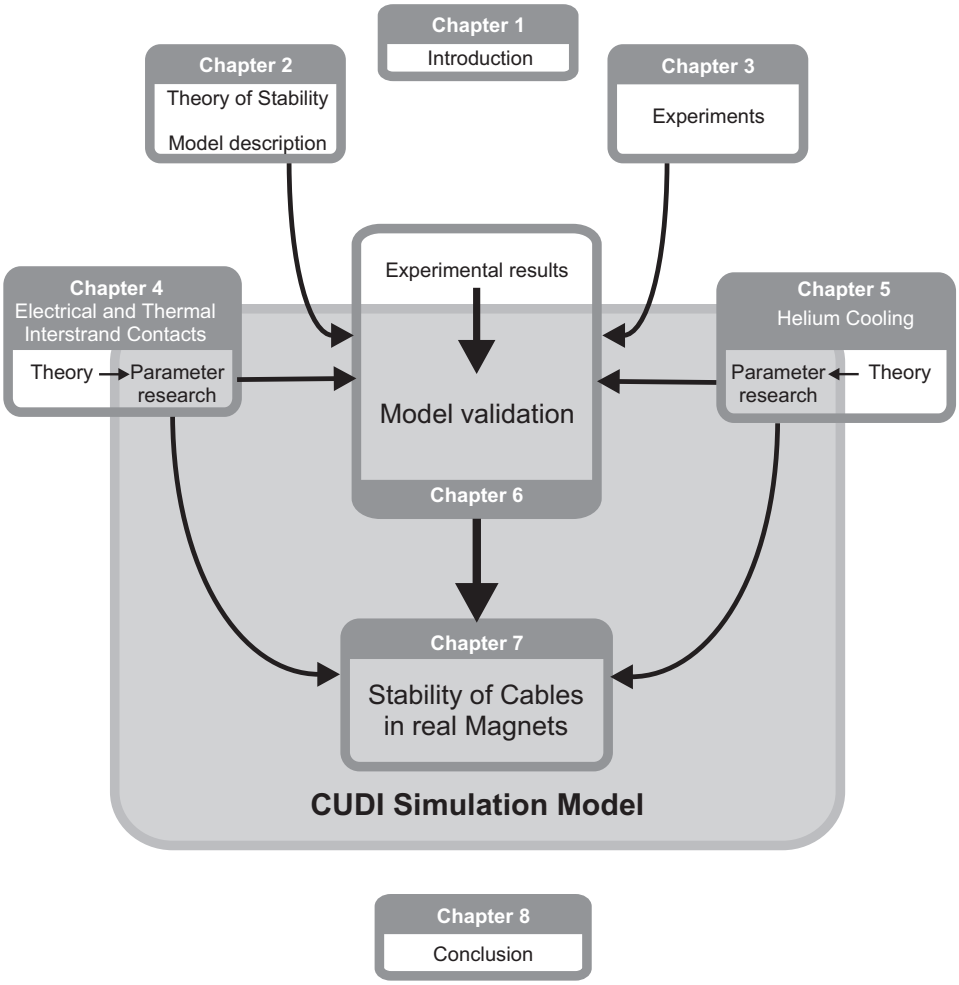

Figure 1.10: Outline of the thesis. The arrows show the flow of information and the connection between the chapters. The part of the chapters that overlap with the gray area, rely on simulations with CUDI.

Chapter 2

Superconductor Stability

The main goal of this chapter is to describe the electrodynamic and thermodynamic mechanisms that contribute to the stability of a superconducting Rutherford cable.

The sources of heat in accelerator magnets and the impact on cable stability are investigated. The relevance of the experiments and simulations for the various disturbances is discussed.

Stability of superconducting wires is well defined in literature by a reliable model consisting of basic thermal and electrical equations. For superconducting cables featuring a complex network of strands and strand-to-strand contacts, current distribution in the network has to be taken into account. Therefore, a proper definition of cable stability is far more complex as compared to single wire stability.

Models for investigation of cable stability are described and the most detailed model, the numerical network model CUDI*, is presented.* CUDI *is used to provide detailed information about stability behavior.*

Investigation of transversal normal zone propagation into adjacent strands and crossing strands, provides a good basis for defining quench criteria. Multiple quench criteria are defined and used for a reconstruction of the MQE *curves for local transient heat depositions in cables. With the quench criteria, multiple stability regimes are presented. The relevance of the electrodynamics and thermodynamics for each quench criterion is discussed.*

The variations in geometrical parameters across the cable width are investigated. A set of values depending on the cable width is given for the interstrand contact areas, the area cooled by helium and the void volume for LHC *01 and* LHC *02 cables.*

2.1 Sources of heat

Heat sources in accelerator magnets can be subdivided in steady state and transient heat sources. Steady state heat sources deposit energy in the magnet coils over a long period. The cooling of the coils is designed to maintain the operation temperature and to extract the heat from the system. Transient heat sources occur suddenly at random places, in some cases initiating a local normal zone in the conductor. A second subdivision is made by identifying the heated volume of conductor from local, i.e. a small length of one strand, to global, i.e. a volume across the full cable width. An overview of several sources of heat in accelerator magnets is given in figure 2.1.

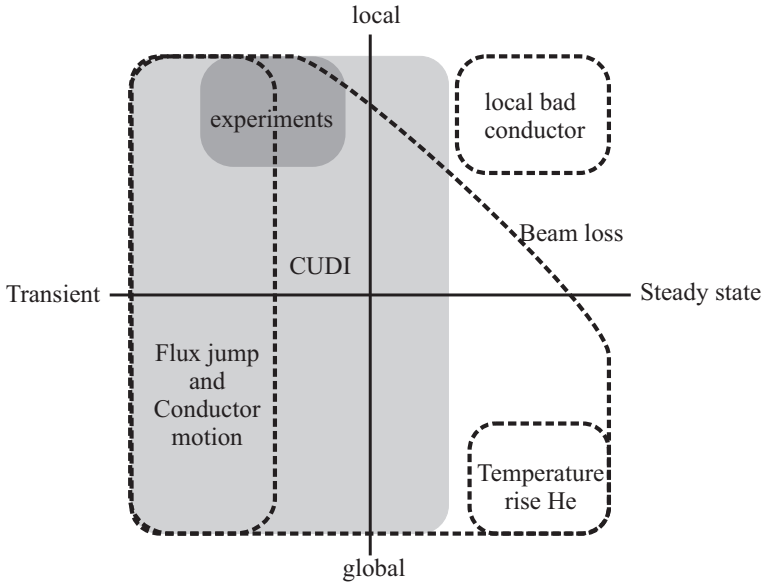

Figure 2.1: Illustration of the duration and heated volume of several sources of heat in accelerator magnets. The light gray area indicates roughly the valid range of cable stability simulations with CUDI. The dark gray area shows the range of experimental data in this thesis.

The volume, duration and intensity of each heat source are very hard to quantify. An estimated range of the energy deposited by heat sources is given in figure 2.2.

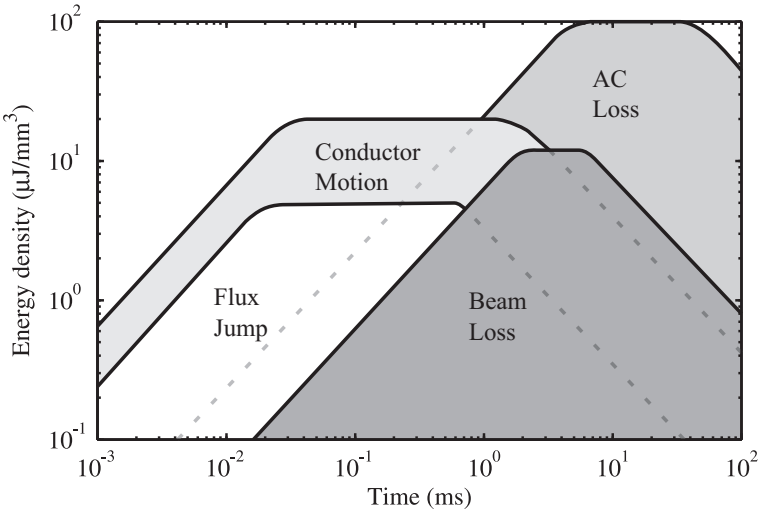

Figure 2.2: Expected spectrum of heat sources for superconducting accelerator magnets built with low-T_c superconductor [12].

The enhancement of stability in a cable compared to strands is dominated by the ability of current redistribution. In order to facilitate this enhancement an important condition needs to be fulfilled: If a part of the strands is normal conducting then other strands need to be superconducting to provide a current redistribution path. If a local normal zone is created, time scales involved in quench decision are small, normally in the order of 0.1 to 10 ms. Cable stability research is therefore mainly interesting when dealing with local transient heat depositions.

The experimental set-up, see chapter 3, is designed for short and local heat pulses to the cable, with a heater diameter of 0.5 mm and a pulse duration of 100 μs. In figure 2.1 the range of experimental investigation in this thesis and the possible investigation with CUDI simulations is shown.

2.1.1 Steady state loss

The energy deposited by steady state heat sources needs to be extracted from the conductor to maintain the operation temperature. In the superfluid helium cooled LHC magnets, the windings comprise channels in the cable insulation wrapping that are filled with helium II to remove the heat from the system. Due to the high and effective heat transfer in helium II the temperature is maintained at an acceptable level [13]. In magnets containing supercritital helium, like in the SIS accelerators, heat is extracted mostly by a forced flow of supercritical helium.

Four sources of steady state heat are shortly discussed:

- Steady state beam loss is inherent to accelerator magnets. Charged particles that are deviated from their path, will produce synchrotron radiation, which is mostly intercepted by the beam pipe. Calculation of the steady state beam loss in LHC dipole magnets at operation magnetic field shows a global energy deposition in the order of 4.5 μW/mm^3 [1].
- Local heat deposition is expected if the superconducting properties of a strand is locally reduced. If the conductor is locally at the transition from superconducting to normal state, Joule heating starts. Part of the current will be redistributed into neighboring strands. For low current density and sufficient cooling, this will not necessarily lead to a quench.
- Global and steady state heating of the conductor can be present in accelerator magnets that are placed in series. When a neighboring magnet has quenched, the other magnets are ramped down slowly, during which the overall helium temperature increases. The temperature of non-quenched magnets can increase gradually, and in some cases a quench follows [11].
- Variation in time of the magnetic field induces various types of AC loss in the conductor. Hysteresis loss in a filament is linearly related with the filament diameter. In particular interfilament currents and interstrand currents generate heat in the matrix and at the interstrand contacts. A requirement for the minimum interstrand resistances is defined to limit the induced interstrand currents. Fast ramping magnets require higher interstrand resistances than slow ramping magnets.

The effect of steady state heating is not investigated in this thesis. In experiments and simulations homogeneous initial temperature conditions are assumed. However, local variations of the operation temperature in time and space may influence stability.

2.1.2 Conductor motion

In the main magnets of the current superconducting accelerators non-impregnated NbTi conductors are used. Strand movement in non-impregnated conductors is caused by the Lorentz force F_L which is the product of magnetic field B, current I and conductor length l:

$$F_L = BIl \quad [N], \tag{2.1}$$

see figure 2.3. For example in strands of LHC magnets, carrying 420 A at 8.3 T a force of 190 N per half a twist pitch is generated. The so-called slip-stick movement or microslips produce heat due to friction and elongation. The unstable sliding behavior of different materials causes instant heat pulses, while stable sliding would reduce the chance of instant heat dissipation. Stable sliding can be achieved by using strand coating materials with a high level of hardness [14]. Training quenches are mostly attributed to stick-slip movement of a strand, when during the increase of field and current the Lorentz force increases and heat is released in the conductor [15, 16, 17].

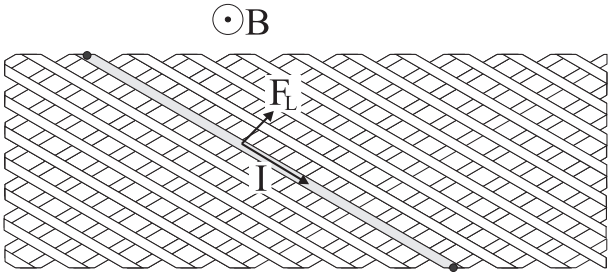

Figure 2.3: A strand carrying current I in a perpendicular magnetic field B is subjected to the Lorenz Force F_L. The assumed strand length subjected to motion is half a twist pitch, shown in gray. Dots show the assumed fixation points.

Two techniques are used to detect motion induced disturbances during a current ramp, namely Quench-Antenna pickup-coils (QA) and Voltage-Taps (VT) [18]. The QA measurements are sensitive to count the number of events, while VTs are used to find the amplitude of voltage spikes. The measurements show that conductor motion is not just an event that occurs once during a ramp up, but it happens many times. As an example, for three full scale LHC magnet prototypes that are ramped at a rate of 0.007 T/s, the number of events with an amplitude above the threshold of 0.1 mV are recorded in the last 9 seconds before quench. The number of events are 2000, 5000 and 9250 for a first ramp of the magnet at fields of 7.46, 8.07 and 8.23 T, respectively. The typical duration of a spike is 0.1 - 10 ms, see figure 2.4, with the longest duration for the highest spike voltage.

The motion-induced voltage in one strand is described by

$$V_{emf} = Bl\frac{dx}{dt} \quad [V], \tag{2.2}$$

with the movement of the strand over a distance dx and a length l during a time dt [6]. The work on the strand by the Lorentz force is described by

$$dW = F_L dx \quad [Nm]. \tag{2.3}$$

By combining (2.1), (2.2) and (2.3) and assuming that all the energy is dissipated as heat in the strand, the upper limit of energy dE dissipated per unit cross-section is

$$dE = V_{emf} J dt \quad [J]. \tag{2.4}$$

By integrating over time and and space, the total energy Q is calculated by

$$Q = J\frac{\pi d_s^2}{4}\int_0^t V_{emf} dt \quad [J]. \tag{2.5}$$

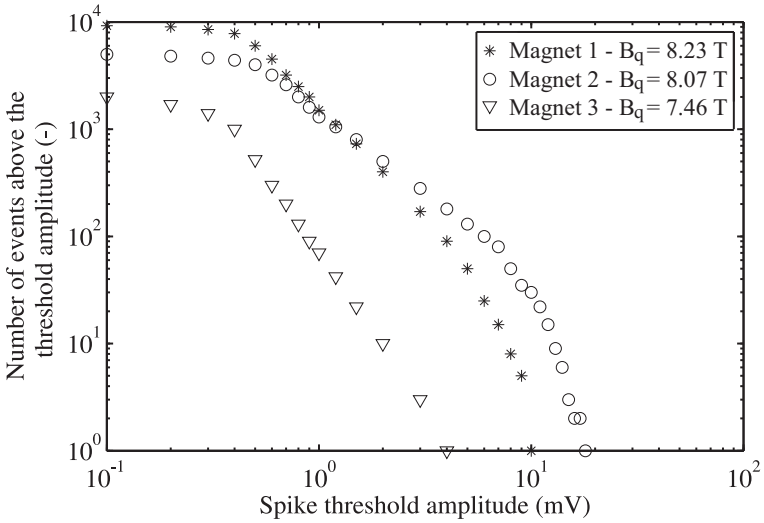

Figure 2.4: Number of recorded spikes with a voltage above the threshold voltage for the last 9 seconds before the first quench of three different full scale LHC prototype dipole magnets [18].

In [19] a measured voltage spike preceding a quench in an LHC prototype dipole is shown with a maximum voltage of 5 mV and a duration of 0.5 ms, with a strand current of about 400 A. With an assumed triangular shape of the spike, $Q \approx 500$ μJ. For the data shown in figure 2.4, the highest recorded voltage was 18 mV, with a duration of the spike of about 10 ms. Assuming dx is 5.5 cm, or half a twist pitch, see figure 2.3, $dx/dt = 0.4$ m/s and $Q \approx 35$ mJ. Since this value is much higher than 500 μJ, it is likely that a large fraction of training quenches in this type of accelerator magnets is due to strand movement [17].

2.1.3 Epoxy cracking

In the main magnets of the current superconducting accelerators non-impregnated NbTi conductor is used, while magnets with Nb_3Sn conductor are typically impregnated. Although conductor motion is eliminated by the impregnation, large shear stresses in the coil can cause epoxy cracking. Conductor motion caused by micro-cracks is determined by Acoustic Emission (AE) measurements for pairs of wires and braid cables [15]. AE measurements during the first ramp of current in a conductor show irreversible motions that are absent during the second ramp. The floating-coil design [20] was introduced to eliminate most of the shear stress in the coil and the problem of epoxy fracture [21]. However, this method may not be appropriate for high-field magnets exhibiting large forces.

2.1.4 Transient beam loss

Transient beam losses are expected to provide much higher instantaneous rates as compared to steady state beam losses. Transient beam losses can originate as a result of injection errors, the fast growth of beam amplitude and beam manipulations [22]. Due to the high energy and the velocity near the speed of light, the particles deposit a trace of heat possibly in multiple strands.

The chance of transient beam deposition is the highest at the midplane of the accelerator, i.e. turns 1 and 25 in the LHC dipole magnet and turn 1 in the SIS 300 quadrupole magnet, see figure 1.3. The highest energy deposition is near the aperture of the magnet [23]. Therefore the thin edge is the most likely part of the cable to be affected by heat deposition from beam loss.

2.2 Definition of stability

Practical superconductors are vulnerable to losing their superconducting ability after an increase in temperature in the vicinity of the critical temperature T_c. When the temperature exceeds the local T_c the conductivity of the material decreases to its normal conductivity and the resistance increases rapidly with orders of magnitude. If a source that is finite in time and duration deposits heat in a superconductor, it will recover only if locally the cooling of the conductor exceeds the heat generation.

Pure superconductors tend to be unstable and generally not suitable for practical use in applications with high current density. Stable operation of superconductors in high magnetic field requires superconducting filaments embedded in a well conducting matrix, normally copper. Accelerator magnets are always wound from cables. In this section stability is defined for wires, cables and magnets.

2.2.1 Single wires

The thermal process within a wire is described by a general heat balance equation [8]

$$c\frac{\partial T}{\partial t} = \nabla(\kappa\nabla T) + p_{ext} + p_{diss} + p_{He} \qquad [Wm^{-3}], \tag{2.6}$$

where c is the volumetric heat capacity, T temperature, t time, κ thermal conductivity. p_{ext} is the heat flux from any external source per unit volume, p_{diss} is the heat dissipation per unit volume and p_{He} the cooling heat flow to the surrounding per unit volume, which is in most cases helium.

The heat capacity of Cu and Nb_3Sn depend only on temperature, while for NbTi it depends also on magnetic field for $T < T_c$. The heat capacity of helium depends only on pressure and temperature, for the various values see figure 2.5a.

The thermal conductivity of NbTi and Nb_3Sn can be neglected compared to the thermal conductivity of Cu. In pure metals at low temperatures, the thermal con-

ductivity and electrical conductivity are both dominated by free electrons. Therefore the thermal and electrical conductivity can be coupled by the Wiedemann-Franz law, although the ratio may vary as function of magnetic field [24]. The thermal conductivity is described by

$$\kappa_{cu} = \frac{L_0 T}{\rho_{cu}} \quad [WK^{-1}m^{-1}], \tag{2.7}$$

with L_0 the Lorentz number and ρ_{cu} the resistivity of copper. For copper $L_0 = 2.45{\cdot}10^{-8}$ WΩ/K^2. Figure 2.5b shows κ_{cu} at a field of 9 T for RRR = 150.

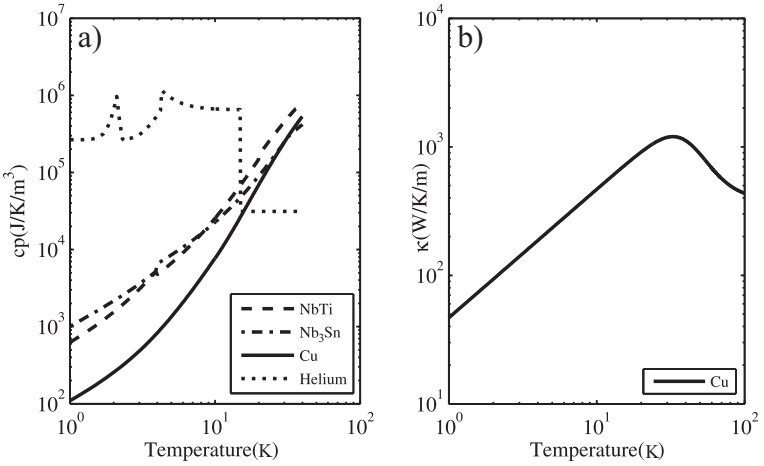

Figure 2.5: a) Specific heat as a function of temperature at $B = 9$ T of copper, helium, NbTi and Nb_3Sn. b) The thermal conductivity of copper with RRR = 150 at $B = 9$ T.

Under certain conditions it is justified to assume homogeneous temperature in the cross-section of the wire, giving a homogeneous c, κ and ρ throughout the cross-section. The assumption of homogeneous parameters in the cross-section is justified only when the characteristic thermal diffusion time in the filament $\tau_{\theta,f}$ is smaller than the characteristic magnetic diffusion time in the composite $\tau_{m,c}$ [8]:

$$\tau_{\theta,f} < \tau_{m,c} \quad [s]. \tag{2.8}$$

The diffusion time constants are described by

$$\tau_{\theta,f} = \frac{1}{1+\lambda} d_f^2 \frac{c_{sc}}{k_{sc}} \quad [s] \tag{2.9}$$

and

$$\tau_{m,c} = \frac{\lambda}{1+\lambda} d_s^2 \frac{\mu_o}{\rho_{cu}} \quad [s], \tag{2.10}$$

where c_{sc} the heat capacity of the superconductor, k_{sc} the thermal conductivity of the superconductor, d_f the filament diameter and d_s the strand diameter. For a NbTi strand, with $d_s = 1$ mm, $d_f = 7$ μm, $T = 1.9$ K, $B = 9$ T, $\lambda = 1.6$, $c_{sc} = 5000$ J/K/m^3, $k_{sc} = 0.1$ W/K/m and $\rho_m = 7{\cdot}10^{-10}$ Ωm the obtained value of $\tau_{\theta,f}/\tau_{m,c}$ is $9{\cdot}10^{-4}$. Therefore, NbTi strands fulfill the condition in (2.8) and the use of a homogeneous temperature throughout the cross-section of a strand is validated.

Now (2.6) can be replaced by the simplified one-dimensional heat balance equation in the longitudinal wire direction z

$$c\frac{\partial T}{\partial t} = \frac{\partial}{\partial z}\left(\kappa\frac{\partial T}{\partial z}\right) + p_{ext} + p_{diss} + p_{he} \qquad [Wm^{-3}]. \tag{2.11}$$

The various external heat sources p_{ext} are discussed in section 2.1. The heat dissipation in a normal conducting wire section with length ∂z is defined by

$$p_{diss}A_m\partial z = J_m^2 A_m \rho_{cu}\partial z \qquad [W], \tag{2.12}$$

with J_m the current density in the matrix, A_m the cross-sectional area of the matrix. ρ_{cu} is assumed to be constant below 10 K, where it is only depending on purity and magnetic field. The residual resistivity ratio RRR is defined as $\rho_{T=293,B=0}/\rho_{T=0,B=0}$ and gives an indication of the purity of copper. In figure 2.6 the resistivity of copper is given for a magnetic field of 0 and 9 T and for varying purity. For the LHC main magnets RRR $\geq$ 150 with the operation magnetic field close to 9 T, ρ_{cu} at low temperatures is dominated by its magnetoresistivity.

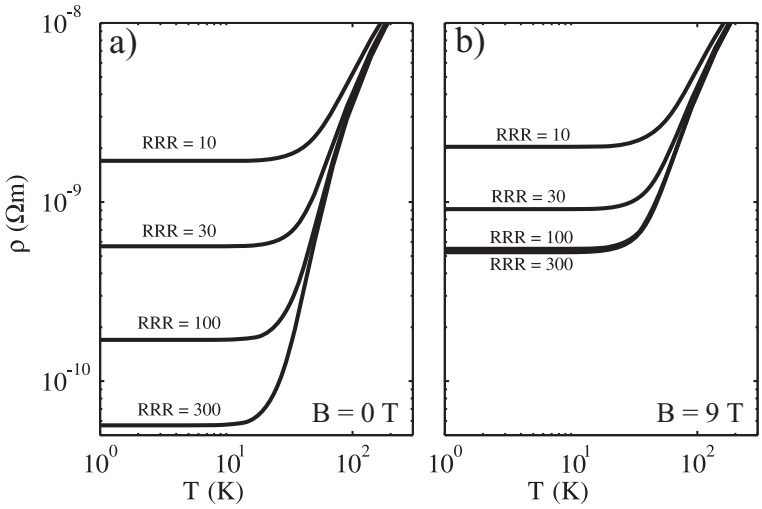

Figure 2.6: Temperature dependence of the electrical resistivity of copper for different purities at a magnetic field of a) 0 T and b) 9 T.

The heat flow to the coolant through the wire surface in a section with length ∂z is

$$p_{He} A \partial z = h_{He} P \partial z \, (T - T_{He}) \qquad [W], \tag{2.13}$$

where A_s is the area of the cross section of the wire, h_{He} is the heat transfer coefficient and P is the perimeter of the wire wetted by helium. As discussed in chapter 5, h_{He} is very complex to describe, due to its dependence on many variables and the many phase-transitions of heat transfer.

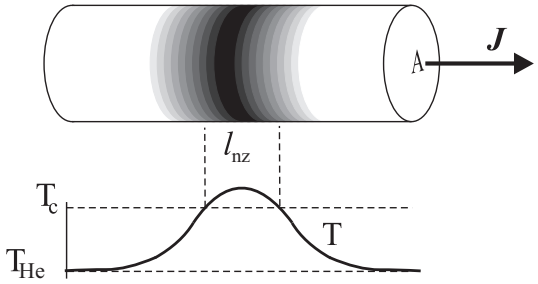

Figure 2.7: Temperature distribution in a wire after applying an external heat pulse. The temperature exceeds T_c over a length l_{nz}.

Minimum Propagation Zone

Equation (2.11) describes the behavior of the wire when a heat pulse enters the conductor. Figure 2.7 shows schematically the effect of a local heat release. The temperature of the wire, initially at T_{He}, exceeds T_c for a length of l_{nz}. If $T > T_c$ heat is dissipated as described in equation (2.12). By following the approach of [8] one can find the length of the normal zone l_{nz} at which heating and cooling are balanced, thus defining the Minimum Propagation Zone (MPZ). When $l_{nz} > l_{MPZ}$ the normal zone will expand and lead to a quench [25]. In a rough approximation of a square temperature profile in the wire and homogeneous cooling, from (2.11) follows:

$$J_m^2 A_m \rho_m l_{MPZ} = \frac{2\kappa A_m \, (T_c - T_{He})}{l_{MPZ}} + h_{He} P l_{MPZ} \, (T_c - T_{He}) \qquad [W]. \tag{2.14}$$

After rewriting l_{MPZ} is found:

$$l_{MPZ} = \left[\frac{2\kappa A_m \, (T_c - T_{He})}{J_m^2} \rho_m A_m - h_{He} P \, (T_c - T_{He}) \right]^{\frac{1}{2}} \qquad [m]. \tag{2.15}$$

For the LHC 01 type wire in the operation conditions of an LHC dipole magnet, l_{MPZ} is in the order of 1 to 10 mm [26].

Minimum Quench Energy

The Minimum Quench Energy (MQE) is introduced to quantify the heat needed to increase the temperature of a wire segment with length l_{MPZ} from T_{He} to T_c:

$$\text{MQE} = \frac{\pi}{4} d_s^2 \int_{l_{MPZ}} \int_{T_{He}}^{T_c} c\,(T)\, dT dz \qquad [J]. \tag{2.16}$$

In the strictly theoretical approach, MQE is defined for a transient heat deposition in a small volume. Due to thermal diffusion times that are involved in forming the normal zone with length l_{MPZ} a pulse duration of about 10 μs represents MQE correctly.

In measurements pd is in the order of 100 μs or longer. Therefore, in practical measurements situations the MQE of a conductor strongly depends on the heat deposition volume and the pulse duration pd. In measurements of the MQE it is clearly shown that MQE$= f(pd)$. In figure 2.25 MQE is displayed as function of i for different pulse duration. In the single strand stability regime, for $i > 0.48$, the dependence on pd is clearly shown. In the cable stability regime, $i < 0.48$, MQE is independent of pd. For single strand stability, the MQE(pd) is always overestimated compared to MQE($pd \downarrow 0$).

Cooling of the wire by helium is in the case of a large wire surface higher than the longitudinal cooling component in (2.11). Transient cooling by superfluid helium or liquid helium is much larger than cooling by supercritical helium. Due to the efficiency of helium cooling a significant increase in l_{MPZ} is expected, depending on the wetted perimeter, the bath temperature and the helium phase conditions, see figure 2.8a [26].

For similar value of i in adiabatic conditions the single wire MQE is lower at a temperature of 1.9 K compared to 4.3 K, due to the decreased specific heat of the copper and NbTi. When cooled by helium, the MQE at 1.9 K is generally much higher compared to 4.3 K, indicating that superfluid helium is much more efficient as a coolant compared to liquid helium. The efficient steady state cooling by superfluid helium can exceed the heating power in the wire, the MQE is strongly improved [26]. The enhancement of stability is seen for an LHC 01 wire in open bath condition for a values of $I/I_c < 0.9$, see figure 2.8a.

In a Rutherford cable the wetted surface is typically about 30% of the strand surface, see section 2.5.3. Figure 2.8b shows the enhancement at $I/I_c \approx 0.5$. However, the volume of helium in the cable voids is very small, about $\pm$ 5 to 10 % of the strand cross-section, see section 2.5.4. Therefore it is not likely to see the enhancement by superfluid helium in cables.

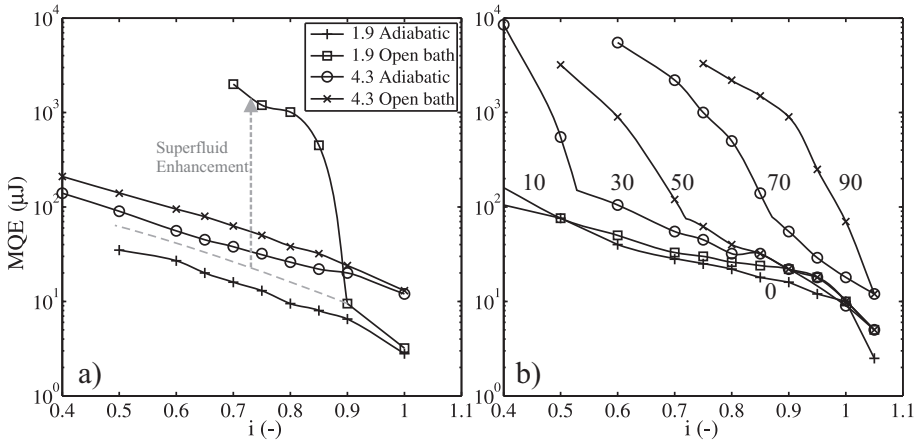

Figure 2.8: Measured MQE vs i curves for single LHC 01 wires, with data from [26]. a) Measurements for the adiabatic case and the open bath case, at a temperature of 4.2 K at 6 T and a temperature of 1.9 K at 9 T. b) Results of variation in cooled perimeter from 0 % to 90 % of the strand at 1.9 K and 9 T.

2.2.2 Cables

Superconducting cables differ in stability behavior from wires by the virtue of interstrand current and interstrand heat exchange. In a Rutherford cable each strand is in contact with other strands by the cross contacts, with contact area A_c. A strand has in total $2N_s - 2$ cross contacts per twist pitch.

A strand is only in contact with two adjacent strands. The contact area A_a is discretized over a length of $l_p/(2N_s)$, thus defining the contact resistance R_a.

Heat balance equation

The heat balance in a strand can be described by (2.11) with the addition of interstrand heat transfer p_{is}

$$c\frac{\partial T}{\partial t} = \frac{\partial}{\partial z}\left(\kappa\frac{\partial T}{\partial z}\right) + p_{ext} + p_{diss} + p_{he} + p_{is} \qquad [Wm^{-3}]. \tag{2.17}$$

The heat dissipation p_{diss}, described in (2.12) for a single strand, is expanded with the Joule heating due to strand-to-strand currents that are present in a cable. For a section in strand j with the discretized length of $l_p/(2N_s)$ the heat dissipation is described by:

$$p_{diss}A_s\frac{l_p}{2N_s} = J_m^2\rho_m A_m\frac{l_p}{2N_s} + \frac{1}{2}I_c^2R_c + \frac{1}{2}I_{a,j-1}^2R_{a,j-1} + \frac{1}{2}I_{a,j+1}^2R_{a,j+1} \qquad [W]. \tag{2.18}$$

The interstrand joule heating is caused by the strand-to-strand current between crossing strands I_c and adjacent strands I_a through the interstrand resistances R_c

and R_a. For a single wire configuration, the current density J_m is constant in time until quench detection, but for a strand it is varying as a function of time and position.

The total interstrand thermal heat transfer for a section in strand j with the discretized length of $l_p/(2N_s)$ is described by:

$$p_{is}\frac{A_s l_p}{2N_s} = h_{is}A_c\left(T_j - T_{cross}\right) + h_{is}A_a\left(T_j - T_{j-1}\right) + h_{is}A_a\left(T_j - T_{j+1}\right) \qquad [W], \tag{2.19}$$

where h_{is} is the interstrand heat transfer coefficient. h_{is} is depending on the strand coating material, material roughness, oxidization, pressure and temperature [27]. The value of h_{is} is discussed in more detail in section 4.1. In figure 2.9 some of the heat exchange paths in the cross-section of a cable are shown.

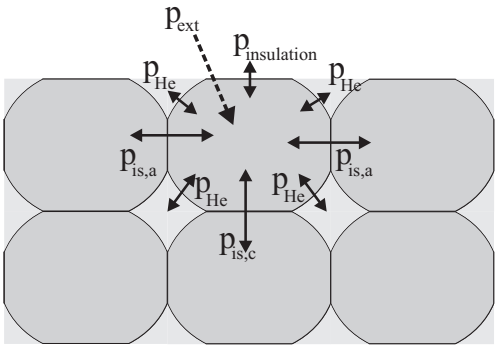

Figure 2.9: Illustration of the heat exchange between a strand and its crossing neighbor, the adjacent neighbors and the helium coolant.

Minimum Quench Energy

The definition of MQE for cables differs from the definition of MQE for single strands in many ways.

Chapter 7 shows that the MQE for a cable is not always the energy put locally in a single strand with a very short pulse duration. In various cases, the MQE for a pulse given to a large volume in multiple strands is lower than the MQE for a pulse given to a small volume in a single strand. Therefore, throughout this thesis, MQE denotes the minimum quench energy for a specified case. For a cable l_{MPZ} can be defined per strand as function of I_{strand}.

Stability definition

The definition of stability of a superconducting cable is only straightforward for the following two cases:

1. Stable if $l_{nz} < l_{MPZ}$ for all strands,
2. Unstable if $l_{nz} > l_{MPZ}$ for all strands.

In all other cases a specific calculation is needed by combining the electrical and

thermal model. The stability against short local heat pulses is distinguishable in multiple regimes. Each regime has one stability criterion as described in section 2.4. The electrical and thermal parameters that determine the stability in strands vary along the twist pitch of a strand. Therefore, each measurement and calculation of cable stability can only describe the stability for one specific condition.

2.2.3 Magnets

A cable wound in a superconducting magnet has no additional features of current redistribution compared to a single cable. Superconducting magnets like LHC dipoles and SIS 300 quadrupole, see figure 1.4, are wound from one or more superconducting cables with electrically insulated turns. In case of NbTi cables the insulation of polyimide tapes is hundreds of micrometers thick and has a relatively low thermal conductivity. The cables in LHC magnets are wrapped with three partially overlapping layers, which provides open channels for helium cooling, see figure 2.10.

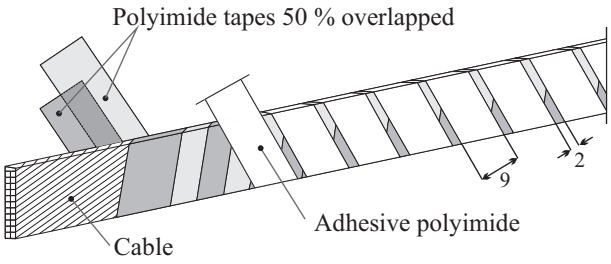

Figure 2.10: The insulation wrapping of 3 partially overlapping Kapton tapes around the cable used in LHC dipole and quadrupole magnets [1].

In LHC magnets, the voids filled with helium are specially dimensioned to optimize the steady state cooling of the coils. However, heat generation in the case of a normal zone is much higher than the steady state loss in the cable. The thermal conductivity of Kapton insulation layers is low, about 100 $\mathrm{WK^{-1}m^{-2}}$, but it is enhanced by the helium in the channels up to orders of magnitudes for low ΔT [28]. In the case of a normal zone in a strand the local temperature rise is in most cases to above 5 K. In simulations throughout this thesis the heat exchange with other turns and the helium bath outside the coil is neglected, because partial filling of the cable voids by Kapton reduces the helium volume and the cable contact surface with the helium, see figure 2.11 [13]. The cooling by helium is therefore reduced, thus reducing the MQE. The Kapton displacement into the cable voids is measured for a layout that is similar to the layout in the FRESCA test station. A stack of two LHC 02 cables is made and two layers of adhesive Kapton tape are attached to both sides of the cables, as visualized in figure 2.12a. The average thickness of one Kapton layer under constant pressure of 50 MPa is plotted versus time in figure 2.12b. The curve shows a reduction of thickness of Kapton in time, thus

confirming Kapton flow. Throughout this thesis the insulation material is assumed to fill the outer voids completely.

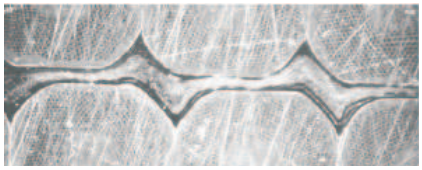

Figure 2.11: Kapton insulation wrapping has moved into voids of the LHC cable after applying a pressure of 60 MPa [13].

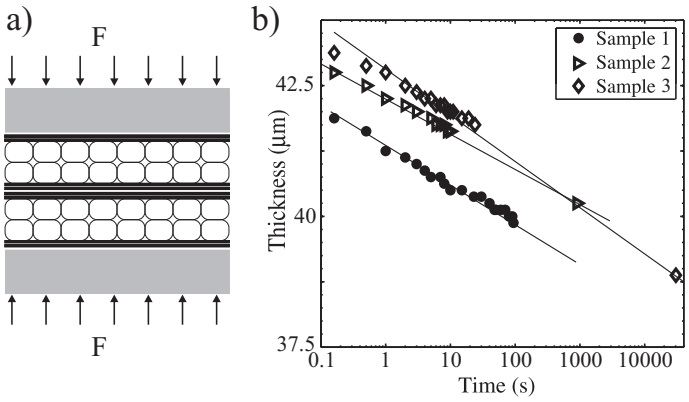

Figure 2.12: a) Illustration of a stack of 2 LHC 02 cables with 2 layers of adhesive Kapton tape (in black) on each side of both cables. A pressure of 50 MPa is maintained. b) The development of average thickness of the Kapton layers in time for 3 identical samples.

The magnetic field in accelerator magnets is not homogeneous, as shown in figure 1.3, with dB/dx up to 0.3 T/mm in LHC dipole turn 26. Due to the twisting of the strands, each strand is exposed to field variations in the length direction of the strand. In LHC dipole magnets turn 40, the upper left turn as shown in figure 1.3, is exposed to the highest maximum and highest average field. The mid plane turn, turn 26, is of interest as it is the most exposed to beam losses. Variation in magnetic field implies also variation in I_c and T_m. In figure 2.13 the variation in B, I_c and T_m is shown by following a strand along one twist pitch for turn 26 and turn 40. The implementation of field variation in simulations is very important to obtain realistic results.

In SIS 300 quadrupole magnets, the magnetic field variation in turn 20 is from 3.6 T at the thin edge to 3 T at the thick edge for an aperture field gradient of 45 T/m.

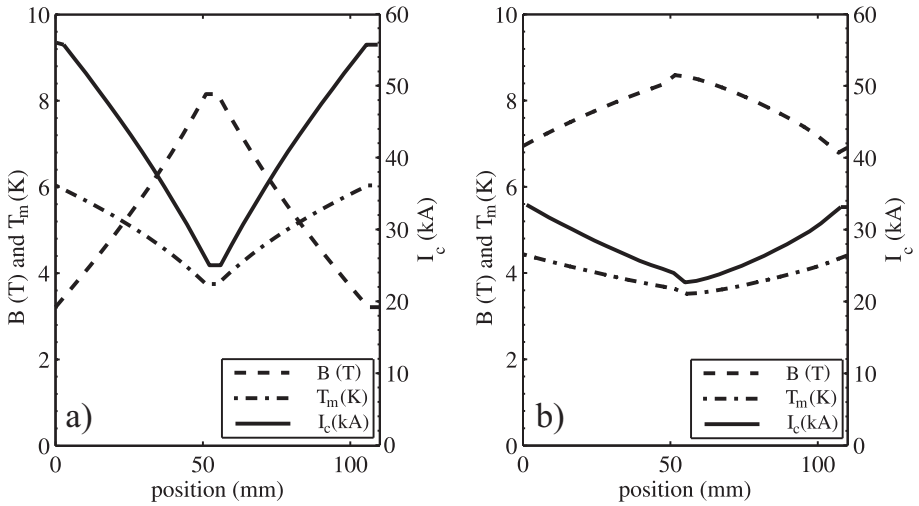

Figure 2.13: Magnetic field, temperature margin and the critical current along a strand, followed over the length of a twist pitch in an LHC dipole magnet for a central field of 8.33 T in a) a strand in turn 26 and b) a strand in turn 40.

2.3 Modeling cable stability

A Rutherford type cable consist of multiple strands that are all interconnected by cross contacts and adjacent contacts. For the investigation of the stability of a superconducting cable against a heat deposition a model needs to address the network of strands properly, both for the electrical as well as the thermal interaction. In general, the coupling between the electrical and thermal model is difficult to address, due to the sudden transition between the superconducting and resistive states of the conductor for small ΔT.

Electrical model

In figure 2.14 the electrical model of the cable is schematically introduced, showing possible current paths in strands and interstrand contacts. The contact resistance between crossing strands, also indicated as cross-contact resistance R_c, is defined as a local point contact, while the contact surface area is typically smaller than d_s^2. The contact resistance between adjacent strands, indicated as adjacent contact resistance R_a, is a discretized value, although two adjacent strands follow a parallel path and are in contact along the full length of the cable. The length over which R_a is discretized is $l_p/(2N_s)$, with l_p the length of the strand per twist pitch and N_s the number of strands. Both R_c and R_a vary across the width of the cable, as is described in more detail in section 2.5.

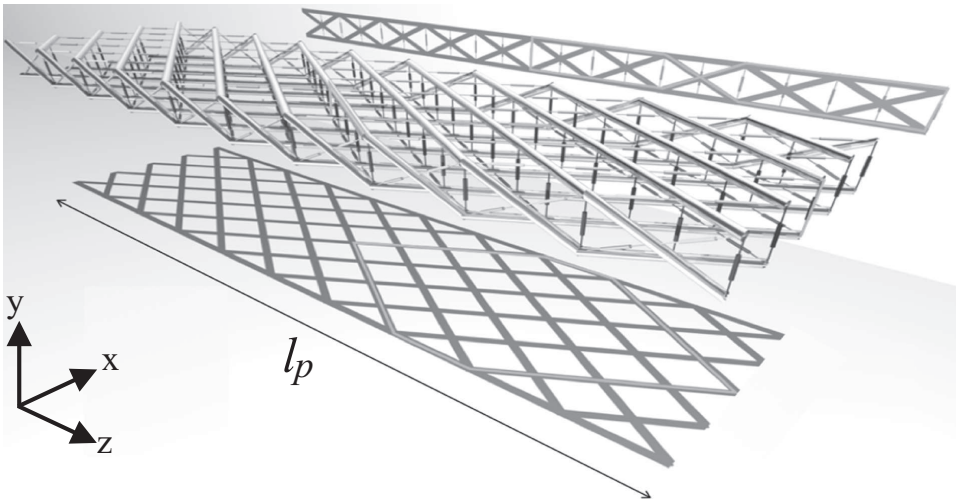

Figure 2.14: Network of strands in a Rutherford-type cable. Vertical connections indicate R_c and horizontal connections indicated R_a. The top-view and side-view are shown.

Most models that describe the electrical behavior of Rutherford cables are designed to study the current distribution due to changing magnetic fields and the accompanied AC loss. In figure 2.15 current loops are shown that are induced by a change in the perpendicular magnetic field component. The so-called interstrand coupling currents (ISCCs) have a characteristic loop length of one twist pitch and exhibit time constants of typically 0.01 to 10 s. Boundary induced coupling currents (BICCs) are mainly induced by variations in the field sweep rate along the length of the cable and exhibit time constant that can be several orders of magnitude larger than those of the ISCCs [29]. Typically ISCCs and BICCs follow a current loop with a large enclosed surface and with a corresponding large inductance. The current redistribution resulting from the sudden start of a local normal zone follows current loops with an inductance as small as possible, namely through the adjacent strands.

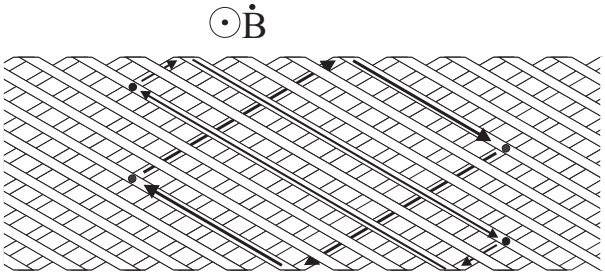

Figure 2.15: The arrows indicate two possible current paths that carry current induced by a varying magnetic field $\dot{B}$. The currents pass through the cross contacts, with resistance R_c, indicated by the dots.

2.3.1 Analytical approach

The complex structure of a Rutherford cable comprises many current paths. The current path with the lowest inductance has the shortest time constant. A first analytical approach to solve the current distribution in insulated parallel strands is given in [30] for large time constants over long lengths. It is adapted in [31] for describing current redistribution in non-insulated parallel strands, with a sudden start of a resistive zone in one strand. A survey of existing models is listed in 2.1.

Table 2.1: Survey of useful references for analytical models that describe the current distribution in parallel strands.

Year	Author	Ref.	Model characteristics	Approach
1974	Turck	[30]	2 insulated strands	Analytical
1980	Ries	[31]	Multiple non-insulated strands	Analytical
1992	Mulder	[32]	6 insulated parallel strands	Analytical
1997	Yoshino	[33]	3 strands	Semi-analytical
2000	Kim	[34]	2 and 3 strands	Qualitative
2000	Bottura	[35]	2 strands, general model	Analytical
2000	Mitchell	[36]	Full CICC, clustered strands	Analytical
2004	Lei	[37]	3 strands, based on [38]	Analytical

The approach described in [31] is useful to estimate the length of the cable that supports the current redistribution into the two nearest neighbors. Only the adjacent contacts, with resistance R_a are taken into account. In figure 2.16 the electrical network is shown with a resistive zone in one strand with R'_s the normal zone resistance per meter, L' the effective inductance per meter, S' the interstrand conductance per meter. For a typical cable S' is in the order of $3{\cdot}10^8$ to $3{\cdot}10^4$ Sm^{-1}.

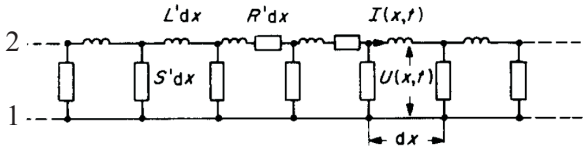

Figure 2.16: Electrical scheme of two parallel strands. In strand 2 a normal zone is induced with resistance per unit length R' [31].

The analytical approach can be used to estimate the relative contribution of all the neighboring strands. In table 2.2 the inductance of the various current paths are shown, with the electrical conductance and the calculated time constants for current redistribution. For a go and return path $L_{eff} = 4 \cdot 10^{-7} \left(ln\,(ratio) - \frac{1}{4}\right)$ [19]. The time constant for current redistribution in each current path is determined relative to the time constant into the nearest neighbor.

Table 2.2: Inductance, electrical conductance and the calculated time constants for current redistribution between parallel strands with variable distance from each other.

Neighbor	L (μH/m)	$S'/S'_{(+1)}$	$\tau/\tau_{(+1)}$
+1	0.4	1	1
+2	0.7	0.5	4
+3	0.8	0.3	7

For stability calculations the variations in temperature as function of time and space are important. In [31] a very simplified approach is followed to calculate the maximum temperature of the cable. All material parameters are kept temperature independent, a linear cooling characteristic is assumed, the size of the normal zone is constant and current sharing is not taken into account.

Most analytical models listed in table 2.1 use a very simplified approach of Rutherford cables with a 2 or 3 strands cable. The analytical approach of modeling stability provides limited accuracy in describing the complex behavior of the electrical and thermal behavior in superconducting cables for multiple reasons:

- The interstrand parameters along the length of a strand are inhomogeneous, due to the variation in magnetic field and the geometry of the strands.
- Analytical models provide limited possibility to describe normal zones covering multiple strands.
- The full electrical and thermal network cannot be described by analytical equations.
- $\dot{B}$ and B vary along the cable length.

Table 2.3: Survey of the existing numerical models that describe the current distribution in parallel strands. Only models that are suitable for stability calculations are described.

Year	Author	Ref.	Model characteristics
1973	Morgan	[42]	Metal-filled Braid cable
1989	Sytnikov	[43]	Full Rutherford cable
1990	Niessen	[44]	Full Rutherford cable
1994	Amemiya	[38]	3 non-insulated strands, non-twisted
1995	Verweij	[29]	Full Rutherford cable
1996	Tsuda	[45]	3 strands, twisted
1997	Wilson	[19]	Full Rutherford cable, Multiple clustered strands
2006	Breschi	[40]	Full Rutherford cable, clustered strands
2006	Bottura	[41]	Full Rutherford cable, clustered strands, based on [35]
2006	Verweij	[46]	Full Rutherford cable, based on [29]

2.3.2 Numerical approach

A sufficiently accurate description of thermal and electrical phenomena in a cable is only possible with a numerical approach. A few numerical models, listed in table 2.3, are available that are suitable for simulation of stability related problems. The model described in [19] divides the cable in five clusters of strands and is focused on describing the MQE of a cable against a heat deposition in a local strand section. The comparison of the calculations of MQE in [19] with measurements in [39] shows the ability of the model to describe the stability mechanisms well. More recent models, described in [40] and [41], also describe the full cable with clustered strands, so-called superstrands. Both models are mainly used to provide more accurate data of the quench energy margins against heat depositions in multiple strands. The models with clustered strands lack the possibility to implement detailed input for the inhomogeneities in the Rutherford cable.

A discrete approach to solve the currents in each strand [42] is adapted by multiple authors and evolved into a full electrical model described in [29]. Through the work in this thesis the model, called CUDI, described in [29] is extended to a full electrical and thermal model in [46]. CUDI provides the possibility to define all the parameter variations throughout the cable due to inhomogeneous magnetic field and geometry variations. The simulations presented in this thesis are performed using the code CUDI, therefore CUDI is described in the following section in more detail.

2.3.3 Electrodynamic and thermal cable simulation model CUDI

CUDI is an extensive Fortran code to calculate the electrodynamic and thermal behavior of any type of Rutherford cable subject to global and local variations in field, transport current and external heat release. The CUDI software package consist of a user-friendly input module and the calculation code. The input possibilities for

the cable simulations are very extensive, permitting realistic simulations for both a Rutherford cable in the FRESCA test station, see section 3.1, as well as in magnet conditions, like in LHC dipoles and in SIS 300 quadrupoles. CUDI is presently the most advanced cable simulation code available.

Figure 2.14 shows the basic three-dimensional network of strand sections interconnected by contact resistances. The network defines the possible current paths in the cable and it defines the possible interstrand heat exchange through strand-to-strand contacts. The thermal model is completed with the heat exchange between a section of the strand and the attached volume of helium, see figure 2.9. Throughout this thesis, the cooling through the Kapton insulation by conduction in Kapton and convection of He through channels is neglected. The cable is discretized over the cross section in $2 * N_s - 2$ sections, with N_s the number of strands. The cable is discretized in the longitudinal direction in N_b number of bands with a length of l_p/N_s.

Providing the correct input parameters is essential for an accurate calculation of the stability behavior of cables. Important characteristics and input features of the model are listed below.

- Each strand section is assumed to have homogeneous T, B, I, I_c, c_p, κ, ρ.
- Attempts to describe the stability of a cable with a downscaled number of strands to reduce calculation time has failed, due to the inhomogeneities of all parameters across the cable width. In general, for accurate calculation of MQE, the full number of strands has to be used during the simulation.
- A volume of helium V_{He} is assigned to each section, with contact surface A_{He}. V_{He} and A_{He} vary as function of the geometry. The helium volumes are assumed to be stationary and no heat exchange in between the helium volumes is taken into account.
- The applied magnetic field can be varied across the cable width and in the longitudinal direction to match the magnetic field in a magnet or a test station. The contribution of the self field of the cable can be included.
- Each strand can have its individual properties for: the RRR value, the Cu/NbTi ratio and the current in the initial condition of the cable.
- The critical current of each section is calculated with locally specified parameters by [47]:

$$I_c = (C_1 + C_2 B)\left[1 - \frac{T}{T_{c2,0}}\left(1 - \frac{B}{B_{c2,0}}\right)^{-0.59}\right] \quad [A], \tag{2.20}$$

  with conductor specific constants $C1$ (A) and $C2$ (A/m) for characterizing I_c.
- The electrical resistance in each section is calculated from the parallel resistance of the matrix and the superconductor. The superconducting resistivity is described by $\rho_{sc} = 10^{-14}(I/I_c)^n$ [Ωm], where n is a measure for the resistive transition.

- The position of the sections is defined by the cable width and varying cable thickness due to the keystone angle.
- The input of interstrand contact surfaces and volumes vary across the cable, as described in section 2.5.
- The contact resistance can be varied over the cross-section of the cable as function of the interstrand contact area. The contact resistance can as well be varied along the length of the cable, thus the low resistance in the soldered joints can be accounted for.
- The program will iteratively calculate the solution of the currents and temperatures everywhere in the cable in user defined timesteps. The program sub-divides the time step if requirements for maximum temperature and current change are not met or if convergence cannot be reached. The typical time step for quench calculations is in the order of 1 μs to 1 ms.
- With the specified quench criteria, see section 2.4, the program automatically calculates MQE curves.
- An external heat pulse can be deposited in one or more sections and in one or more strands. The minimum length of the heated section is $l_p/(2N_s)$.

Limiting calculation time

The calculation of one MQE value for a cable takes about 5 to 10 simulations iterating between quench and non-quench energy levels. The calculation time involved is strongly dependent on the quench criteria, the number of strands and the length of the cable.

The boundary condition that defines the minimum simulated length is given by the length of the cable that contributes significantly to the current redistribution process. This length is strongly dependent on R_a and R_c. In general, $N_b = 50$ is sufficient for cables with R_a or $R_c < 10$ $\mu\Omega$, and $N_b = 500$ is sufficient for R_a and $R_c > 1000$ $\mu\Omega$. To provide a full MQE curve for a 36 strand cable with high R_a and R_c, the calculation time may be in the order of one day on a desktop PC.

A significant reduction of calculation time is obtained by an halting the simulation with and early decision of quench or no-quench. The quench criteria presented in section 2.4 are used to define the quench criteria, based upon the resistivity of the strands. Full recovery of the cable is defined by

$$\rho_{max} < 100\rho_c,$$

with the superconductor criterion $\rho_c = 10^{-14}$ Ωm and ρ_{max} the maximum resistivity of any section at any moment after the end of the external pulse. The value of $100\rho_c$ is chosen empirically.

A quench of the cable is defined dependent on the applying stability criterion after a heat pulse in strand j. For the stability regimes the following criteria are defined:

Regime I	$\rho_{j,max} > 5000\rho_c$
Regime II	$\rho_{j\pm1,max} > 5000\rho_c$
Regime III	$\rho_{j\pm2,max} > 5000\rho_c$
etc.	

The value of 5000 is chosen empirically, with $\rho_{i,max}$ just below the resistivity of

the matrix.

2.3.4 Limitations of simulations with CUDI

The network model as used in CUDI has a discretization length dz of the strand section of $l_p/(2N_s)$. The discretization length is in the order of 1.4 to 2 mm. In stability regime I, the single strand stability regime, very short timescales are involved in MQE calculations. The heat diffusion in the length direction of the strand is limited. The 1-dimensional heat diffusion equation in the strand is written as

$$\frac{\partial^2 T}{\partial z^2} = \frac{1}{\alpha}\frac{\partial T}{\partial t} \qquad [Km^{-2}], \tag{2.21}$$

with diffusivity $\alpha = \kappa/(\rho c)$ and ρ the material density. For NbTi strands $\alpha \approx 0.05$ $\mathrm{m^2 s^{-1}}$ between 1.9 and 4.3 K. For a step function in temperature at one location, for instance induced by a heat pulse, the solution for (2.21) is written by:

$$T(z,t) = T_0 + \Delta T \cdot erf\left(\frac{z}{2\left(\alpha t\right)^{1/2}}\right) \qquad [K] \quad [48]. \tag{2.22}$$

In figure 2.17 the normalized temperature profile in a superconducting strand is shown for $\alpha = 0.05 m^2 s^{-1}$ at different moments after a stepwise temperature increase at $z = 0$ and $t = 0$. For an accurate numerical model to describe the temperature profile the condition $dz << (t/\alpha)^{1/2}$ needs to be fulfilled, with dz the spatial step.

For a valid calculation of MQE in the single strand stability regime with pulse duration pd the condition $pd >> \alpha dz^2$ needs to be fulfilled, with $\alpha dz^2 \approx 40$ μs. In the single strand stability regime the relevant quench decision moment, see section 2.4.4, is in the order of the pulse duration. Therefore, the calculation of MQE in the single strand stability regime with a pulse duration below about 100 μs is not accurate. In general for calculations with strand diameter $d_s << (t/\alpha)^{1/2}$, only a 3D FEM-model can describe the heat diffusion process accurately.

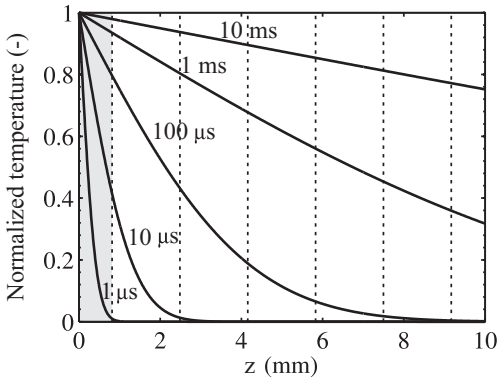

Figure 2.17: Normalized temperature profile as a function of z at 1 μ to 10 ms after the stepwise increase of temperature at z = 0. The dashed lines show the boundary of a typical section in CUDI.

For the cable stability regimes, the discretization length is fine enough, since the relevant time scales are generally much larger than 100 μs.

The possible length of a normal zone in a model is a multiple of the discretization length, with $l_{nz} = n \cdot dz$. The possibilities for the minimum propagation zone are therefore also discretized by $l_{MPZ} = n \cdot dz$. In the single strand stability regime the discretization of l_{MPZ} can lead to a stepwise increase of MQE, specially for a small n. In the cable stability regimes the error is small, since n is generally large enough.

2.4 Cable stability regimes

MQE is recognized for years as a good measure for the stability of a conductor. Nevertheless, the number of MQE measurements is limited. Most reported measurements of MQE on superconducting cables with point-like heaters show a stepwise decrease in MQE when the current is increased. Above the kink current I_{kink} the cable MQE is equal to the single wire MQE, see figure 2.18.

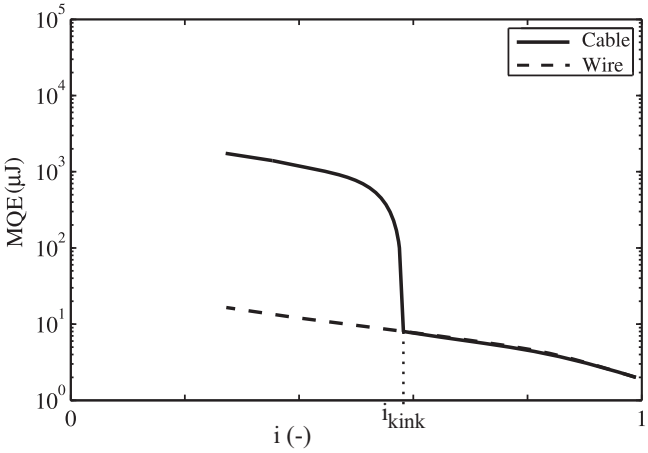

Figure 2.18: Characteristic MQE dependence on the normalized current for a cable (solid line) and a single wire (dotted line).

Below I_{kink} the cable MQE can be more than two orders of magnitude higher than the MQE of a single wire. This effect has been observed in Rutherford cables [49, 50, 51], but also in a 3-strand cable [52]. In table 2.4 the measurements performed prior to this research are listed, with the obtained values of i_{kink}.

The value of I_{kink}/I_c is strongly dependent on the used coolant, the current density, and the interstrand contact conditions. Therefore it varies between different cables. Throughout this thesis values for i_{kink} between 0.4 and 1 are reported. In figure 2.19 the response behavior of the cable in terms of quench and recovery is shown. A heat pulse with an energy between the wire and cable MQE leads to a local normal zone in the cable, which recovers. For a heat pulse with an energy below the dashed line, the full cable remains superconducting. For a pulse energy above the solid line, a propagating normal zone is leading to a cable quench. In this section, the response behavior of a cable after a heat deposition in one strand

Table 2.4: Survey of stability measurements on NbTi and Nb_3Sn cables until 2007, except for this research. Some measurement characteristics are shown.

Year	Author	Ref.	cable type	N_s	d_s (mm)	heater type	T (K)	i_{kink}
1997	Ghosh	[39]	Rutherford	28	1.065	graphite paste	1.9 - 4.3	0.75 - 1
1996	Tsuda	[45]	triplex	3	0.2	manganin wire	4.2	0.5
1997	Hirano	[53]	Rutherford	11	0.81	graphite paste	4.2	0.7 - 0.9
1998	Kim	[50]	Rutherford	28	1.065	graphite paste	1.9 - 4.5	0.7 - 1
1998	Amemiya	[52]	triplex	3	0.81	graphite paste	4.2	0.5
1998	Ghosh	[54]	Rutherford	28	1.065	graphite paste	1.9 - 4.4	0.7 - 0.95
1999	Ghosh	[51]	Rutherford	28	1.065	graphite paste	1.9 - 4.4	0.8 - 1.05
2002	Kawagoe	[55]	Rutherford	18	0.59	graphite paste	4.2	-
2003	Amemiya	[56]	triplex	3	0.81	graphite paste	-	0.3

is described.

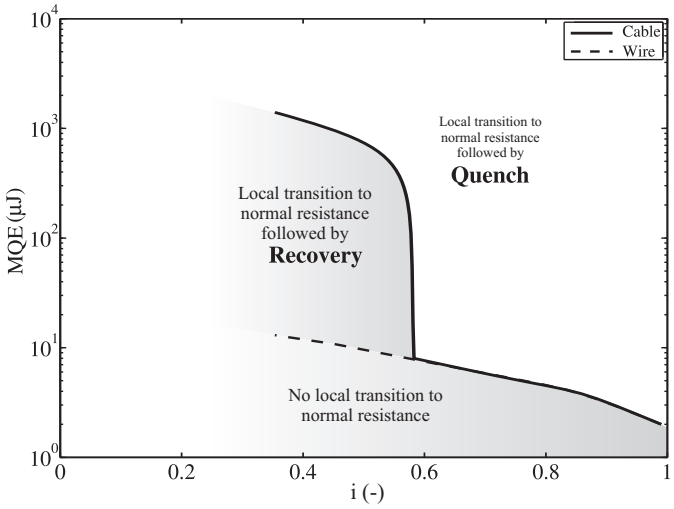

Figure 2.19: Response behavior in different areas of the MQE versus i curve in cable measurements.

2.4.1 Transversal normal zone propagation

Detailed simulation results with CUDI reveal the sequence of normal zone propagation through the cable. Two directions of normal zone propagation are distinguished: longitudinal and transversal. Interstrand heat exchange causes the neighboring strands to warm up, thus normal zone propagation in the transversal direction is possible.

Two possibilities for transversal normal zone propagation are distinguished: transversal propagation into one of the adjacent strands or transversal propagation into one of the crossing strands. Simulations show a special case of adjacent propagation at the edge of the cable, so-called edge propagation. A visualization of the three possibilities of transversal propagation is shown in figure 2.20.
The transversal normal zone propagation modes can be described as:

- **Adjacent propagation**
  The current and temperature in the adjacent strands increase and lead to a normal zone in the adjacent strand. The main mechanism of adjacent propagation is the fast growth of current locally to above I_c. Therefore adjacent propagation is the primary mode of transversal normal zone propagation in cables with low R_a or R_c. For most cables this propagation mode determines I_{kink}.

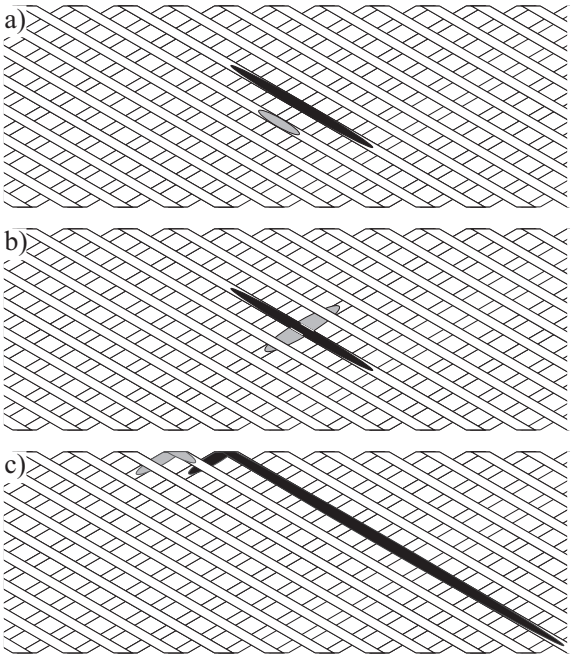

Figure 2.20: Three different possibilities for transversal quench propagation. The normal zone in the heated strand is indicated in black, the normal zone in a neighboring strand is indicated in gray. a) Adjacent propagation, b) Cross propagation and c) Edge propagation, which is a special form of adjacent propagation.

- **Cross propagation**
  The current increase in the crossing strand due to the normal zone in strand j is very small, see section 4.2. Therefore the mechanism for propagation in the crossing direction is heat exchange between the heated strand and the crossing strand. The heat exchange between crossing strands is larger than between adjacent strands, therefore in the case the propagation is based mainly on heat exchange, the cross propagation is faster than adjacent propagation. Adjacent propagation is dominant around I_{kink}, but cross propagation can be dominant at lower currents, in the range where MQE is much larger than the single strand MQE. In cored cables cross propagation is expected to be less significant as the core reduces heat exchange between crossing strands.

- **Edge propagation**
  The longitudinal normal zone propagation is fast and reaches the cable (thin) edge before it has propagated into the adjacent and crossing strands. Due to the high thermal conductivity between strands at the edges of the cable, the normal zone can propagate into neighboring adjacent strands faster. Hence, edge propagation is a special case of adjacent propagation since the propagation is not coupled to the position of the heat pulse. Edge propagation is dominant for heated positions close to the edge, and it dominates the adjacent quench behavior in general for cables with R_a and $R_c > 1000\ \mu\Omega$, in which, due to slow current redistribution, the longitudinal normal zone grows faster and extends further. In section 6.10 the effect of edge propagation is shown.

The mode of transversal normal zone propagation is often be different between a cable test experiment and a cable in real magnet conditions, mainly due to variations in the magnetic field pattern. In the experimental set-up the chance of cross propagation is increased due to a reduction in T_c in the crossing strands, see the field pattern figure 3.3. In magnet conditions, see the field pattern in figure 1.8, T_c and I_c are strongly reduced in the thin edge, therefore the chance of edge propagation is increased.

2.4.2 Criteria

The modes of transversal propagation are very useful to define criteria for cable stability. In this section, cable stability criteria are defined for a heat pulse in strand j. In figure 2.21 the naming of the adjacent strands and the crossing strand is shown.

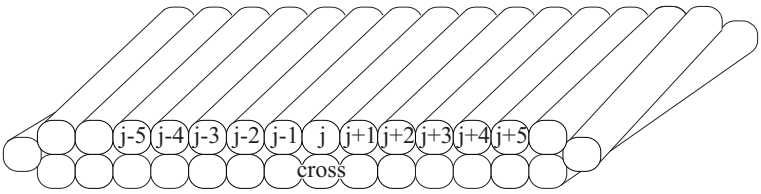

Figure 2.21: Schematic drawing of a cable with the strand numbering of the adjacent strands and the naming of the crossing strand. Strand j is the heated strand.

The characteristic measured MQE versus i curve for cables as shown in figure 2.18 shows two regimes, i.e. cable stability for $I < I_{kink}$ and single strand stability for $I > I_{kink}$. However, more detailed experiments and simulations have shown

more distinctive cable stability regimes. In figure 2.22 a representation of stability regimes is shown.

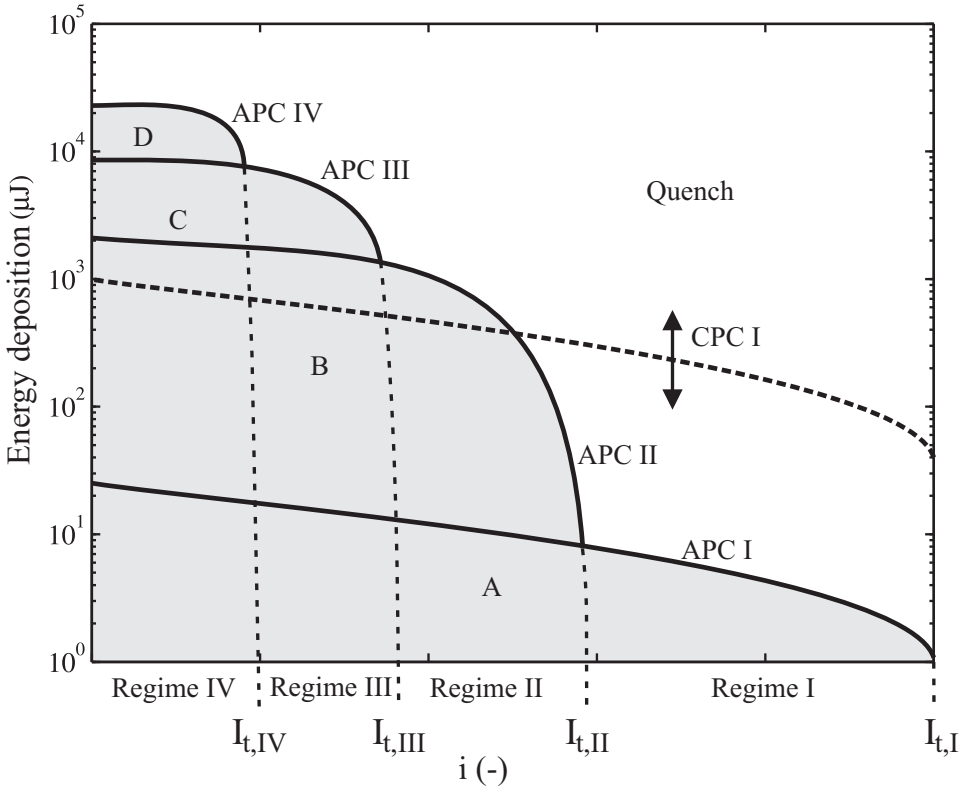

Figure 2.22: Overview of stability regimes depending on current, according to the highest quench criterion at that specific current.

The criteria are characterized by two modes of propagation:

APC - Adjacent Propagation Criterion
CPC - Cross Propagation Criterion

The criteria can be described as follows:

- **Adjacent Propagation Criterion I (APC I)**
  APC I can be described as the single strand regime, where $l_{MPZ,j}$ can be calculated with (2.15). The criterion is defined by the balance between the normal zone length $l_{nz,j}$ and $l_{MPZ,j}$ for the local conditions in the strand. Below APC I in area A no propagating normal zone in the cable exists. Above APC I a normal zone expands in the longitudinal direction of the strand, after which either recovery or cable quench follows.

- **Adjacent Propagation Criterion II (APC II)**
  APC II only appears for energy depositions higher than APC I. If the energy of APC I is exceeded, a normal zone will start to propagate in the longitudinal direction in strand j. Due to Joule heating the temperature in strands j and indirectly in strands $j \pm 1$ rises, while current redistribution increases the current in strands $j \pm 1$. The criterion is defined by the balance equation $l_{nz,j\pm1} = l_{MPZ,j\pm1}$. In the area B below APC II the normal zone that originated after exceeding APC I recovers. Above APC II a normal zone expands in the longitudinal direction in strands $j \pm 1$, after which either recovery or cable quench follows.
- **Adjacent Propagation Criterion III (APC III) and higher**
  Each higher criterion only appears for energy depositions higher than the previous criterion and similar description as for APC II applies. In area C, the normal zones in strands $j-1$ to $j+1$ recover before other strands become normal. In area D, the normal zones in strands $j-2$ to $j+2$ recover before other strands become normal. In area E, the normal zones in strands $j-3$ to $j+3$ recover before other strands become normal, etcetera. In figure 2.22 four regimes are shown, but in theory $N_s/2$ regimes can be defined. However, higher regimes are not expected to play an important role, due to cross propagation.
- **Cross Propagation Criterion I (CPC I)**
  CPC I is defined by the balance equation $l_{nz,cross} = l_{MPZ,cross}$. If a longitudinally propagating normal zone exists in the crossing strand, a quench follows in most cases. The level of the CPC I compared to the adjacent criteria depends mainly on the thermal contact between the crossing strands. In case of a cable with a stainless steel core between the layers, CPC I is much higher, due to reduced thermal contact. If CPC I is lower than one of the other criteria the MQE is defined by CPC I. A normal zone in the crossing strand increases the temperature in the strands $j \pm 1$ as well, causing transversal adjacent propagation in the initial heated layer. The cable will quench in most cases, therefore only one CPC I is defined.
- **Cross Propagation Criterion II (CPC II) and higher**
  For cross propagation multiple criteria can be defined as well. Once APC I and CPC I are exceeded, in both layers a normal zone exists in one strand. The current redistribution from the normal zone in strand j is independent from the normal zone in strand *cross*, since only the adjacent strands contribute to the redistribution process. Heat exchange is the only interaction between the layers of the cable. The upper limit of i for the curve of CPC II is i_{kink} and CPC II is always higher than CPC I.

In table 2.5 four adjacent stability criteria and one cross criterion are listed. For simulations an alternative criterion for quench is defined, as in practice the criterion is reached when the resistivity of one or a few sections of the strand becomes normal conducting.

The MQE curve, either measured or calculated, is composed of the quench cri-

Table 2.5: Naming of stability criteria.

Criterion name	Criterion	Alternative Criterion	Decisive strand	# strands with $\rho_{max} >> \rho_{sc}$
APC I	$l_{nz,j} = l_{MPZ,j}$	$\rho_{max,j} >> \rho_{sc}$	j	1
APC II	$l_{nz,j\pm1} = l_{MPZ,j\pm1}$	$\rho_{max,j\pm1} >> \rho_{sc}$	$j \pm 1$	3
APC III	$l_{nz,j\pm2} = l_{MPZ,j\pm2}$	$\rho_{max,j\pm2} >> \rho_{sc}$	$j \pm 2$	5
APC IV	$l_{nz,j\pm3} = l_{MPZ,j\pm3}$	$\rho_{max,j\pm3} >> \rho_{sc}$	$j \pm 3$	7
CPC I	$l_{nz,cross} = l_{MPZ,cross}$	$\rho_{max,cross} >> \rho_{sc}$	cross	variable

teria. In figure 2.23 two possible curves are visualized. In a) three adjacent criteria are followed before the crossing criterion dominates the MQE. It is unlikely to observe more than 2 adjacent regimes in cables without core that reduces the thermal conduction between the crossing strands. In b) a case with good thermal contact between crossing strands is shown, with CPC I dominating a large part of the MQE curve. The curve exhibits an almost stepwise transition from APC I to CPC I.

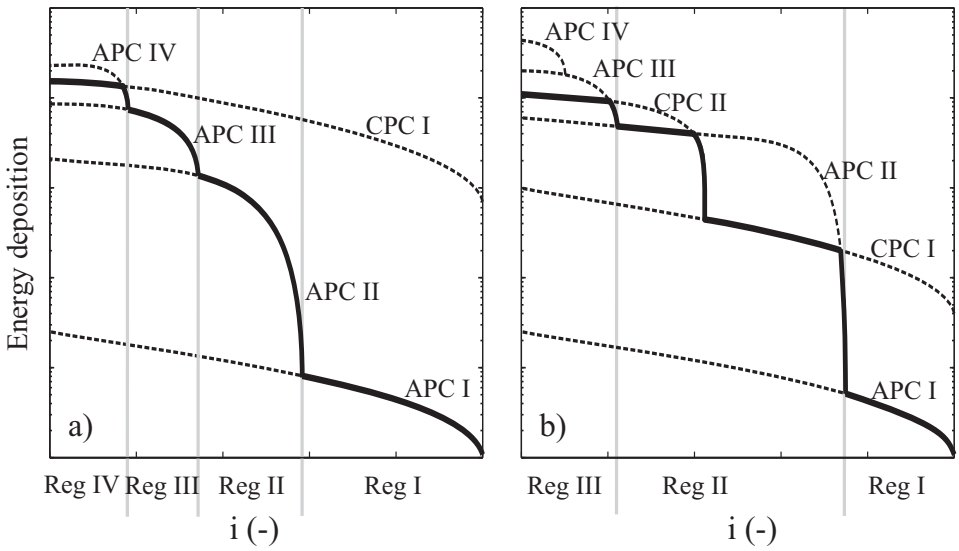

Figure 2.23: MQE curve (solid line) composed of the different stability criteria (dashed lines) visualized for two situations. The gray lines indicate the distinguished stability regimes.

The position of I_{kink} for cables is always defined by APC II, indicating that current increase in strands $j \pm 1$ implies adjacent propagation before heat exchange with the crossing strand implies cross propagation. The number of visible criteria in a measured MQE curve of a cable is very dependent on the cable characteristics and the application conditions, such as cooling and magnetic field. Due to the inhomogeneous conditions and geometry of the cable, the number of criteria may vary between different positions in the cable as well.

2.4.3 Transition current and stability regimes

The position of I_{kink} is defined by the intersection of APC I and APC II, see figure 2.22. By extrapolating the curves for $E \downarrow 0$, the upper limit in I of each adjacent propagation criterion k is defined by $I_{t,k}$. The values of $I_{t,k}$ provide a cable intrinsic value for the adjacent propagation criteria.

By definition we could propose $I_c \equiv I_{t,I}$, giving a more accurate I_c, which is specific to the cable in its local condition. However the normal definition $\rho_{sc} = 10^{-14}$ Ωm, defined by global voltage versus current measurements is more practical to use.

Since the curve of APC II is generally very steep I_{kink} is only slightly lower than $I_{t,II}$. Therefore I_{kink} is a good measure for characterizing cable stability. The accuracy of the determination of I_{kink} is high and the influence of the pulse size is small.

To distinguish the stability behavior in a cable in a practical way, the MQE curve is separated in a number of regimes. Regimes start at the intersection of two criteria. Regime I is used for the area in the curve defined by the currents at which the MQE is defined by APC I. Regime II is used for the area in the curve defined by the currents at which the MQE is defined by APC II. Similarly the regimes III and higher are defined. If CPC I intersects with criterion k, than the highest regime is regime k.

2.4.4 Quench and recovery of a local normal zone

Local measurements and simulations of voltages on a strand validate the separation into regimes. An example of just recovery in regime II and an example of just quench for the same situation are given.

When a heat pulse is given to strand j in a cable, with a pulse energy in area B, just below APC II in figure 2.22, a normal zone appears in strand j for a few milliseconds. In figure 2.24a the voltage in strand j indicates the existence of a normal zone, while the voltage in other strands remains 0. Initially the normal zone propagates longitudinally and the voltages increase. The resistive voltage across the normal zone forces the current to redistribute and the current in strand j decreases, counterbalanced by an increase in strands $j \pm 1$. Therefore, Joule heating reduces in strand j until cooling exceeds heating, enabling the strand to recover into the superconducting state.

In figure 2.24b the pulse energy is slightly increased to just above APC II in figure 2.22. Comparing a) and b) shows that until about $t = 6$ ms both curves are similar and the mechanism of recovery is similar. At 6 ms a normal zone in one of the strands $j \pm 1$ is suddenly formed. The voltage increase is much faster and the voltage reaches a much higher value compared to the maximum voltage in strand j in figure 2.24a. The fast voltage increase indicates a much faster longitudinal propagation in strands $j \pm 1$ due to the increased current in strands $j \pm 1$. The voltage rise in strand j after the start of a normal zone in strands $j \pm 1$ shows a second start of longitudinal propagation in strand j and a cable quench follows.

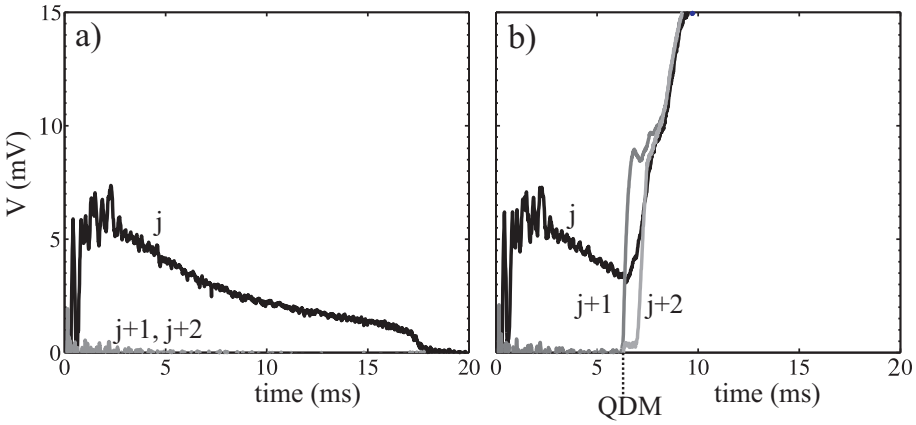

Figure 2.24: a) Characteristic measured curve of the voltage in strand j recovering after a few ms. b) Voltage trace in strand j is the same as in a), until strand $j+1$ becomes normal conducting and the cable quenches. The time where the voltages of the quench and no quench curves split is defined as QDM.

At the start of the normal zone in strands $j \pm 1$ the decisive criterion, APC II, is clearly reached. The moment at which the decisive criterion is reached is defined as the Quench Decision Moment (QDM). QDM is dependent on cable characteristics, on pulse characteristics and on cooling and field conditions. In regime I, QDM depends on the time necessary for $l_{nz,j}$ to reach $l_{MPZ,j}$, therefore it depends on the heat diffusion in the strand. Typically QDM is in the order of μs. However in practical cases of experiments and simulations QDM $\cong$ *pd* in regime I.

In regime II and higher QDM is typically between 100 μs and 10 ms. In general, the pulse duration has only a small effect on the MQE in regime II and higher, but it has a strong effect in regime I. In figure 2.25 the influence on the pulse dependence on APC I and APC II is shown.

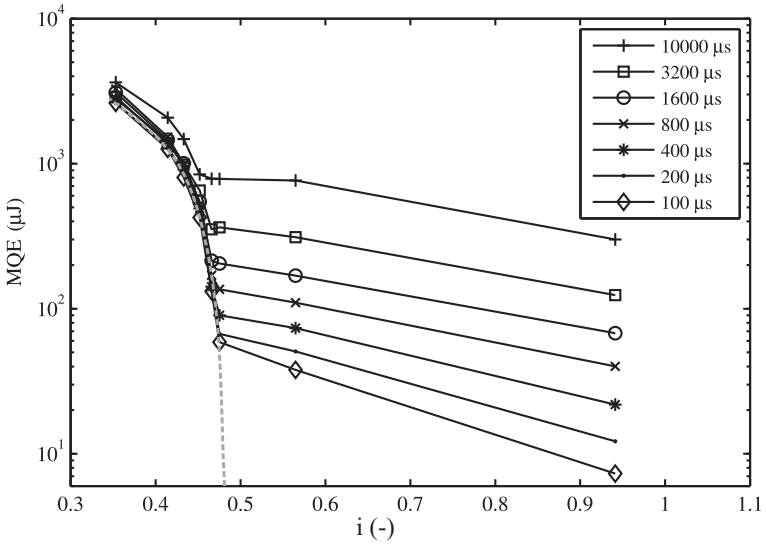

Figure 2.25: By varying the pulse duration from 100 μs to 10 ms the experimentally obtained MQE variation is significant for APC I, while the variation is not significant for APC II.

2.5 Cable geometry

Cable stability against a short local heat disturbance is strongly dependent on the exact position in the cross-section of a Rutherford cable. Measurements [57] show that the cable edge is more likely to quench than the cable center position. The exact geometry of a cable determines thermal and electrical exchange between strands.

During cabling the strands are forced into position by 4 cylindrical rollers to give the exact cable dimensions. Due to rolling, the strands are compressed and deformed most at the edges, and especially at the thin edge [58]. As a result of the keystone angle, the compaction factor increases from the thick edge towards the thin edge, therefore interstrand contact areas, helium contact areas and void volumes vary as a function of the position in the cable.

To provide a good understanding of the variations of cable stability across the cable width and to provide the correct input geometrical data for stability simulations, the geometrical variations are investigated. A set of geometry parameters is proposed for LHC 01 cables and LHC 02 cables.

Neutron tomography experiments and optical measurements have been performed on LHC 01 cables to reveal all geometry parameters of the cross-section of the cable [57]. Neutron tomography provides cross-section images obtained by analyzing transparency variations between the different materials. For an LHC 01 cable and a pixel size of 13.5 μm, 265 cross-section images per twist pitch and 3D images

were analyzed. Figure 2.26 shows 5 cross-sections on different positions relative to the twist pitch. During tomography, the cable was not completely compressed, thus the cable voids are oversized.

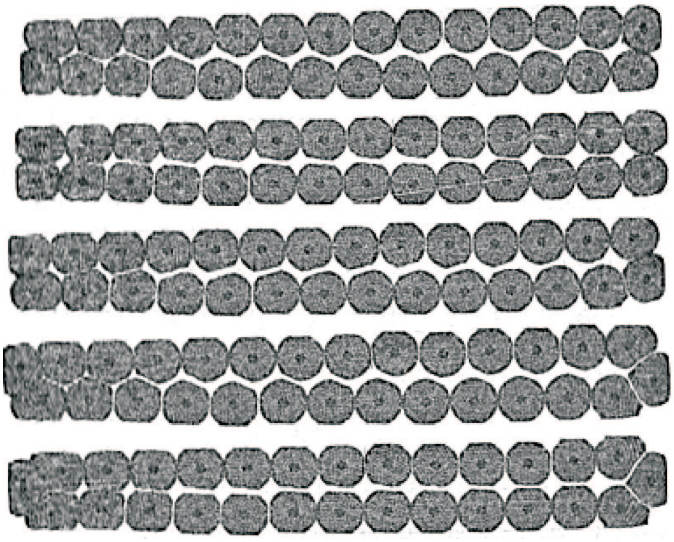

Figure 2.26: Five cross-section images of an LHC 01 cable different longitudinal positions produced by neutron tomography measurements.

By combining all cross-sections into a 3D image, a detailed view of the cable voids and strand positions can be obtained, see figure 2.27.

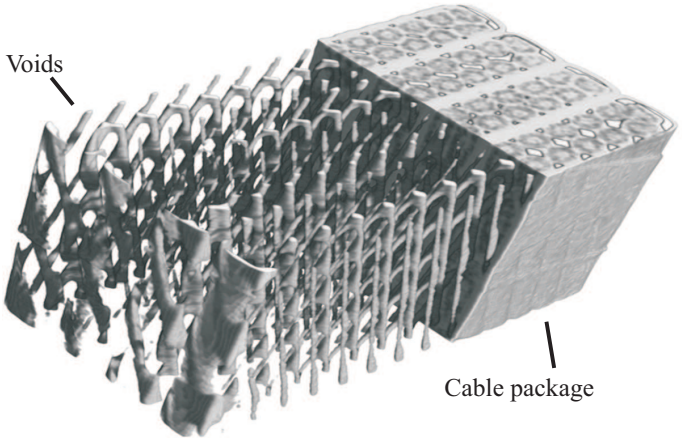

Figure 2.27: 3D image of a stack of four LHC 01 cables. On the left side only the cable voids are shown. On the right the cross-section of the cable package is visible.

2.5.1 Cross contact surfaces

The interstrand cross contacts between the two layers in a Rutherford cable are formed during cabling by the pressure on two initially cylindrical shaped strands, that are positioned with an angle 2α with respect to each other. A saddle shaped contact surface between the two crossing strands is formed by the pressure, with an oval shape projection as shown in figure 2.28.

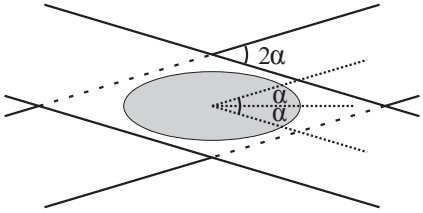

Figure 2.28: Oval contact area between two strands in the two layers of a Rutherford cable, shown in gray.

Figure 2.29a shows the outer cable surface and 2.29b shows the inner cable surface after removal of the upper layer. The saddle shape of the imprint of the upper layer on the lower layer is visible. By means of optical imaging in [59] and [60] A_c is determined. Good agreement between both sources is shown in figure 2.29c.

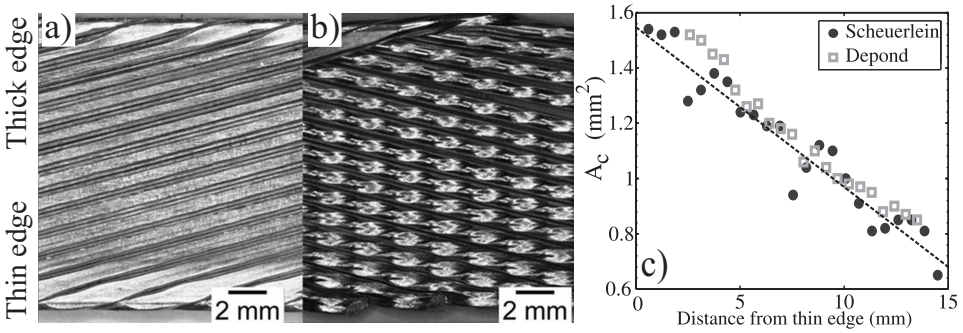

Figure 2.29: Cable topography obtained from optical measurements. a) The broad face of the cable. b) The inner surface of the cable. c) Cross-section surface area of an LHC 01 cable measured by Depond [59] and Scheuerlein [60]. The dashed line shows the used value of A_c in simulations throughout this thesis.

For simulations in this thesis a linear fit of the data from [60] is used for LHC 01 cables with A_c depending on the cable width position x (mm) from the thin side as $A_c = 1.55 - 0.058x$ mm^2. The average A_c for LHC 02 cables is 1.7 times smaller than the average of A_c for LHC 01 cables [59]. Scaling by this factor results in $A_c = 0.92 - 0.034x$ mm^2 for LHC 02 cables.

2.5.2 Adjacent contact surfaces

Calculation of the adjacent contact surface area is performed by averaging the flat touching areas in 3 cross-sections as shown in figure 2.26, evenly spread over a distance l_p/N_s. The adjacent contact is, contrary to the cross contact, a continuous contact between two neighboring strands and therefore not naturally discretized. Values for A_a are therefore given in area per meter strand length.

In figure 2.30 the local cross-sections of the cable at the thin edge, center and thick edge positions are shown. The indicated contacts of A_a are significantly larger at the edges, compared to the center of the cable. Figure 2.31 shows A_a, gained from neutron tomography experiment [61] and from [59].

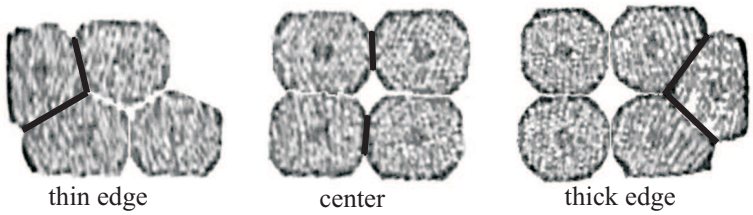

Figure 2.30: Cross-section of the thin edge, center and thick edge of the cable. The black lines emphasize the adjacent contact area.

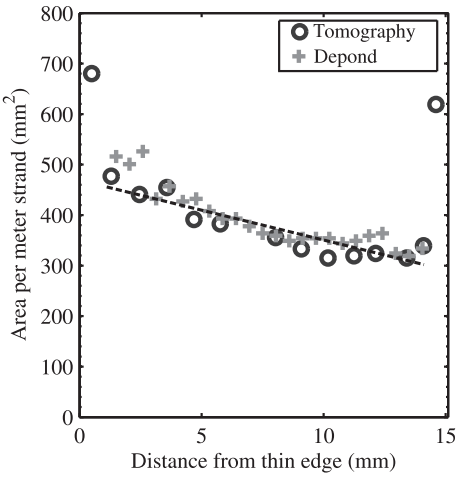

Figure 2.31: Adjacent contact area data from neutron tomography measurements and by Depond [59]. The dashed line shows the used area in simulations throughout this thesis.

In this thesis a linear fit is used for A_a depending on the cable width x, with $A_a = 461 - 11.9x$ mm^2/m for LHC 01 cables. For the thin and thick edges a value of 680 and 620 mm^2/m are used, respectively. The average A_a for LHC 02 cables is 1.9 times smaller than the average of A_a for LHC 01 cables [59]. Scaling by this factor results in $A_a = 248 - 6.40x$ mm^2/m for LHC 02 cables. For the thin and thick edge A_a is set to 366 and 333 mm^2/m, respectively.

2.5.3 Helium contact surface

The outer voids of the cable are assumed to be mostly filled with Kapton, see section 2.2.3, both in the measurement set-up and in accelerator magnets, therefore only the inner voids are accounted for. In [59] a nearly linear distribution of A_{He} is obtained by optical imaging for an LHC 01 cable, see figure 2.32. Results for the edges are not presented in [59], therefore by analyzing multiple cross-sections of an LHC 01 cable obtained by neutron tomography, A_{He} for the thick and thin edges are determined and added to figure 2.32.

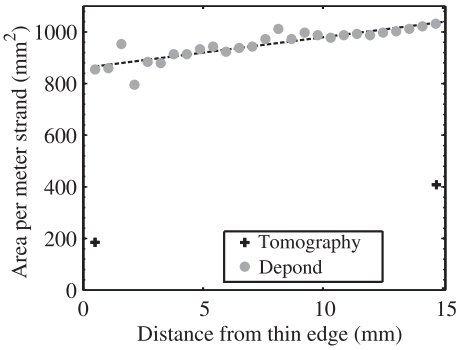

Figure 2.32: The inner free surface area of LHC 01 cable by Depond [59]. The data points at the cable edges are obtained by tomography images. The dashed line shows the used value in simulations throughout this thesis.

In this thesis a linear fit is used for A_{He} depending on the cable width x, with $A_{He} = 11.8x + 861$ mm^2/m for LHC 01 cables. For the thin and thick edges values of 189 and 413 mm^2/m are used, respectively. The average A_{He} for LHC 02 cables is 1.4 times smaller than the average of A_{He} for LHC 01 cables [59]. Scaling by this factor results in $A_{He} = 8.26x + 603$ mm^2/m for LHC 02 cables. For the thin and thick edge A_{He} is set to 132 and 289 mm^2/m, respectively.

2.5.4 Void size

The envelope of the cross-section of a Rutherford cable is filled for about 90 % with the cable. As discussed in section 2.2.3 the outer voids are filled with Kapton insulation tape both in the measurement set-up and real magnets [59]. Therefore only the inner void is of interest, since the helium in this volume will enhance the heat capacity of the cable and hence its stability.

Neutron tomography [61] is used to get a detailed measure of the void fraction as function of the cable width. The difference in transparency of the cable materials is used to create a gray scale image showing the accumulated thickness of the voids, see figure 2.33a. The void fraction as function of the cable width is determined [61] and shown in figure 2.33b, with data from [59] for comparison. Both sources show similar values for the center part of the cable, but show some difference in the edge regions.

A polynomial fit is used to define the helium volume V_{He} as a function of the position in the cable. $V_{He} = -0.555x^2 + 10.17x + 5.12$ mm^3/m for LHC 01 cables, with x the distance from the thin edge. For the thin and thick edges values of 10 and 60 mm^3/m are used, respectively. The average V_{He} for LHC 02 cables is 1.9 times smaller than the average of V_{He} for LHC 01 cables [59]. Scaling by this factor results in $V_{He} = -0.297x^2 + 5.44x + 2.74$ mm^3/m for LHC 02 cables. For the thin and thick edges V_{He} is set to 5.35 and 32.1 mm^3/m, respectively.

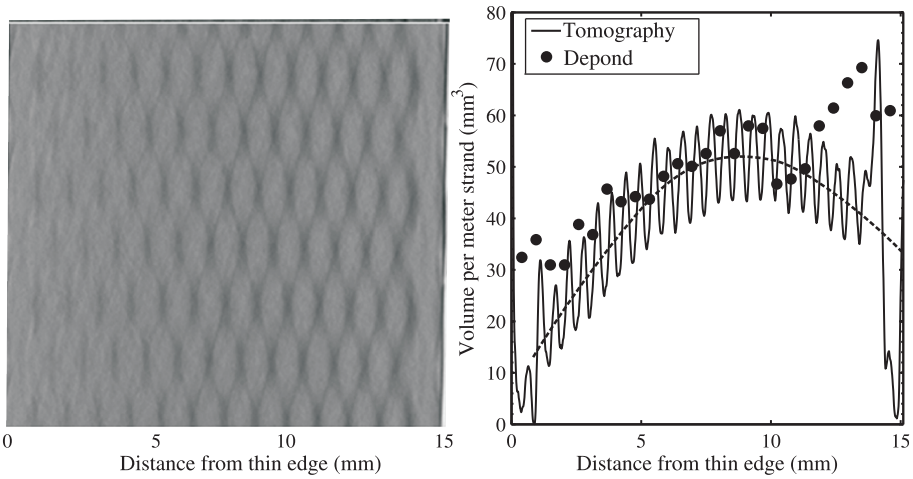

Figure 2.33: a) Gray scale picture of the transparency of an LHC 01 cable, obtained by neutron tomography [61]. b) The line shows the volume of helium deduced from the absorption level and the dots show data from Depond [59]. The dashed line shows the applied fit for simulations.

Network of voids filled with helium.
In CUDI, the helium voids are attributed to one strand section and no heat exchange with helium in other void sections is assumed. The helium volume defined per strand section is small, but all voids are interconnected by small channels. In figure 2.34 the 3D network of inner voids filled with helium is shown for an LHC 01 cable.

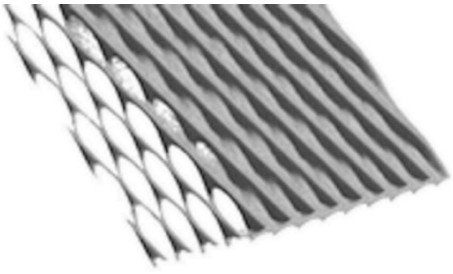

Figure 2.34: 3D image from neutron tomography of the inner voids in a Rutherford cable [61]. The solid layer in the right half is due to insufficient compression during imaging.

To ways of addressing the center voids to the strand sections are possible, see figure 2.35:

a) - The total center void size is connected to each strand section.
b) - One quarter of the center void size is connected to each strand section.

In situation a), the total void size of the cable is overestimated by a factor of 4, giving an increased APC II and higher and an increased CPC I. However, situation a) gives a more realistic cooling scenario for APC I. In situation b), the total void size is correct and is the most realistic description for APC II and higher and CPC I. However, APC I can be strongly underestimated. Since cable stability is investigated situation b) is used throughout this thesis. Therefore calculations for the single strand stability regime are influenced by the simplification.

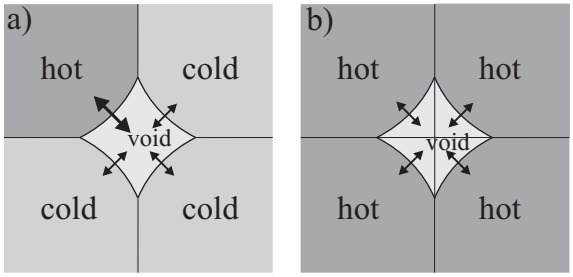

Figure 2.35: Illustration of two possibilities for addressing the center void to four strand sections.

2.6 Conclusion

The sources of heat in an accelerator magnet are categorized by the heated volume and the duration of the heat deposition. The experiments focus on transient and local heat deposition, covering three possible sources of heat: Flux jumps, conductor movement and beam loss. Simulations performed with CUDI cover heat depositions in larger volumes as well.

Cable stability is dominated by longitudinal as well as transversal normal zone propagation. Longitudinal normal zone propagation is related to single wire normal zone propagation. However, current decrease due to current redistribution slows the longitudinal normal zone propagation, providing a possibility for recovery.

Transversal normal zone propagation is described in two main propagation directions: Adjacent propagation and cross propagation. Transversal propagation is determined by an increase of current in neighboring strands to above I_c, an increase of temperature to above T_c, or a combination of both.

Since transversal normal zone propagation is a discretized process, propagation criteria can be defined accurately into two types of criteria: Adjacent Propagation Criteria (APC) and Cross Propagation Criteria (CPC), see figure 2.22. The MQE as function of i is composed of multiple decisive criteria, see figure 2.23.

By means of local voltage investigation the moment at which the decisive criterion is reached can be defined, the so-called Quench Decision Moment QDM. QDM is very small for APC I, therefore the effect of a variation in pulse duration on APC I can be strong. For APC II and higher and CPC I and higher, QDM is much larger, in the order of hundreds of μs to tens of ms after the start of the heat pulse. Therefore, the pulse duration has no significant effect on the MQE in regime II and higher.

Defining cable stability with analytical models has proven to be difficult, due to the coupling between thermodynamics and electrodynamics in the complex network of strands in a Rutherford cable. In CUDI the cable is described as a network of strand sections interconnected by contact resistances. CUDI calculates the current and temperature of each strand section and the interstrand currents in detail as a function of time and position, thus providing a powerful tool to investigate the stability mechanisms in a Rutherford cable.

An accurate description of cable geometry is essential for APC and CPC, therefore it is determined in detail. CUDI allows a very detailed input of local variations in geometry parameters.

Chapter 3

Advanced Measurement Techniques

The first objective of this chapter is to present the measurement set-up. The second objective is to discuss the relevance of experimental results on cable stability for magnets applications.

The limitations of cable stability measurements are presented. The influence of a non-uniform magnetic field on the cable caused by self-field variations due to a locally different critical current is discussed. The representativity of the stability of a cable in test conditions for the stability of a cable in a real magnet conditions is argued.

Fast heat exchange between pulse heater and sample is vital for accurate determination of MQE. *Five types of heaters are introduced and the suitability for cable stability measurements is examined. The graphite paste heater, the heater of choice, is presented in more detail. The delay of the heat pulse, due to the limited heat transfer from the heater to the sample, is investigated and a correction factor for measured* MQE *values is determined.*

Hall probe arrays are used to measure self-field along a cable, thus enabling the characterization of current distribution in the cable. Measurements and simulations of self-field are compared and the current distribution in the cable is investigated.

Finally, the results from local voltage tap measurements are discussed. Local voltages provide valuable information on the length and duration of a normal zone. The sequence of longitudinal and transversal normal zone propagation is investigated.

3.1 Experiment

3.1.1 FRESCA cable test facility

The test facility called FRESCA is built for the reception tests of superconducting cables for LHC magnets [62]. The main features of the test station are:

- A magnetic field of 10 T homogeneous within 1 % along a sample length of 56 cm, provided by a superconducting dipole magnet, cooled separately from the sample [63];
- Sample cooling either by superfluid helium at 1.8 to 2.17 K and by liquid helium at about 4.3 K, both at atmospheric pressure;
- A DC sample current up to 32 kA maximum.

The test station has two cryostat compartments: The outer compartment contains the magnet and the inner compartment holds the sample, see figure 3.1a. For the presented measurements, the field is oriented parallel to the flat side of the cable.

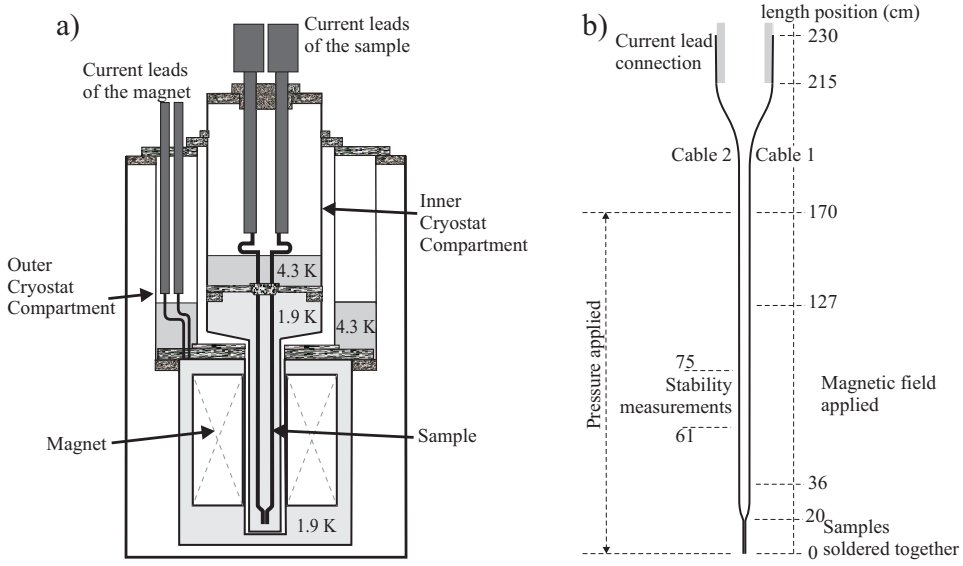

Figure 3.1: a) Schematic overview of the FRESCA inner and outer cryostat compartments, containing the sample and the magnet, respectively. b) Schematic view of the two samples, with the position of the magnetic field, the area of the stability measurements and the soldered splices. The distance between the two cables in the test area varies between 0.2 and 12 mm.

3.1.2 Cable sample

To create a current loop, two cables of about 230 cm long are soldered together in a bottom joint of 20 cm long and they are clamped with soft-solder interface to the current leads at the other end of the cables along a length of 15 cm, see figure 3.1b. The heaters needed to do stability measurements are positioned in the center of the homogeneous magnetic field area at about 61 to 75 cm from the bottom end of the cable sample.

The self-field B_{sf}, produced by the transport current through the cables is significant and inhomogeneous. The total magnetic field, the sum of the applied field B_a and B_{sf}, is visualized in figure 3.2.

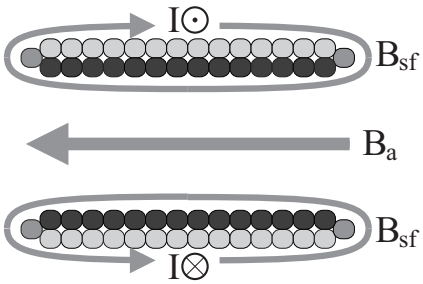

Figure 3.2: Illustration of the self-field and applied field on the cables in the FRESCA set-up. The grey value of the cross section of the strands indicates the strength of the total field.

In figure 3.3 the variation in magnetic field across the cable width is visualized by plotting the total magnetic field along one strand over one twist pitch in an LHC 02 cable sample. In the displayed conditions, at 4.3 K, 6 T and 15 kA, the variation in I_c due to the self-field is more than 15 %. Local variations can have a strong influence on the MQE. Therefore in simulating measurements, the exact magnetic field pattern needs to be accounted for. Heat depositions are applied on the broad cable surface where B_a and B_{sf} have opposite direction, i.e. at a position between 55 mm and 110 mm.

The direction of current is chosen parallel to minimize the torque forces on the sample holder.

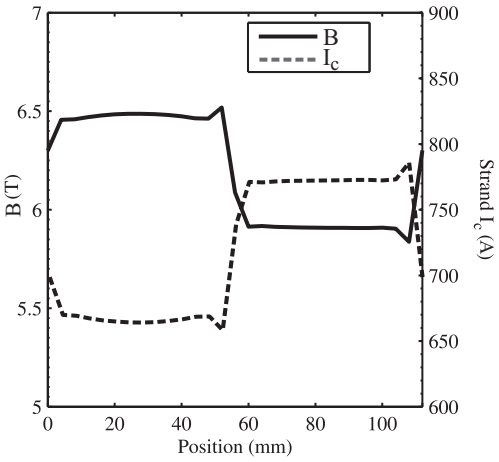

Figure 3.3: The total magnetic field and I_c along the path that one strand follows in the cable in one twist pitch. $B_a = 6$ T, $T = 4.3$ K and $I = 15$ kA.

3.1.3 Sample holder

The cable samples are positioned in a G-10 sample holder enforced by stainless steel bars, see figure 3.4a. The bars spread the force on the sample holder, hence providing a homogeneous pressure on the cable samples. The specific sample holder is designed to hold the 15.1 mm wide LHC 01, LHC 02 and SIS 300 dipole cables. A channel is available for wiring of the heaters, hall probes and voltage taps.

The sample holder is adapted at the position of the stability measurements. Along the thin edge of the test sample, cable 2, a Hall probe array is positioned, see figure 3.4b. To minimize the influence of the self-field from cable 1 on the measurements, the distance between the cables is taken as large as possible. A 12 mm thick G-10 bar is used to separate the two cables. The open channel on the left side of the samples provides a working area for applying the heaters and the voltage taps.

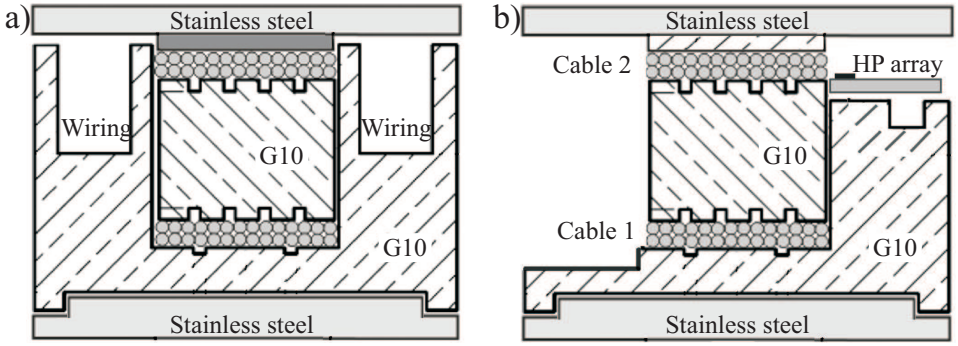

Figure 3.4: a) Cross-section of the standard section of the sample holder. b) Cross-section of the sample holder at the position of the heaters and hall probes.

3.1.4 Sample insert

Many bolts over a length of 170 cm in the stainless steel sample insert provide pressure on the cable samples, see figure 3.5. The stainless steel bars of the sample holder distribute the pressure evenly, hence providing a homogeneous pressure of 50 MPa on the cables. For cables with a keystone angle the thick side of cable 2 is positioned above the thin edge of cable 1, to prevent inhomogeneous thickness of the total package.

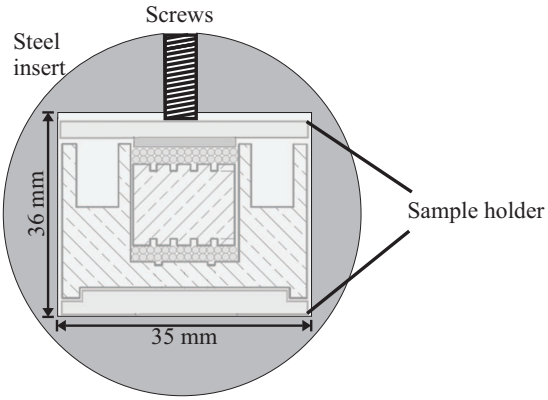

Figure 3.5: Cross-section of the stainless steel sample insert, with the sample holder clamped inside.

3.1.5 Representativity of the measurements

Cable stability in an accelerator magnet is influenced by the local condition of:

- The magnetic field in the cable;

- The pressure, phase and temperature of the helium coolant;
- The insulation wrapping around the cable;
- The pressure on the cable;

The impact of the variation in magnetic field on I_c and T_c is large. Hence the local quench propagation velocity and MQE are far from constant. Both longitudinal and transversal normal zone propagation is affected by the variation of the magnetic field across the cable sample. For comparison of B and I_c in magnet conditions and experimental conditions, see figures 2.13 and 3.2. The magnetic field profile on a cable in magnet cannot be applied on a cable in a test station, due to the high field gradient in a magnet and the self-field profile in the experimental set-up. Measurement results on cable stability are therefore not capable of producing exact stability characterization of a cable in magnet conditions.

Superfluid helium at a pressure just above atmospheric pressure is available in FRESCA and a bath temperature is maintained at 1.9 K during the test, similar to conditions in LHC magnets. The test station FRESCA is not suitable for measurements in supercritical helium, as is used in SIS magnets. The effect of a possible temperature gradient across the cable width is assumed to be small and it is not considered in this thesis.

In the experiments the cable is wrapped locally with insulation tape. Similar to the condition in LHC magnets, Kapton is assumed to fill the outer cable voids completely, see section 2.2.3. The helium volume and the area in contact with helium are influenced, thus impacting the cable stability, see chapter 5.

The pressure on the cable affects the interstrand electrical and thermal conductivity, hence influencing cable stability, see chapter 4. In the experimental set-up a constant homogeneous pressure is applied on the broad surface of the cable. In the magnet set-up the pressure depends on the magnetic field.

For correct measurements of MQE, the cable needs to possess homogeneous R_a and R_c over a length similar to the length over which significant current distribution takes place. Simulations show that for very high R_a and R_c the length of the cable in the test station is not sufficient to represent the long length of cable in a real magnet. In figure 3.6 the current profile in the heated strand is shown for different moments after the start of the heat pulse. Up to 1.2 ms, the current redistribution occurs between the splices. Above 1.2 ms the curves show significant current redistribution in the joint regions during the existence of the normal zone and also before the QDM, hence the MQE is overestimated in the test set-up for cables with very high R_a values.

The length from the bottom joint to the heater in FRESCA of about 50 cm is sufficient for LHC 01 cables with R_a and $R_c < 0.5$ mΩ and for LHC 02 and SIS 300 cables with R_a and $R_c < 1$ mΩ.

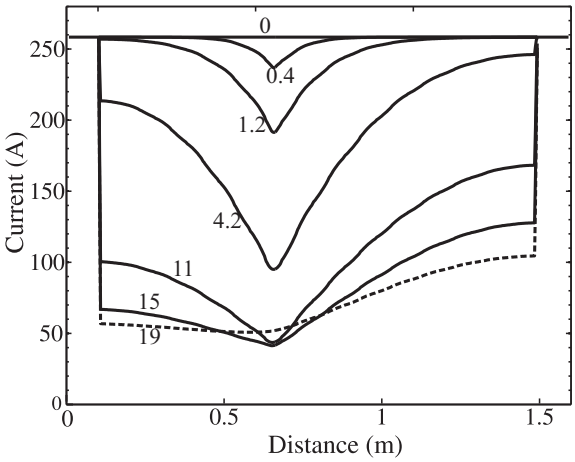

Figure 3.6: The current in strand j as a function of distance from one joint at different times from 0 to 19 ms after a heat deposition in strand j. At 19 ms, the normal zone is recovered. Simulations performed on a 1.6 m long SIS 300 type cable, $R_a = 8.5$ mΩ and $R_c = 20$ mΩ, with a heater at 0.7 m.

3.2 Heat deposition

To perform MQE measurements on a cable, a pulse heater needs to satisfy the following conditions:

- Fast heat transfer into the conductor.
- Small physical dimensions, comparable to the strand diameter.
- Accurate heat generation between 5 μJ and 10 mJ.
- Possibility to make reproducible measurements.
- Strong enough to deal with the pressure of 50 MPa.
- Small heat capacity.

Multiple types of heaters have been developed and used in MQE measurements, especially on strands. In this section the specifications of 4 heater types are discussed. Thereby a strong focus is on the two heater techniques, i.e. strain gage heaters and graphite paste heaters, used in the research for this thesis.

3.2.1 Heaters

Tip heaters
Tip heaters consist of a cylindrical shaped tube with a resistive coating on the tip.

By applying a voltage between the conducting tube and a sample, heat is generated at the contact. A major part of the heat is generated near the surface of the strand, allowing fast entry of the heat to the strand. Reproducible MQE measurements on LHC 01 strands have been performed in [64] with a cylindrical tip heater with a diameter of 0.6 mm and a 40 μm thick graphite paste layer and a tip resistance of 20 to 40 Ω.

Laser deposition
A new technique is the laser deposition as described in [65, 66]. An optical fiber is aligned perpendicular to a strand and connected with a single-mode diode laser at room temperature. The absorption of the bare copper surface or the AgSn surface of the strand is relatively low, but it can be increased up to 22% by oxidizing the strand locally. The size of the deposition area is about 3 mm^2. Major drawbacks of the laser technique for application in cable stability measurements are the limitation in the deposited energy and the positioning problems in the case of a pressurized cable.

Strain gages
Strain gages typically consist of a constantan resistance with a meander structure, deposited on a Kapton film, see figure 3.7. Resistance values are relatively high in the order of 100 Ω. This heater type was initially chosen for MQE measurements on cables, for its flat structure that can cope relatively well with the high pressure in the sample holder. In a first measurement the heater was separated from the cable with 30 μm of Kapton and the thermal contact with the sample was found to be too low. In a second measurement, a film of 8 μm of Kapton was used, therefore reducing thermal resistance sufficiently for an effective pulse duration much lower than 1 ms [67]. However, the 8 μm Kapton heaters showed mechanical failure in too many occasions.

Figure 3.7: Typical strain gage layout, overall size 0.8*2.4 mm^2.

Graphite paste heater
Graphite paste heaters were used for wire stability measurement by [68] and for all cable stability measurements reported in [69, 39, 54, 51, 56]. The heat is produced with a current through the resistive paste. Due to the direct contact of the heater with the cable, fast heat exchange is possible. Due to the high reliability and excellent performance under pressure, the graphite paste heater is chosen to perform most of the measurements reported in this thesis.

3.2.2 Heater production

Multiple heaters are placed on each cable sample on the broad surface of the cable, in order to provide a statistically relevant number of measurements and to act as voltage taps, see figure 3.19. Holes of 0.5 mm diameter are created in an adhesive Kapton tape with a thickness of 50 μm. The holes are spaced by a distance l_p/N_s, allowing one heater per consecutive strand. Copper strips of 1 mm wide and 50 μm thick act as current leads. The strips are attached on Kapton film and spaced by the same distance as the holes.

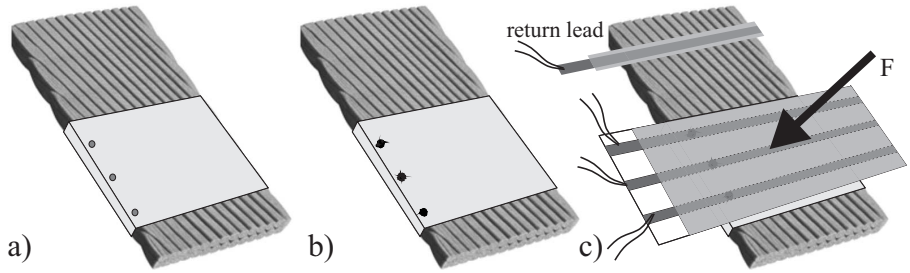

Figure 3.8: Three steps in the preparation of a graphite past heater: a) An adhesive Kapton tape with prefabricated holes is attached to the cable; b) The holes are filled with graphite paste; c) Copper strips on Kapton tape are positioned on top of the heaters.

In figure 3.8 the heater preparation scheme is shown. First the Kapton tape with holes is positioned on the broad side of the cable, with the hole covering only one strand each. In the next step the holes are filled with graphite paste. In step three the copper current leads are positioned above the holes, while a part of the strip sticks out over the edge of the cable for connection to the pulse generator. Pressure is applied to control the heater resistance and the sample is left overnight allowing the paste to solidify. A return lead for the current through the heaters is positioned. Finally wires are soldered to connect the heaters with the measurement instrumentation and the pulse generator. The cross-section of the prepared heater is shown in figure 3.9.

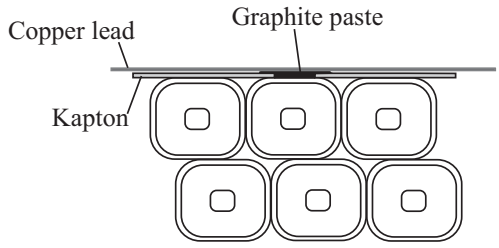

Figure 3.9: Cross-section of a graphite paste heater (black) mounted on the cable.

Table 3.1: List of MQE measurements as function of pulse duration for different heater types.

Heater type	Reference	Sample	Temperature K	Field T	I/I_c -
Tip	[64]	LHC 01 wire	4.2	8	0.7
Laser	[66]	LHC 01 wire	4.3	7	0.85
Strain gage 8 μm Kapton	This thesis	LHC 01 cable	4.3	6	0.9
Strain gage 30 μm Kapton	This thesis	LHC 01 cable	4.3	6	0.9
Graphite paste	This thesis	LHC 01 cable	4.3	6	0.9

After preparation and cool-down of the sample, the heaters undergo a training by consecutive increasing heat pulses that reduces the resistance to a value of typically 1 to 5 Ω [67].

Heater comparison

Since in stability regime I QDM is similar to the pulse duration pd, MQE measurements as a function of pd in regime I give a good indication for the thermal response time of a heater. Figure 3.10 shows the dependence of MQE on the pulse duration for sample conditions given in table 3.1. Steeper curves indicate a faster response to the heat pulse.

Specially the strain gage with a 30 μm Kapton insulation layer shows no significant variation in MQE up to $pd = 2$ ms, indicating a slow thermal response. With the layer of 8 μm of Kapton a major improvement of the thermal response is observed. The pulsed laser heater exhibits the fastest response. The graphite paste heater is the fastest heater type that is suitable to be applied in large numbers in cable stability measurements.

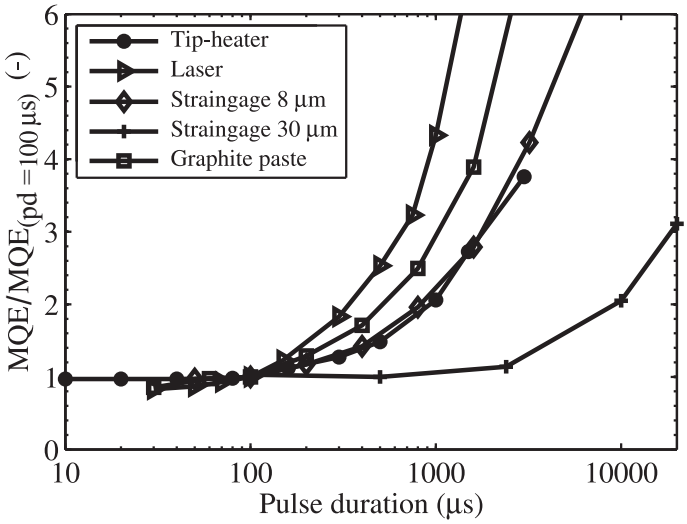

Figure 3.10: MQE values, normalized to the MQE for pulse duration at 100 μs, versus the pulse duration for 5 different heater configurations.

3.2.3 Effective heat flow into a strand

Heat release due to strand movement in magnets are believed to flow directly and homogeneously into the strand. In measurements however, a graphite paste heater is used, thus generating heat outside the strand. The limited heat exchange between heater and strand causes a delay of the pulse and a fraction of the heat flows elsewhere, influencing the measured minimum energy pulse E_p.

By estimating the thermal conductivity between the graphite paste and the strand from [27], the shape of the heat flow into the strand is calculated for a square input pulse [70]. A typical shape of the heat flow from heater to strand is shown in figure 3.11. From the curve a time constant of 60 μs is deduced.

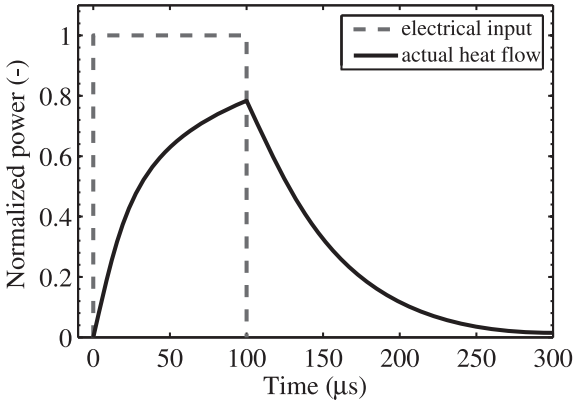

Figure 3.11: Calculated typical response of the heat flow from the heater into the strand for a squared pulse of 100 μs.

Only the heat deposited on the cable before QDM contributes effectively to MQE. To deduce the real value of MQE, the energy flow into the strand is integrated:

$$MQE = \int_0^{QDM} P_p(t) \cdot dt \quad [J], \tag{3.1}$$

with P_p the pulse power.

Since the value of QDM and P_p are very difficult to obtain for most measurement cases, MQE is calculated with:

$$MQE = f_{corr} E_p \quad [J], \tag{3.2}$$

where f_{corr} is a correction factor. f_{corr} is calculated for the specific heater and pulse duration. Simulations have shown that QDM in the single strand stability regime is just after the maximum of the heat flow into the cable, in this case at about 100 μs. The effective heat that has entered the cable at QDM according to the calculated curve of P_p in figure 3.11 is $0.6E_p$. Therefore f_{corr} is assumed 0.6 in regime I.

Exact data for thermal conductivity of the heater are not available, thus uncertainty of the calculated values is high. Measurements in [66, 64] show an overestimated MQE compared to calculations, with MQE $\approx 0.5\ E_p$.

In the stability regimes II and higher, where stability is affected by current redistribution, QDM is in the order of 0.2 to 10 ms. For such long times only heat loss to the environment plays a role, which is in the order of 5 to 20% [70]. The following correction factors are obtained from the estimated heat exchange parameters:

Regime I - $0.4 < f_{corr} < 0.7$
Regime II and higher - $0.8 < f_{corr} < 0.95$.

Correction factor in simulations and measurements

To avoid difference between measurement and simulation, the curve of figure 3.11 is used when simulating measurement conditions. In simulations with CUDI for this thesis, two different pulse shapes are applied:

- Simulations that describe measurements, mainly in chapter 6, use the pulse shape of figure 3.11 as the input pulse shape. The MQE for both simulations and measurements is calculated by $f_{corr}E_p$. The factor $f_{corr} = 0.6$ is applied for regime I and $f_{corr} = 0.9$ for regime II and higher. The effect of f_{corr} on the relation between E_p and MQE is shown in figure 3.12.
- Simulations for parameter research in chapters 4 and 5 and simulations for real magnets in chapter 7 use rectangular pulses with no loss, hence $f_{corr} \equiv 1$ and MQE $= E_p$.

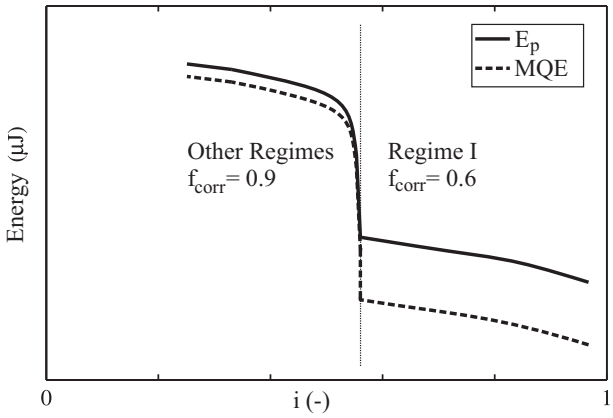

Figure 3.12: The measured input pulse value and the corrected value. For regime I a correction factor of 0.6 is used and for the other regimes a factor of 0.9.

3.3 MQE measurement

MQE measurements are performed by applying an electrical pulse with a duration of 100 μs to the heater and the response of the sample is simply 'quench' or 'no quench'. E_p is determined with an error < 5 % by iterating between quench and no quench cases, see figure 3.13a. For locating the steepest part of the curve, the same method is used to find the transition current with an error < 0.5 % for a fixed E_p value, see figure 3.13b.

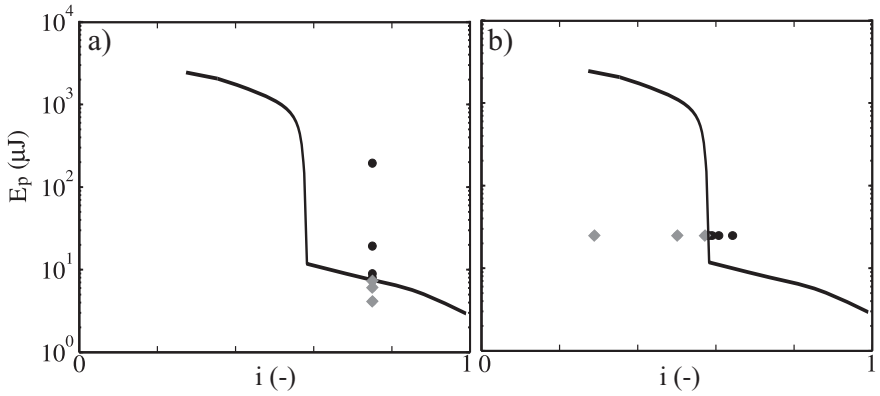

Figure 3.13: E_p measurement procedure of consecutive pulses: a) for constant current and b) for constant MQE. The black dots indicate a quench, the grey diamonds indicate recovery.

With typically 6 to 8 pulse energies needed per MQE value, the method is time consuming. After each pulse the virgin state needs to be recovered, before proceeding. In the case of a quench the quench detection switches off the current supply. The temperature in the sample typically rises up to 20 to 40 K, and a waiting period in the order of one minute is necessary for temperature recovery and return of the helium in the voids, for both superfluid helium as well as liquid helium.

In the case of recovery, the current can be distributed inhomogeneously, and a cable quench is needed before a new 'virgin' run is started. Therefore, even in the case of recovery from a heat pulse a quench is manually triggered.

3.4 Local self-field measurement

To determine the current distribution in the cable, an array of 26 Hall probes is positioned next to the cable, see figures 3.4b and 3.14. The Hall probes measure the summation of the self-field of all the strands and the background magnetic field. The centers of 26 Hall probes, measuring 1 by 1 mm, are located 1 mm from the cable thin edge and are separated 4 mm from each other, which is about l_p/N_s.

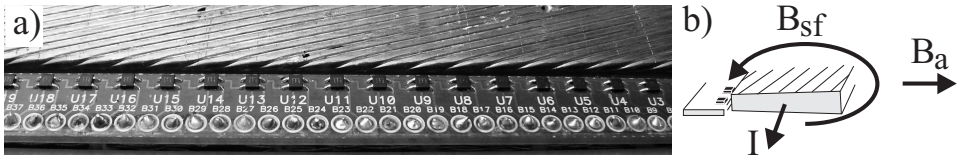

Figure 3.14: a) Photograph of a part of the Hall probe array, positioned next to the sample. The black squares are the Hall probes. b) The direction of the self-field of the cable and the applied field with respect to the Hall probes.

Simulations have shown that most of the current that leaves a strand in the case of a local normal zone will enter the two neighboring strands. Figure 3.15 shows the self-field next to the cable at the position of the Hall probes in the case one strand carries no current, while both adjacent strands carry 50 % extra current. The change in signal is rather small; only a maximum relative variation of 3 % is seen. The relative variation in measured Hall probe signals is even smaller due to:

- The background field, increasing the offset of the Hall probes by up to 200 mT.
- Current decrease in the heated strand is always less than 100 %, see section 4.2..
- Current redistribution takes place only over a limited length, depending on R_a and R_c, see section 4.2.

Hence, the relative variations are small, difficult to measure in short time scales and the accuracy is very case specific. In this section examples of current distribution measurements are given and discussed.

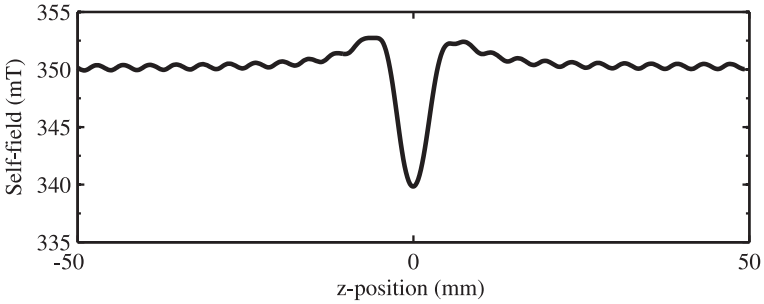

Figure 3.15: Calculated self-field using CUDI on the line along the cable at the Hall probe positions, for LHC 01 cable with $I = 10$ kA. Strand j, closest to 0 mm, carries no current, strands $j \pm 1$ carry 1.5 times the average strand current.

3.4.1 Hall probe signals for $E_p <$ MQE

The self-field measured with the Hall probe array gives a qualitative indication of the rate of distribution and a quantitative measure of the time scales involved in

stability measurements. This section shows the results for a recovery case in area B of figure 2.22 for sample LHC 01 - A, see chapter 6. Locally a normal zone is introduced in one strand with a heater at the center position on the broad surface of the strand. The measured and calculated self-field profile are presented and the current distribution pattern is obtained by calculations, see figure 3.16.

Figure 3.16a shows the measurement of self-field with 8 Hall probes along sample LHC 01 - A, see chapter 6. The most inhomogeneous self-field pattern at 4.5 ms coincides with the full recovery of the normal zone. The self-field profile at 4.5 ms is shown in figure 3.16b. Due to the discretization of the Hall probes, the exact minimum of the self-field can not be measured, but only estimated.

Results from simulations with CUDI are presented in figure 3.16c and d. The qualitative description of the measured and calculated self-field profiles is similar, with a strong reduction of self field over a length of about 8 mm. Since figures 3.16b and d show similar patterns, the assumption of primary current distribution into the adjacent strands is justified.

Since the longitudinal normal zone propagation and current redistribution are strongly influenced by local variations in the interstrand contact and helium cooling conditions, deviations in time constants between measurement and simulations are unavoidable.

The calculated current distribution in the strands is shown in figure 3.16e and f. The curves show a clear minimum of current in strand 4 and thus the recovery of the normal zone at about 2 ms. Figure 3.16f shows the decrease of current in the heated strand, strand 4, and the increase of current in the adjacent strands, strands 3 and 5. After the recovery, the current redistributes to a more homogeneous distribution. The self-field measurements in figure 3.16a show a more homogeneous distribution after the recovery from the normal zone.

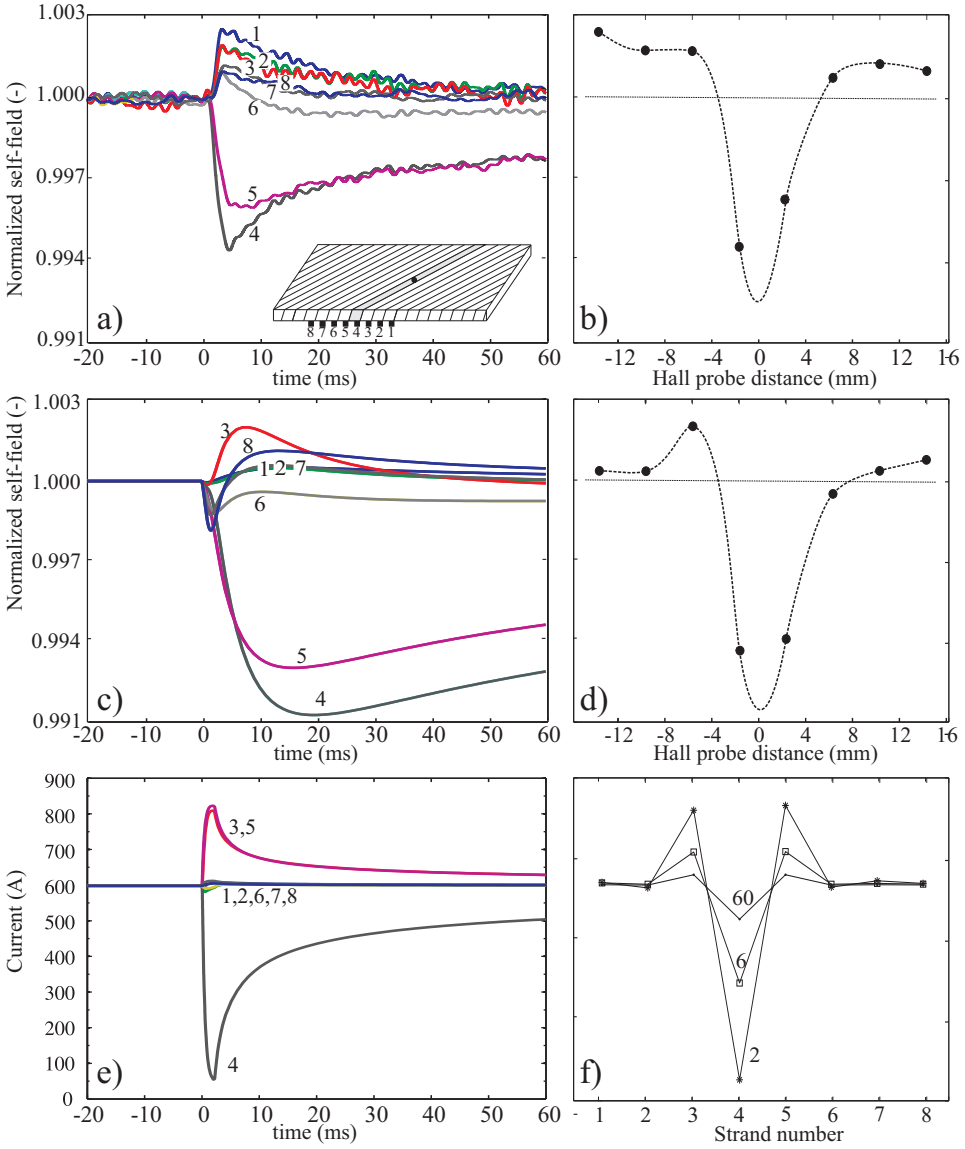

Figure 3.16: Self field and current data for 8 consecutive Hall probes along sample LHC 01 - A, see chapter 6, with $B = 6$ T, $I = 16.75$ kA, $T = 4.3$ K. The pulse, with $E_p = 1.03$ mJ and $pd = 100$ μs is applied to a center heater. The inset in a) shows the position of the heater and the 8 Hall probes. a) Normalized self-field data from measurements, with in b) the self-field profile at 4.5 ms. c) Normalized self-field data from simulations, with in d) the field self-field profile at 6 ms. e) The current obtained from simulations in 8 strands, with in f) the current profile at 2, 6 and 60 ms.

3.4.2 Hall probe signals for $E_p >$ MQE

The development of Hall probe signals for a heat pulse with E_p just above MQE in regime II is similar to Hall probe signals E_p just below MQE, until the QDM is reached. After the QDM, the transversal normal zone propagation is fast, affecting the current distribution and self-field patterns strongly.

Figure 3.17 shows the measurement for the same conditions as in figure 3.16a, but with a slightly higher pulse energy. Up to the QDM at 2 ms both figures show similar curves. The downward trend after 8 ms originates from the cable current decrease, since the power supply cannot maintain the current in the sample in the case of a quench.

The large decrease of self-field around 3 ms for all the Hall probes indicates that the current is decreased more at the thin edge compared to the other parts in the cross-section of the cable. The most likely propagation mode in this case is edge propagation at the thin edge, therefore the thin edge will become normal before the center and the thick edge of the cable.

The self-field is equal for all Hall probes after 8 ms, indicating that the current is distributed homogeneously again.

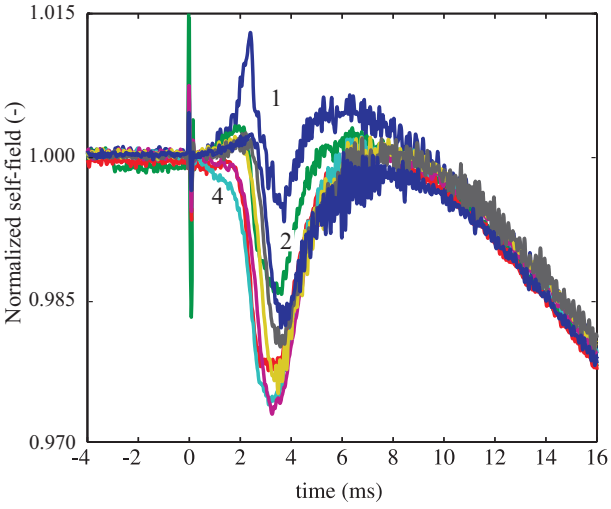

Figure 3.17: Hall probe signals for the same sample conditions as figure 3.16a, but with a sligthly higher pulse of 1.19 mJ. Note the scale difference. A cable quench follows. The initial signal spike at $t = 0$ is due to noise from the electric pulse.

3.4.3 Hall probe signals in case of non-uniform transport current distribution

Non-uniform current distribution exists in cables of superconducting magnets and is generally caused by BICCs, ISCCs and non-uniform joint resistance. Hall probes have been used to determine BICCs in [29, 71]. Non-uniform joint resistance can cause current redistribution with time constants in the order of 10^4 s in LHC dipole magnets [72].

Samples measured in the FRESCA test station are only 2 m long between the joints and they exhibit much smaller inductance. Normally the joints of samples are soldered and uniform joint resistance is obtained. However, one test was performed on a cable with Al_2O_3 coated strand that in the first cool-down accidentally was soldered without removing the Al_2O_3 coating, resulting in a very non-uniform joint resistance.

The normal procedure for stability measurements with a current ramp rate of 1 kA/s to a value of 16 kA ($i = 0.76$) results in non-uniform current distribution demonstrated by longitudinal variations of the self-field, see figure 3.18. The current redistribution process has a time constant of about 50 s. The profile of self-field is sinusoidal in shape. A plausible cause is the variation in contact length between current lead and strand, which is varying in a triangular way when the contact length is not a multiple of the twist pitch length. The current in each strand and its effect on MQE is investigated in section 7.2.

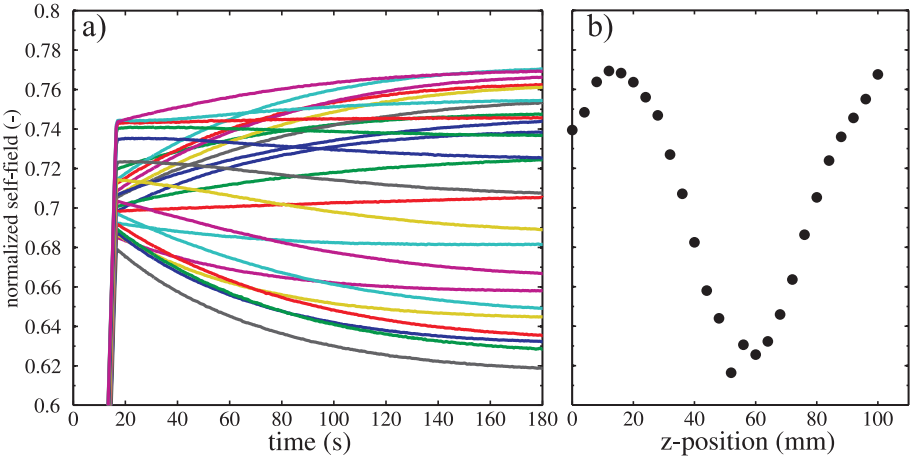

Figure 3.18: a) Cable self-field measurement with Hall probes as a function of time after a fast current ramp to 16 kA in 16 s, normalized to uniform distribution for $i = 1$. b) Spatial profile of self-field along the cable 180 s after the start of the ramp.

Increasing the current with a slow ramp rate allows the current to distribute into a pattern dominated by the resistance of each strand with the current lead.

Due to the non-uniform current distribution the value of i for each strand varies. Therefore some strands will reach the transition to normal resistance before other strands. The resistance of strands carrying more current than average increases, forcing the current to distribute more uniformly.

A non-uniform current distribution causes a locally reduced MQE in strands with higher currents. In section 7.2 the effect of non-uniform current distribution is investigated in more detail.

3.5 Strand voltages

A second measure for current distribution in superconducting cables is the resistive voltage of normal strand sections. The graphite paste heaters are suitable for local voltage measurements, since they are in direct contact with a strand by a resistance of only a few ohm. By placing the heaters in a well defined position, the voltage of multiple strand sections can be measured simultaneously. An example of heater positioning on strands j to $j+4$ is given in figure 3.19, showing how the voltages over half a twist pitch of 5 adjacent strands can be measured. In this section, the information obtained from voltage measurements in multiple strands is discussed.

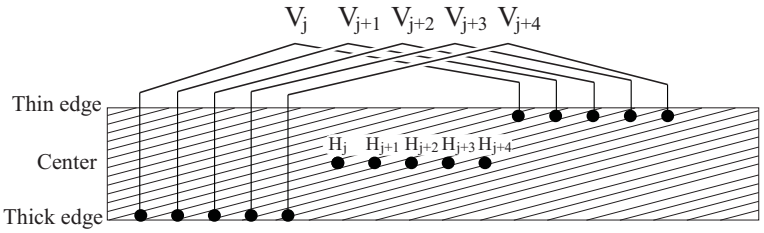

Figure 3.19: Schematic view of 15 graphite paste heaters on the cable at the thin edge, center and thick edge. The edge heaters are used for voltage measurements, with V_j the voltage in strand j, V_{j+1} the voltage in strand $j+1$, etc... H_j indicates the center heater in strand j.

Analysis of local voltage measurements provides the following information of local normal zones in a cable [73]:

- The existence of a normal zone between the voltage taps;
- The average current in the strand between the voltage taps;
- The transversal normal zone propagation.

The voltage taps are analyzed by means of a simulation case in order to give a proper insight in the transversal and longitudinal normal zone propagation, the current distribution and the voltage on a strand. To compare simulations with measurements, sample SIS 300 dipole - C, see section 6.7, is used, at $T = 4.3$ K, $B = 3$ T, $I_c = 26.6$ kA and $E_p = 200$ μJ. The measured voltages are shown in figure 2.24, with the pulse start at $t = 0$ ms. In the no-quench case $I = 17.38$ kA and in

the quench case $I = 17.46$ kA.

In figures 3.20a and b, the voltage across the voltage taps is shown. In figure 3.20c and d, the total resistance between the voltage taps is presented. In figure 3.20e and f the current, averaged between the voltage taps is shown.

No-quench case

In the no-quench case, only the voltage in strand j shows a clear signal, for about 11 ms. The current redistribution starts at the onset of the normal zone in strand j. The resistance in strand j becomes almost similar to the resistance of a full normal zone between the voltage taps of 10.2 mΩ, see 3.20c.

The maximum voltage is reached before the maximum resistance has been reached, meaning that the current in strand j decreases strongly, see figure 3.20e. The current increase in strand $j + 1$ is almost half the current decrease in strand j. The currents in strands $j + 2$ to $j + 4$ only show a minor variation. The current in strand j already increases again before the normal zone in strand j is recovered.

Quench case

In the quench case, each curve shows similar values as the no-quench case up to QDM at 8 ms. Both measurements and simulations show the sudden voltage increase in strand $j + 1$ at QDM, see figure 3.20b. The increase in voltage in strand $j + 1$ at 8 ms is much faster and to a higher value than in strand j at 0 ms. In figure 3.20d is shown that the longitudinal normal zone propagation in strand $j+1$ is much faster than in strand j. The reason for the fast longitudinal normal zone propagation is the high current and small temperature margin in strand $j + 1$ at 8 ms, see figure 3.20f.

Figures 3.20d and f reveal the sequence of transversal normal zone propagation in a nice way:

1. The normal zone in strand j forces an increase of I_{j+1} and T_{j+1}.
2. The increase in I_{j+1} provokes a local normal zone that propagates quickly, thus forcing a quick increase of I_{j+2}. The increase T_{j+2} is less than the temperature increase in T_{j+1}, due to the shorter heat exchange time.
3. The increase in I_{j+2} provokes a local normal zone that propagates quickly, thus forcing a current increase of I_{j+3}, etc.

In table 3.2, the characteristics of the quench case are listed. The higher quench current I_q in strand $j + 2$ compared to strand $j + 1$ is explained by the higher temperature at quench in strand $j + 1$, since the temperature in strand $j + 1$ is increased due to the long lasting normal zone in strand j.

Table 3.2: Characteristic points and data from measurement curves of quench data in figure 3.20.

Strand	I_q	t_{nz}	$v_{q,trans}$	$v_{q,long}$
	A	ms	m/s	m/s
j	485	18	-	16
$j+1$	673	36	0.1	103
$j+2$	727	72	0.8	24
$j+3$	642	12	1.2	18
$j+4$	599	14	1.4	17

The steepness of the voltage curves is a good measure for the longitudinal quench propagation velocity. At 103 m/s, the longitudinal quench propagation in strand $j+1$ is very high, indicating that $i \approx 1$ over the full length between the voltage taps.

The start of the normal zone in strand $j+1$, see figure 3.20d, validates APC II, as discussed in section 2.4.2.

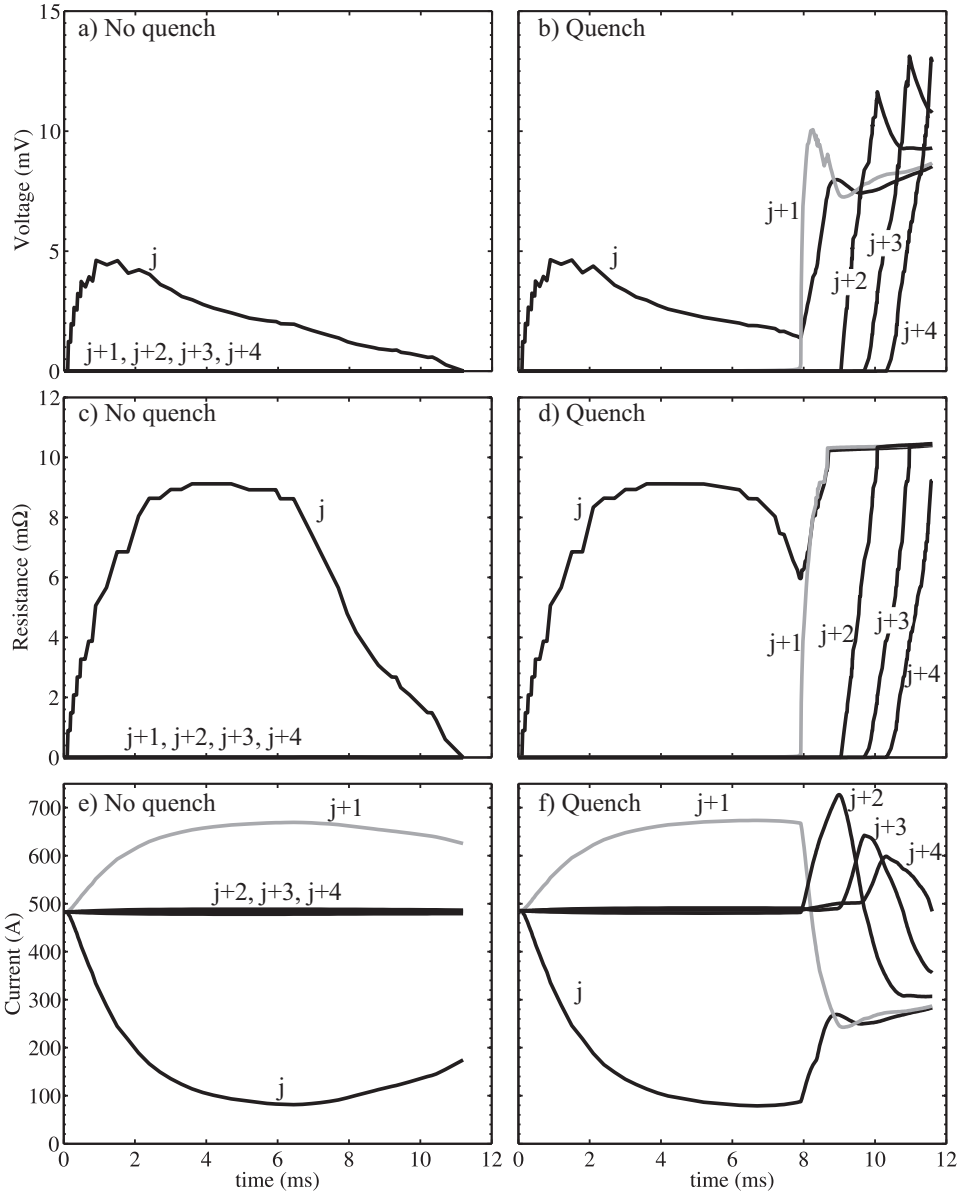

Figure 3.20: Simulation results for a no-quench case (left) at $I = 17.38$ and a quench case (right) at 17.46 kA. Sample SIS 300 dipole - C. $T = 4.3$ K, $B = 3$ T, $I_c = 26.6$ kA and $E_p = 200$ μJ. In a) and b) the voltage, in c) and d) the total resistance and in e) and f) the average current between the voltage taps in strands j to $j + 4$. For comparison with the measuremed data, see figure 2.24.

3.6 Conclusion

The FRESCA cable test facility provides space for a 2.3 meter long cable sample. Heaters are positioned about 0.5 m from the soldered bottom splice. The effective length of current redistribution for cable stability mechanisms depends strongly on R_a and R_c. The length is sufficient to fulfill the boundary conditions for samples with R_a or R_c below about 0.5 to 1 mΩ. For samples with both high R_a and R_c the effective current distribution length is longer than 1 m. Therefore the measured MQE will be overestimated above about 0.5 mΩ for LHC 01 cables and 1 mΩ for LHC 02 and SIS 300 cables.

Due to the non-instantaneous diffusion of heat from a heater into the cable, the effective heat is smaller than the applied heat pulse. Graphite paste heaters provide a fast response, with a time constant for heat exchange in the order of 60 μs. The correction factor for the different quench propagation criteria is determined.

Local self-field measurements along the cable thin edge provide useful information on the current distribution in the case of a local normal zone. The recovery of a local normal zone in the cable is demonstrated in measurements, thus proving the influence of current redistribution on the stability of a cable.

Measurement of local voltages across strands in the cable provides information on the length and duration of a local normal zone. The investigation of the voltage across multiple adjacent strands reveal the sequence of transversal normal zone propagation. Simulations with CUDI provide information on the local currents as well and additionally shows the spatial distribution of current and temperature.

Both the local self-field measurements and the local voltage measurements support and validate the stability models presented in chapter 2. Simulations with CUDI show a comparable behavior of current distribution and normal zone propagation as measured. This proves the validity of CUDI simulations and the ability of CUDI to qualitatively describe the stability mechanisms.

To apply the magnetic field pattern on a cable in a test station as it is on a cable in a real magnet, is virtually impossible. Validity of CUDI makes it possible to calculate cases that can normally not be done in a cable test station, but are occurring in a real magnet.

Chapter 4

Interstrand Contacts Affecting Stability

The distribution of current and the longitudinal and transversal propagation of normal zones in a superconducting cable are strongly affected by the electrical and thermal properties of interstrand contacts.

The most common coatings and heat treatments are described. The resistivity of the metal-oxide layer grown on the strand coating determines the electrical interstrand resistance to a great extend. The thermal interstrand conductance is determined mostly by the contact conductance. The dependence of the thermal conductance of magnetic field is discussed.

The current redistribution patterns caused by the sudden onset of a normal zone in one strand are investigated with simulations using CUDI. *Primary and secondary current paths through R_a and R_c are defined. The time constants of interstrand heat diffusion are discussed.*

The influence of variations in R_a and R_c on the MQE *is investigated for various cable designs and helium cooling conditions.*

MQE *simulations are performed to identify the influence of the interstrand thermal conductance for various cable designs and helium cooling conditions.*

4.1 Interstrand contacts

Cable stability is strongly affected by the electrical and thermal interstrand contacts. The term *contact resistance* is rather misleading, since the electrical resistance between the low resistive (Cu) cores of two strands is a combination of multiple resistances in series, see figure 4.1. Similarly, the thermal conductance is a combination of multiple conductances in series. In table 4.1 the electrical resistance and thermal conductance of each layer are labeled.

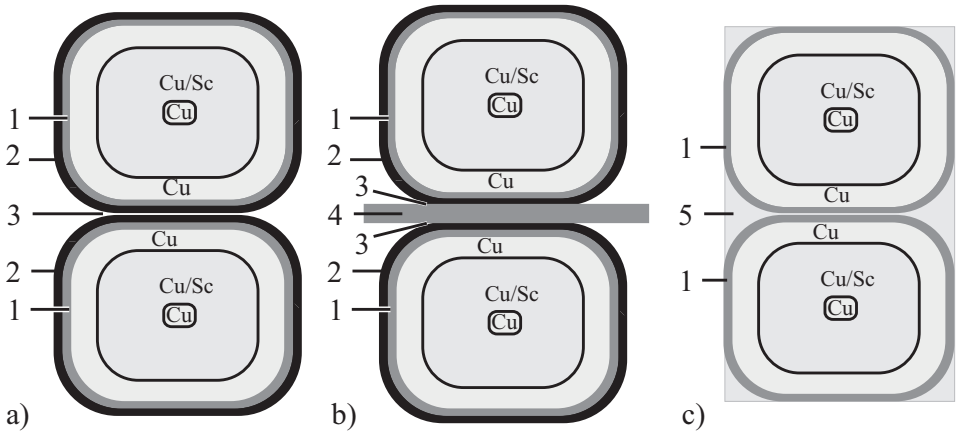

Figure 4.1: Schematic drawing of the series of resistances between the low resistive cores of two strands for a) a non-cored cable, b) a cored cable and c) a soldered cable. The labels are described in table 4.1

Table 4.1: Resistances between the low resistive cores of two strands. The naming of the electrical resistance and thermal conductance is given.

#	Resistance type	Electrical resistance Ω	Thermal conductance $W/K/m^2$
1	Coating	$R_{coating}$	$\kappa_{coating}$
2	Oxide	R_{oxide}	κ_{oxide}
3	Contact	$R_{contact}$	$\kappa_{contact}$
4	Core	R_{core}	κ_{core}
5	Solder	R_{solder}	κ_{solder}

The specific electrical and thermal interstrand contacts are discussed for a non-cored cable, a cored cable and a soldered cable. Values for the interstrand resistances R_a and R_c and the interstrand thermal conduction parameters $F_{int,a}$ and $F_{int,c}$ are presented.

4.1.1 Non-cored cable

Materials

Common surface materials found on superconducting strands and commonly applied heat treatments are:

- Bare copper strand - stored at room temperature.
  On a bare copper surface stored at room temperature a layer of Cu_2O grows slowly and is typically 1 - 5 nm thick [74].
- Bare copper strand - heat treatment at 200 °C in air.
  At 200 °C the copper oxide layer on the surface grows quickly. After 3 minutes, a layer with a thickness of about 50 nm has formed, with Cu_2O at the outer surface. After 30 minutes the surface consists of Cu_3O_2, with a total layer thickness of about 100 nm [75].
  Heat treatment of a cable with bare copper strands under transverse pressure shows a reduction in interstrand electrical resistance. It is assumed that the surface layer of the strand is sealed of from air. Therefore the oxygen from the oxide layer will dissolve in the underlying Cu bulk [76], resulting in a much thinner oxide barrier as compared to a heat treatment without pressure.
- $SnAg_{5\%wt}$ coated copper strand - stored at room temperature.
  The typical coating thickness is 0.5 to 1 μm. An oxide layer with a mixture of SnO and SnO_2 will form on the surface, with a thickness of typically 1 - 5 nm [74].
- $SnAg_{5\%wt}$ coated copper strand - heat treatment at 200 °C in air.
  The typical coating thickness is 0.5 to 1 μm. During a first heat treatment Cu and Sn interdiffuse and form Cu_3Sn [77]. On the outermost surface a very thin layer of CuO grows on top of a Cu_2O layer. During a second heat treatment at 200 °C in air the 0.5 μm Sn coating transforms into a 2 μm thick Cu_3Sn coating, on which a Cu_2O layer with a thickness of typically 20 nm is present. An illustration of the outer layer of an LHC 01 strand is shown in figure 4.2. Since the Cu_3Sn layer acts as a barrier for the oxide to diffuse into the Cu, treatment under pressure does not affect the thickness of the oxide layer much.
- Al coated copper strand - heat treatment at 200 °C in air.
  A layer of Al_2O_3 is formed during heat treatment of aluminum coated strands in 100 % humid air at 200 °C. After 8 hours a 9 nm thick layer of Al_2O_3 is formed [60].

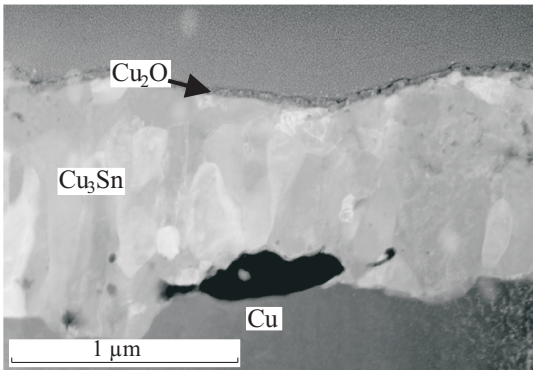

Figure 4.2: STEM image of a cross-section of the Cu_3Sn intermetalic layer and the strand oxide layer, which are formed during the 200 °C cable heat treatment in air. The Cu_2O layer is about 20 nm thick [77].

Electrical contact

As is discussed extensively in [74], in most non-cored cables the electrical interstrand resistance is dominated by R_{oxide}. The thickness of the metal-oxide layer depends on the coating, the heat treatment temperature and duration and the partial oxide pressure. The resistivity of the metal-oxide layer is hard to obtain, since it depends strongly on the purity and phase. Table 4.2 shows the thickness and calculated resistivity as a function of heat treatment for Cu_2O and Al_2O_3.

Table 4.2: Survey of Cu_2O and Al_2O_3 thickness, heat treatment, resistance and calculated resistivity.

Sample and treatment	$R{\cdot}A_{T=4K}$ $10^{-12}\Omega m^2$	thickness nm	$\rho_{T=4K}$** $10^{-3}\Omega m$	Ref.
Cu substrate, 30 min. 200 °C air	220	100 *	1.1	[78]
Cu substrate, 15 min. 200 °C air	50	50***	0.5	[78]
Cu substrate, no treatment	12	5****	1.1	[78]
Cu_2O layer on SnAg coated strand, 8h at 200 °C in air	11	30	0.2	[77]
Cu_2O layer on SnAg coated strand	10 - 40	20	0.25 - 1	[77]
Al_2O_3 on superconducting strand	640	9	35	[60]

*Using the thickness data from [75]
**Calculated values.
***Extrapolated from the data of 30 min. heat treatment at 200 °C
****Using the thickness data from [74]

By applying a variety of oxidation treatments, the thickness of the Cu-O layer on copper plates is varied [78]. The heat treatments correspond to a thickness of the oxide layer of 0 to 100 nm [75]. The surface resistance between the plates as a function of temperature is displayed in figure 4.3 for samples Nilles-1 to 4. Measurements by Lei [79] on the interstrand resistance of a stack of strands, either

with a bare copper surface or an SnAg coating are shown for comparison. The figure shows a large spread in surface resistance, proving the influence of the oxide layer on R_a and R_c. The temperature dependence is negligible in the interesting range of up to 40 K. The sample description and the resistance normalized by the contact surface area are listed in table 4.3.

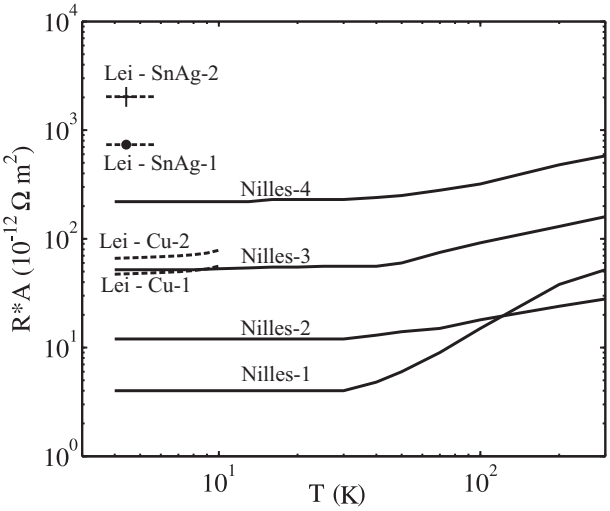

Figure 4.3: Electrical surface resistance between treated copper plates by Nilles [78] and bare Cu strands and SnAg coated strands by Lei [79] as a function of temperature.

Table 4.3: Sample description from [79] and [78] with characteristics at $T = 4.3$ K.

Name	Ref.	Coating and treatment	Pressure MPa	$R \cdot A$ $10^{-12}\Omega$ m^2	κ kW/K/m^2	F_{int} W/K^{1+b}/m^2
Nilles-1	[78]	Cu - Inert gas	13.1	4	18.1	1580
Nilles-2	[78]	Cu - No treatment	13.1	12	14.8	1300
Nilles-3	[78]	Cu - 15 min. air 200 °C	13.1	52	3.8	330
Nilles-4	[78]	Cu - 30 min. air 200 °C	13.1	220	3.8	330
Lei-SnAg-1	[79]	SnAg	154	66	2.6	230
Lei-SnAg-2	[79]	SnAg	229	47	2.4	220
Lei-Cu-1	[79]	Cu	100	2020	1.5	130
Lei-Cu-2	[79]	Cu	155	735	2.0	174

The influence of the surface roughness and pressure on R_a and R_c is regarded as non significant, since a dominance of R_{oxide} is assumed.

Thermal contact

The interstrand thermal conductance is defined by the limited conductance of the

strand coating, the metal-oxide layer and the contact, see figure 4.1. The thermal conductivity λ of a bulk material is governed by two mechanisms, electron conduction λ_e and phonon conduction λ_p. For pure metals $\lambda_e >> \lambda_p$, therefore high electrical conductivity is combined with high thermal conductivity.

The thermal conductivity of the metallic coating layers as well as the Cu matrix material can be regarded as very high, since λ_e is high. The metal-oxide layers on the coating are known to be semi-conducting or insulating, with the electrical conductivity estimated in the order of 0.2 to $40{\cdot}10^{-3}$ Ωm. Therefore, the conductivity λ_e is low and the thermal conductivity is much lower compared to metallic materials. Generally one can assume that in materials with $\rho > 10^{-6}$ Ωm thermal conduction is dominated by phonon conduction and $\lambda_e << \lambda_p$ [80].

The resistance of the oxide layer dominates the electrical interstrand resistance. However, due to λ_p the restrictive part for the interstrand thermal conductance is not necessarily coupled to the restrictive part of the electrical interstrand resistance. Decoupling of the thermal conductance and electrical resistance is proven by measurements performed by Nilles [78]. Measurements on electrical and thermal conductance on four treated copper plate samples have been performed as a function of temperature, see figure 4.4. The heat treatments and value of κ at 4.3 K are listed in table 4.3.

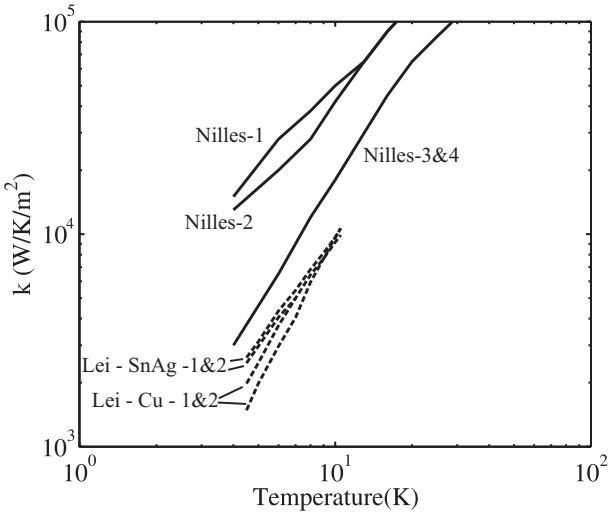

Figure 4.4: Thermal interstrand conductance as a function of temperature for various samples at 4.3 K listed in table 4.3. Data are compiled from [78] and [79].

Due to longer heat treatment of sample Nilles-4 as compared to sample Nilles-3, one may expect a thicker oxide layer. Measurements of electrical resistivity show a 4 times higher resistance, see figure 4.3. However, the thermal conductance between the samples is similar. Therefore, the thermal interstrand conductance is limited by $\kappa_{contact}$ and not by κ_{oxide}.

Providing an accurate description of $k_{contact}$ for a surface material containing impurities is very difficult. Since the phonon wavelength can vary strongly between different materials, energy transport by phonons across a gap smaller than the wavelength is possible. The following factors influence the thermal conductance strongly:

- **Surface material.**
  Measurements show that κ_c is almost twice as high for SnAg coated strand compared to a bare copper surface at 4.3 K [79]
- **Pressure and surface roughness.**
  Higher surface roughness decreases the thermal conductivity. Reported values for bare copper strands at 4.3 K show a decrease of a factor of 1.5 between roughness of 0.1 and 0.4 μm [78]. However, other reports show that the contact resistance only depends on the total force on the contact for any surface, regardless of the total area and the roughness [27]. The total force determines the number of microscopic contact points and therefore the contact resistance $R_{contact}$.
  For the samples described in this thesis the roughness is determined by the application process of the coating, either a hot dip process for SnAg coating or electrolytic process for Al coating.

Due to the theoretical complexity the value of κ is obtained from reported measurements, see section 4.1.5.

4.1.2 Cored cable

Electrical contact

The structure of Rutherford cables favors large current loops, perpendicular to the magnetic field, see figure 2.15. Coupling currents through these loops create ohmic loss that can effectively be reduced by increasing R_c. Therefore, the required minimum value of R_c is much higher than R_a. However, with a resistive coating, R_c is always larger than R_a. By introducing a resistive strip, the so-called core, into the cable R_c can be much higher than R_a and both resistances are controlled separately.

The core is typically made of stainless steel of the type 304 [5] or 316L [81] with a thickness of ~ 25 μm. The electrical resistance of both types of stainless steel at $T < 20$ K is $5.3{\cdot}10^{-7}\Omega$m [82, 83]. For a typical cross contact area of 1 mm^2 the contribution of R_{core} to R_c is 14 $\mu\Omega$. However, the main contribution to R_c comes from the $R_{contact}$ between the strand and the core. The obtained R_c for a cable with a core is tens of mΩ.

Thermal contact

In a cored cable, the stainless steel barrier reduces the cross interstrand thermal conductance. With $\lambda \approx 0.2$ W/K/m at $T = 4$ K [83] and a core thickness of 25 μm, κ_{core} in the order of $8{\cdot}10^3$ W/K/m^2. The effective conductance κ is the determined by 2 contact layers with $\kappa_{contact}$ and by κ_{core}. The value of $\kappa_{contact}$ depends on

the surface composition of the core and the strands, therefore an exact value for κ is hard to obtain.

Compared to a non-cored cable one can assume a reduction of κ by a factor of more than 2 due to the core. From MQE simulations on cored cable samples a reduction by a factor of 5 is found and therefore used throughout this thesis in case of a cored cable.

The electrical resistance and thermal conductance in the adjacent directions are not influenced by the core and are similar to the value in a non-cored cable.

4.1.3 Soldered cable

Three solder techniques have been used on superconducting cables to create highly conductive electrical and thermal contacts between strands. The absence of the oxide layer and the metallic bond enables very low R_a and R_c.

- **Partial soldering**
  Partial soldering is a method to solder the strands at the contact points, but leave voids to enable helium to cool the cable. Solder cream consisting of a mixture of flux and spheroidal solder powder of 30 μm particle size is applied to the outer surface of the cable [84]. The grooves are filled and excess material is wiped off. Heat treatment is performed in an inert atmosphere at a temperature of about 30 °C above the melting point of the solder. The solder flows into all the capillaries between the strands, filling about 20 % of the voids.
- **Full soldering**
  Another way to decrease R_a and R_c is full soldering of the cables, filling the cable voids completely and leaving no space for helium. The process adds rigidity to the cable compared to partial soldering, but the cable MQE is generally less due to the strongly reduced helium content. Sample LHC 01 - treatment F, see chapter 6, was fully soldered, however investigations showed that small helium filled voids remained.
- **Porous-metal filled soldering (Pormet)**
  Pormet soldering shows to be a good option to increase cable stability [54]. A similar solder cream is used as in the partial soldering process, but it is filled with silver grains with a size < 25 μm. In a continuous process the cable is opened and the solder mixture is injected in the cable to assure proper cable filling. After heat treatment a metal sponge is created, consisting of 75 % silver grains and 25 % $SnAg_{4\%wt}$ solder.

Although in general the soldering improves the mechanical stability and the mechanical rigidity of the cable it has never been applied in accelerator magnets. The values of R_a and R_c are simply too small to meet the requirements for limiting AC losses and field errors.

4.1.4 Interstrand electrical resistance

Most cables are first heat treated without pressure, to create an oxide layer on the strand surface, followed by a second heat treatment in the magnet structure, thus under pressure. Heat treatment under pressure reduces the thickness of the oxygen layer, since oxygen diffuses into the strand and the influx of oxygen is limited due to the compression. The effect of the second heat treatment temperature on R_c in LHC 01 cables is shown in figure 4.5 from data by [4] and [74]. Increasing the heat treatment temperature improves the diffusion of oxygen out of the metal-oxide layer, thus decreasing R_c.

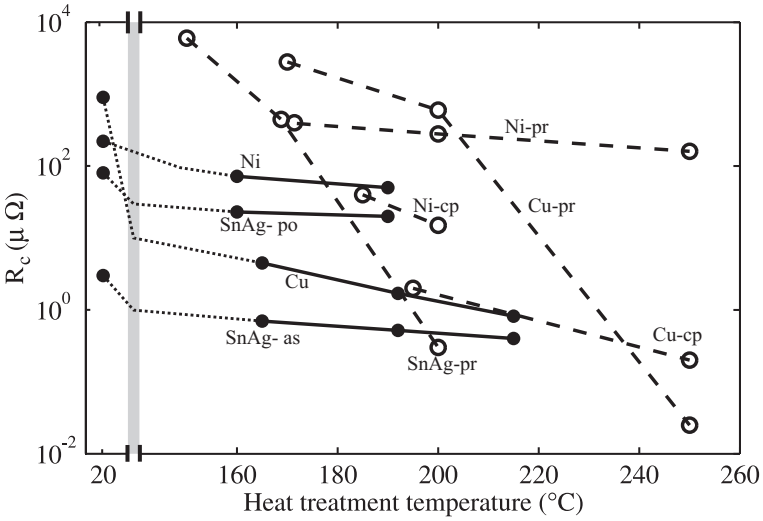

Figure 4.5: Effect of heat treatment temperature on R_c of pressurized LHC 01 cables. Solid dots redrawn from [4], open circles from [74]. Strands are bare copper (Cu), coated with Ni or SnAg. Cables are kept under constant pressure (cp) or R_c is measured after pressure release (pr). SnAg coated cables are heat treated as-received (as) or after pre-oxidation (po).

For an accelerator magnet minimum values of the electrical resistances R_a and R_c are defined to comply with the requirements for AC-loss and field errors. Therefore many reports are available on controlling and varying the resistances by coatings and treatments for values of R_c between 0.5 and 60000 $\mu\Omega$. In this section the conditions that influence R_a and R_c are investigated.

A variety of coatings, cores, solder methods and heat treatments is applied on different Rutherford type cables. In table 4.4, a compilation of various values of R_a and R_c is given for several cables, with strand diameter d_s, number of strands N_s and with or without a resistive core. Table 4.4 shows that many cable variations were tried in order to manipulate R_a and R_c. Dependent on the application restrictions a proper choice of interstrand contact can be made and the cable stability

can be strongly influenced.

Table 4.4: Compilation of measured values for R_a and R_c with different coatings.

Coating/solder material	Treatment	d_s mm	N_s -	Core	R_a $\mu\Omega$	R_c $\mu\Omega$	Ref.
$SnAg_{4\%wt}$	Pre-annealed 4h 200 °C + 0.5h 195 °C	0.825	36	No	-	140	[85]
Bare	as received	1.065	28	No	-	80 - 700	[76]
Bare	0.5 h 190 °C, dry air	1.065	28	No	-	0.5 - 1.6	[76]
$SnAg_{5\%wt}$	as received	1.065	28	No	-	1.7 - 30	[76]
$SnAg_{5\%wt}$	0.5 h 190 °C, dry air	1.065	28	No	-	15 - 20	[76]
$SnAg_{5\%wt}$	0.5 h 190 °C, dry air	1.065	28	Yes	-	300	[76]
Ni	0.5 h 190 °C, dry air	1.065	28	No	-	15 - 20	[76]
$SnAg_{5\%wt}$	as received	0.825	36	SS*	65	>20000	[86]
$SnAg_{5\%wt}$	4h 200 °C	0.825	36	SS	650	>20000	[86]
$SnAg_{5\%wt}$	18 h 215 °C in vacuum + 58h 210 °C air	0.825	36	SS	8500	>20000	[86]
SnAg	0.5 h 185°C air	0.825	36	No	168	21	[81]
Bare	240 h 660 °C Argon	0.825	36	No	10.3	1.1	[81]
Bare	240 h 660 °C vacuum	0.825	36	Yes	1.7	275	[81]
Ni	240 h 660 °C vacuum	0.825	36	No	151	505	[81]
Al_2O_3	6 h 200 °C in humid air	1.065	28	No	-	640	[60]
$SnAg_{5\%wt}$	15 min 225 °C	0.641	30	SS	18 - 100	12500 - 62500	[87]
$SnAg_{5\%wt}$	15 min 225 °C	0.641	30	Brass	8.5	660	[87]
SnAg	Fully soldered	1.065	28	No	< 0.1	< 0.1	this thesis
SnAg	Partially soldered	0.825	36	SS	< 1	> 20000	this thesis
SnAg	Partially soldered	1.065	28	No	-	0.1 - 0.3	[39]
25% SnAg + 75% Ag	Pormet filled	1.065	28	No	-	~ 3	[39]

*SS denotes stainless steel

Coupling between R_a and R_c

The interstrand contact surface areas are defined by the cabling process, see section 2.5. The adjacent contact area A_a is about half the size as the cross contact area A_c. Based on the contact surface area the relation $R_a \approx 2R_c$ may be expected.

The interstrand resistances are measured according to a DC electrical method: Two opposite strands of a cable are connected to a power supply, while the voltage between one strand and all the other strands are measured [76]. Most reports on interstrand resistance of non-cored cables only comprise R_c, since it is easier to measure than R_a. In measurements it is generally assumed that R_a is much higher than R_c. Reports with measurement data on both variables show a large spread in R_a/R_c. For this thesis a value of $R_a = 8R_c$ is used for non-cored cables, according to [81]. In table 4.4 some measured values of R_a and R_c are shown.

Since the interstrand resistance is mainly dominated by the metal-oxide layer, it makes sense to address the differences between R_a and R_c to the variation in growth of the oxide layer. During cable production, the pressure on the cross-contacts is much higher than on the adjacent contacts. Due to the formed saddle shape the cross contact may be more sealed of from the atmosphere compared to the adjacent

contacts, hence the oxide layer may grow slower. A more thorough investigations is needed to properly identify the coating thickness in the cross contact and the adjacent contact.

Variations in R_a across the cable width
Strong evidence is found in measurements that R_a is much smaller at both the thick and thin edge of the cable compared to the broad faces of the cable [87, 88]. A cable sample with length $L_p/4$ is cut from a cable with 30 strands of 0.641 mm diameter, coated with $SnAg_{5\%wt.}$ and with 2 layers of 25 μm stainless steel core. With a DC-current measurement method, the local R_a is measured across the cable. After curing the average resistance $R_{a,av}$ is 22 $\mu\Omega$. Local R_a varies from $0.1R_{a,av}$ in the thin edge, to $5R_{a,av}$ at the center of the cable. This large difference in R_a may cause variations in current distribution pattern at the front of the normal zone.

The reduced contact resistance A_a with about a factor of 1.5, see section 2.5.2, is insufficient to account for the variation by a factor of 50. Since the interstrand resistance is dominated by the resistivity of the oxide layer, the existence of a significant oxide layer at the thin and thick edge may be doubted. A possible explanation is given by the locally high compaction, sealing the contacts from the atmosphere. A more thorough investigation is necessary to address the mechanisms.

For simulations throughout this thesis, R_a and R_c are linearly linked to the variation in contact surface across the cable width, as described in section 2.5. However, the variation in contact surface cannot account totally for the described variation of R_a, thus the local R_a value is underestimated in simulations.

4.1.5 Interstrand thermal conductance

For cable stability simulations the thermal conductance between strands κ is an important parameter. The curves in figure 4.4 between $T = 4.3$ K and 30 K can be described with

$$\kappa = F_{int} \cdot T^b \quad [W/K/m^2], \tag{4.1}$$

with $1.4 < b < 2$. For reducing the number of variables in simulations, a constant value for b of 1.67 is assumed. For the data shown in figure 4.4, the value of F_{int} at 4.3 K varies between 130 and 1580 $W/m^2/K^{1+b}$, as listed in table 4.3.

Since only few data are available on interstrand thermal conductance, especially as a function of the magnetic field, in simulations of MQE measurements the parameters $F_{int,a}$ and $F_{int,c}$ are used as free fitting parameters. The best fit values for $F_{int,c}$ as a function of magnetic field are shown in figure 4.6. The values from [79, 78] and the estimated range of $F_{int,c}$ obtained in [19] are projected as well.

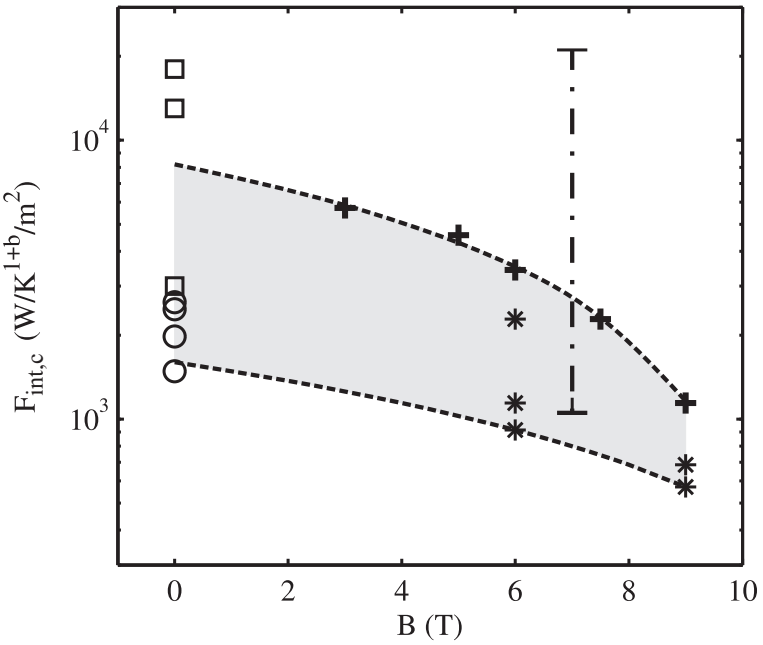

Figure 4.6: Thermal interstrand conductance as a function of magnetic field for various samples at 4.3 K. Squares and circles are measured values from [78] and [79]. Best fit values for $F_{int,c}$ for LHC 01 - sample B are shown with the + sign. The * signs are best fit values for $F_{int,c}$ for other samples in this thesis. The vertical dash-dotted line at 7 T is the extreme range determined in [19] for a bare Cu cable. The dashed lines are linear guidelines.

Best fit values for simulations clearly decrease with higher field. A linear correlation of $F_{int,c}$ with the magnetic field between 3 T and 9 T is found. The linear relationship is drawn through the minimum and maximum values for $F_{int,c}$ in figure 6.6. For the measured samples the following range of $F_{int,c}$ is obtained:

$$720 - 70B > F_{int,c} > 140 - 10B. \tag{4.2}$$

Extrapolation of the data to $B = 0$ shows that the values from literature may agree with the suggested range. The range of $F_{int,c}$ used for simulations in [19] is very large, but it partially overlaps with the range found in this thesis.

In simulations the adjacent surface A_a is smaller than the cross surface A_c. However, the difference is too small to use the same value for $F_{int,a}$ as for $F_{int,c}$. Simulations with non-cored cables require $F_{int,a} \approx 0.5F_{int,c}$ and for cored cables $F_{int,a}$ is generally larger than $F_{int,c}$, see chapter 6.

4.2 Current and heat distribution

Cable stability regime II and therefore the transition current I_t as defined in section 2.4 depend on the transversal normal zone propagation. A local heat deposition in strand j causes an instant increase in local resistance. Due to the increased resistance Joule heating starts and combined with the heat from the pulse, the temperature in a normal conducting section raises by about 1 to 20 K.
Two processes are very important for the transversal normal zone propagation:

- The current redistribution that is initiated by a local normal zone in strand j;
- The diffusion of heat from strand j to neighboring strands.

4.2.1 Current redistribution paths

In most cases of local normal zone recovery, the normal zone in a single strand stretches over a length of a few cm just before the QDM is reached. For comparison of the current redistribution a fixed normal zone length of 40 mm is introduced stepwise in one strand. The current pattern is investigated at 0.8 ms after the start of the normal zone. The value of 0.8 ms is chosen since it is a relevant timescale in most simulations and the difference between the various curves is significant.

Two combinations of R_a and R_c values are used in simulations to distinguish the contribution of each type of contact:

1. R_a 10 or 100 $\mu\Omega$ and $R_c = \infty$. The influence of current distribution through R_a is visible.
2. $R_a = \infty$ and R_c is 10 or 100 $\mu\Omega$. The influence of current distribution through R_c is visible.

The current distribution caused by the normal zone is shown in figure 4.7.

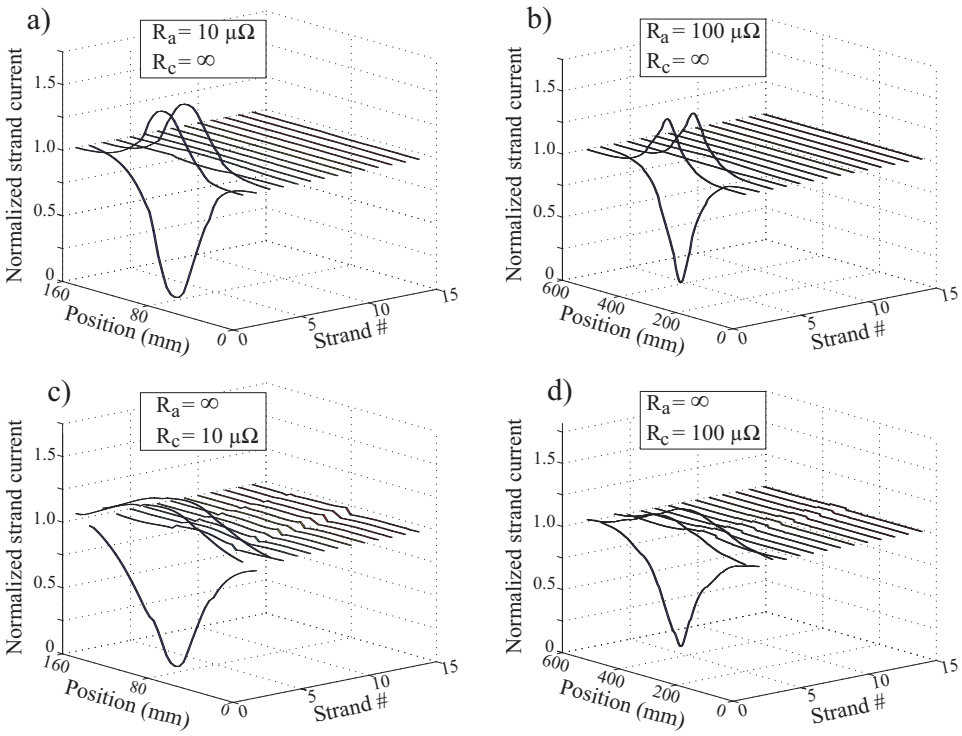

Figure 4.7: Normalized current in 14 strands of a 28 strand cable at 0.8 ms after the onset of the normal zone in strand 2. The figures on the left have a lowest value for R_a or R_c of 10 $\mu\Omega$, the figures on the right of 100 $\mu\Omega$.

Examination of the current distribution for the different cases in figure 4.7 shows that the effective current decay in the strand with the normal zone is primarily balanced by a current increase in the two nearest neighbors. Even for a cable with $R_a = \infty$, thus current redistribution is only through R_c, the current increase is mainly in the adjacent strands $j \pm 1$.

Figures 4.7c and d, with $R_a >> R_c$ show a slight increase in current in strands 4 to 14 the current over one twist pitch. This increase is absent in figures 4.7a and b where the current is only redistributed through R_a. It shows that current redistribution through R_c into the opposite plane of the cable exists, but that it is small.

The current redistribution through R_a and R_c from strand j into strands $j \pm 1$ and $j \pm 2$ is shown in figure 4.8 for a one cable with $R_a = \infty$ and one cable with $R_c = \infty$.

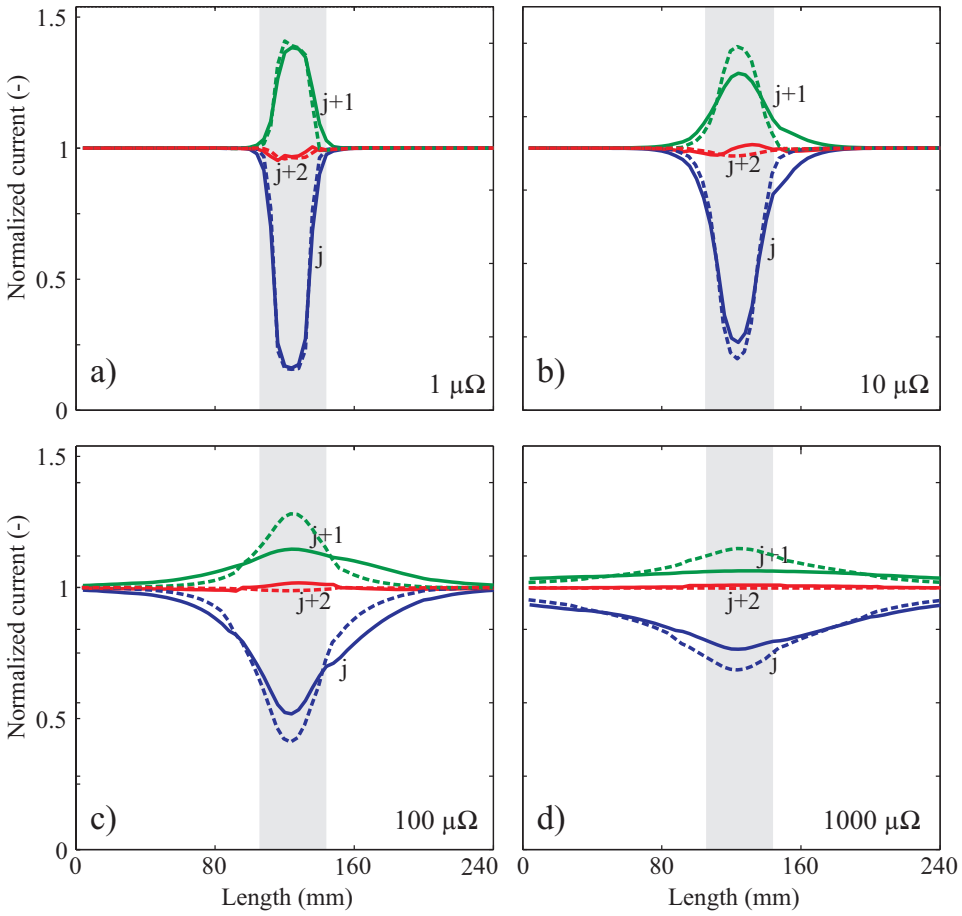

Figure 4.8: Normalized current versus position in strand j, $j+1$ and $j+2$ at 0.8 ms after the onset of the normal zone of 40 mm length in strand j. The dashed lines show the data for $R_c = \infty$ and R_a varying from 1 to 1000 $\mu\Omega$. The solid lines show the data for $R_a = \infty$ and R_c varying from 1 to 1000 $\mu\Omega$. The normal zone is indicated by the grey area.

For the two lowest R_a values, the current is only redistributed in the close vicinity of the normal zone. For higher R_a, current redistribution is forced over a longer part of the cable.

The curves in figure 4.8 are characterized by the value of $I_{j,min}$ and $I_{j+1,max}$. In figure 4.9a the characteristic points are given as a function of the smallest value of either R_a or R_c. The curves show clearly that the current decrease at 0.8 ms in strand j is much less for high R_a and R_c, compared to low R_a or R_c.

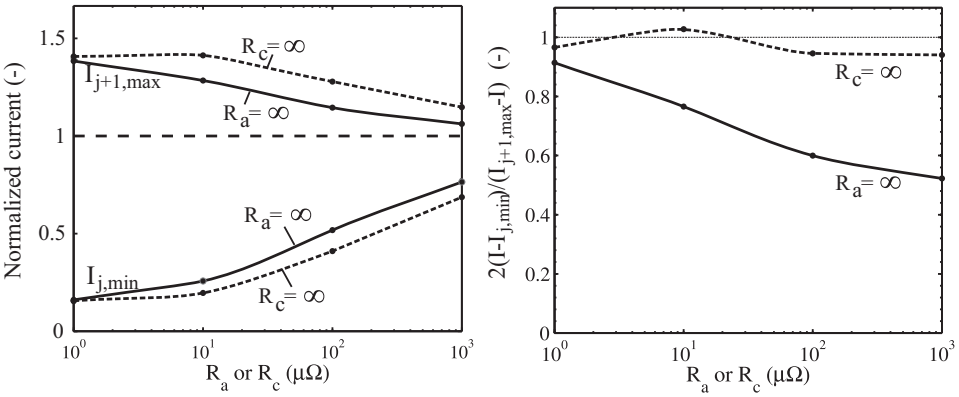

Figure 4.9: a) $I_{j,min}$ and $I_{j+1,max}$ at 0.8 ms after the onset of a normal zone in strand j. In the cable with $R_a = \infty$ R_c is varied and in the cable with $R_c = \infty$ R_a is varied. The dashed line shows the initial current. b) The fraction of current redistribution through the primary current path as a function of R_a or R_c, for three simulation situations at 0.8 ms after the onset of a normal zone in strand j.

A measure for the pattern of the current redistribution is given by the ratio $2\,(I - I_{j,min})\,/\,(I_{j+1,max} - I)$. In figure 4.9b, the ratio is shown for the two investigated cases. If the ratio is about 1, the current decrease is counterbalanced by an increase of current in strands $j \pm 1$. This is the case for the cables where the current distribution is through R_a, with $R_c = \infty$.

For redistribution through R_c, with $R_a = \infty$, the ratio indicates that for high R_c the current redistribution is effectuated not only into the two adjacent neighbors, but also in other strands. For $R_c = 1000$ $\mu\Omega$ and $R_a = \infty$, only 50 % of the current decrease in strand j is balanced by a current increase in the nearest neighbors strands $j \pm 1$.

Effect of current distribution

One important effect of current redistribution is the reduction of Joule heating a the normal zone. For a sample with $R_c = \infty$, the current in strand j is decreases to a value between $0.16 I_{init}$ and $0.69 I_{init}$ after 0.8 ms for R_a between 1 and 1000 $\mu\Omega$, respectively, see figure 4.8. Thus, Joule heating in the normal zone is reduced to a value between 2.6 % and 47 % of the initial Joule heating within 0.8 ms. The

reduction of Joule heating is the key to recover from a normal zone, therefore a smaller R_a contributes to cable stability.

Current redistribution from strand j into strand $j+1$ through R_c is very similar to current redistribution through R_a, see figure 4.7. However, the maximum current decrease is a bit less, with a minimum value of I_j between $0.16I_{init}$ to $0.76I_{init}$. Since the effective resistance into the adjacent neighbors is $4R_c$ or $2R_a$ the effective time constant is larger, assuming a similar effective induction of the redistribution path. Therefore, the current redistribution through R_a is faster than current redistribution through R_c, as is shown in figure 4.8.

The effective current redistribution patterns show that current redistribution through R_a and R_c have qualitatively and quantitatively a similar effect of cable stability.

4.2.2 Primary and secondary current redistribution paths

In section 4.2.1 the current distribution patterns are shown after the sudden onset of a local normal zone. For each case, most of the current is redistributed into the nearest adjacent strands. The simulation results, as given in figure 4.7, show that the primary current redistribution paths can be defined through R_a and R_c, as shown in figures 4.10a and b, respectively.

Figure 4.9b shows that for $R_a = \infty$ and R_c is high $\Delta I_{j-1} + \Delta I_{j+1} < |\delta I_j|$. Therefore the current distribution is using more strands to redistribute. Simulation results reveal the secondary current redistribution paths through R_a and R_c, as illustrated in figures 4.10c and d, respectively. The secondary paths through R_c exhibits a total resistance of $2R_c$, compared to $4R_c$ for the primary paths through R_c, thus explaining the importance of the secondary current paths through R_c for high R_c. In a practical case, the secondary current paths will only play a minor role in non-cored cables with high-resistive coating and $R_a > R_c$.

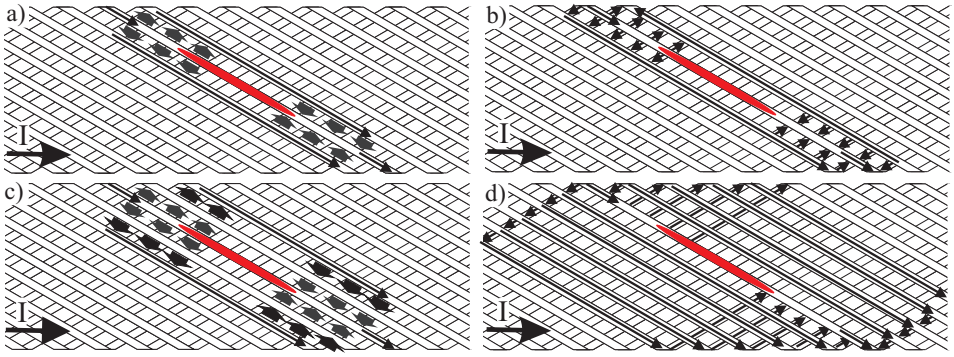

Figure 4.10: a) Primary paths of redistributing current through R_a. b) Primary paths of redistributing current through R_c. c) Secondary paths of redistributing current through R_a. d) Secondary paths of redistributing current through R_c.

4.2.3 Interstrand heat diffusion

The temperature in strand j can increase quickly after the onset of a normal zone, with an observed temperature difference between strands in the order of 1 to 20 K. The diffusion of heat between the strand depends on the interstrand thermal conductivity κ and the contact surface.

The temperature profile in strand $j+1$ is calculated after a stepwise increase in T_j for two cable conditions: a soldered cable with $\kappa = 100$ kW/K/m^2 and a cable with high resistive coating with $\kappa = 100$ kW/K/m^2. The value of κ is 100 and 1 kW/K/m^2 for the soldered and coated cable, respectively. Adiabatic conditions are assumed for strand $j+1$. Strands with length l, diameter $d_s = 1$ mm, $c_p = 2500$ J/K/m^3 and the interstrand contact surface A $= 0.5 d_s l$ are investigated. Since a normal zone implies current redistribution the temperature margin $T_{m,j+1}(B, I)$ reduces in time, see figure 4.11.

The intersection of curves T_{j+1} and $T_{m,j+1}$ indicates the moment at which the stability criterion is reached. Due to differences in Joule heating, the increase of T_j is generally smaller for the soldered cable, compared to the coated cable. The ratio $T_{m,j+1}/T_j$ is small for the coated cable. $T_{m,j+1}$ in figure 4.11b indicates that to reach the stability criterion a higher T_j, or in practice a higher heat pulse, is necessary.

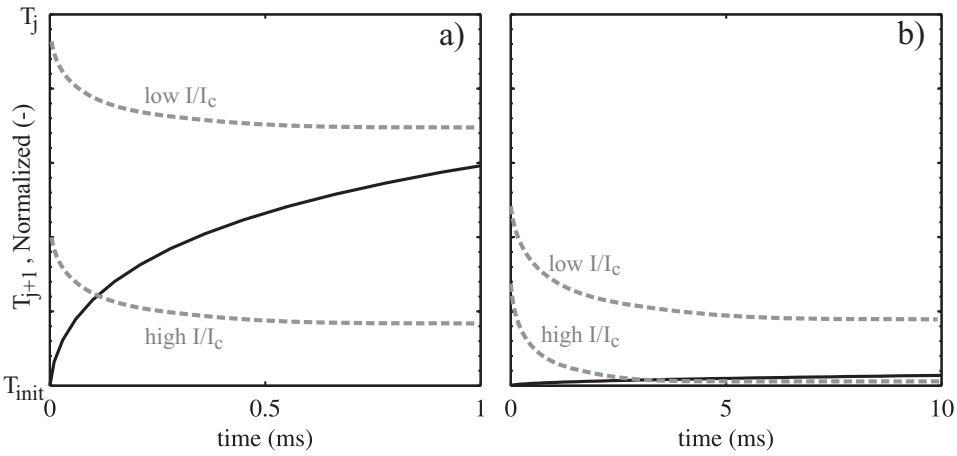

Figure 4.11: Normalized temperature profiles in strand $j+1$ after a stepwise increase in temperature of strand j in a) for a soldered cable with $\kappa = 100$ kW/K/m^2 and in b) for a cable with high resistive coating with $\kappa = 1$ kW/K/m^2. The dashed lines are the profile of $T_{m,j+1}(I_j + 1)$ for low and high i.

4.3 Influence of R_a and R_c on stability

The influence of R_a and R_c on cable stability is investigated with MQE simulations for three cable designs: a non-cored Rutherford cable, a cored Rutherford and a Nuclotron cable. All three designs have been applied in accelerator magnets. The Nuclotron cable provides an example of a cable with homogeneous parameters across the cable width, therefore providing a case with only transversal propagation in the adjacent direction. The longitudinal normal zone propagation is therefore more homogeneous.

The Rutherford cables are non-homogeneous across the cable width, see section 2.5. Strand intrinsic parameters are kept constant between the cables. The resistances in the three cable designs are defined by:

Non-cored Rutherford cable	R_c is variable and $R_a = 8R_c$.
Cored Rutherford cable	R_a is variable and $R_c = \infty$.
Nuclotron cable	R_a is variable and $R_c = \infty$.

In figure 4.12 the cable types are visualized. For the simulations a cable with 18 LHC 01 strands is used, reducing the simulation time significantly compared to a 28 strand LHC cable.

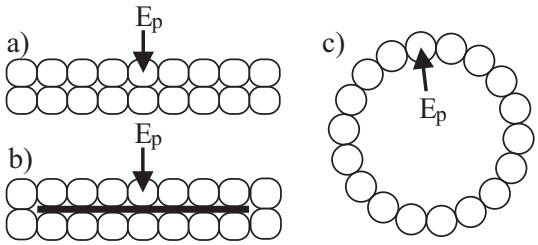

Figure 4.12: Schematic drawing of the cable types used for simulations. a) Non-cored Rutherford cable, b) cored Rutherford cable, c) Nuclotron cable. The arrows indicate the position of the heat pulse with energy E_p.

The influence of R_a and R_c on MQE depends on the cooling in varying situation, therefore four types of cooling and temperature conditions are defined: Supercritical helium at 4.5 K, adiabatic conditions at 4.3 K, liquid helium at 4.3 K and superfluid helium at 1.9 K, see table 4.5. The magnetic field is taken constant across the cable width, but it varies to keep I_c in the same range for different temperatures. The value of $F_{int,a}$ and $F_{int,c}$ are varied as function of magnetic field, as is discussed in section 4.1.5.

Table 4.5: Cooling types used in simulations.

Helium type	T (K)	B T	I_c kA	$F_{int,a}$ W/K^{1+b}/m^2	$F_{int,c}$ W/K^{1+b}/m^2
Supercritical	4.5	5	15.8	200	400
Liquid	4.3	6	13.5	150	300
Superfluid	1.9	9	14.3	50	100
Adiabatic	4.3	6	13.5	150	300

For the various cases, MQE is calculated with CUDI. The curve for the single strand stability regime, regime I, is calculated with a square pulse with a duration of 100 μs, as is discussed in section 2.3.4. For the curves in regime II and higher, a squared pulse with a duration of 10 μs is used.

The sensitivity of the cable stability regimes to parameter variations is investigated. Since the cable edge is very sensitive to local variations, the simulations are performed on center heaters, to avoid the influence of edge effects, see figure 4.12.

The influence of R_a and R_c on the MQE for the three cables in liquid helium cooling conditions are shown in figure 4.13. The data points in the curves for regime II and higher are connected by the most plausible relation, based on the shape of the stability criteria as shown in figure 2.22. The curves are extrapolated to the curve calculated in regime I.

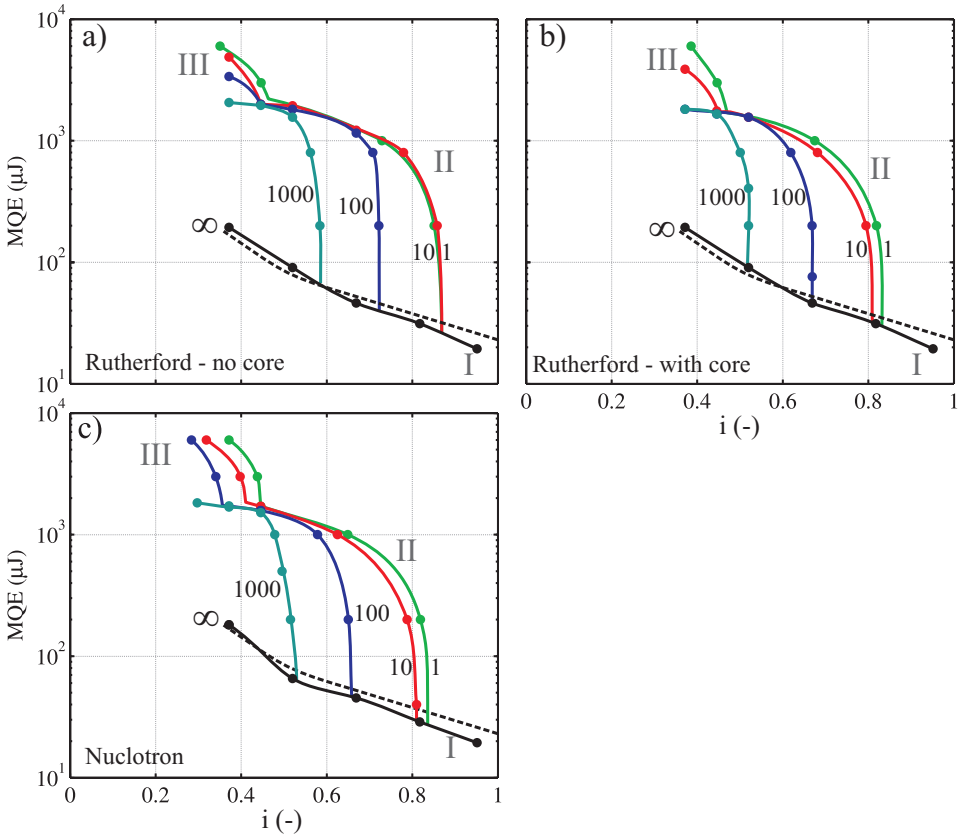

Figure 4.13: MQE data points as function of i for cables cooled by liquid helium as function of R_a and R_c. Three cable types are used: a) a non-cored Rutherford cable (R_c varies from 1 to ∞), b) a cored Rutherford cable (R_a varies from 1 to ∞) and c) a Nuclotron cable (R_a varies from 1 to ∞). The dashed lines show calculated data of MQE on single wires with a pulse duration of 100 μs [26].

All the curves show an improvement of i_{kink} for a smaller interstrand resistance, either R_a or R_c. The increase in I_{kink} is large, about 20 to 30 %, for a decrease of R_a or R_c from 100 to 10 $\mu\Omega$. The stability criterion APC II merges together for all curves at low i. Most curves show the start of regime III at i of 0.3 to 0.5. The calculated single strand MQE data from [26] on a similar strand cooled by liquid helium at 4.3 K and 6 T corresponds within a margin of 20 % with the calculation by CUDI.

In accelerator magnets with a required value of $R_c \approx 1000\mu\Omega$ two options are possible: a cored cable with $R_a << R_c$ and a non-cored cable with $Ra \approx R_c$. The cored cable with $R_a = 10\ \mu\Omega$ $i_{kink} = 0.82$ provides a much better stability as compared to a non-cored cable with $R_a = 1000\ \mu\Omega$ $i_{kink} = 0.57$.

Figure 4.14 shows the influence of R_c on the MQE for the non-cored Rutherford cable for the four defined cooling conditions.

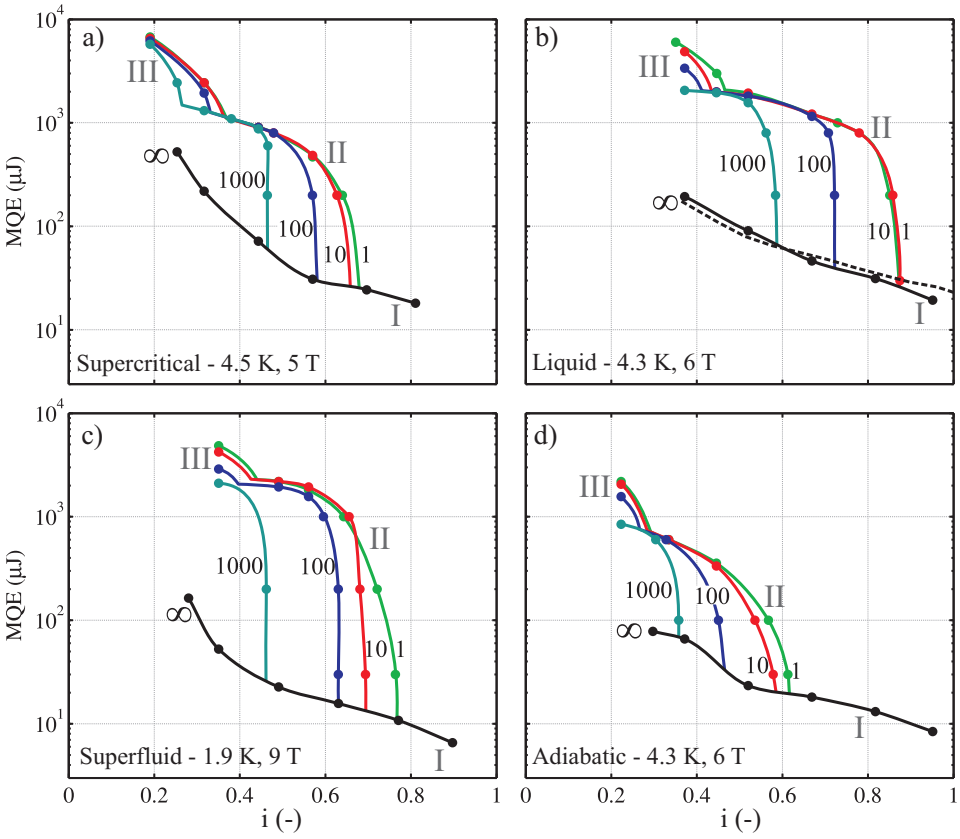

Figure 4.14: MQE data points as function of i for a Rutherford cable without a core and varying R_c from 1 to ∞. Four temperature and cooling conditions are used: a) Supercritical helium, b) liquid helium, c) superfluid helium and d) adiabatic conditions at 4.3 K. The dashed line in b) shows calculated data of MQE on single wires with a pulse duration of 100 μs [26].

For all the helium cooling conditions a similar response is shown, with a higher i_{kink} for a lower R_a and R_c. The sensitivity of the MQE curve to variations in R_a and R_c can be summarized by:

- A decrease in R_a or R_c improves I/I_{kink} strongly;
- A variation in R_a or R_c has no significant effect on stability criterion APC II for low i.

4.4 Influence of interstrand thermal conductance on stability

Generally the impact of an increase in F_{int} is twofold: Cooling into the crossing strands provides reduction of longitudinal normal zone propagation and heat exchange with adjacent and crossing strands raises the transversal normal zone propagation velocity [41].

The influence of a variation in F_{int} on MQE is investigated by a series of simulations. The influence of F_{int} may vary between the different helium cooling modes and between cable types, therefore several cases are simulated and presented. The three cable designs, see for illustration figure 4.12, are investigated:

- Non-cored Rutherford cable $R_a = 160\ \mu\Omega$ and $R_c = 20\ \mu\Omega$
- Cored Rutherford cable $R_a = 160\ \mu\Omega$ and $R_c = 10000\ \mu\Omega$
- Nuclotron cable $R_a = 160\ \mu\Omega$

Each cable has 18 LHC 01 strands. The Nuclotron cable exhibits homogeneous cable parameters across the cable width. Rutherford cables have a varying geometry across the cable width, and therefore the parameters A_a, A_c, A_{He} and V_{He} vary according to section 2.5, thus influencing local stability mechanisms.

To study the influence of the full range of F_{int}, the value of $F_{int,c}$ is varied from 20 to 1000 $\mathrm{W/K^{1+b}/m^2}$, with $F_{int,a} = 0.5F_{int,c}$. The range of F_{int} depends on the magnetic field. For cored cables, $F_{int,c}$ is reduced by a factor of 5 and $F_{int,a} = 2.5F_{int,c}$.

The influence of $F_{int,a}$ and $F_{int,c}$ on MQE depends on the cooling in varying situation, therefore four types of cooling and temperature conditions are defined: Supercritical helium at 4.5 K, adiabatic conditions at 4.3 K, liquid helium at 4.3 K and superfluid helium at 1.9 K, see table 4.5. The magnetic field is taken constant across the cable width, but it varies to keep I_c in the same range for different temperatures. The value of $F_{int,a}$ and $F_{int,c}$ are varied as function of magnetic field, as is discussed in section 4.1.5.

For the various cases, MQE is calculated with CUDI. The curve for the single strand stability regime, regime I, is calculated with a square pulse with a duration of 100 μs, as is discussed in section 2.3.4. For the curves in regime II and higher, a squared pulse with a duration of 10 μs is used.

The sensitivity of the cable stability regimes to parameter variations is investigated. Since the cable edge is very sensitive to local variations, the simulations are

performed on center heaters, to avoid the influence of edge effects, see figure 4.12.

The influence of $F_{int,c}$ on the MQE for the three cable designs in liquid helium cooling conditions are shown in figure 4.15. The data points in the curves for regime II and higher are connected by the most plausible relation, based on the shape of the stability criteria as shown in figure 2.22. The curves are extrapolated to the curve calculated in regime I.

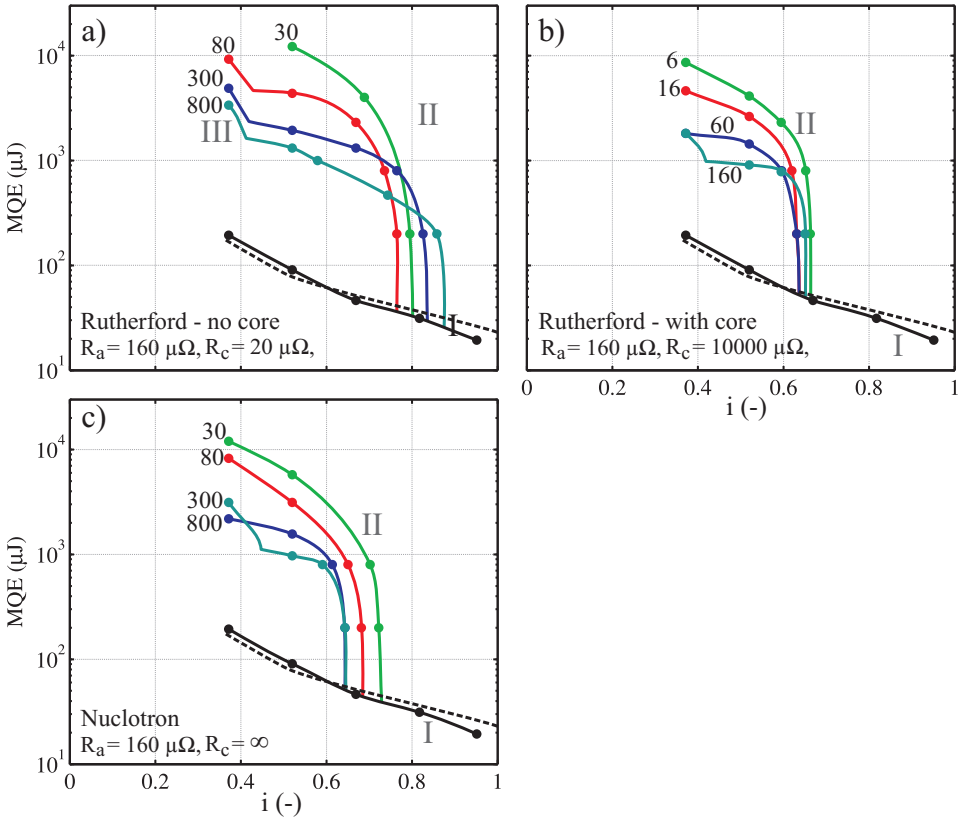

Figure 4.15: MQE data points as function of i for cables cooled by liquid helium. Three cable types are used: a) a non-cored Rutherford cable, b) a cored Rutherford cable and c) a Nuclotron cable. $F_{int,c}$ varies from 6 to 800 $W/K^{1+b}/m^2$. The dashed lines show calculated data of MQE on single wires with a pulse duration of 100 μs [26].

A change in F_{int}, c by a factor of 25 changes i_{kink} only by about 10 %. A higher $F_{int,c}$ increases i_{kink} for the non-cored Rutherford cable, while it reduces i_{kink} for the Nuclotron cable. In the non-cored Rutherford cable, i_{kink} is influenced the most by a higher $F_{int,c}$, improving the cooling of strand j to the crossing strand, thus reducing longitudinal and transversal normal zone propagation. In the Nuclotron

cable, i_{kink} is only influenced by a higher $F_{int,a}$, improving the heat transfer to strand $j+1$, thus increasing the transversal normal zone propagation velocity.

For all cables, the quench level of stability criteria APC II and CPC I for $i << i_{kink}$ are influenced by F_{int}. An increase in F_{int} by a factor of 25 reduces the quench levels by a factor of about 10.

Some of the curves show a sign of the start of regime III around $i = 0.4$.

Figure 4.16 shows the influence of F_{int} on the MQE for the non-cored Rutherford cable for the four defined cooling conditions.

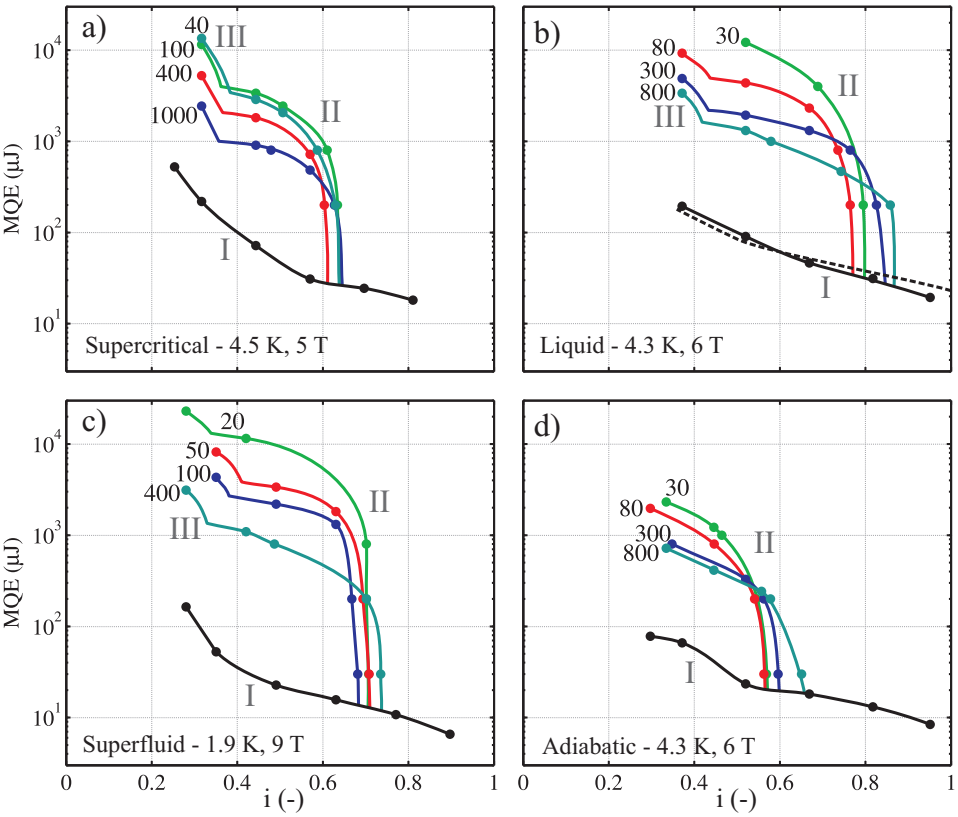

Figure 4.16: MQE data points as function of i for a non-cored Rutherford cable with $R_a = 160\ \mu\Omega$ and $R_c = 20\ \mu\Omega$ with varying $F_{int,c}$ from 20 to 1000 $\mathrm{W/K^{1+b}/m^2}$. Four temperature and cooling conditions are used: a) Supercritical helium, b) liquid helium, c) superfluid helium and d) adiabatic conditions at 4.3 K. The dashed line in b) shows calculated data of MQE on single wires with a pulse duration of 100 μs [26].

For all the helium cooling conditions a similar response is shown. The influence

of F_{int} on i_{kink} is minor, while the effect on stability criteria APC II and CPC I are significant.

In the superfluid cooled case, see figure 4.16c, a decrease of F_{int} improves the MQE generally. For the adiabatic case, see figure 4.16d, the best option to improve MQE seems an increase of F_{int}.

The sensitivity of the MQE curve to variations in $F_{int,a}$ and $F_{int,c}$ can be summarized by:

- A decrease in $F_{int,a}$ improves I/I_{kink} slightly;
  A decrease in $F_{int,c}$ reduces I/I_{kink} slightly;
- A decrease in $F_{int,a}$ improves stability criterion APC II for low i;
  A decrease in $F_{int,c}$ improves stability criterion CPC I for low i.

4.5 Conclusion

The electrical and thermal interstrand contact resistances play a key role in the stability mechanisms of a cable:

- Current redistribution through the adjacent and cross contacts causes a reduction of the current in local normal zones. Therefore dissipation by Joule heating and the longitudinal normal zone propagation are reduced. A reduction in R_a or R_c improves the speed of current redistribution and therefore the overall cable stability.
- The interstrand heat exchange provides cooling of the local normal zones and heating of neighboring superconducting strands. Therefore an increase of interstrand heat exchange reduces the longitudinal normal zone propagation, but speeds up the transversal normal zone propagation. The variation of interstrand thermal conduction on cable stability is specific to local conditions.

The primary current redistribution through the cross contacts leads to the same current distribution as through the adjacent contacts: The current decrease in the strand with the normal zone is counterbalanced with a current increase in the two nearest adjacent strands.

Simulations prove that in non-cored Rutherford cables the current redistribution through adjacent contacts is only a small fraction of current redistribution through the cross contacts when $R_a >> R_c$. For cored Rutherford cables, current redistribution through adjacent contacts is much larger than current redistribution through cross contacts.

The electrical and thermal interstrand resistances are determined by different resistive barriers between the cores of the strands. The electrical interstrand resistance depends on the metal-oxide layer, grown on the strand coating. R_a and R_c are controlled by the coating material and the thickness of the metal-oxide layer. The thermal interstrand resistance proves to be determined by the contacts. Therefore the electrical and thermal resistance can be controlled independently.

The influence of R_a and R_c on the MQE is qualitatively similar for the investigated cable types and helium cooling conditions. A change in either R_a or R_c has a strong impact on i_{kink}. For an increase in resistance from 10 to 1000 $\mu\Omega$, the value of i_{kink} is reduced by up to 30%. Therefore, the values of R_a and R_c need to be as small as possible in an accelerator magnet to provide optimum stability.

The influence of variation in interstrand thermal conductance on i_{kink} is case dependent:
An increase in adjacent interstrand thermal conductance speeds up adjacent propagation and slows down cross propagation. Vice versa, an increase in cross interstrand thermal conductance speeds up cross propagation, but slows down adjacent propagation.

The best stability of a cable is obtained by low electrical resistivity and low interstrand thermal conductance.

Chapter 5

Helium Cooling Affecting Stability

Cooling by helium of local hot zones in a superconducting cable has a significant effect on cable stability, due to the direct contact of helium with the strands. The cooling process due to the helium in the voids is complex to describe and a practical and simplified description of the heat flow is needed for simulations.

The heat flow to helium is characterized by several heat flow regimes. The available data and theory on cooling of a surface for three phases, namely superfluid helium, liquid helium and supercritical helium, are compiled.

For each helium phase and cooling regime a set of parameters for the heat flow as a function of time and temperature are presented for the use in simulations with CUDI.

The influence of variations in the most important parameters of heat flow is investigated for each phase.

5.1 Introduction

The temperature of a superconducting magnet needs to be maintained below T_c. A traditional way of removing energy from any system is by forcing a fluid through the system. For NbTi and Nb_3Sn superconductors helium is the most obvious candidate, giving optimal cooling at operating temperatures between 1.8 and 5 K. Three phases of ^{4}He are available in this temperature range: superfluid helium at 1.8 to 2.17 K at a pressure of about 100 kPa, boiling liquid helium at 4.2 to 4.3 K at a pressure of about 100 kPa and supercritical helium at a temperature between 4.5 and 5 K at a pressure of about 500 kPa. In figure 5.1 the phase diagram of ^{4}He is shown, with typical operating points in superfluid, liquid, and supercritical helium.

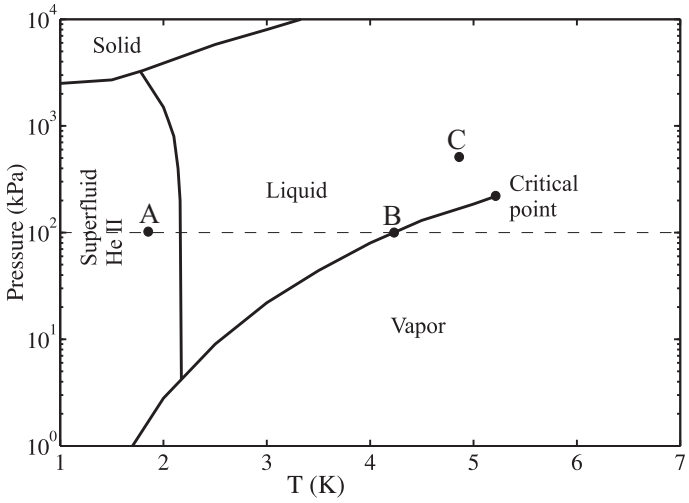

Figure 5.1: ^{4}He phase diagram. The dashed line indicates the atmospheric pressure and the points denote typical operating points in superfluid helium (A), liquid helium (B) and supercritical helium (C).

For the accelerators described in table 1.3 the used coolant is supercritical helium, except for the LHC, which is cooled with superfluid helium. Boiling liquid helium, or He I, lacks the possibility to extract large amounts of heat originating from beam loss and coupling loss in accelerator magnets. In the case of a large system it is always advantageous to use pressurized supercritical helium over liquid helium, for heat extraction and therefore stability [89]. However, liquid helium is described here since it is available for stability measurements in the experimental set-up, while supercritical helium is not available.

Advantageous characteristics of superfluid helium He II are the high volumetric heat capacity and very high thermal conductivity, improving magnet stability and heat extraction from the coils. Since He II is applied without any flow the extraction

of heat is limited. However, the low temperature allows to obtain higher current densities and magnetic fields.

Helium provides a relatively high heat capacity per unit volume compared to the heat capacity of metals at low temperature. In figure 5.2, the density and heat capacity of ^{4}He is shown as a function of temperature and pressure. Cooling improves cable stability strongly due to the reduction of both the longitudinal as well as transversal normal zone propagation.

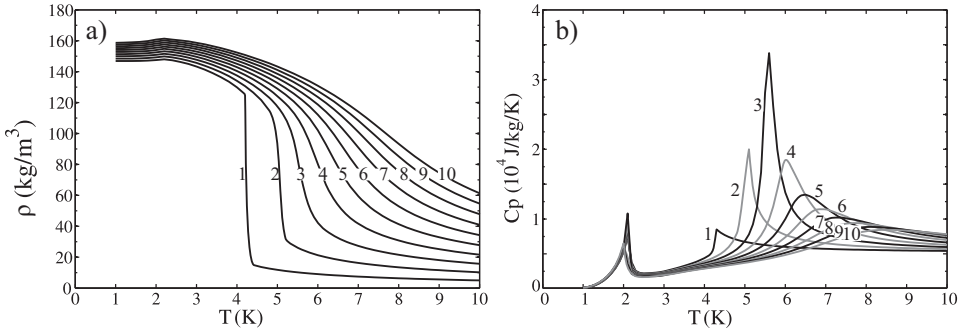

Figure 5.2: a) Density and b) heat capacity of ^{4}He as a function of temperature for a pressure from 1 to 10 atm. [90].

Heat flow to helium from an instantly heated surface into a limited volume of helium is bound to many heat transfer phases and phase limits. The different heat flow phases depends on diffusion times, strand surface material and helium volume. Cooling of a strand in a Rutherford cable is complex, due to the semi-closed voids filled with helium and small volume to surface ratios V_{He}/A_{He}. Furthermore, the surface area and volume are complex of shape, see section 2.5.

In section 5.2 the available experimental data in literature is compiled and it is correlated to the cable specific geometry. The relevant heat flow parameters and heat flow limits are specified for simulations with CUDI. In section 5.3, 5.4 and 5.5 the influence of superfluid helium, liquid helium and supercritical helium on cable stability is investigated, respectively.

5.2 Helium as a coolant

Single strand stability against short pulses of 100 μs depends on cooling by helium, see figure 2.8. In open bath He II the MQE can increase with more than one order of magnitude, while He I has a much smaller effect on MQE. In Rutherford cables the helium volume is limited to the cable voids, that cover about 5-15% of the cross-section of a cable. The helium contact area is limited to 25-50 % of the strand surface. In this section the heat flow to limited volumes of helium is discussed for three phases of helium.

5.2.1 Superfluid Helium

The helium phase and heat flow regime are affected by the temperature and pressure of the helium. In figure 5.3 the sequence of heat flow regimes and helium phases after a sudden temperature increase of a surface cooled by He II is illustrated.

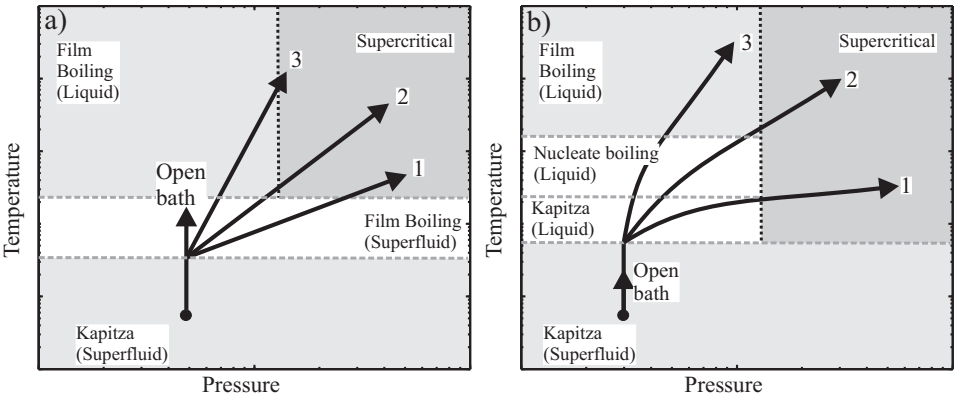

Figure 5.3: Schematic drawing of the evolution of heat flow phases into He II as function of temperature and pressure. Curves 1, 2 and 3 show the behavior for increasing V_{he}/A_{he} ratio. a) Situation for very high heating power. b) Situation for low heating power.

For an open bath of helium the two cooling regimes are the Kapitza regime and the superfluid film boiling regime. For closed volumes the behavior can be more complex. Low heating power will raise the temperature of the helium slowly to above the transition temperature T_λ into the liquid phase or finally into the supercritical phase.

In section 2.5.4 the geometry of the helium filled voids is discussed. It shows that small helium volumes are connected to each other by small channels. Therefore, neither the assumption of open bath nor the assumption of a closed volume will be accurate.

The heat flow into superfluid helium is limited by four mechanisms:

1. The heat exchange between a material surface and superfluid helium is limited by the Kapitza conductance.
2. High heat flux through a channel filled with He II is limited by the onset of quantum turbulence. The second sound regime is dominant only for low heat flux. For high heat heat flux the Gorter-Mellink limit applies [91].
3. High surface temperatures may induce a film of gas near the strand surface. After the onset of film boiling the heat flow is reduced drastically compared to the Kapitza conductance.

4. The energy needed to raise the helium temperature T_{He} to T_λ limits the heat flow to He II. At 1.9 K this value is 236 kJ/m^3 [92]. The typical value of V_{He}/A_{He} is roughly in the order of 0.05 mm^3/mm^2 for Rutherford cables, giving an energy limit per surface area of about 10 J/m^2 at 1.9 K.

Kapitza conductance

The Kapitza conductance denotes the limit in thermal conductance between a material surface and helium and is attributed to an acoustic mismatch between the two bulk media. The boundary resistance occurs as the result of scattering by phonons at the interface. The phonon energy density is proportional to T^{-3} and is therefore only significant at low temperatures. A rather large variation in Kapitza conductance between surfaces is found, with soft metals exhibiting generally higher conductance than hard metals [93].

The heat flux by phonons h_K^p is described theoretically by

$$h_K^p \equiv 4a_K T^3 \quad [WK^{-1}m^{-2}], \tag{5.1}$$

with

$$a_K = \frac{\pi^4}{10\hbar}\left(\frac{k_B}{\Theta_D}\right)^2 \frac{3N}{4\pi V}^{2/3} \quad [WK^{-4}m^{-2}]. \tag{5.2}$$

a_K is the Kapitza conductance parameter, $\hbar$ the Planck constant, k_B the Boltzmann constant, Θ_D the Debye temperature and N/V the number of particles per volume. Θ_D and N/V are material dependent and consequently the cooling from a surface will vary as function of the material properties. A number of problems with the phonon radiation limit for a solid-He II interface is described in [91], nevertheless the theory can be used in practice. In table 5.1 Θ_D, the theoretical value h_k^p and the highest measured value for heat flux h_K at 1.9 K are listed for several materials.

The overestimation of the theoretical value is for some materials more than a factor of 10. In analogy to [91] the effective measured value of h_K at 1.9 K is plot versus Θ_D^{-1}, see figure 5.4. The empirical linear fit through the values is described by

$$h_K = 2.1 \cdot 10^6 \Theta_D^{-1} \quad [WK^{-1}m^{-2}]. \tag{5.3}$$

For materials with unknown Kapitza resistance to He II, but known Θ_D, an estimate of h_K is made with (5.3). For the samples used in this thesis, the material on the surface layer is described in more detail in section 4.1.4. For as-received SnAg coated strands the surface layer is mainly SnO_2 with a small fraction of SnO. Heat treated SnAg coated strands exhibit a surface layer of Cu_2O due to the diffusion of Cu through Sn also bare copper strands exhibit a Cu_2O surface layer. For these three materials Θ_D is found in literature and h_K is calculated with 5.3, see table 5.1.

Table 5.1: Survey of Θ_D, h_K^p and h_K at 1.9K for several materials.

Solid	Θ_D K	h_K^p kW/K/m^2	h_K kW/K/m^2	a_K * W/m^2/K^4	Ref.
Ag	226	55	6	219	[91]
Al_2O_3	1000	1.5	1.6	56	[91]
Au	162	155	8.8	321	[91]
Cr_2O_3	370	-	5.7*	207**	[94]
Cu	343	30	7.5	273	[91]
CuO	392	-	5.4*	195**	[95]
Cu_2O	188	-	11.4*	416**	[95]
Hg	72	440	30	1093	[91]
In	111	171	11	401	[91]
Ni	440	19	4.0	146	[91]
NiO	317	-	6.6*	241**	[96]
Pb	100	190	32	1166	[91]
Sn	195	54	12.5	456	[91]
SnO	181	-	11.8*	432**	[97]
SnO_2	243	-	8.8*	322**	[97]

* Calculated with (5.3)
** Calculated with (5.3) and (5.1)

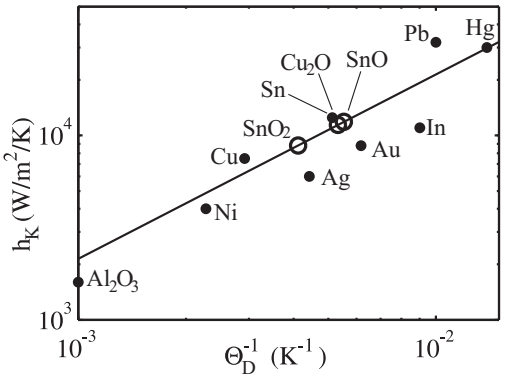

Figure 5.4: Kapitza conductance h_K at 1.9 K as a function of Θ_D^{-1}. The dots show measured values, the line is a fit described in (5.3) and the circles are suggested values of h_K for Cu_2O, SnO and SnO_2.

For practical application and for large heat flux the Kapitza conductance is written as [91]

$$h_K = a_K(T_s^{n_K} - T_b^{n_K}) \quad [WK^{-1}m^{-2}]. \tag{5.4}$$

A range of experimental values for a_K and n_K are reported for different materials and a survey of the values is shown in table 5.2.

Table 5.2: Survey of experimental values for Kapitza heat transfer parameters at 1.8 K.

Material	a_K $\mathrm{W/m^2/K^{n_K+1}}$	n_K -	**Reference**
Cu, as received	486	2.8	[98]
Cu, polished	200	3.8	[98]
Cu, annealed	455	3.45	[98]
Cu, oxidized in air 1 month	458	3.46	[93]
Cu, oxidized in air at 200 °C for 40 min.	518	3.69	[93]
Cu, coated with 50-50 PbSn solder	760	3.4	[93]
Cu, polished	701	3	[99]
Cu, oxidized	203	2.86	[99]

Measurement data points from [93] are shown in figure 5.5 together with two curves for a_K respectively 180 and 300 $\mathrm{W/m^2/K^4}$, both with $n_K = 4$. The value of n_K varies roughly between 2.8 and 4, but it is impossible to relate the literature values to the cable samples, as the exact composition of the surface material is not known precisely. To reduce the number of simulation parameters n_K is set to the theoretical value of 4, for simulations throughout this thesis.

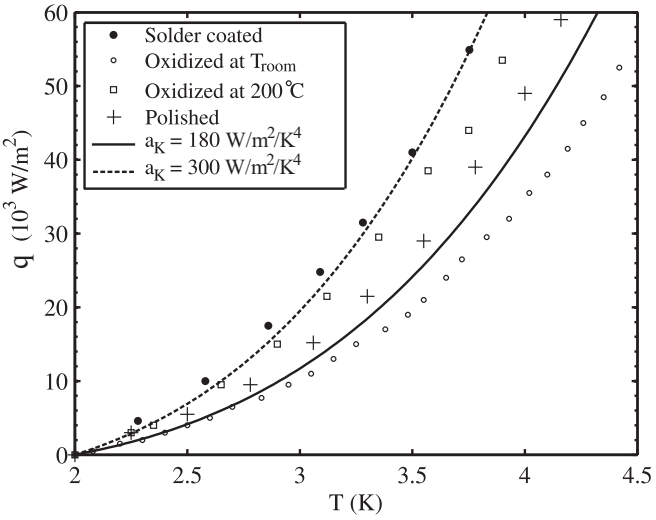

Figure 5.5: Measured heat flux as a function of temperature from [93] for four different preparations of copper samples at $T_{He} = 2$ K. The lines show the theoretical curve for $a_K = 180$ and 300 $\mathrm{W/m^2/K^4}$, with $n_K = 4$.

In simulations performed for SnAg coated samples, a value of $a_K = 300\ \mathrm{W/m^2/K^4}$ is taken. For Al coated samples the value $a_K = 60\ \mathrm{W/m^2/K^4}$ is used.

Heat transfer in small channels filled with He II

Heat transfer in He II is governed by two main heat flow regimes, the second sound regime for low heat flux and the Gorter-Mellink regime for high heat flux [91].

Second sound heat transfer is similar to first sound transfer where density fluctuations are transported through matter. For liquid helium, the velocity of sound is of the order of 200 m/s. Second sound results from entropy fluctuation that transports energy with a velocity of around 20 m/s for a temperature between 1 and 2 K. In non-turbulent He II the wave equation for second sound can be written as

$$\nabla^2 T = \frac{\rho_n}{s^2 \rho_s} \frac{\partial^2 s}{\partial t^2}, \tag{5.5}$$

with entropy s and ρ_n/ρ_s the ratio between normal and superfluid helium density. The time τ needed to initiate turbulence after a heat pulse q larger than the critical heat flux q_c is usually expressed as

$$\tau = \alpha q^{-3/2} \qquad [s]. \tag{5.6}$$

The criterion parameter α determines the time needed to enter the Gorter-Mellink regime. For an open bath configuration α increases for increasing pressure. At atmospheric pressure the empirically found criterion is

$$\alpha = -193.0 \left(\frac{T}{T_\lambda}\right)^2 + 329.8 \frac{T}{T_\lambda} - 136.7 \qquad [W^{3/2} m^{-3/2}] \quad [100]. \tag{5.7}$$

For channels of 30 to 50 mm and a cross-section of 0.5 to 12 mm^2 the value of α is deduced from measurements by [101]. Figure 5.6a shows the range of α compiled from [100] and [101]. The range for the heat flow limit for the onset of turbulence in helium for the channels is shown in figure 5.6b.

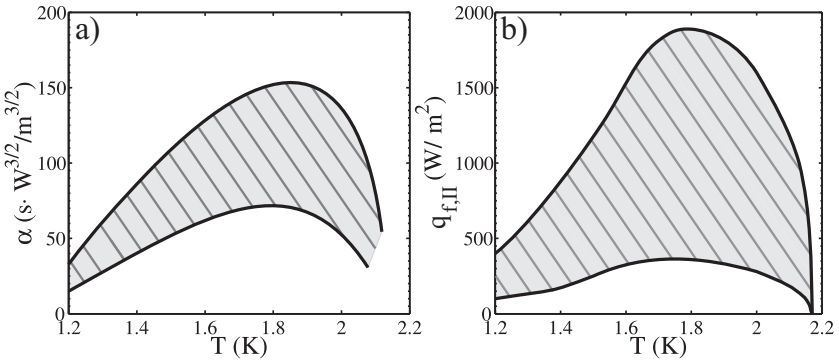

Figure 5.6: a) Range of α for various channels [101]. b) Range for steady state critical heat flux density as a function of temperature for different open channel geometries.

Heat transfer from a surface into He II is restricted by time and geometry dependent heat flow limits. A large amount of data is available for heat flow through a small channel to an open bath. Experiments and theory agree on the dependence of the heat transfer on the channel length. Both data for open as well as closed channels is available. For this thesis the main interest is in transient heat transfer limits for short channels up to 1 mm.

Enthalpy limit and onset of film boiling
Particularly useful in simulations is measured data [100] that relates the onset time of film boiling to the heat flow, see figure 5.7a. The total energy that is transfered before the film boiling starts is calculated by $Q_{f,II} = qt_{f,II}$.

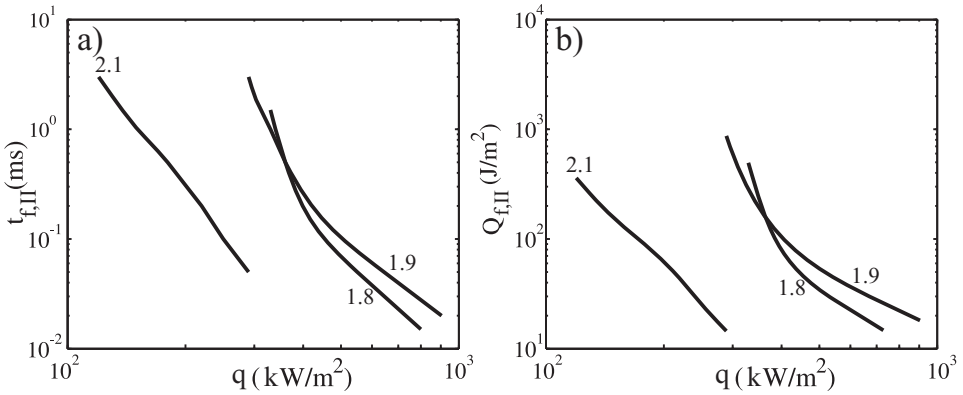

Figure 5.7: a) The onset time of film boiling in He II at 0.1 MPa for 1.8, 1.9 and 2.1 K in open bath configuration [100]. b) The calculated total energy transfered per unit surface area before the onset of film boiling.

The energy ΔE transferred into a helium volume is normalized to the enthalpy increase ΔE_0 from T_b to T_λ. Figure 5.8a shows $\Delta E/\Delta E_0$ for many configurations of open and closed channels at 1.8 and 2.0 K, compiled by [92]. $\Delta E/\Delta E_0$ can be written as a function of the heat flux q and channel length L by

$$\Delta E/\Delta E_0 = f\left(qL^{1/3.4}\right) \qquad [-]. \tag{5.8}$$

With a geometry as shown in figure 2.34b an average channel length of $L \approx 10$ μm can be assumed without taking the narrow channels between helium volumes into account. The value of $\Delta E/\Delta E_0$ q is calculated for q, see figure 5.8b. For a heat flow up to 100 kW/m^2 the temperature in the cooling is restricted mainly by the enthalpy limit.

The value of 0.1 $\Delta E/\Delta E_0$ is chosen to provide a limit for heat flow $q_{f,II}$ to He II, see figure 5.8b. A reasonable agreement between simulations and measurements is obtained for $q_{f,II} = 600$ kW/m^2.

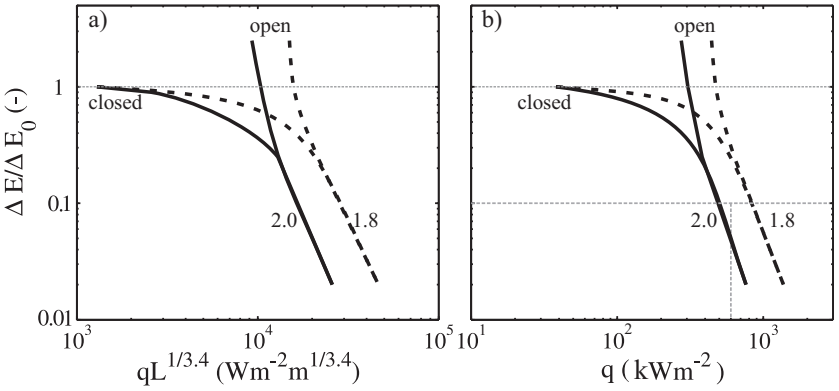

Figure 5.8: a) Fraction of enthalpy in the Kapitza heat transfer regime as a function of $qL^{1/3.4}$ at a bath temperature of 1.8 (dashed lines) and 2.0 K (solid lines), with open and closed channels [92]. b) Fraction of enthalpy calculated for a channel length of 10 μm. ΔE_0 is 285 kJ/m^3 at 2.0 K and 169 kJ/m^3 at 1.8 K.

After the onset time of film boiling in He II $t_{f,II}$ a vapor film exists close to the strand surface, reducing the heat flow drastically. The limiting mechanism is the heat transfer at the vapor to superfluid boundary and the vapor film thickness. The heat transfer coefficient in film boiling is described by

$$h_{f,II} = a_{f,II}\,(T_s - T_{He}) \qquad [W/m^2]. \tag{5.9}$$

The heat transfer coefficient $a_{f,II}$ varies with orientation and shape of the cooled surface and values between 100 and 2000 W/m^2/K are reported [91]. Throughout this thesis a value of $a_{f,II} = 500$ W/m^2/K is assumed.

5.2.2 Liquid Helium

Liquid helium, having a temperature above T_λ and a pressure below p_c, exhibits thermodynamic properties similar to gaseous helium. Helium has the second lowest density of fluids and the intermolecular interaction is weak. Saturated helium is only about 7.5 times more dense than its vapor at normal boiling point. In this section the heat transfer into liquid helium, subject to many limits and geometric variables, is discussed.

Heat transfer from strand to liquid helium.
Depending on the heating power, the heat transfer will start in the transient cooling regime. It is followed by the nucleate boiling regime and finally it enters the film boiling regime. In figure 5.9 the possible sequence of heat flow regimes and helium phases are illustrated for the cooling of a surface by helium.

In an open bath situation, the helium temperature will increase at constant pressure, passing from the transient regime via the nucleate boiling regime into

the film boiling regime. In a closed volume, pressure will build up due to the expansion of helium. When the critical pressure is reached, the heat exchange is in the supercritical cooling mode. However, before entering the supercritical regime, it is possible that it enters the nucleate or film boiling regime. Whether this happensor not is strongly dependent on the volume to surface ratio and the heating power.

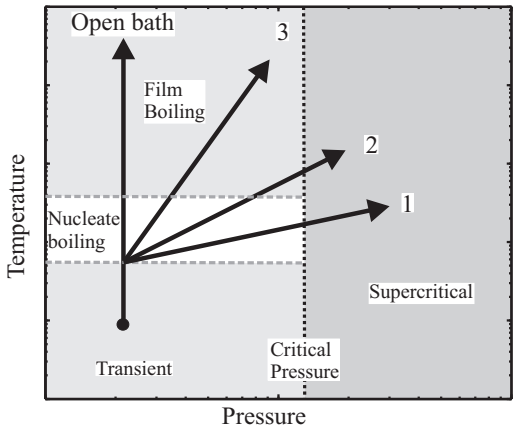

Figure 5.9: Schematic of the evolution of heat flow phases into He I as function of temperature and pressure. Curves 1, 2 and 3 show the behavior for increasing V_{he}/A_{he}. The temperature limits between the transient and nucleate boiling regimes and between the nucleate boiling and film boiling regimes depend strongly on the heating power.

Heat transfer into a volume of liquid helium is characterized by multiple regimes with many influencing parameters. A measurement by Steward gives a good insight of the heat transfer regimes [102]. Figure 5.10 shows the temperature rise of a flat heater placed vertical in a saturated bath of liquid helium at 4 K. The onset times of the different heat transfer regimes are identified. For increasing heat flux a following regime is reached earlier.

Four important limitations in heat flow to fluid helium are discussed:

1. Kapitza conductance in the transient regime.
2. Nucleate boiling.
3. The onset of the film boiling regime.
4. The phase transition to supercritical helium in closed volumes.

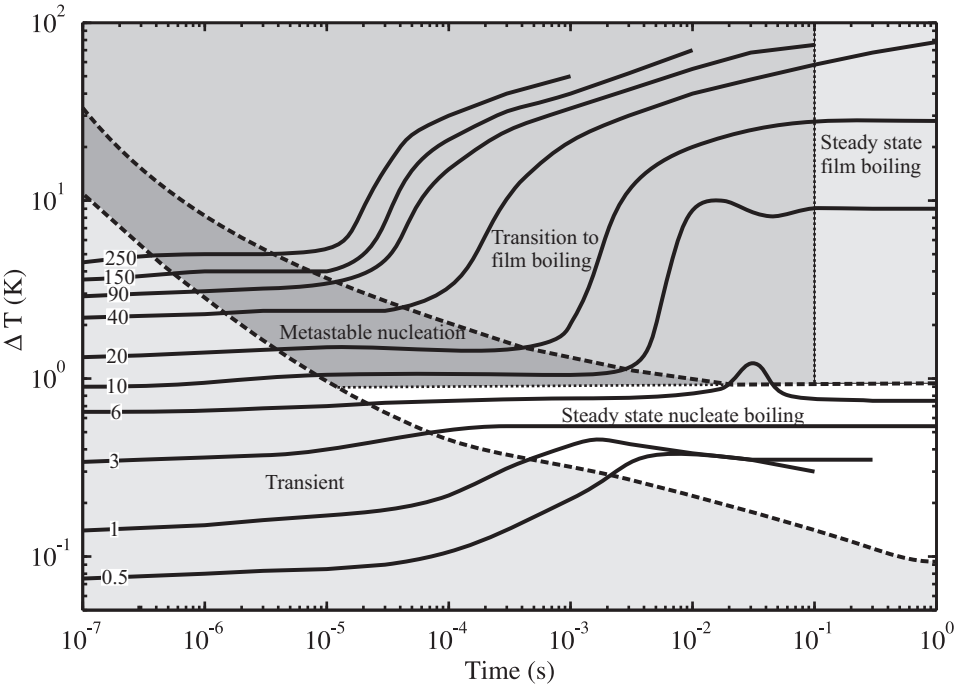

Figure 5.10: Heat transfer regimes into an open bath of saturated liquid helium at 4 K from a vertical heater for heat flows of 0.5 to 250 kW/m^2. Redrawn from [102].

Kapitza cooling and nucleate boiling

For q > 10 kW/m^2 the transient and nucleate boiling regime have a similar heat flux for a similar ΔT, see figure 5.10. The heat flow regimes are very hard to separate and might be described with a single formula with an acceptable error. In the film boiling regime a much higher ΔT is necessary to maintain the heat flux. The heat flow in the Kapitza an nucleate boiling regime are combined and described by (5.4), see section 5.2.1.

For $q < 7$ kW/m ^{2} a steady state nucleate boiling regime is reached, see figure 5.10. Many reports on the limit for steady state nucleate boiling exist and show strong dependence on heater orientation and surface roughness. Theory and experiments show values between 5 and 15 kW/m^2 [91].

Onset of film boiling

The heat flow to liquid helium from a surface is limited by the diffusion of heat into a small and relatively hot surface layer. The thickness x of the diffusion layer of helium close to the heated surface is described by

$$x = \gamma \left(\frac{k}{C} t \right)^{1/2} \qquad [m], \tag{5.10}$$

with k the thermal conductivity, C the heat capacity, t the time and γ a proportionality factor to account for the phase transformation from liquid to gas. The proportionality factor is fitted to measurement data and set at 1.8 [103]. The total energy that diffuses into the thin layer before film boiling starts can be described as

$$Q_{f,I} = q \cdot t_{f,I} = xL \quad [J], \tag{5.11}$$

where L is the heat of evaporation per unit volume. Combining 5.10 and 5.11, the onset time of the film boiling regime can be described by

$$t_{f,I} = \gamma^2 \frac{k}{C} \left(\frac{L}{q} \right)^2 \qquad [s]. \tag{5.12}$$

At 4.2 K, the numerical values for this equation are $k/C = 3.2 \cdot 10^8$ m^2/s, $L = 2600$ J/m^3. Now $t_{f,I}$ can be described as a function of the heat transfer q as

$$t_{f,I} = 6.9 \cdot 10^5 q^{-2} \quad [s]. \tag{5.13}$$

Measured $Q_{f,I}$ and $t_{f,I}$ for open bath situation by [102] and [103] agree well in the steady state limit, see figure 5.11. For small V_{He}/A_{He} ratio and high q, $Q_{f,I}$ is nearly independent of q. For other cases, the transition to film boiling depends on q, $t_{f,I}$ and V_{He}/A_{He} and it is therefore complex to describe.

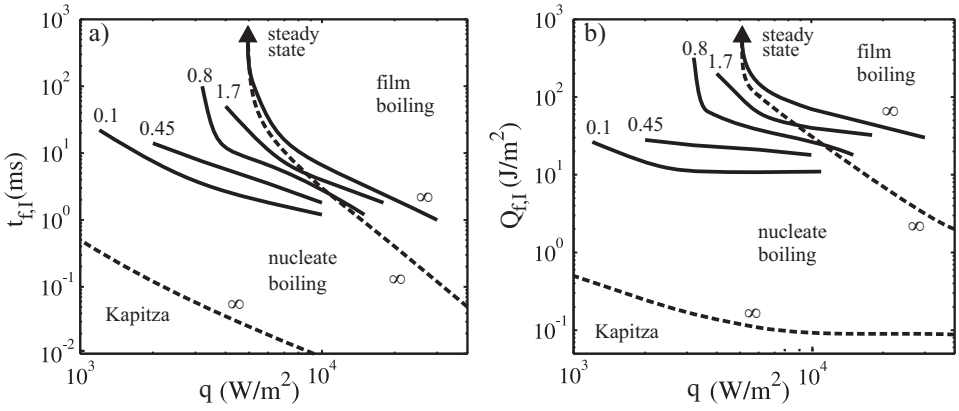

Figure 5.11: a) The onset time of film boiling for varying V_{He}/A_{He} ratio from 0.1 mm^3/mm^2 to open bath geometry with $V_{He}/A_{He} = \infty$. b) The total heat transfered into the helium before the onset of the film boiling regime. Solid lines show data from [103] at 4.2 K and the dashed lines data from figure 5.10 at 4 K including the transition between the transient and nucleate boiling regime [102].

Critical pressure

In closed volumes, the pressure of the helium builds up, due to the expansion of helium from the liquid to the gas phase. Once the critical pressure is reached, heat flow will enter the supercritical cooling mode. Measurements show that the critical pressure is reached after a heat input per unit volume of $Q_{p,I} = 53$ kJ/m^3, reasonably close to the predicted value of 37 kJ/m^3 [103]. The time to reach the critical pressure is written as

$$t_p = 5.3 \cdot 10^4 \frac{V_{He}}{A_{He}} q^{-1} \qquad [s]. \tag{5.14}$$

The resulting curves are shown in figure 5.12 and show that for small V_{He}/A_{He} ratio the onset of the supercritical regime is reached before the film boiling regime. For Rutherford cables $V_{He}/A_{He} \approx 0.05$ mm^3/mm^2, but the helium is not confined in a closed volume, neither it is in the condition of open bath. Therefore only complex 3D simulations can accurately describe the heat flow from the Rutherford cable into helium.

The onset time of the nucleate boiling $t_{n,I}$ and film boiling $t_{f,I}$ are extracted from 5.10. Measurement data from [103] for a closed volume of helium is plotted in figure 5.11a.

The total energy transfer per surface in each regime can be calculated with $Q_{f,I} = qt_{f,I}$, resulting in figure 5.11b. The total energy transfer in the transient regime is rather small compared to the nucleate boiling regime. Due to the difficulty of distinguishing the transient from the nucleate boiling regime in [103] only the film boiling onset time is used in simulations.

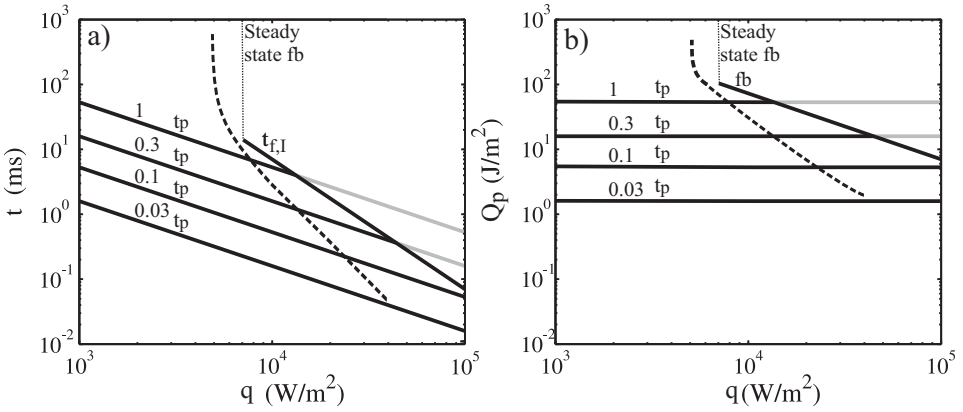

Figure 5.12: a) t_p as a function of q for V_{He}/A_{He} from 0.03 to 1 mm^3/mm^2 and $t_{f,I}$ for the open bath condition. b) The total energy transfered per surface area until the critical pressure or film boiling regime is reached. Data from 5.14 and 5.13 [103]. The dashed lines show the film boiling limit from figure 5.11.

For simulations in CUDI of a Rutherford cable cooled by liquid helium, the

transient and nucleate boiling regime are combined and a single energy limit $Q_{f,I}$ is defined. Although it is a rough simplification, $Q_{f,I}$ is set at 20 J/m^2 as obtained from fitting the simulations with experiment.

In the film boiling regime the heat flow is described as

$$q_{f,I} = a_{f,I}\Delta T \quad [Wm^{-2}]. \tag{5.15}$$

Values of $a_{f,I}$ between 300 and 10000 W/m^2/K are reported, the latter for fine wires [91]. For simulations throughout this thesis a value of 300 W/m^2/K is used.

5.2.3 Supercritical Helium

Above the critical point in the phase diagram of ^{4}He, there is no discontinuity in physical properties and the liquid and gaseous phase can not be distinguished. Therefore, heat transfer phenomena can be described by one phase as is visualized in figure 5.13.

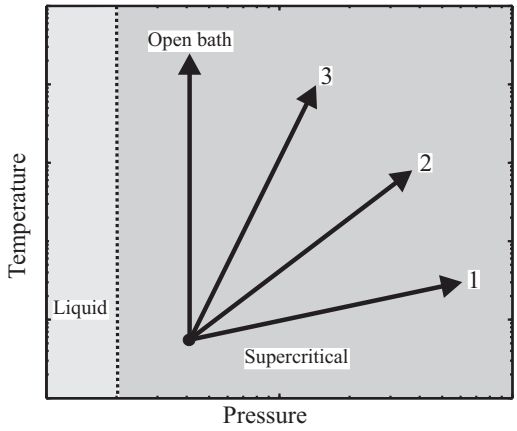

Figure 5.13: Schematic drawing of the evolution of heat flow phases into He I as a function of temperature and pressure. Curves 1, 2 and 3 show the behavior for increasing V_{he}/A_{he} ratio. The heat flow remains in the supercritical regime.

Heat transfer from strand to supercritical helium.
The flow of helium inside a Rutherford cable is restricted by small channels. The channels between the helium inside and outside the cable are even smaller. Therefore, the flow rates inside the cable are regarded negligibly small. With the short timescales involved in stability mechanisms, the helium is assumed to be static in Rutherford cables. In Nuclotron cables, helium channels are as long as the cable and therefore homogeneous in cross-section. The channels are not interconnected with each other and the helium flow in the channels is less restricted.

Heat transfer into supercritical helium is limited by diffusion for the entire range of temperature and pressure [104]. The one dimensional diffusion equation can be solved and the heat transfer is written as

$$h = \frac{1}{2}\left(\frac{\pi C_v k}{t}\right)^{\frac{1}{2}} \qquad [WK^{-1}m^{-2}]. \tag{5.16}$$

For closed volumes, the specific heat does not vary much in the temperature range between 4 and 6 K and in the pressure range around 4 bar, with a mean value of $C_v = 340$ kJ/m^3/K [103]. The thermal conductivity stays almost constant in the considered ranges with a mean value of $k = 0.022$ W/m/K.

Measurements on heat flow to supercritical helium on a short timescale with fast temperature measurement are presented in [102]. Heat transfer data to an open bath of helium at 4.0 K and a pressure of 3 bar is extracted and shown in figure 5.14. The curves for three different values of heat flux q of 1, 10 and 50 kW/m^2 are all within a relatively small range. For comparison, equation 5.16 is shown. Up to 10 ms, the theoretical behavior corresponds well with the experimental values for heat transfer.

To account for the steady state heat conduction, a term $a_{sc,ss}$ is added to (5.16) and we can write

$$h = a_{sc,c}\frac{1}{2}\left(\frac{\pi C k}{t}\right)^{\frac{1}{2}} + a_{sc,ss} \qquad [WK^{-1}m^{-2}] \tag{5.17}$$

with $a_{sc,ss}$ set to 500 W/m^2/K and compensation factor $a_{sc,c} = 0.45$. The obtained correlation is shown in figure 5.14.

Experiments for thesis did not include supercritical helium, therefore no comparison between measurement and simulation data can be made. Simulations throughout this thesis are performed with equation (5.17).

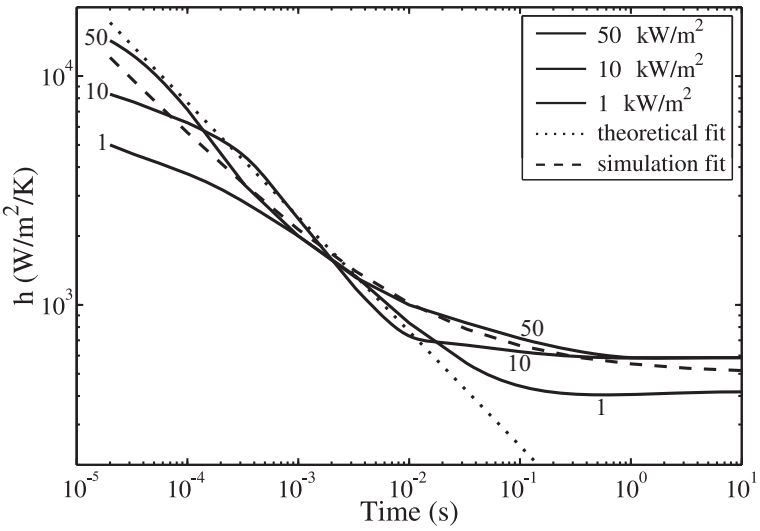

Figure 5.14: Measured heat transfer coefficients to static supercritical helium at a temperature of 4 K and a pressure of 3 Atm with heat flow from 1 to 50 kW/m^2, data from [102]. For comparison, the theoretical closed volume equation (5.16) (dotted line) and the used simulation fit (5.17) (dashed line) are shown.

5.3 Influence of superfluid helium on stability

The influence of superfluid helium on cable stability is investigated by varying the most significant helium cooling parameters in simulations with CUDI. The influence of a_K, $q_{f,II}$, A_{He} and V_{He} is illustrated for the model cable, a non-cored Rutherford cable with 18 LHC 01 strands, see table 1.4. The relevant sample parameters are listed in table 5.3. The heat is deposited in the center position of a strand.

Table 5.3: Model cable properties used in CUDI simulatoins.

Parameter	Unit	Value
T	K	1.9
B	T	9
I_c	kA	14.3
R_a	$\mu\Omega$	160
R_c	$\mu\Omega$	20
F_{int}	W/K^{1+b}/m^2	100
A_{He}	mm^2	see section 2.5.3
V_{He}	mm^3	see section 2.5.4
a_K	W/m^2/K^4	300
$q_{f,II}$	kW/m^2	60

The curves for the single strand stability regime, regime I, are calculated with a fixed condition of helium cooling. For regime I a square pulse with a duration of

100 μs is applied, as is discussed in section 2.3.4. For the curves in regime II and higher, a squared pulse with a duration of 10 μs is taken.

The sensitivity of the cable stability regimes to parameter variations is investigated. Since the cable edge is very sensitive to local variations, the simulations are performed on center heaters, to avoid the influence of edge effects, see figure 4.12. The data points in the curves for regime II and higher are connected by the most plausible relation, based on the shape of the stability criteria as shown in figure 2.22. The curves are extrapolated to the curve calculated in regime I.

Simulations for the sample in adiabatic and helium cooled conditions show the strong influence of superfluid helium on stability, see figure 5.15.

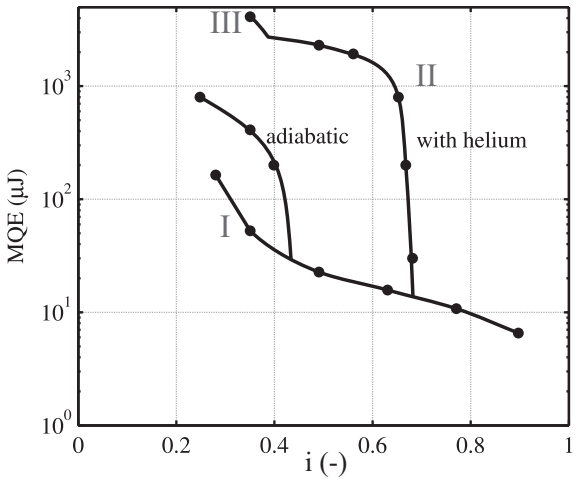

Figure 5.15: Simulated MQE versus I/I_c for the model cable in adiabatic and helium cooled conditions. $T = 1.9$ K, $B = 9$ T and $I_c = 14.3$ kA.

The calculation results show a large increase in i_{kink} by a factor of 1.5. The operation current of the LHC dipole magnet would be beyond I_{kink} if no helium cooling would be available and the cable stability would be determined by the strand only.

Influence of the Kapitza conductance on stability

In figure 5.16 the MQE values for simulations with varying a_K are shown. A general increase of MQE is obtained for an increase in a_K. Since the total cooling of a strand section is a function of $A_{He}a_K$, the influence of an increase in A_{He} for a fixed value of a_K can be derived.

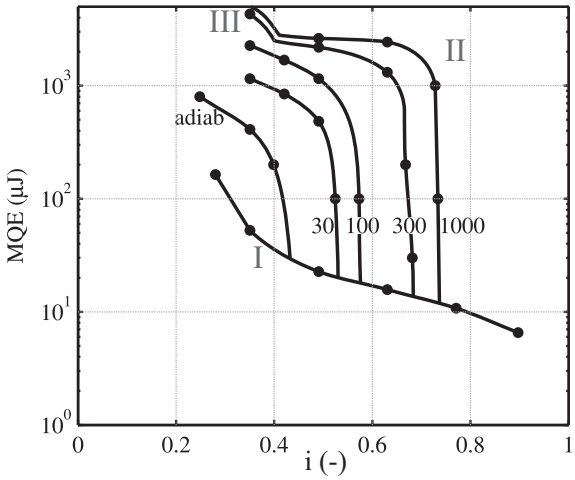

Figure 5.16: MQE versus I/I_c for varying Kapitza heat flow parameter a_K between 30 and 1000 W/m^2/K^4. The adiabatic case is shown for comparison.

For an Al coated sample with $a_K = 60$ W/m^2/K^4 i_{kink} would be reduced by about 20 % compared to a SnAg coated sample with $a_K = 300$ W/m^2/K^4. Similarly the MQE at $I/I_c = 0.45$ shows a reduction by a factor of 2 for the Al coated sample compared to an SnAg coated sample. The exact composition of the strand surface has large effect on MQE.

The sensitivity of the MQE curve to variations in $A_{He}a_K$ can be summarized by:

- An increase in $A_{He}a_K$ improves I/I_{kink} slightly;
- An increase in $A_{He}a_K$ improves stability criterion APC II and CPC I.

The results show that a local reduction of A_{He}, for instance at the cable edge, potentially has a large influence on stability.

Influence of the heat flow limit on stability

The heat flow in the Kapitza cooling regime is limited by the onset of film boiling with a heat flow limit $q_{f,II}$. Theoretical considerations show a limitation of the heat flow above 300 kW/m^2 for open channel configuration and above about 60 kW/m^2 for a closed channel configuration, see figure 5.7 and 5.8, respectively.

The influence of the variation of $q_{f,II}$ is studied with MQE simulations on non-cored Rutherford cable, with $q_{f,II}$ between 10 and 240 kW/m^2, see figure 5.17. An increase in $q_{f,II}$ above 30 kW/m^2 does not affect the MQE. Simulation data reveal that the maximum heat flow to the helium is only higher than 30 kW/m^2 for a small number of sections, so the effect of variation in $q_{f,II}$ above 30 kW/m^2 on the quench decision is not significant.

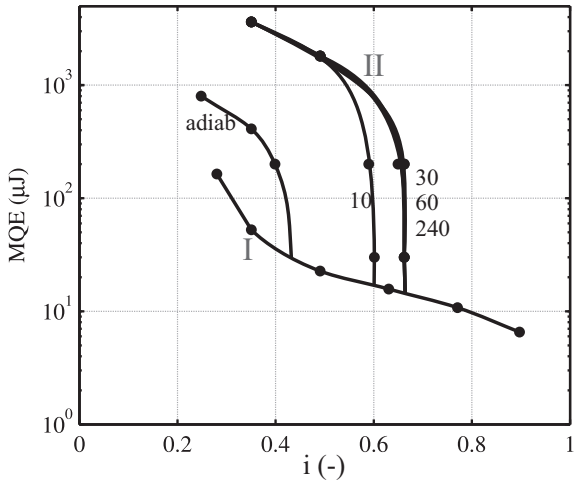

Figure 5.17: Influence of Kapitza heat flow limit between 10 and 240 kW/m^2 at 1.9 K and 9 T. The adiabatic case is shown for comparison. a_K = 300 W/m^2/K^4 and I_c = 14.3 kA.

Compaction factor and wetted surface fraction

The heat flow to the helium volume is a function of $a_K \cdot A_{He}$, therefore a variation in A_{He} will have a similar influence as a variation in a_K. The volume of helium V_{He} in the cable voids has a strong influence, because it determines the total enthalpy limit until T_λ is reached. V_{He} is maximum when the compaction factor f_c of the cable is at its minimum value of $\pi/4$. The fraction of the strand surface that is in contact with the strand is called the wetted strand fraction f_w, with a value between 0 and 1. For a cable with the outer voids filled with Kapton, the maximum value for f_w is about 0.5.

The value of i_{kink} is determined for MQE = 200 μJ for varying f_c and f_w. In figure 5.18a the results are shown. The value of i_{kink} varies from 0.42 for the adiabatic case to 0.89. Figure 5.18a shows that for f_c between 0.88 and 1, the influence of f_w is relatively small for $f_w > 0.1$. For $f_c < 0.88$, the influence of increasing the void size does not add much to i_{kink}.

In a similar way figure 5.18b shows MQE as a function of f_c and f_w for I/I_c = 0.49. The curve shows that the increase of MQE in regime II is the strongest for decreasing f_c from 1 to 0.94 and increasing f_w from 0 to 0.3. The typical values $f_c \approx 0.90$ and $f_w \approx 0.25$ leave room for improvement of stability. However, increase of A_{He} implies an increase of R_a and R_c and an increase in V_{He} decreases the mechanical stability of the cable.

A reduction of A_{He} and V_{He} in the LHC 01 dipole operation conditions would have a strong negative impact on both i_{kink} and APC II for low I/I_c, see figure 5.18. An increase of A_{He} and V_{He} has a less profound positive impact.

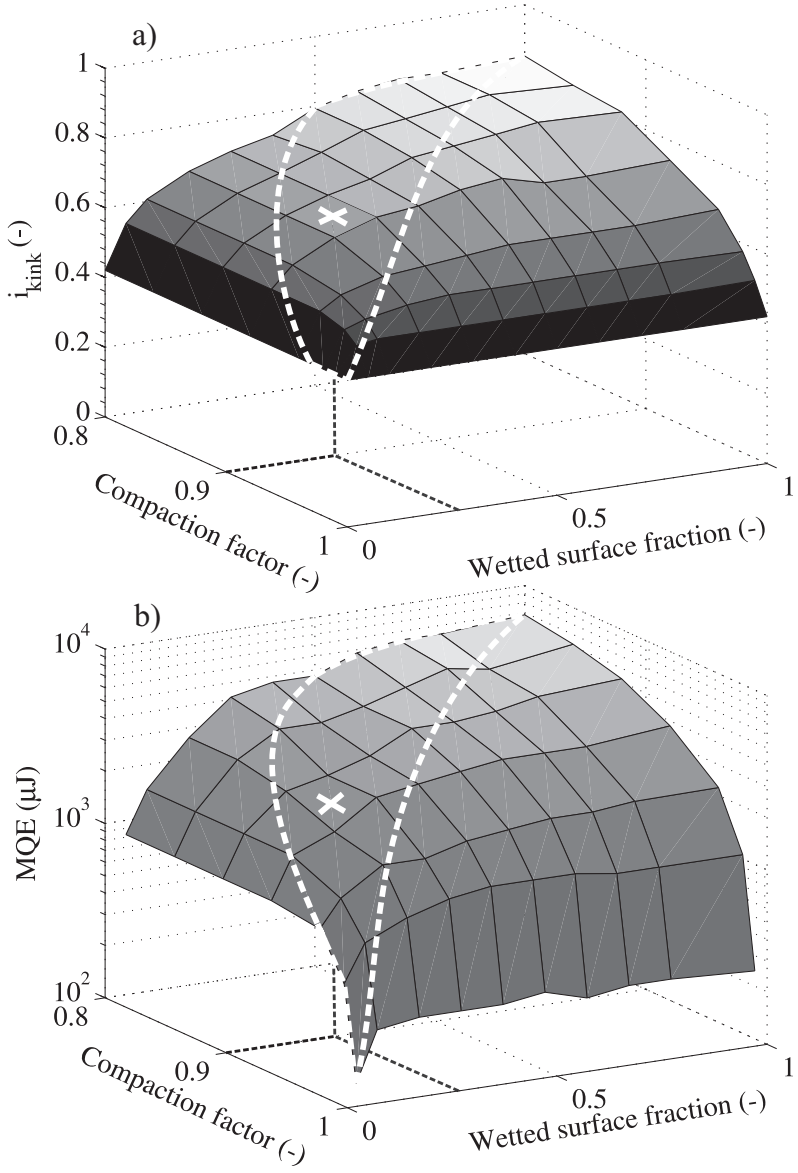

Figure 5.18: Simulation results with a) i_{kink} at MQE = 200 μJ and b) MQE at $I/I_c = 0.49$ as a function of compaction factor and wetted surface. Simulations are performed with the 18 strand model cable, as defined in section 1.3.2, cooled with superfluid helium at 1.9 K, 9 T, $I_c = 14.3$ kA. The white cross indicates the calculated value of f_c and f_w for LHC 01 cables. The estimated physically possible combination of f_c and f_w in Rutherford cables is indicated by the area enclosed by the white dashed line.

5.4 Influence of liquid helium on stability

Simulations to reveal the influence of liquid helium cooling on cable stability are performed on the model cable, a non-cored Rutherford cable with 18 LHC 01 strands, see table 1.4. The simulation parameters are given in table 5.4. The results in adiabatic and helium-cooled conditions show a strong improvement of stability in the case of liquid helium cooling, see figure 5.19. The strong increase of MQE in regime II and large increase in i_{kink} by a factor of 1.4 indicates a strong effect of the efficient heat transport from the normal strand to the liquid helium in the cable voids.

Table 5.4: Model cable properties used in simulations.

Parameter	Unit	Value
T	K	4.3
B	T	6
I_c	kA	13.5
R_a	$\mu\Omega$	160
R_c	$\mu\Omega$	20
F_{int}	$W/K^{1+b}/m^2$	300
A_{He}	mm^2	see section 2.5.3
V_{He}	mm^3	see section 2.5.4
a_K	$W/m^2/K^4$	300
$Q_{f,I}$	J/m^2	20
$a_{fb,I}$	$W/m^2/K$	300

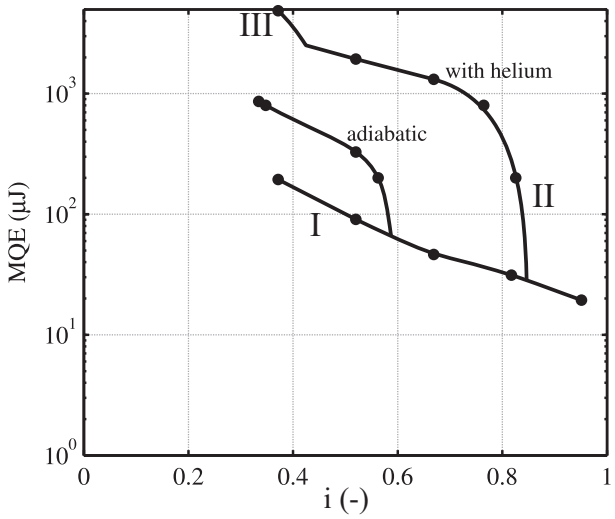

Figure 5.19: Simulation of MQE as a function of I/I_c for the model cable in adiabatic and helium-cooled conditions. $T = 4.3$ K, $B = 6$ T and $I_c = 13.5$ kA.

Influence of variation in the Kapitza conductance

The values for the Kapitza conductance parameters a_K are material dependent and similar to the values discussed in section 5.2.1. Simulations on the model cable with varying a_K reveal its influence on stability, see figure 5.20. The variation in MQE and the characteristic point i_{kink} is small, especially for $a_K > 100$ W/m^2/K^4. Compared to the superfluid helium curves shown in figure 5.16, the variation in a_K has a much smaller influence. This is due to the reduced fraction of the heat capacity of the helium to the total heat capacity of the conductor and the higher interstrand thermal conductance at 4.3 K.

The variation of a_K has a small impact on the MQE of liquid helium cooled cable. The sensitivity of the MQE curve to variations in a_K can be summarized by:

- An increase in a_K improves I/I_{kink} slightly;
- An increase in a_K improves stability criterion APC II and CPC I sligthly.

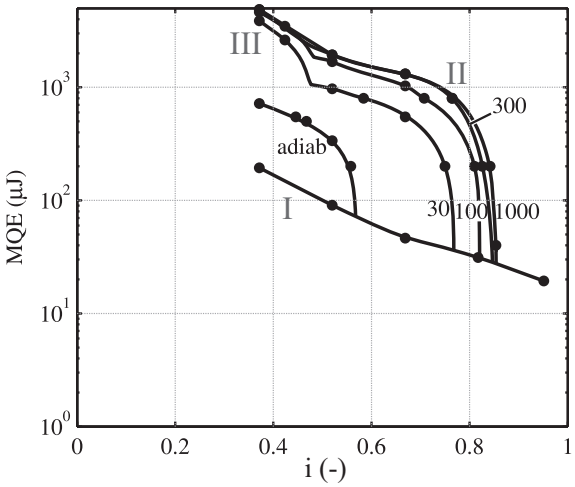

Figure 5.20: MQE versus I/I_c for varying Kapitza heat flow parameter a_k between 30 and 1000 W/m^2/K^4 at 4.3 K and 6 T. The adiabatic case is shown for comparison. $I_c = 13.5$ kA.

Influence of the onset of film boiling on stability

The transition to the film boiling regime is limited by an energy limit $Q_{f,I}$ in J/m^2. MQE simulations with varying $Q_{f,I}$ between 4 and 50 J/m^2 are performed, see figure 5.21, showing a strong influence of $Q_{f,I}$ on MQE. In section 5.2.2 $Q_{f,I}$ is discussed and figure 5.11b shows a compilation of the energy limit for closed volumes with various V_{He}/A_{He}. For the Rutherford cables a value of $V_{He}/A_{He} \approx 0.05$ mm^3/mm^2 is determined and the accompanying $Q_{f,I} \approx 20$ J/m^2, corresponding to 400 kJ/m^3.

The variation in I_{kink} between the theoretical value of 53 J/m^2 and the fit value used in this thesis of 20 J/m^2 is about 4 %.

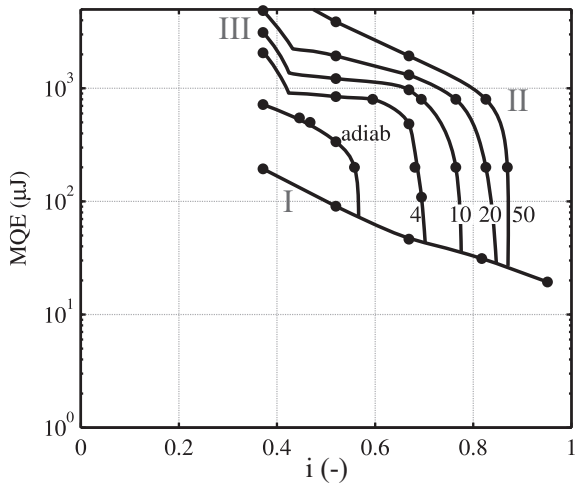

Figure 5.21: Influence of Kapitza energy limit between 4 and 50 J/m^2, which is equivalent for this cable to 80 and 1000 kJ/m^3. $T = 4.3$ K, $B = 6$ T and $I_c = 13.5$ kA.

The variation of $Q_{f,I}$ has a strong impact on the MQE of liquid helium cooled cable. The sensitivity of the MQE curve to variations in $Q_{f,I}$ can be summarized by:

- An increase in $Q_{f,I}$ improves I/I_{kink} significantly;
- An increase in $Q_{f,I}$ improves stability criterion APC II and CPC I significantly.

Compaction factor and wetted surface fraction

The effect of V_{He} and A_{He} on the characteristics of the MQE curve, namely i_{kink} and MQE in regime II, are studied with simulations for the model cable. In figure 5.22 the results are shown with a variation in compaction factor f_c and wetted surface fraction f_w of the strands. For $f_w > 0.4$ the increase in i_{kink} is limited by the helium volume only. A strong increase in i_{kink} from $f_w = 0$ to 0.4 is shown. Both V_{He} and A_{He} influence the i_{kink} strongly.

The MQE at $I/I_c = 0.52$, see figure 5.22b, shows a similar dependence. The difference between the adiabatic case and the LHC 01 cable case is about a factor of 5. The maximum of the curve shows an additional possible increase with a factor of 2.5. It that a large part of the possible gain in MQE is already obtained by the LHC 01 cables in magnet operation conditions.

A reduction of A_{He} and V_{He} has a strong negative impact on both i_{kink} and APC II for low I/I_c, see figure 5.22.

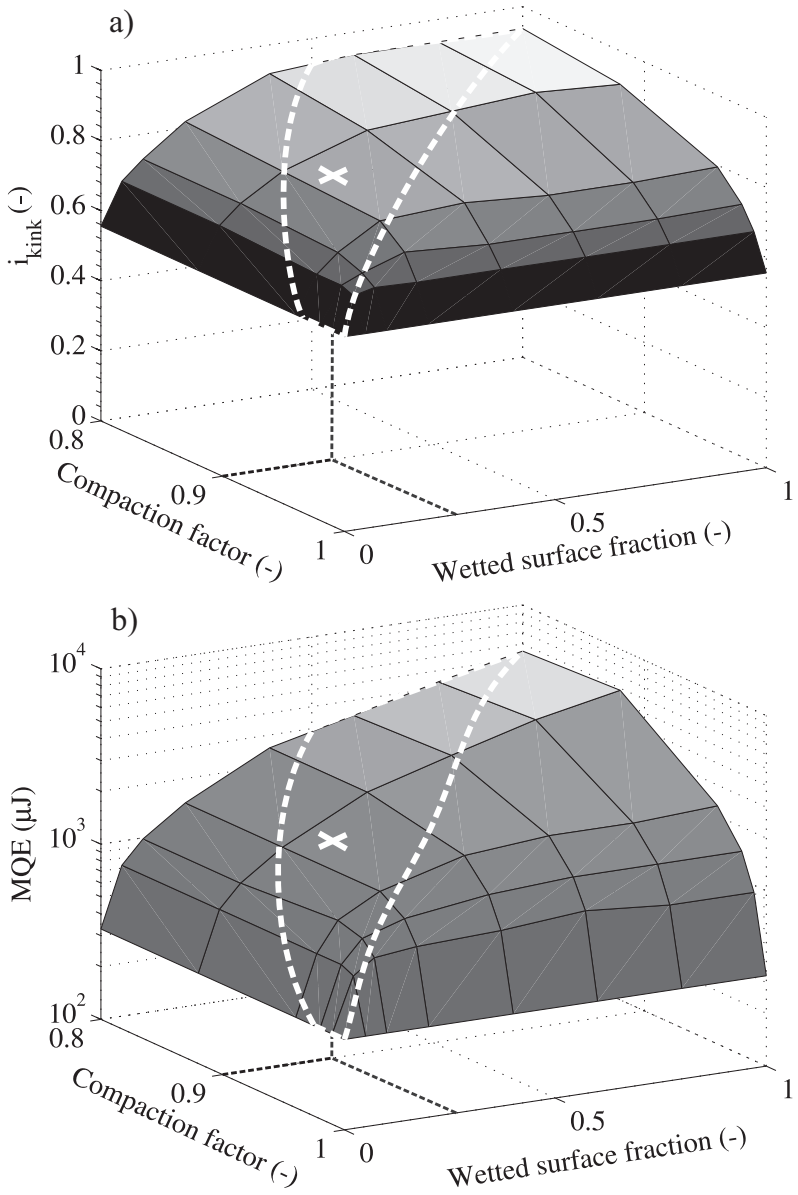

Figure 5.22: Simulation results with a) i_{kink} at MQE = 200 μJ and b) MQE at $I/I_c = 0.52$ as a function of compaction factor and wetted surface. Simulations are performed with the model cable. $T = 4.3$ K, $B = 6$ T and $I_c = 13.5$ kA. The white cross indicates the calculated value of f_c and f_w for LHC 01 cables. The estimated physically possible combination of f_c and f_w in Rutherford cables is indicated by the area enclosed by the white dashed line.

5.5 Influence of supercritical helium on stability

The impact of supercritical helium cooling on cable stability is investigated by simulations on the model cable, a non-cored Rutherford cable with 18 LHC 01 strands, see table 1.4. In table 5.5 the main simulation parameters are listed. In figure 5.23 the simulation results for the adiabatic and the helium cooled condition are shown.

Table 5.5: Model cable properties used in simulations.

Parameter	Unit	Value
T	K	4.5
B	T	5
I_c	kA	15.8
R_a	$\mu\Omega$	160
R_c	$\mu\Omega$	20
F_{int}	$\mathrm{W/K^{1+b}/m^2}$	300
A_{He}	$\mathrm{mm^2}$	see section 2.5.3
V_{He}	$\mathrm{mm^3}$	see section 2.5.4
$a_{sc,c}$	$\mathrm{W/m^2/K}$	0.45
C	$\mathrm{kJ/m^3/K}$	340
k	W/m/K	0.022
$a_{sc,ss}$	$\mathrm{W/m^2/K}$	0.45

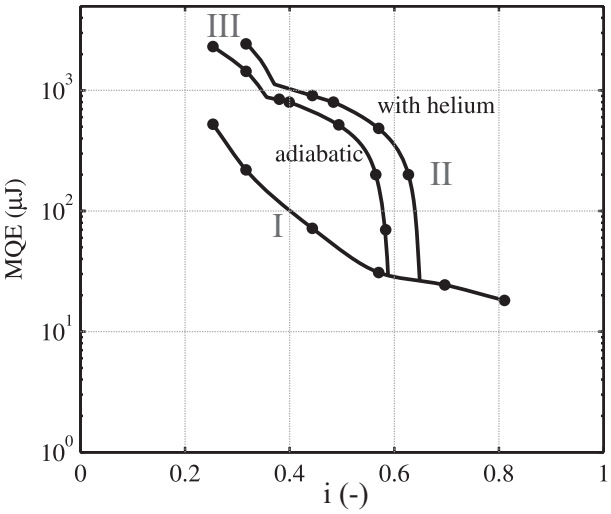

Figure 5.23: Simulation of MQE versus I/I_c for the model cable in adiabatic and helium cooled conditions. $T = 4.5$ K, $B = 5$ T and $I_c = 15.8$ kA.

Compared to the influence of superfluid helium and liquid helium, see figures 5.15 and 5.19, the influence is relatively small in this case. However, the increase of i_{kink} by 10 % due to the cooling may provide a vital improvement in stability

in magnet operation.

The MQE variation between the adiabatic case in liquid and superfluid helium, compare figures 5.19 and 5.23, are small, since the conditions are rather similar. However, the difference in the helium cooled case is large, indicating the weak influence of supercritical helium cooling compared to liquid helium cooling.

In regime II, the MQE is relatively low, with less than 1 mJ for the supercritical helium cooled case at $I/I_c = 0.4$.

Compaction factor and wetted surface fraction

As described in section 5.2.3 only on cooling regime is active in supercritical helium, therefore the amount of parameters is small, compared to the superfluid or fluid case. Since C and k are well known physical properties for supercritical helium, the main unknown parameters are V_{He} and A_{He}.

Simulations are performed on the model cable and the characteristic points are calculated: i_{kink} at MQE = 200 μJ and the MQE in regime II at $I/I_c = 0.32$. In figure 5.24 the simulation results are shown.

The change in MQE characteristics from the adiabatic case to the optimum cooled cable is relatively small for the supercritical helium cooled cable. The variation for superfluid and liquid helium cooled cables, shown in figures 5.18 and 5.22, is much larger.

The characteristic i_{kink} varies between 0.57 and 0.75, see figure 5.24a. The strongest increase in i_{kink} is for a decrease of the compaction factor from 1 to 0.96. Reducing f_c from 0.92 to 0.8 increases i_{kink} only marginally, indicating that the cooling is mainly limited for these values by f_w. Figure 5.24b shows a similar variation for MQE in regime II. At a compaction factor below 0.98 the helium cooling limitation is mainly due to f_w. It can be concluded that the MQE calculation is not very sensitive to V_{He} and A_{He} for cables cooled by supercritical helium with the typical $f_c = 0.90$ and $f_w = 0.25$.

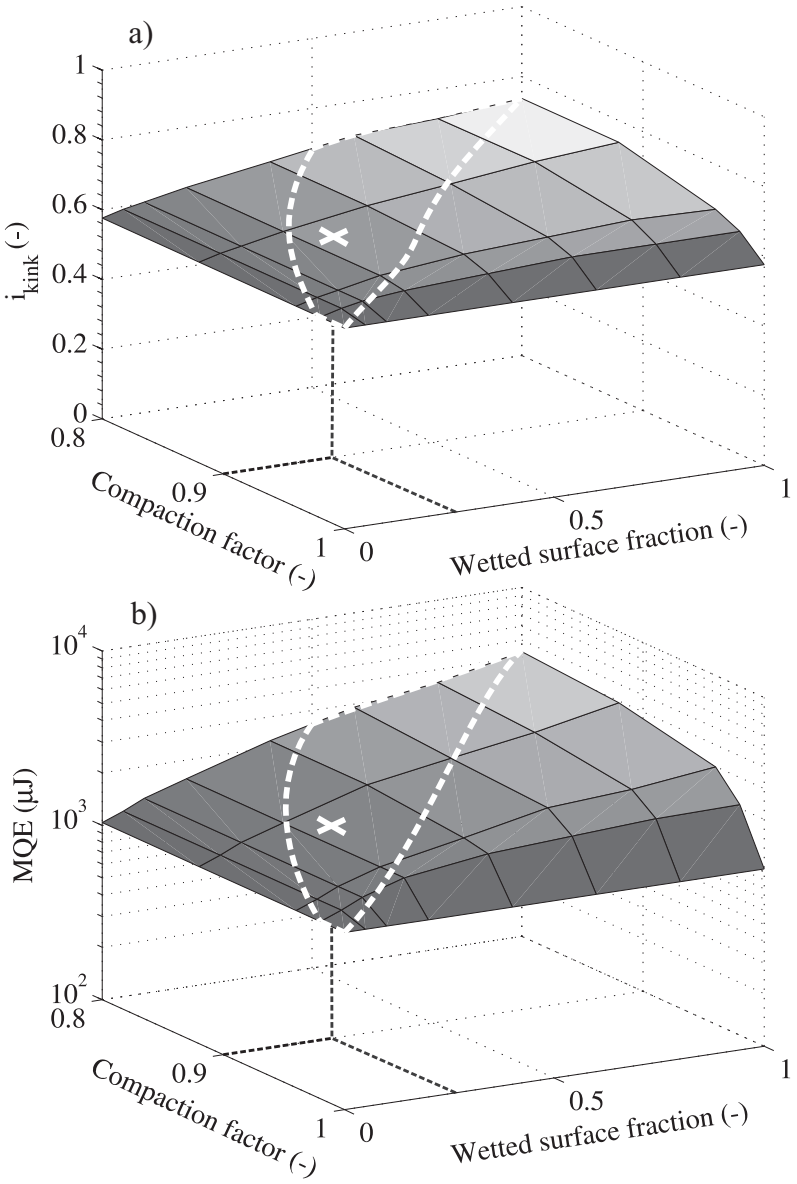

Figure 5.24: Simulation results with a) i_{kink} at MQE = 200 μJ and b) MQE at $I/I_c = 0.32$ as a function of compaction factor and wetted surface fraction. Simulations are performed with the model cable. $T = 4.5$ K, $B = 5$ T and $I_c = 15.8$ kA. The white cross indicates the calculated value of f_c and f_w for LHC 01 cables. The estimated physically possible combination of f_c and f_w in Rutherford cables is indicated by the area enclosed by the white dashed line.

5.6 Conclusion

Helium is a good coolant with a high heat capacity compared to copper and superconducting material. Although in LHC cables typically 5 % of the volume is occupied with helium, the heat capacity increases by a factor of approximately 40, 12 and 10 for superfluid, liquid and supercritical helium, respectively. The effect of helium cooling on stability is due to two conditions:

1. The high heat capacity of helium.
2. The ability to use the heat capacity fast.

The improvement of stability by helium cooling is due to the reduction of both longitudinal and transversal normal zone propagation.

Heat transfer differs strongly between the three helium phases. The highest heat exchange rates between a hot surface and the coolant is found for superfluid helium and the lowest for supercritical helium. Simulation results show a significant increase in stability of cables against short local heat depositions compared to adiabatic conditions for all helium phases. A gain in i_{kink} by a factor of 1.5 and 1.4 is seen for superfluid and liquid helium cooled cables, respectively. For supercritical helium the gain is just 1.08.

Superfluid helium

The cooling of a superconductor by superfluid helium is mainly restricted by the Kapitza conductance. The values of a_K for coating with Al and SnAg are 60 and 300 $\mathrm{W/m^2/K^4}$, respectively. This results in a 20 % higher i_{kink} for the SnAg coated sample compared to the Al coated sample. The influence of the heat flow limit obtained for parameters is much less, due to the limited volumes of helium addressed to each strand section.

The gain in stability of cooled LHC 01 cables compared to adiabatic conditions is strong. Reduction of the compaction factor and increasing the wetted surface would provide an additional gain that is much smaller. Since a looser cable reduces the mechanical rigidity, more and higher input of mechanical energy can be expected and a reduction of the compaction factor is not profitable.

Superfluid helium proves to have a major impact on the stability of superconducting cables in magnet applications.

Liquid helium

The heat exchange of a surface with liquid helium is very high in the Kapitza and nucleate cooling regime, which is rather similar in size and hard to distinguish. Therefore the heat flow regimes are combined.

Since the heat flow is limited by the Kapitza conductance the stability is strongly improved due to the cooling, similarly to superfluid helium. For liquid helium, the Kapitza conductance parameter a_K as well as the heat flow limit for the onset of film boiling have a strong influence on the stability of a cable.

A strong gain in stability can be obtained by reducing the compaction factor or increasing the wetted surface.

Supercritical helium

Heat flow to supercritical helium is simply described with a single cooling regime. It only depends on heat diffusion in the helium boundary layers and therefore it varies with time. The influence of supercritical helium on the MQE curve is small compared to superfluid and liquid helium.

The MQE is not very sensitive to changes in the cooling parameters. Therefore for an increase of stability of cables cooled with supercritical helium, other parameters, like the interstrand contact parameters, are of more interest.

Chapter 6

Experiment and Simulation

The results of cable stability measurements are presented. MQE *is measured as a function of i for ten samples with different coatings and heat treatments. The samples are of the type* LHC *01 cable and* SIS *300 dipole cable.*

Measurements of local voltage and self-field provide valuable information on the stability mechanisms. Calculations are compared with measurement to validate the calculations.

The validity of CUDI *is demonstrated by systematic comparison of simulation and measurement results.*

Simulations with CUDI *are performed to investigate the accuracy of the program across the entire range of cable samples and local variations of parameters.*

6.1 Introduction

The stability of superconducting Rutherford cables depends strongly on the local magnetic field pattern as well as cooling and experimental conditions. The development of a normal zone initiated locally shows cable specific behavior. Small local variations have a strong impact on the stability measurements. Measurements in an experimental set-up are qualitatively representative for cable stability in magnets.

The measured MQE, self-field and voltages of sample LHC 01 - C are used to validate the calculations with CUDI. By curve fitting, the most plausible cable properties are obtained. The comparison provides a good base for discussing the validity of CUDI. The range and sensitivity of the obtained parameter specifications in chapters 4 and 5 are used in the fitting process.

For other LHC 01 and SIS 300 dipole samples the MQE measurements are presented. Calculations for the samples with the expected expected local properties are added.

Experimental results

Experiments are performed on cable samples with properties as listed in table 6.1.

Table 6.1: Properties of the measured samples.

Sample name	Coating	Core	Impregnation	RRR	R_a ($\mu\Omega$)	R_c ($\mu\Omega$)
LHC 01 - A	SnAg	No	No	200	150-200**	15-20**
LHC 01 - B	SnAg	No	No	90	20-300**	2-30**
LHC 01 - C	Al	No	No	250	>1000**	640*
LHC 01 - D	SnAg	No	No	200	150-200**	15-20**
LHC 01 - E	SnAg	No	Yes	200	150-200**	15-20**
LHC 01 - F	Soldered	No	No	300	< 0.1**	< 0.1**
SIS 300 dipole - A	Soldered	Yes	No	346	< 1*	> 20000**
SIS 300 dipole - B	AgSn	Yes	No	89	60-70*	> 20000**
SIS 300 dipole - C	AgSn	Yes	No	245	600-700*	> 20000**
SIS 300 dipole - D	AgSn	Yes	No	272	8000-9000*	> 20000**

*Measured

**Data determined from literature values.

The measurements are performed with local heaters at the center and at the edges of the cable, at 1.9 K and 4.3 K and at various values of magnetic field. Since I_c is varying across the cable width, the local value of I_c at the position of the heater is used for the normalized i value.

All MQE measurements and simulations are performed with a pulse duration of 100 μs. MQE is obtained by multiplying E_p with the correction factor f_{corr}, see section 3.2.3. For regime I f_{corr} is 0.6 and for regime II and higher, f_{corr} is 0.9.

Simulations

The pulse shape presented in figure 3.11 is used as simulation input. The f_{corr} applied on the measured data is applied in calculated data as well. The realistic cable geometry and the local field variations due to the self-field are taken into account.

To find a proper fit of the calculated MQE to the measurement results requires a lot of computing time. Several attempts are made to downscale the number of strands in calculations to reduce the simulation time [86]. However, due to the strong impact of local variations across the cable width, the accuracy of the results proved not to be sufficient. Therefore all simulations are performed on the full cable.

The fitting process is shown for the calculation of MQE for one case, see section 6.2. For the other measurement data, the parameters are estimated and no curve fitting is applied.

Overview of the measured MQE

An overview of all the measured MQE versus i curves for the center heaters on the six LHC 01 samples is shown in figure 6.1a cooled by liquid helium and in figure 6.1b cooled by superfluid helium. The lowest curves in both figures show the adiabatic case, sample LHC 01 - E. Details of all curves will be given in sections 6.5 to 6.9.

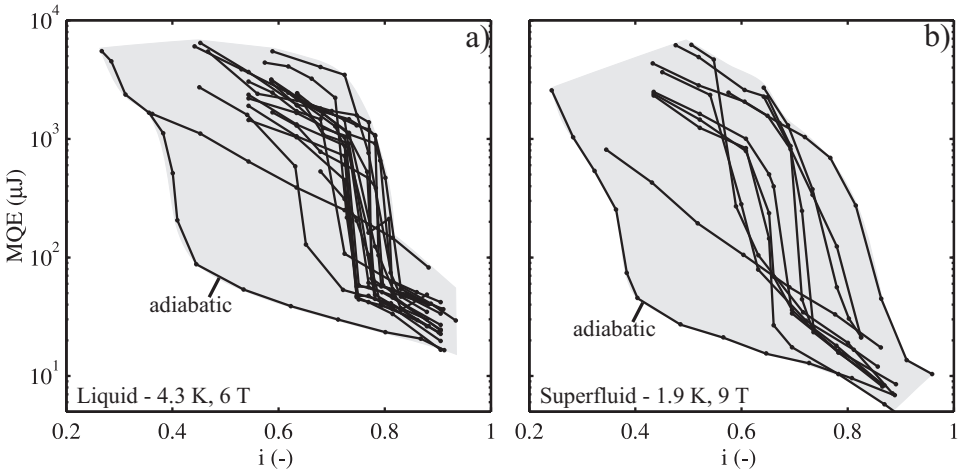

Figure 6.1: Survey of measured MQE as a function of i for central heaters on the six LHC 01 samples at a) $T = 4.3$ K and $B = 6$ T and at b) T = 1.9 K and B = 9 T. $I_c = 22 \pm 0.5$ kA.

In the framework of a collaboration with GSI a set of 4 cored SIS 300 dipole cables with different cable treatment is measured. In figure 6.2 an overview of the MQE curves is shown.

The range of variation in MQE is large, with a generally higher MQE and i_{kink} for lower interstrand resistance R_a. Further details are presented in section 6.10.

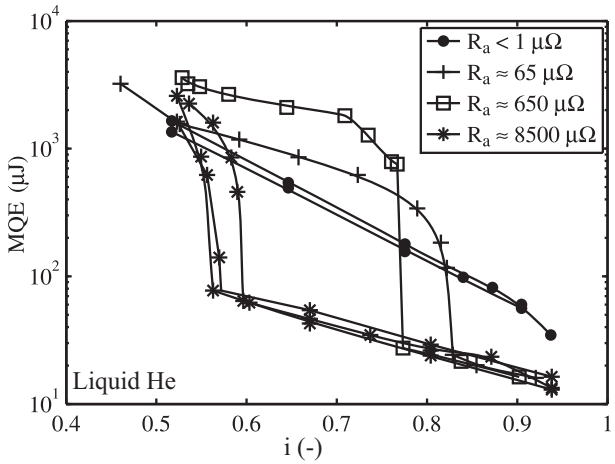

Figure 6.2: MQE versus normalized cable current for 4 cored SIS 300 dipole cable samples with different treatment. $T = 4.3$ K, $B = 6$ T and $I_c = 15.3 \pm 0.3$ kA.

The measured values of MQE for center heaters in the single strand stability regime are presented in figure 6.3, except for the adiabatic case. It shows the variation between cables and heaters for different cooling conditions. The variation in MQE in regime I is mainly caused by differences in the local conditions of cooling and heat transfer between the heater and the cable.

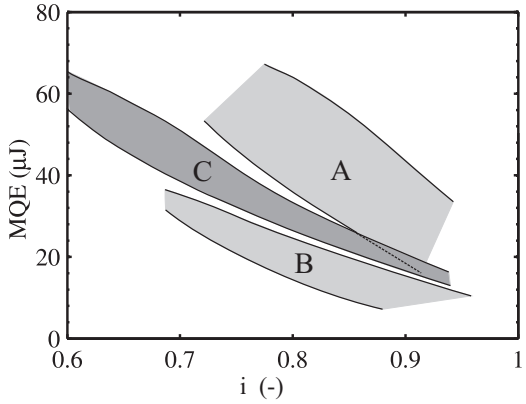

Figure 6.3: The range of measured MQE in regime I for area A LHC 01 cables at 4.3 K and 6 T, area B LHC 01 cables at 1.9 K and 9 T and area C SIS 300 dipole cables at 4.3 K and 6 T.

6.2 Fitting of calculated to measured MQE

To fit MQE calculated by CUDI to measured MQE, a large number of parameters can be varied. In chapters 4 and 5 the sensitivity of the MQE curve to a variation in electrical and interstrand contacts and to a variation in helium parameters is presented. The following three characteristics are important in fitting the calculated and simulated data, see figure 6.4:

A - MQE in regime II, strongly affected by the interstrand thermal conductances $F_{int,a}A_a$ and $F_{int,c}A_c$ as well as the helium cooling.

B - The transversal propagation mode for regime II. A sharp transition indicates CPC I left from B and a less sharp transition normally APC II, see figure 2.23.

C - i_{kink}, strongly influenced by R_a and R_c and the helium cooling. In some cases $F_{int,a}$ and $F_{int,c}$ also have a significant influence on i_{kink}.

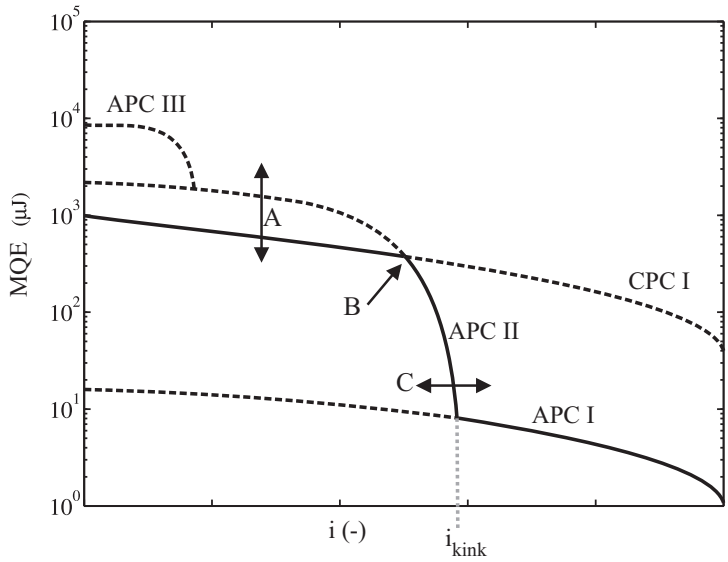

Figure 6.4: MQE as a function of i with three characteristics, A to C, used for fitting calculations to measurements.

The fitting process is demonstrated for the MQE measurements of one center and one edge heater on sample LHC 01 - A, see figure 6.5a. First the propagation criteria are determined: The sharp transition indicated by the arrow, suggests that two criteria intersect at that point, APC II and CPC I. The MQE at $i = 0.45$ deviates from CPC I, indicating a change in criterion, probably to APC II, see figure 2.23b.

At the edge all criteria are of the type APC, since cross propagation is not possible.

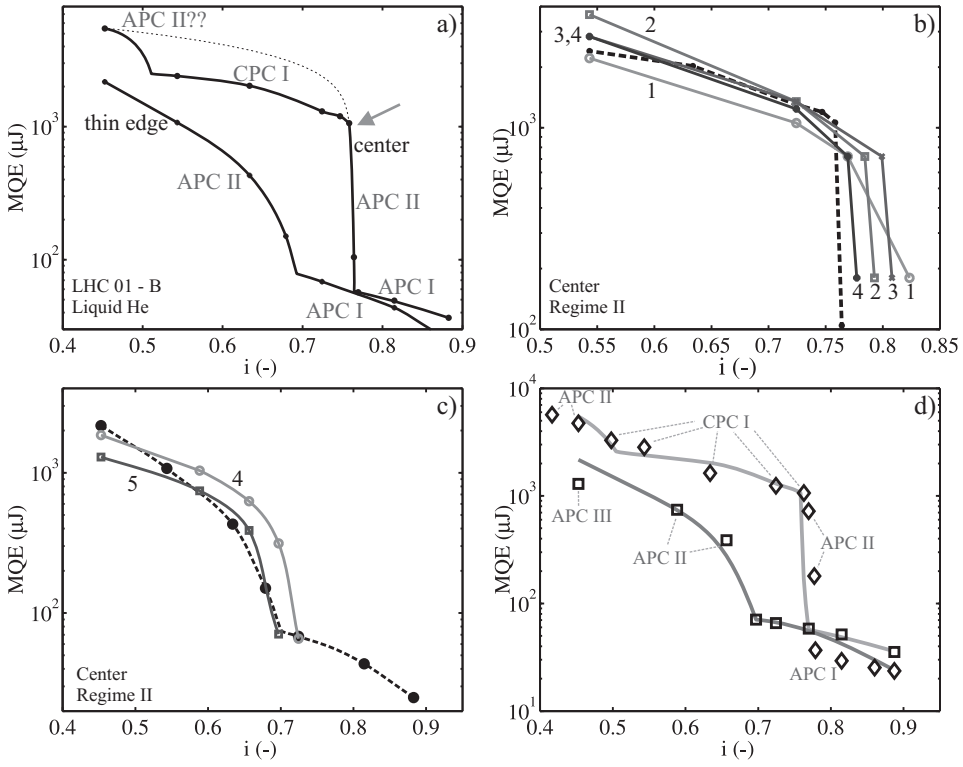

Figure 6.5: a) Measured MQE as a function of i for one center heater and one edge heater for sample LHC 01 - A, cooled by liquid helium at 4.3 K and 6 T, with $I_c = 22.1$ kA. b) Four calculated curves for the center heater in regime II. c) Two calculated curves for the edge heater in regime II. d) Measured MQE (lines) and calculated MQE (squares and diamonds) for the best fit parameters.

The well-known parameters are fixed to reduce the number of free parameters. R_a is set to 8 R_c and for the transient cooling $a_K = 300$ W/m^2/K^4 is taken, see chapters 4 and 5. The cable geometry is described in section 2.5. For the used sample and heat treatment type, $R_c \approx 20$ $\mu\Omega$ [76].
First the curve of the center heater is fit for regime II with three free parameters: R_c, $F_{int,a}$ and $F_{int,c}$. The following calculation steps are performed, see figure 6.5b:

1. The initial parameter values are applied, see table 6.2. The calculation shows that all points are of APC II. Furthermore, MQE is too low for $i < i_{kink}$. To increase MQE for $i < i_{kink}$, $F_{int,a}$ is decreased in the next calculation. $F_{int,c}$ is taken the same as $F_{int,a}$, since decoupling of both parameters is not shown before.

2. All points are still defined by APC II and MQE at $i = 0.54$ is too high. APC II at $i = 0.54$ may be correct, but CPC I is too high. For the next calculation $F_{int,c}$ is reduced while $F_{int,a}$ is not changed.
3. The MQE at $i = 0.54$ and 0.72 are defined by CPC I and agree well with the measured curve. However i_{kink} is too high. For the next calculation, R_c is increased, since it only affects i_{kink} and not MQE a lower i, see section 4.3.
4. i_{kink} is reduced sufficiently and all calculated points are within a few percent of the measured points.

Table 6.2: Parameter values for the curve fitting calculations, see figure 6.5b.

Calculation	R_c	$F_{int,a}$	$F_{int,c}$	V_{He}	$A_{a,edge}$
	$\mu\Omega$	$\mathrm{WK}^{-(1+b)}\mathrm{m}^{-2}$	$\mathrm{WK}^{-(1+b)}\mathrm{m}^{-2}$	mm^3	mm^2
1	20	200	200	See section 2.5.4	2.5
2	20	100	100	”	2.5
3	20	100	200	”	2.5
4	40	100	200	”	2.5
5	40	100	200	”	10
6	40	100	200	” Multiplied by 2	10

Next the curve of the edge heater is fit for regime II, see figure 6.5c:

4. The parameters obtained in calculation 4 by fitting the results for the center heater are now applied for the edge heater. Due to local differences in geometry and field the calculation result varies from the center heater results. The calculated MQE is generally too high. In analogy with a strongly reduced R_a in the edge, see section 4.1.4, the value of $F_{int,a}$ may be increased significantly. In the next calculation $F_{int,a}$ is increased by a factor of 4, only in the edge section.
5. Except for the lowest i, curve 2 resembles the measured curve within accuracy limits. An even better agreement can be achieved by variations in the cooling at the edge. However, many combinations of parameter changes may give a satisfactory result.

Additional points are calculated to complete the curves, see figure 6.5d. CUDI shows that the decisive criterion for the center heater at i is 0.42 and 0.45 is APC II. The MQE curve for the center heater is composed of APC II, APC I and CPC I as expected. For the edge heater the MQE curve is composed of APC I, APC II and APC III. It shows that the transition between criteria is not always seen in an MQE curve, due to the limited amount of data points.

The deviation for the MQE in regime I is within the variation shown in figure 6.3. Regime I is very sensitive to local variations of cooling and variations of the heater. Therefore curve fitting in regime I can be speculative, since multiple local variables influence APC I strongly.

Measurements on the same sample with the same heaters have been performed at 1.9 K, see figure 6.6a. The arrow indicates two possibilities to draw the curve for the

center heater for a limited number of points. A sharp transition indicates the start of CPC I, otherwise the decisive criterion is APC II. R_a is obtained in calculation 5 and is used for calculating the MQE for the center and edge heater. $F_{int,a}$ and $F_{int,c}$ are taken half the value obtained by calculation 5, since the magnetic field is much higher.

The fitting process is continued for MQE measurements of the cable cooled by superfluid helium:

5. The calculated i_{kink} is too low for the center and edge heater. CUDI shows that the propagation mode for the center heater around i_{kink} is edge propagation, see section 2.4.1. To increase i_{kink} in case of edge propagation, the longitudinal normal zone propagation velocity $v_{q,long}$ needs to be reduced. The parameters strongly influencing $v_{q,long}$ are: R_c, $A_{He} * a_K$ and V_{He}. R_c is already determined by the fitting process, a_K is fixed for the surface material and A_{He} is fixed by geometry. An increase in V_{He} is plausible, since for APC II only one strand is hot and locally more helium volume is available, see figure 2.35. For the next calculation the helium volume is increased by a factor of 2.
6. The calculated curves fit the measured curve much better, see figure 6.6b. For the center heater at $i = 0.43$ the calculated MQE is much higher than the measured MQE.

The propagation criteria are illustrated, showing that CPC I is the dominant criterion for most of the MQE curve for the center heater. CPC II applies at $i = 0.43$. For uniform B APC II is expected to be lower than CPC II, however in the experimental set-up B is strongly increased in the cross layer, thus increasing the propagation in the cross layer, see figure 3.2.

For the edge heater, the criteria APC I to APC IV apply. In the measured MQE curve no clear transitions are seen between APC II, APC III and APC IV, possibly due to the limited amount of data points.

A higher level of agreement between calculation and measurement can be obtained by extending the fit process. The measured MQE shows a spread between the heaters, therefore the accuracy of the calculation is satisfactory.

The difference between measurements and calculations for APC I can be due to a combination of multiple causes: The discretization of CUDI, the way of addressing the volume of helium to the strands and variations between heaters, see figure 6.3.

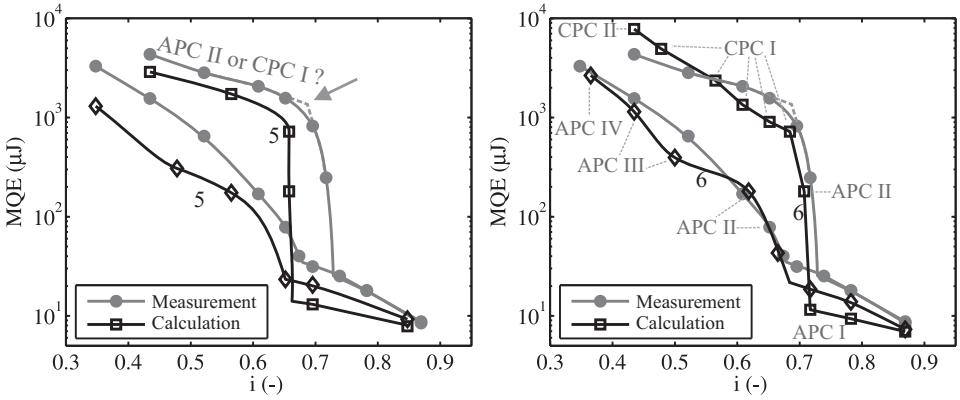

Figure 6.6: Measured and calculated MQE for one center heater and one thin edge heater on sample LHC 01 - A. Cooled by superfluid helium, $T = 1.9$ K, $B = 9$ T and $I_c = 23.0$ kA.

The shown example of curve fitting for heaters at two locations cooled with superfluid and liquid helium, ilustrates the ability of CUDI to accurately calculate the obtained curves when the local parameters are known.

The calculations show that the ratio $F_{int,a}/F_{int,c} \neq 1$. The correlation between interstrand thermal conductance in the cross and adjacent directions may vary due to the orientation of the mechanical pressure and the magnetic field. By comparing calculations and measurements $F_{int,a}/F_{int,c} = 0.5$ is found as a reasonable value for non-cored Rutherford cables. In cored Rutherford cables $F_{int,c}$ is reduced due to the core and $F_{int,a}/F_{int,c} > 1$ is taken.

Fitting the curves is very time consuming and may require many iterations, since local variation of the parameters has a strong influence on MQE. Especially the impact of a variation in $F_{int,a}$, $F_{int,c}$ and the helium volume and surface at the edge of the cable are hard to implement. However, the calculation show that a curve for edge heaters can be fit with reasonable values for the local parameters.

The calculated MQE in regime I is generally underestimated, since the helium volume addressed to the strand sections is underestimated by a factor of up to 4, see section 2.5.4. The influence of V_{He} is strong, especially for lower values of i.

6.3 Local voltage and self-field

The quench propagation modes and the influence of current redistribution on stability with R_a and R_c values varying from 0.1 to 10000 $\mu\Omega$ are very case specific. More detailed information about the existence, length and duration of the normal zone as well as the values of longitudinal and transverse normal zone propagation can be obtained by local voltage and self-field measurements [73], see sections 3.4 and 3.5.

Since the duration and voltage increase for higher R_a and R_c, the most clear voltage data is obtained for measurements with a high R_a and R_c.

The measurements and simulations of sample LHC 01 - C are highlighted, with $T = 4.3$ K, $B = 6$ T and $I_c = 22.2$ kA. The strand voltages and self-field are investigated around $I = I_{kink}$ (14.45 kA) for a center heater at a pulse energy of 150 μJ, see figure 6.17.

The moments of "just quench" and "just recovery" are investigated at $I = 14.4$ kA and 14.5 kA. Because I_{kink} is higher in the simulation, 14.9 and 15.7 kA are used to obtain similar longitudinal and transversal normal zone propagation patterns.

Normal zone recovery

Figure 6.7a shows three measured voltage traces on strand j for a center heater: Voltage V_j over about half a twist pitch, from the thick edge to the thin edge of the cable. Voltage V_{ja} and V_{jb} each covering half of V_j under the condition of $V_{ja} + V_{jb} = V_j$.

At 0 ms a normal zone starts in the center of strand j, propagating in the directions of ja and jb.

At 6 ms V_{jb} has become 0, indicating the recovery of the superconducting state in the strand part close to the thick edge. However, in the thin half a semi-static normal zone is present, finally disappearing after 21 ms, see V_{ja}. The normal resistance of the strand is about $7 \cdot 10^{-4}\Omega$ per meter length. With the maximum voltage of 5 mV and a nominal current of 514 A per strand, the length of the normal zone is about 18 mm. Due to the redistribution of current out of strand j, the normal zone length is underestimated.

Simulation results shown in figure 6.7b show similar curves, with the asymmetry of the normal zone propagation and a semi-static normal zone up to 20 ms.

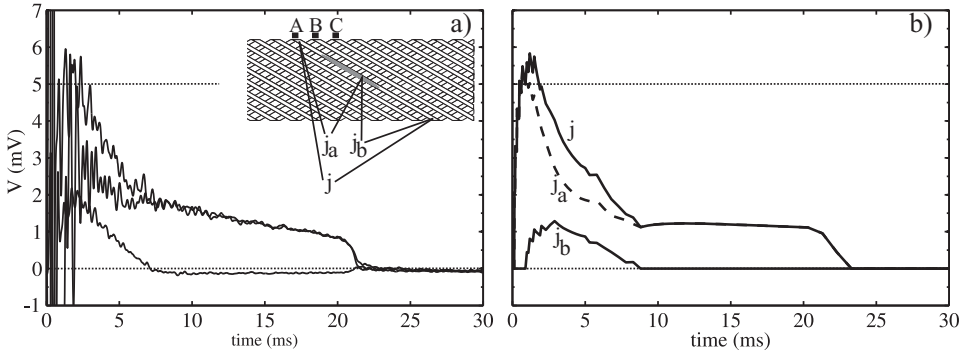

Figure 6.7: a) Measured and b) calculated voltages for sample LHC 01 - C, at I just below I_{kink}, with an energy pulse of 150 μJ. The inset shows the location of the voltage taps.

In figure 6.8 the self-field profile for three neighboring Hall probes spaced 4 mm apart is shown. Between 6 and 20 ms, the self-field is almost constant, indicating a

minor redistribution of current. The semi-static current distribution is defined by the current redistribution in the joints.

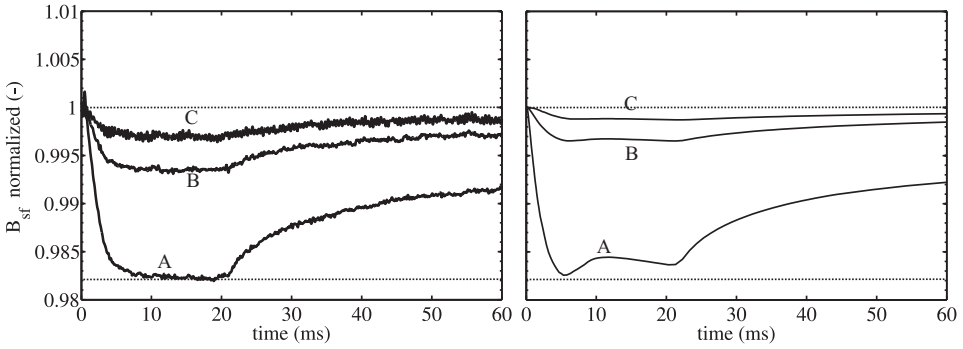

Figure 6.8: a) Measured and b) calculated self-field along the sample LHC 01 - C, at I just below I_{kink}, with an energy pulse of 150 μJ. The positions of Hall probes A, B and C are shown in the inset in figure 6.7a.

Normal zone leading to quench

The voltage traces for the "just quench" case are shown in figure 6.9. During the first 3 ms, until APC II is reached, V_j is similar in figures 6.7 and 6.9.

At about 3 ms, a sudden rise is visible in V_{j+1} and shortly after in V_{j+2}. The voltages across the three strands raise with about a similar speed, until the measured sections are fully normal, about 1.5 ms later. The current is distributed almost uniformly after 4.3 ms when the voltage plateau is reached in the three strands.

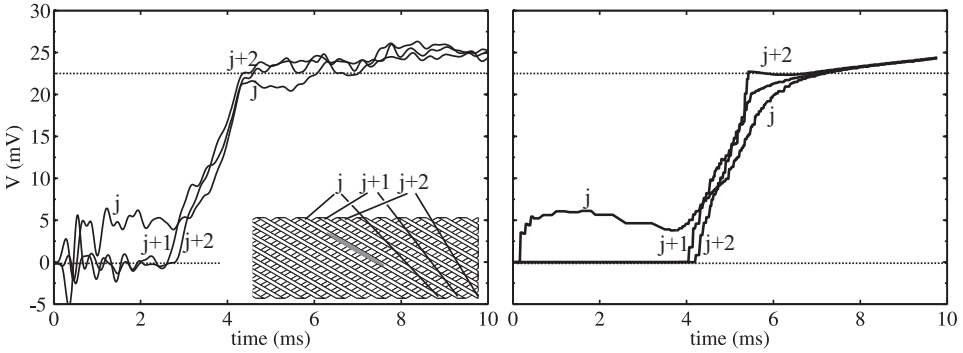

Figure 6.9: a) Measured and b) calculated voltages for the aluminum coated sample for an energy pulse of 150 μJ at $I \approx I_{kink}$ in the case of a quench. The inset in a) shows the location of the voltage taps.

The measured and calculated self-field profiles are shown in figure 6.10. Until

the start of the normal zone in strand $j+1$, the self-field evolves similarly to the recovery case described in figure 6.8.

The decrease in self-field from 4 to 8 ms, is discussed in section 3.4.2.

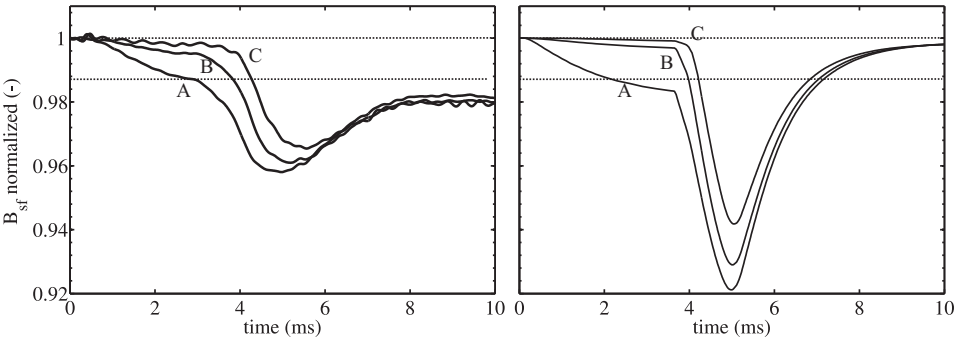

Figure 6.10: a) Measured and b) calculated self-field along the cable for 3 Hall probes spaced 4 mm apart for the same case as shown in figure 6.9. The Hall probes are similar to the ones shown in figure 6.8.

The voltages and self-fields in both the quench and recovery cases show similar behavior in measurements and CUDI simulations. The simulations prove to give an accurate description of the current distribution, voltages, self-field and longitudinal and transversal normal zone propagation.

6.4 Validation of CUDI

In sections 6.2 and 6.3 measurements and CUDI calculations of MQE and voltage and self-field are compared.

A good agreement of calculations with CUDI is shown for:

- MQE as a function of i, see section 6.2.
- Local voltages on a strand, see section 6.3.
- Local self-field along the cable edge, see section 6.3.

Since many parameters can vary locally, numerous solutions are possible to fit each measured curve exactly. By combining the MQE results with local voltage and self-field data, an even more accurate curve fit can be obtained. However, the process would take many fit steps and long calculation times.

Comments on the validity of CUDI are:

- **Mechanisms**
  The mechanisms of current redistribution and the propagation of the normal zone in the longitudinal and transversal directions are shown in both measurement and simulations. The sharp transitions in the MQE curves are convincingly demonstrated in the calculations, indicating a correct simulation of the stability mechanisms.

- **Parameter sensitivity**
  The characterization of a sample with MQE is strongly dependent on the interstrand thermal and electrical parameters and the cooling parameters. The sensitivity of the measured MQE is qualitatively similar to the sensitivity of the calculated MQE, as studied in chapter 4 and 5.
- **Regimes**
  The discretization of strand sections in CUDI is too course to address the fast and very local temperature variations in stability regime I for $i \approx 1$, since the section length is in the order of l_{MPZ}. Furthermore, variations between heaters and local variations in cooling strongly influence MQE. In regime II and higher, the normal zone is much longer and the quench decision is later. Therefore the temperature gradients and variations in time and space due to a heat pulse are reduced. In regime II and higher CUDI is sufficiently accurate.
- **Helium volume**
  The helium volume is locally assigned to one section. Since the helium in the center voids is divided over four strand sections, the effective helium volume assigned to one strand section may be underestimated, see section 2.5.4. For some calculations the effect of a variation in V_{He} on MQE may be significant.
- **Local parameter variations**
  The propagation of normal zones in the longitudinal and transversal directions is very sensitive to the local conditions of magnetic field, cooling and interstrand thermal contact. Therefore simulations need to address all the local parameters accurately. Although the local geometry is studied accurately, see section 2.5, the exact condition of the strand coating is unknown, especially at the contacts between adjacent strands at the cable edges. Simulations show an overestimated value of MQE for most edge heaters, probably due to a local increase in $F_{int,a}$ in analogy with a local reduction in R_a.

In general CUDI simulates the mechanisms accurately. The local MQE of a cable can be calculated when all parameters are sufficiently known. In the following sections, the measurement results of ten samples are discussed and the MQE calculations are performed for comparison.

6.5 Sample LHC 01 - A

Sample LHC 01 - A is a cable with a 0.5 μm $SnAg_{5\%wt.}$ coating. The cables are heat treated at 200 °C for 8 hours under a pressure of 50 MPa in dry air, giving a typical typical R_c of 15 - 20 $\mu\Omega$ [105]. The ratio R_a/R_c is estimated at 8, as discussed in section 4.1.4. The sample is measured twice, inbetween which the sample is stored for 16 months while exposed to air.

Results of MQE measurements performed in liquid helium at 4.3 K and 6 T are shown in figure 6.11. The four center heaters show a value of i_{kink} between 0.74 and 0.77. The thin edge heater has a lower value of i_{kink} of 0.69. The MQE at $i =$ 0.63 is about 1 to 2 mJ for the center heater and about 0.5 mJ for the edge heater.

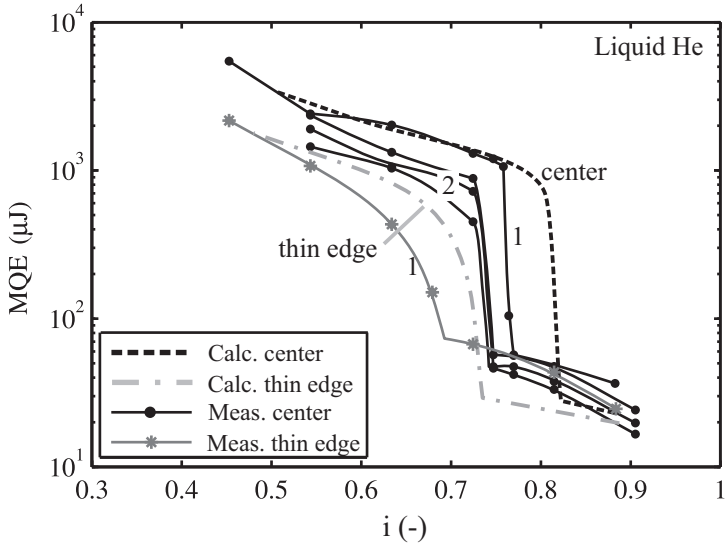

Figure 6.11: Measured and calculated MQE versus normalized cable current for four center heaters and one edge heater. The curves labeled 1 are measured 16 months before the curves labeled 2. Liquid helium cooling at $T = 4.3$ K, $B = 6$ T. $I_c = 21.4$ kA.

The measured and calculated MQE for the sample cooled with superfluid helium at 1.9 K at 9 T are shown in figure 6.12. For measurement 1 i_{kink} is 0.72 significantly higher than i_{kink} between 0.66 and 0.68 of the three curves, labeled number 2, that are measured 16 months later. It is plausible that the interstrand resistance has changed during the storage in air, due to oxidation, however, the value of R_a and R_c have not been measured.

The three curves measured in the same cool down give a good measure for the accuracy of the MQE curves in regime II. The variation in i_{kink} is less than $\pm$ 2 %. For $0.54 < i < 0.66$ the difference between the minimum and maximum MQE is a factor of 2.

For the edge heater $i_{kink} = 0.67$ and therefore it is lower than the value for the center heater in measurement 1.

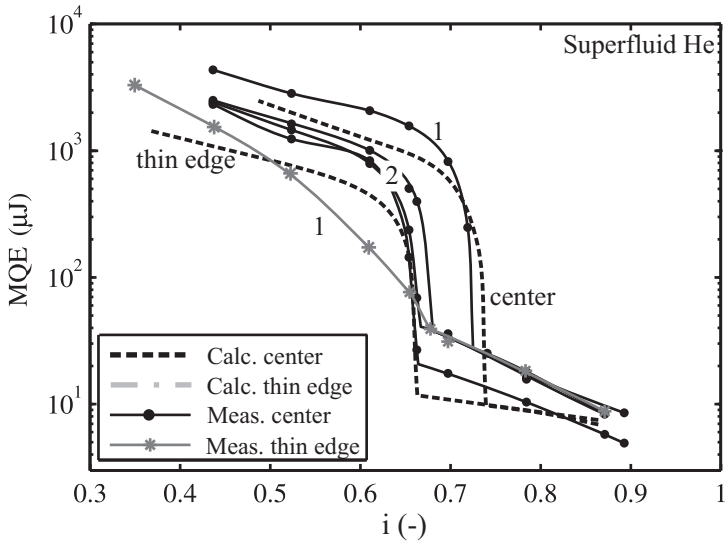

Figure 6.12: Measured and calculated MQE versus normalized cable current for four center heaters and one edge heater. The curves labeled 1 are measured 16 months before the curves labeled 2. Superfluid helium cooling at $T = 1.9$ K, $B = 9$ T. $I_c = 23.1$ kA.

The calculations shown in figures 6.11 and 6.12 are performed with the parameters listed in table 6.3.

Table 6.3: Calculation parameters of sample LHC 01 - A.

T	B	R_a	R_c	a_K	$F_{int,a}$	$F_{int,c}$
K	T	$\mu\Omega$	$\mu\Omega$	$W/m^2/K^4$	$W/m^2/K^{b+1}$	$W/m^2/K^{b+1}$
4.3	6	160	20	300	100	200
1.9	9	160	20	300	50	100

As for all the samples the F_{int} at 1.9 K and 9 T is taken two times lower than at 4.3 K and 6 T, which is necessary to obtain a good agreement between calculations and measurements.

The agreement of the curves at the thin edge is much worse than the curves in the center of the cable, probably due to unknown local variations in the interstrand thermal conductance.

Simulations show that MQE for $i < 0.8$ the stability is limited by cross propagation. This explains the sharp transition in the measured curve as well.

Although the measured MQE curve at $T = 1.9$ K shows a less sharp transition from regime I to regime II, the mechanisms of quench propagation are similar to curves at $T = 4.3$ K.

The three curves of the heaters measured after 16 months of storage in air, are

very similar especially in regime II. The influence of the position of the heaters proves to be small. Variations therefore depend mainly on local differences in parameters.

6.6 Sample LHC 01 - B

Sn-Ag coated LHC 01 cables without heat treatment, here labeled sample LHC 01 - B, have a wide range of R_a between 1.7 and 30 $\mu\Omega$ [76]. The measured value of RRR = 89 is low, due to the absence of heat treatment. Therefore the matrix electrical and thermal resistivity is relatively low.

The measured and calculated MQE for liquid helium are shown in figure 6.13. The cable sample is measured two times with a 3 months interval. In this case, the latter measurement shows the highest MQE for the center heater. The position of i_{kink} varies between 0.78 and 0.80. For the edge heater, i_{kink} is much lower at 0.67. The MQE level at values below $i = 0.75$ is lower compared to sample LHC 01 - A.

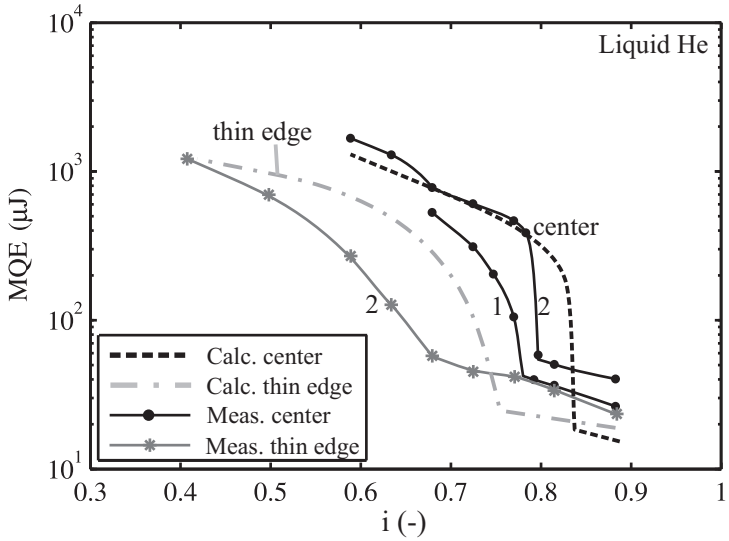

Figure 6.13: Measured and calculated MQE versus normalized cable current for one center heater and one edge heater. The curves labeled 2 are measured 3 months after the curves labeled 1. Cooling with liquid helium at $T = 4.3$ K, $B = 6$ T and $I_c = 22.1$ kA.

Results from measurements performed in superfluid helium at 1.9 K are shown in figure 6.14. i_{kink} is 0.87 and 0.75 for the center and edge heater, respectively. The MQE in regime II is significantly lower for the edge heater, compared to the center heater.

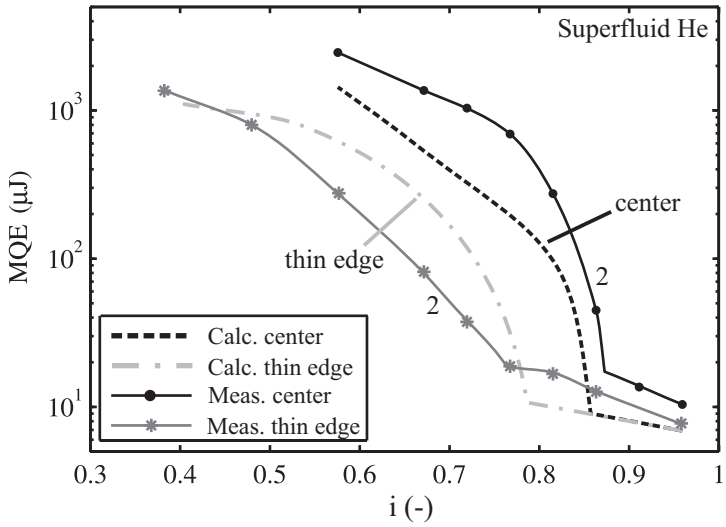

Figure 6.14: Measured and calculated MQE versus normalized cable current for one center heater and one edge heater. Cooling with superfluid helium at $T = 1.9$ K, $B = 9$ T and $I_c = 20.9$ kA.

MQE measurements with one center heater at 4.3 K for three different magnetic fields are shown in figure 6.15. I_c and T_c depend strongly on the magnetic field. Other field dependent parameters are the electrical and thermal matrix resistance.

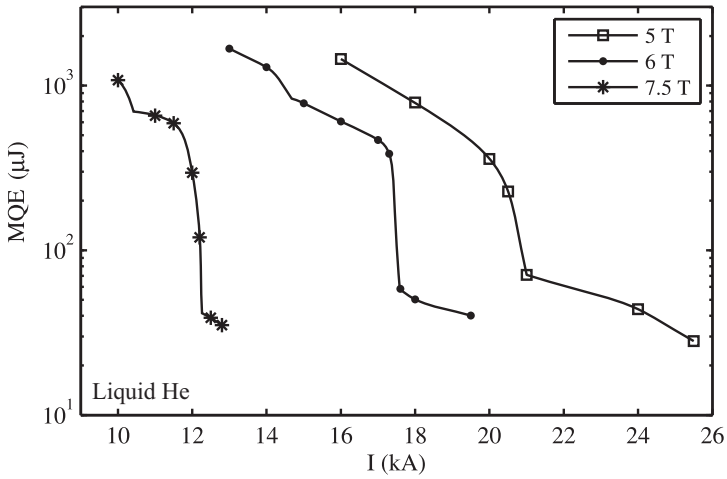

Figure 6.15: Measured MQE as function of I for three magnetic fields at $T = 4.3$ K for one center heater. For $B = 5$, 6 and 7.5 T I_c is 27.3, 21.8 and 13.8 kA, respectively.

In figure 6.16 the MQE is displayed as a function of the normalized current. For higher magnetic field I_{kink} reduces, whereas i_{kink} clearly increases. In regime I, MQE as a function of i for the three magnetic fields show no significant variation.

I_c is about two times higher at 5 T compared to 7.5 T. Therefore at the same i, Joule heating in a normal zone at 5 T is four times higher, compared to 7.5 T. Increased Joule heating increases the longitudinal as well as the transversal normal zone propagation velocity, therefore reducing stability.

At 6 and 7.5 T a second step is clearly visible in the curve, indicating a transition to another normal zone propagation mode, probably from CPC II to APC II, see figure 6.5a.

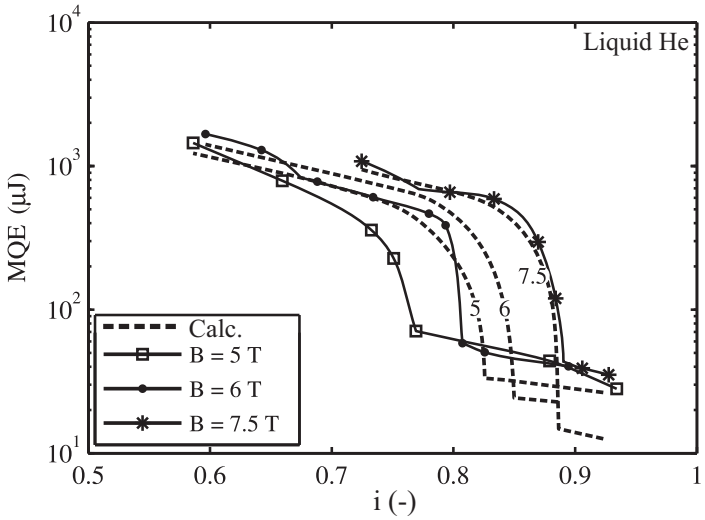

Figure 6.16: a) Measured MQE as function of i for 3 different fields for one center heater cooled by fluid helium at 4.3 K. b) Simulation results. For $B = 5$, 6 and 7.5 T I_c is 27.3, 21.8 and 13.8 kA, respectively.

The MQE calculations have been performed with the simulation parameters as shown in table 6.4. $F_{int,a}$ and $F_{int,c}$ are varied as a function of B, to account for the variations in the curve. Figure 6.16 clearly indicates an overestimation for the calculated i_{kink} at 5 T, whereas the calculation at 7.5 T agrees well with the measured curve. A better agreement between calculations and measurement can be obtained by an additional increase in $F_{int,a}$ and $F_{int,c}$ for low fields. An increase in R_a and R_c has a larger impact on i_{kink} for lower fields, since Joule heating depends quadratic on I.

For both the liquid and superfluid helium cooled case, the difference between MQE of the edge and center heaters is underestimated. An increase in F_{int} at the edge section is not applied here, but would provide a better agreement as discussed in section 6.2.

Table 6.4: Calculation parameters of sample LHC 01 - B.

T	B	a_K	R_a	R_c	$F_{int,a}$	$F_{int,c}$
K	T	$W/m^2/K^4$	$\mu\Omega$	$\mu\Omega$	$W/m^2/K^{b+1}$	$W/m^2/K^{b+1}$
4.3	5	300	160	20	200	400
4.3	6	300	160	20	150	300
4.3	7.5	300	160	20	100	200
1.9	9	300	160	20	50	100

6.7 Sample LHC 01 - C

A 0.5 μm thick aluminum coating is deposited on the strands of sample LHC 01 - C using an electrolytic process. In a 6 hour heat treatment at 200 °C in air with 100 % humidity the Al_2O_3 layer of about 9 nm is formed exhibiting $R_c \approx 600$ $\mu\Omega$ [60]. The Kapitza conductance of Al_2O_3, with $a_K \approx 60$ $W/m^2/K^4$, is about 5 times lower than for Cu surfaces, as is discussed in section 5.2 and supported by [91].

The measured and calculated MQE in liquid helium at 4.3 K are shown in figure 6.17. Due to the high R_a and R_c and the low Kapitza conductance the value of i_{kink} is relatively low; 0.65 and 0.50 for the center and thin edge, respectively. Both values are significantly lower compared to sample LHC 01 - A, with the standard LHC heat treatment, see figure 6.11.

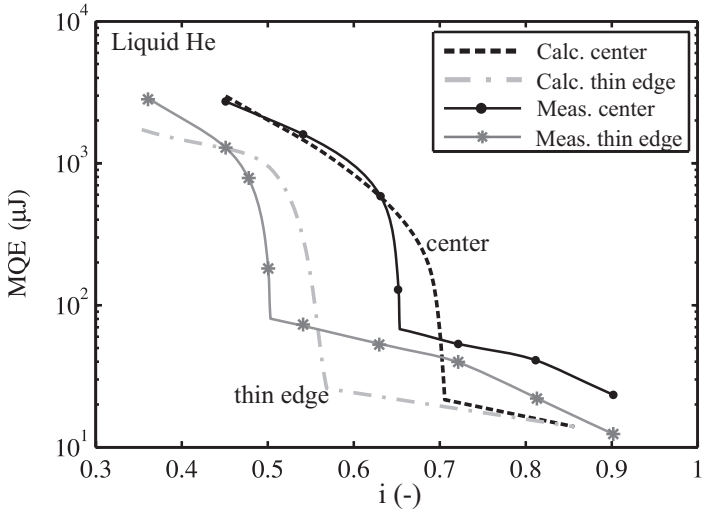

Figure 6.17: Measured and calculated MQE as a function of i for one center heater and one edge heater. Liquid helium cooling at $T = 4.3$ K, $B = 6$ T and $I_c = 22.2$ kA.

The measured and calculated MQE in superfluid helium at 1.9 K are shown in figure 6.18. The transition between regimes I and II is not as clear as compared

to most MQE curves. However, with Hall probe measurements the recovery of the normal zone in regime II is clearly visible and i_{kink} is determined at 0.71 and 0.56 for center and edge heaters, respectively.

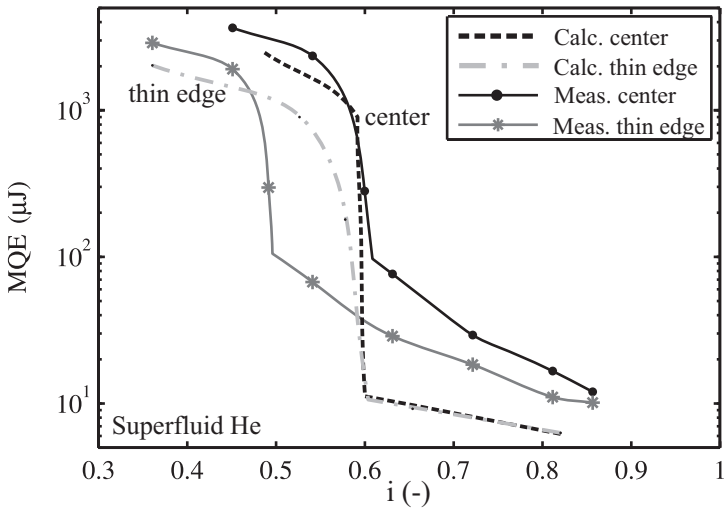

Figure 6.18: Measured and calculated MQE as a function of i for one center heater and one edge heater. Superfluid helium cooling at $T = 1.9$ K, $B = 9$ T and $I_c = 22.2$ kA.

MQE calculations have been performed with the simulation parameters as shown in table 6.5. Simulations for 4.3 K show the same ratio between i_{kink} of the edge and center heater compared to the measured values. At 1.9 K, the difference between the MQE curves for the thin edge and center are small compared to the measurements.

The calculation results for the heaters in regime I show a much lower MQE compared to the measurements, especially at 1.9 K. The difference in regime I can only be explained by the strand cooling or heat deposition properties. The volume of cooling assigned to the strands are underestimated in regime I, see section 2.5.4. Furthermore, the heat deposition might be reduced for this sample, affecting MQE in regime I.

A better agreement between calculation and measurement data for the edge heaters can be reached by locally increasing $F_{int,a}$ at the edge section.

Table 6.5: Calculation parameters of sample LHC 01 - C.

Temperature	Field	R_a	R_c	a_K	$F_{int,a}$	$F_{int,c}$
K	T	$\mu\Omega$	$\mu\Omega$	$\mathrm{W/m^2/K^4}$	$\mathrm{W/m^2/K^{b+1}}$	$\mathrm{W/m^2/K^{b+1}}$
4.3	6	1200	600	60	50	100
1.9	9	1200	600	60	25	50

6.8 Samples LHC 01 - D and E

Two SnAg coated LHC 01 cable samples are heat treated at 200 °C for 8 hours. A strongly oxidized surface is obtained with $R_c \approx 80\ \mu\Omega$ [76]. Sample LHC 01 - E is impregnated after the heat treatment, therefore adiabatic conditions are assumed for the small timescales involved in stability.

The MQE measurement points at 4.3 K for samples LHC 01 - D and E are shown in figure 6.19. For the center as well as the edge heater i_{kink} reduces strongly due to the impregnation from 0.73 to 0.41 for the center heater and from 0.54 to 0.39 for the edge heater.

For the impregnated sample the edge heater still shows a slightly reduced MQE compared to the center heater, indicating that lower MQE in the edge is not only due to a reduced helium content.

The measurements for the impregnated samples show two transitions. The second transition is very likely from APC II to APC III, since the edge as well as the center heater show the same step. A similar transition is seen at 1.9 K, see figure 6.20. Since the MQE is much lower compared to the non-impregnated samples, regime III lies within the experimental limits for the energy pulse.

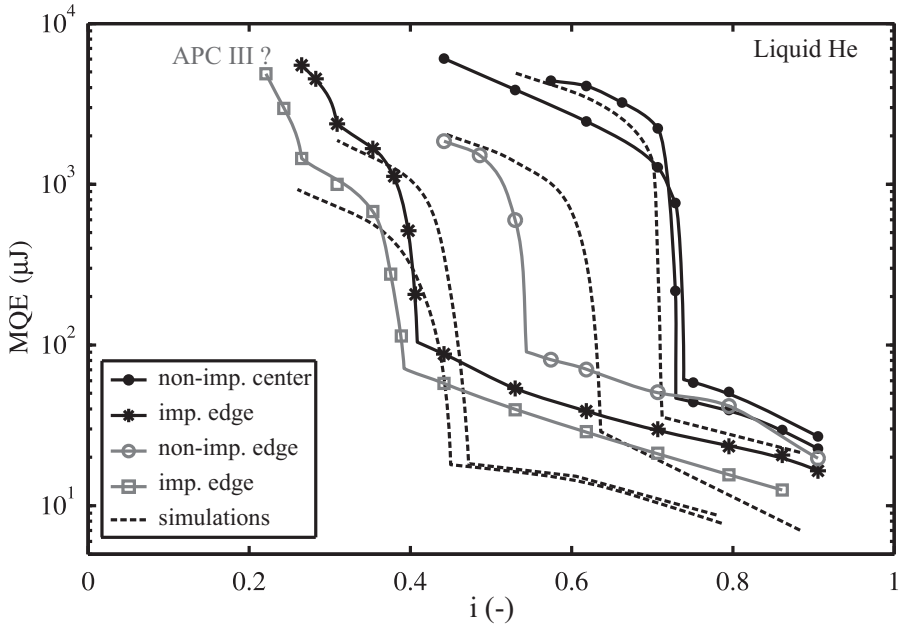

Figure 6.19: Measured and calculated MQE as a function of i for center and thin edge heaters on samples LHC 01 - D and E. Sample D is not impregnated and sample E is impregnated. Liquid helium cooled at $T = 4.3$ K, $B = 6$ T and $I_c = 22.5$ kA.

The measured and calculated MQE using superfluid helium at 1.9 K for samples LHC 01 - D and E are shown in figure 6.19. The measured i_{kink} is strongly reduced due to the impregnation from about 0.6 to 0.4 for the center heater.

Although the variation in MQE at $i \approx 0.9$ is small, the MQE at $i = 0.62$ is a factor 5 higher for the center heater of the non-impregnated sample, compared to the impregnated sample. The difference is due to the improved ratio between transverse cooling and Joule heating. The impact of superfluid helium on the MQE in cable stability regime I is similar to single wire MQE, see figure 2.8b.

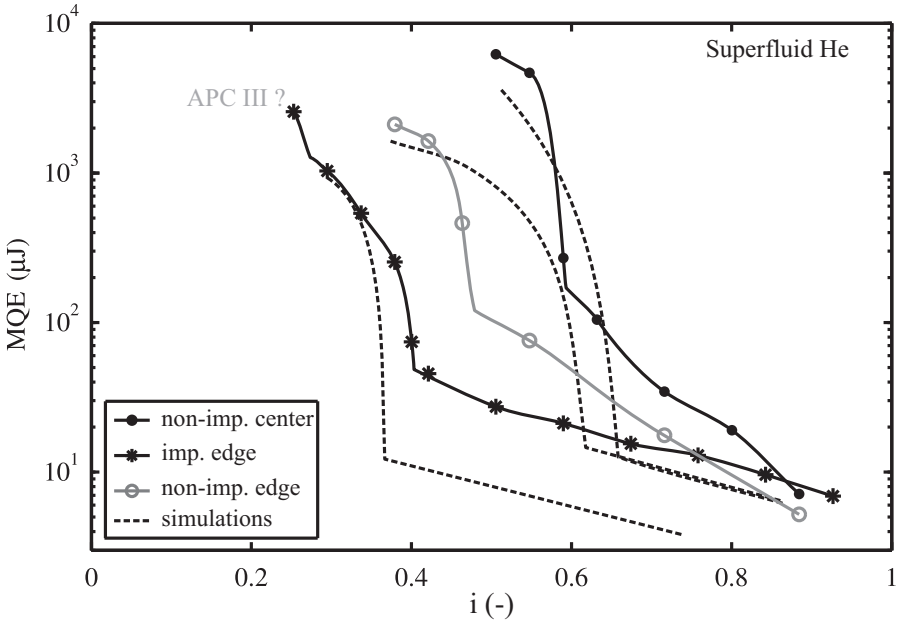

Figure 6.20: Measured and calculated MQE as a function of i for sample LHC 01 - D and E in superfluid helium. Sample D is not impregnated and sample E is impregnated. Measurements are performed on center heaters and thin edge heaters. $T = 1.9$ K, $B = 9$ T and $I_c = 24.3$ kA.

The simulation parameters are shown in table 6.6. For sample LHC 01 E, the helium volume is assumed zero. The simulations for the center heaters at 4.3 K, see figure 6.19, agree well for results in i_{kink} and MQE in regime II.

For the non-impregnated edge, the difference is relatively large between calculated and measured MQE at 4.3 K and 1.9 K. For better calculation results $F_{int,a}$ for the edge section needs to be increased.

Table 6.6: Calculation parameters of samples LHC 01 - D and E.

T	B	a_K	R_a	R_c	$F_{int,a}$	$F_{int,c}$
K	T	$W/m^2/K^4$	$\mu\Omega$	$\mu\Omega$	$W/m^2/K^{b+1}$	$W/m^2/K^{b+1}$
4.3	6	250	640	80	50	100
1.9	9	250	640	80	30	60

6.9 Sample LHC 01 - F

One cable, sample LHC 01 - F, is soldered through with SnAg solder at 210 °C. A pressure of 50 MPa is applied to ensure that the cable dimensions are similar to a non-soldered cable and that the strands are well-connected. Due to the soldering, RRR of this sample is about 300.

The solder is applied on the outer surface of the cable. Therefore voids may remain inside the cable.

R_a and R_c are drastically reduced and estimated to be in the order of 0.1 $\mu\Omega$. Interstrand thermal conductivity is very high and is limited partially by the thermal conductivity of the copper, estimated by the conductance between two strand centers, with the thermal conductivity as a function of T at 9 T for the strand of about $25T$ W/m/K. For a distance between the strand centers of about 1 mm, $F_{int,a}$ and $F_{int,c}$ have a maximum of 25000 $W/K^{1+b}/m^2$, with b = 1.

The measured and calculated MQE at 4.3 K are shown in figure 6.21. Both the center and edge heater show no transition and no signs of different regimes. Since the strands are in almost perfect electrical and thermal contact, the cable behaves as a large single strand and current redistribution can occur up to $i \approx 1$.

Measurements in superfluid helium at 1.9 K show similar behavior, see figure 6.22. The edge heater has a higher MQE value compared to the center heater at 1.9 K, possibly due to helium contact at the edge of the cable, whereas a very limited amount of helium is available at the center of the cable. The effect is not seen at 4.3 K, since the influence of helium cooling is smaller at 4.3 K.

In general the MQE for the soldered cable is lower for $I < I_c$, compared to the other measured cables. The main reason is the improved transversal normal zone propagation due to the reduced helium cooling and increased interstrand heat exchange.

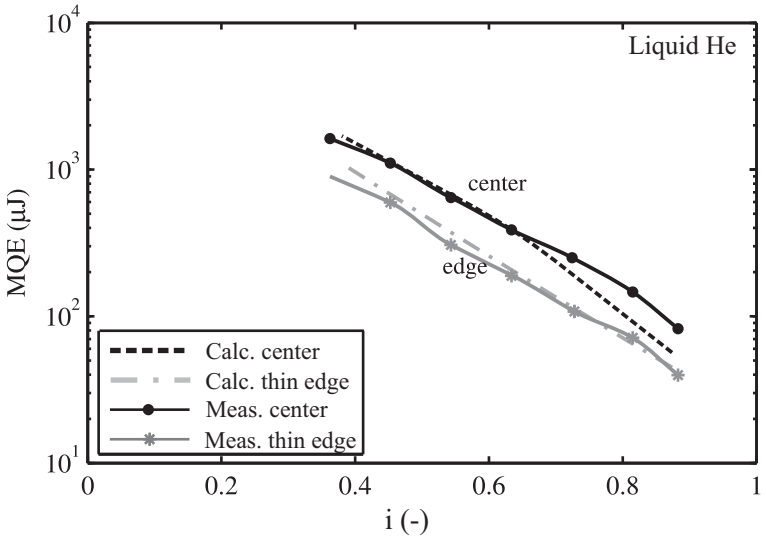

Figure 6.21: Measured and calculated MQE versus normalized cable current for sample LHC 01 - F for one center heater and one thin edge heater. Liquid helium cooling at $T = 4.3$ K, $B = 6$ T and $I_c = 22.1$ kA.

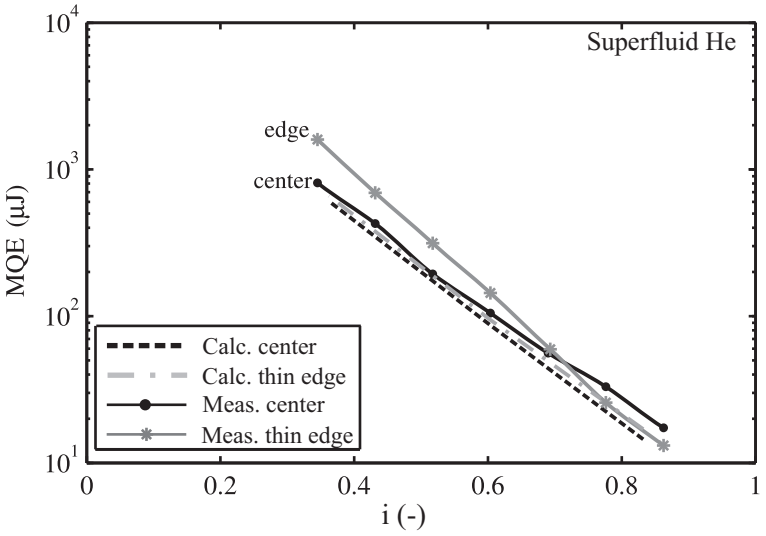

Figure 6.22: Measured and calculated MQE versus normalized cable current for sample LHC 01 - F for one center heater and one thin edge heater. Superfluid helium cooling at $T = 1.9$ K, $B = 6$ T and $I_c = 23.2$ kA.

Simulations are performed for the soldered sample with the parameters listed in table 6.7. Since the helium volume and cable parameters differ from the other cables the volume and contact surface of helium are varied by a factor of F_{VHe} and F_{AHe} to fit the measured curves roughly. R_a and R_c are estimated at 1 $\mu\Omega$.

The best fit is obtained for $F_{int,a} = 20000$, $F_{int,c} = 4000$ W/K^{1+b}/m^2, $F_{VHe} = 0.5$ and $F_{AHe} = 0.5$. Therefore the measurements show voids are filled for 50 % by the solder. Since $F_{int,c}$ is much smaller than $F_{int,a}$, the solder is located mainly between the adjacent strands.

Table 6.7: Calculation parameters of sample LHC 01 - F.

T	B	a_K	b	$F_{int,a}$	$F_{int,c}$	R_a	R_c	F_{VHe}	F_{AHe}
K	T	W/m^2/K^4	-	W/m^2/K^{b+1}	W/m^2/K^{b+1}	$\mu\Omega$	$\mu\Omega$	-	-
4.3	6	300	1	20000	4000	0.1	0.1	0.5	0.5
1.9	9	300	1	20000	4000	0.1	0.1	0.5	0.5

6.10 SIS 300 dipole samples

Four identically cored SIS 300 dipole cables with $SnAg_{5\%}$ coating are given different treatments to vary the range of R_a. The 13 mm wide 25 μm thick core of 304 stainless steel ensures $R_c > 10$ mΩ, thus limiting the interstrand coupling loss and dynamic field errors in magnet applications [5]. Due to the core, the heat conductivity in the cross direction is strongly reduced and CPC I will be increased strongly. Therefore all MQE curves are expected to be defined only by APC.

Sample A is partially soldered by shortly heating the cable after applying solder powder on the surface. Therefore a good connection between adjacent strands is created with a corresponding low R_a. Due to the partial solder V_{He} and A_{He} are reduced by a fraction of about 0.7. The RRR of 346 is very high compared to as received cables.

Sample B is measured as-received, showing $R_a \approx 65$ $\mu\Omega$ and RRR = 89.

Sample C got a heat treatment for 4 hours at 200 °C in normal atmosphere, causing $R_a \approx 650$ $\mu\Omega$ and RRR = 245.

Sample D got a heat treatment of 18 hours in vacuum at 215 °C followed by 58 hours at 210 °C in air and shows $R_a \approx 8500$ $\mu\Omega$ and RRR = 272.

The measured and calculated MQE at 4.3 K are shown in figure 6.23 for sample A to D. The impact of a reduction of R_a is strong, improving i_{kink}. However, in regime II, at i between 0.6 and 0.75 for samples A to C the samples with a lower R_a exhibit a lower MQE. The improvement is ascribed to a reduction of the interstrand thermal resistance. The curve of MQE of sample A shows no transition, similar to sample LHC 01 - F.

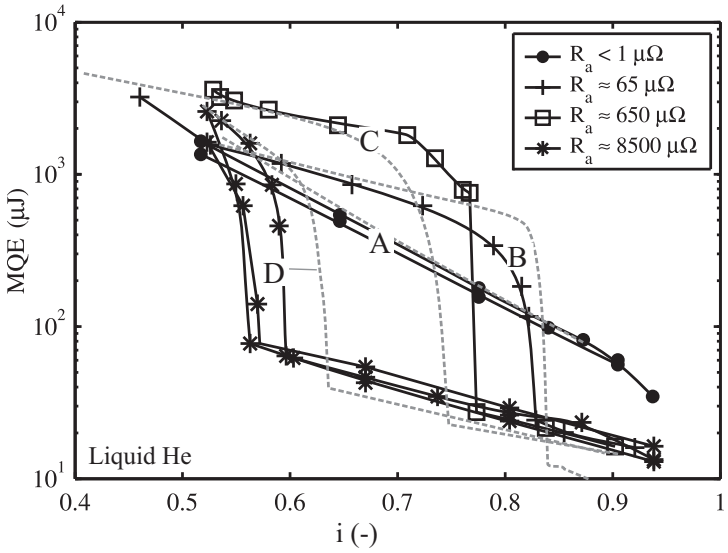

Figure 6.23: Measured and calculated MQE versus normalized cable current on center heaters of samples SIS 300 dipole - A to D. Liquid helium cooling at $T = 4.3$ K, $B = 6$ T and $I_c = 15.3 \pm 0.3$ kA.

In table 6.8 the calculation parameters for the four cables are listed and the simulation results are shown in figure 6.23. The measured and calculated i_{kink} are within ± 5 % for the four samples.

The increase in R_a is accompanied by an increase $F_{int,a}$, although the coupling is not very strong, see section 4.1.

Due to the strand oxidation also $F_{int,c}$ can be changed, but the influence of $F_{int,c}$ is small, since adjacent propagation of the normal zones dictates MQE.

For sample A, the correction factors F_{VHe} and F_{AHe} of 0.7 account for the reduction in helium volume and touching surface, due to the solder material.

Table 6.8: Calculation parameters of sample SIS 300 dipole - A to D.

	T	B	R_a	R_c	a_K	$F_{int,a}$	$F_{int,c}$	b	F_{VHe}	F_{AHe}
	K	T	µΩ	µΩ	W/m^2/K^4	W/m^2/K^{b+1}	W/m^2/K^{b+1}	-	-	-
A	4.3	6	0.1	20000	300	20000	500	1	0.7	0.7
B	4.3	6	65	20000	300	150	60	1.67	-	-
B	4.3	3	65	20000	300	250	100	1.67	-	-
C	4.3	6	650	20000	300	50	40	1.67	-	-
D	4.3	6	8500	20000	300	40	32	1.67	-	-

MQE variations across the cable width

The measured MQE curves for five heaters on one strand of sample SIS 300 dipole

- C at 4.3 K are displayed in figure 6.24a. The heaters are positioned at 0.5, 3.5, 7.5, 11.5 and 14.5 mm distance from the thick edge, for curves 1 to 5, respectively. The center heater number 3, clearly shows the highest position of i_{kink}.

The heaters at the thick and thin edges, numbers 1 and 5, show a reduction in MQE for i between 0.5 and 0.6 by a factor of 3 compared to the other curves. The low stability of both the thick and thin edge is explained by geometry factors, presented in section 2.5. At the thick as well as at the thin edge, the reduction of V_{He} and A_{He} and the increase of A_a is similar in size, therefore the heaters show similar MQE results.

The calculated MQE curves in figure 6.24b show a reduction for MQE towards the edges as well. However, the quantitative effects are not similar.

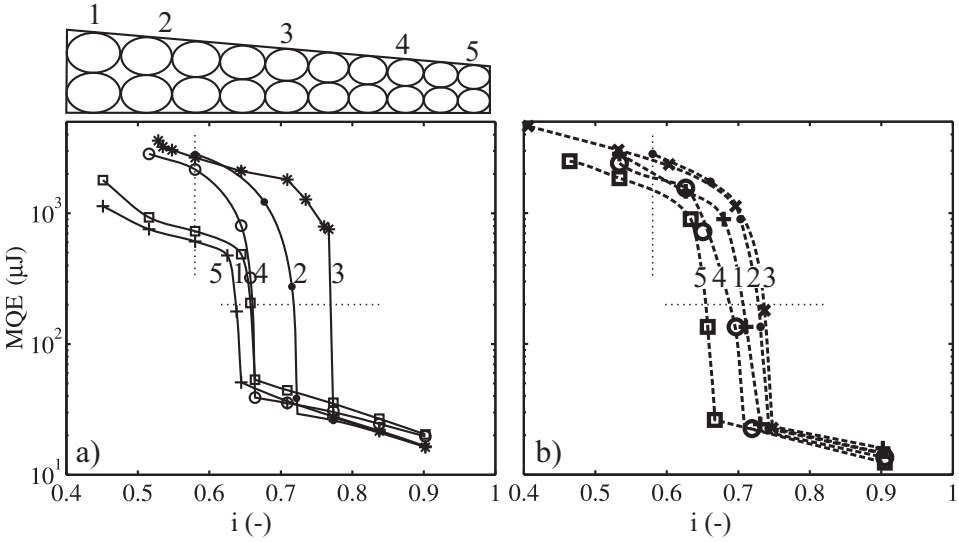

Figure 6.24: MQE as a function of i for 5 heaters positioned at five positions across the width of sample SIS 300 dipole - C, see the inset. a) Measured and b) calculated MQE. Liquid helium cooling at $T = 4.3$ K, $B = 6$ T, $R_a = 650$ $\mu\Omega$ and $I_c = 15.5$ kA.

In figure 6.25a i_{kink} is plotted versus the distance from the thick edge for the measured data and in b) for the simulation data. The value of i_{kink} is obtained from the intersection of the dashed lines and the curves in figure 6.24. Simulations clearly show that the propagation mode is *edge propagation*, see section 2.4.1. From the center heater, the normal zone propagates faster in the direction of the thin edge.

The direction of propagation is distinguished for each MQE data point, see figure 6.25a and b. Extrapolation of the measured as well as the simulation data shows that a heat pulse given at about 6.5 mm from the thick edge and 8.5 mm from the thin edge will propagate into its neighbor at the thin edge of the cable. The

non-symmetry is explained by the non-symmetry in the cable geometry. The value of A_{He} and V_{He} are reduced, see 2.5, decreasing the cooling at the thin side of the cable. Therefore the longitudinal normal zone propagation velocity is increased at the thin side of the cable.

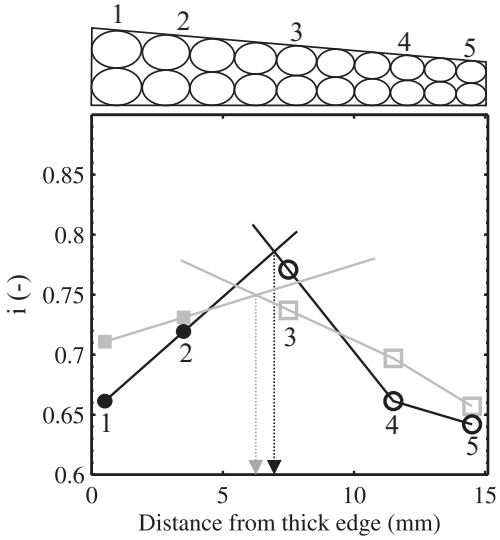

Figure 6.25: i_{kink} as a function of the distance to the thick edge for measurements (black lines and circles) and simulations (grey lines and squares). The solid squares and circles denote the positions that propagate into the adjacent strand at the thick edge at x = 0 mm, while the open squares and circles denote the positions that propagate at the thin edge at x = 15.1 mm.

At $i < 0.63$ the MQE is limited by APC II for all heater positions. The correlation between MQE at $i = 0.58$ and the adjacent contact surface as deduced in section 2.5.2 is shown in figure 6.26. A linear dependence of the MQE on the adjacent contact surface and the MQE is obtained. The simulation data shows a similar but less prominent relation.

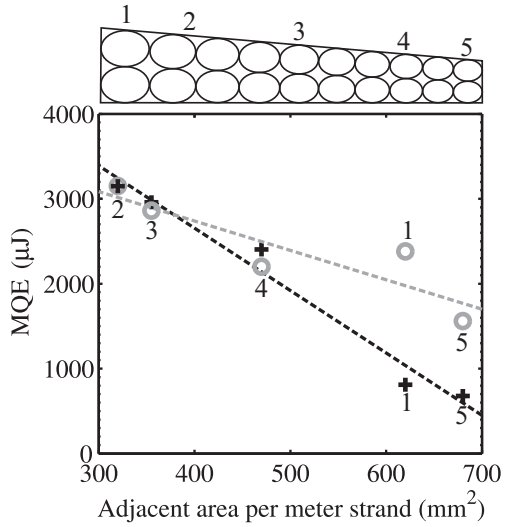

Figure 6.26: MQE versus the adjacent contact area at the heater position. The crosses show the intersection of the dashed line with the curves in figure 6.24a at $i = 0.58$. The black dashed line shows a linear fit of the data. The circles show simulation results, see figure 6.24b.

6.11 Conclusion

Experiments
A large number of MQE measurements on different cable samples are performed. Additional information is provided by local voltage and self-field measurements. The reported characteristic i_{kink} shows a wide spread between the samples. The value of i_{kink} for the samples, except for the adiabatic and soldered samples, are:

Sample type	Center heater	Thin edge heater
LHC 01, (4.3 K, 6 T)	0.65 - 0.82	0.50 - 0.69
LHC 01, (1.9 K, 9 T)	0.60 - 0.87	0.47 - 0.75
SIS 300 dipole, (4.3 K, 6 T)	0.56 - 0.83	-

The data from the soldered cables show no sharp transition and behave like a large single strand. The adiabatic cable shows a strong reduction in MQE and i_{kink}. In general a higher R_a and R_c gives a lower value of i_{kink}.

In some MQE measurements more than one sharp transition is seen, see figure 6.19. A recovering normal zone in more than one strand is seen indicating APC III as the decisive criterion.

An increase in magnetic field from 5 to 7.5 T shows an increase in i_{kink} from 0.76 to 0.86 for a center heater. The improvement is attributed to a reduction of Joule heating in a normal zone at similar i.

Calculations

For two heaters on one sample in two cooling conditions, the MQE curves, calculated by CUDI, are fit to measured MQE curves by varying the interstrand electrical and thermal resistance and the local cooling parameters. The qualitative as well as the quantitative changes of the MQE curve prove to be fit accurately, by varying the input parameters within the realistic values.

For the obtained curve fit, the decisive criteria are APC I, APC II, APC III and CPC I. The measured and calculated MQE curves match very well, thus providing strong support for the theoretical description of the stability mechanisms in chapter 2.

Calculations of local voltages and self-field show that CUDI provides an accurate description of the longitudinal and transversal normal zone propagation. The non-symmetric normal zone propagation across the cable width is shown in both measurements as well as calculations.

The accurate description of the measured data of MQE, local voltage and local self field validates CUDI for calculations on cable stability. The input parameters need to be well-known for an accurate calculation calculation of MQE.

Chapter 7

Impact of cable design on magnet stability

The stability of a cable in magnet operation conditions against short and local heat depositions is investigated with CUDI. *More specifically* LHC *dipole and* SIS *300 quadrupole magnets are analyzed.*

The MQE *is investigated as a function of magnetic field for three turns in the high magnetic field section of the* LHC *dipoles. In the case of the* SIS *300 quadrupole magnets the* MQE *is investigated as a function of* dB_a/dx *for the turn in the peak field. The position and volume most vulnerable to a heat deposition are discussed.*

The effect of non-uniform currents in the cable on the local stability is investigated.

Possible ways of improvement of stability at the least stable position in the cable, the thin edge are presented. This includes improving the cooled surface at the edge and reducing the interstrand heat exchange at the edge, are presented. Simulations show the effect for superfluid and supercritical helium cooled magnets.

The stability of cables with alternating superconducting and normal conducting strands is investigated as well.

Finally, a scheme for the design of cables with optimum stability is presented.

7.1 Stability of cables in magnets.

The large amount of training quenches in the LHC shows that the understanding of stability in magnets is poor. Training quenches are often caused by conductor movement. During operation with a high energy beam, beam loss is an additional source of heat. However, the precise extent, time development and location of an energy deposition is still unknown, see section 2.1. Not only the cause of heat generation, but also the effect of heat deposition on the stability of the magnet is poorly understood. In this chapter the MQE levels are calculated for LHC dipole and the SIS 300 quadrupole magnets.

Previous chapters focused on understanding stability of cables in the experimental set-up. By systematic comparison of measured MQE curves with calculations, the simulations of the software package CUDI has been validated and cable stability mechanisms have been investigated. However, the variations in magnetic field across the cable width and along the cable length are different for cables applied in magnets compared to cables tested in the experimental set-up. T_{margin} and I_c vary across and along the cable accordingly, compare figure 2.13 with figure 3.3. The cable test set-up can therefore not represent in a satisfactory way the cable in magnet operation conditions as discussed in chapter 6.

In this section, the effects of the heat deposition volume on the stability of a cable in magnet operation conditions are investigated. A set of volumes of heat release, that represent heat depositions from strand movement and beam loss, are formulated. With CUDI the MQE for each case is calculated as a function of B_a and dB_a/dx. Cables in the LHC main dipole and the SIS 300 quadrupole are investigated, representing magnets cooled with superfluid and supercritical helium and slow and fast ramping magnets, respectively.

The samples are measured with a fixed applied field and constant I_c. Therefore the MQE curves are visualized as a function of I/I_c. For magnets however I_c varies strongly with the operating current and MQE is represented as a function of B_a or dB_a/dx.

7.1.1 Heat deposition volumes

The highest energy deposition from beam loss in accelerator dipole magnets is expected in the midplane of the magnet [23], i.e. near turn 26 for the LHC dipole magnet, see figure 1.3. The highest energy deposition is closest to the beam pipe at the thin edge of the cable, corresponding with the highest field, the lowest T_{margin}, the lowest I_c and the lowest amount of helium coolant. Therefore the thin edge of the cable is expected most vulnerable to thermal instability. Four volumes are defined to describe possible heat depositions from beam loss, which are labeled 1 to 4 and described in table 7.1 and visualized in figure 7.1.

Training quenches are generally attributed to strand movement most likely in the center position of the cable, see section 2.1. The cases labeled 6 to 8 represent three different strand volumes with lengths varying from a few mm to half a twist pitch.

Table 7.1: Definition of 8 volumes of heat deposition for cables in magnets

Case	Description	Lenght (mm)		Volume (mm^3)	
		LHC	SIS 300	LHC	SIS 300
1	Smallest volume at the thin edge of the cable	3.9	2.8	3.6	1.6
2	Volume at the thin edge in 4 strands	3.9	2.8	25.4	10.9
3	Volume at the thin edge in 8 strands	7.9	5.6	83.5	35.7
4	Full cable width with length $10/N_s{*}l_p$	19.6	13.9	526.4	147.4
5	Smallest volume at the thick edge of the cable	3.9	2.8	3.6	1.6
6	Smallest volume at the center of the cable	2.0	1.4	1.8	0.8
7	Volume in 1 strand at the center, length $5l_p/N_s$	19.6	13.9	18.2	7.8
8	Volume in 1 strand at the center, length $0.5l_p$	51.1	22.2	47.2	12.4

The smallest possible volume at the thick edge is labeled with number 5 and it completes the cases with the smallest volumes and therefore the lowest possible MQE, see table 7.1 and figure 7.1.

The eight cases are used to define a range of MQE for each cable sample.

A very short pulse duration of 10 μs is considered representing a transient heat deposition as expected from conductor movement or beam loss.

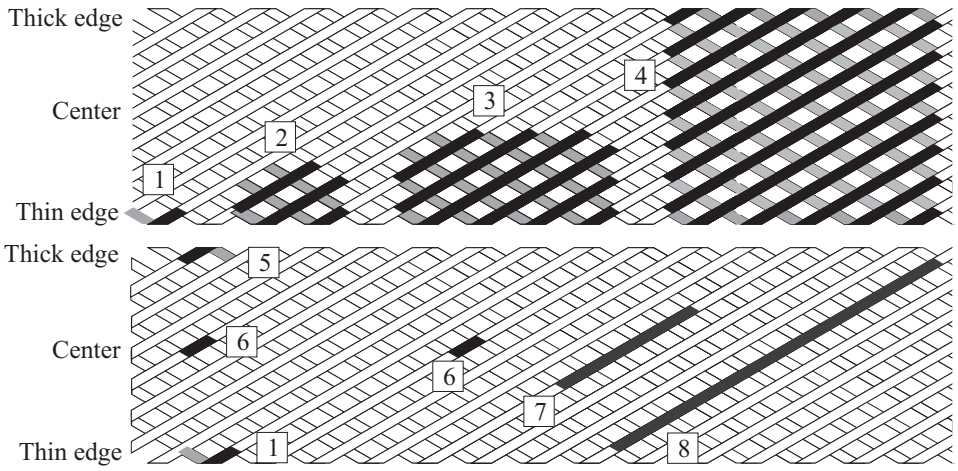

Figure 7.1: Visualization of the 8 defined heated volumes for stability simulations.

7.1.2 Quench energy levels in LHC dipole magnets

In LHC dipole magnets each of the 40 turns is exposed to a different magnetic field and the local MQE of a cable section will vary accordingly. The inner and outer cables have different specifications and for both the MQE needs to be calculated.

In LHC magnets a part of the training quenches originates at the coil ends of the dipole [106]. Due to the bending of the cable, the cable geometry changes and due to sheer stresses the strands are tightened differently. It is nearly impossible

to specify the cable dimensions, resistances and cooling parameters in this area. Therefore the analysis here focuses on the straight part of the magnets.

Three turns of LHC dipole magnets are investigated in this section:

1 Turn 40, exhibiting the highest maximum magnetic field and the highest average magnetic field, see figure 1.3. Therefore it is expected to be most susceptible to heat depositions. At an aperture field of 8.33 T, the field varies from 8.6 T at the thin edge to 6.9 T at the thick edge.

2 Turn 26, subject to the highest beam losses. At an aperture field of 8.33 T, the field varies from 8.4 T at the thin edge to 3.1 T at the thick edge. The average and maximum magnetic field are lower compared to turn 40, there MQE is expected to be higher.

3 Turn 25, exhibiting the highest field in the outer layer, see figure 1.3. At B_a = 8.33 T, the local magnetic field varies from 7.5 T at the thin edge to 6.0 T at the thick edge.

The cable in turns 26 and 40 is of the type LHC 01 and in turn 25 the cable is of type LHC 02. The main characteristics of the cables are listed in table 1.4.

The transfer function B_a/I of the LHC dipole magnet is 0.706 T/kA. At the start of a heat deposition the current distribution is uniform and the cable temperature is 1.9 K. The inner voids between the strands are filled with superfluid helium, while the outer voids are filled with Kapton insulation. To simplify the simulations F_{int} is taken independent of the magnetic field, in contrary to the findings in section 4.1.

With CUDI the MQE is calculated for the eight cases as defined in section 7.1.1 for turn 40. In figure 7.2 the MQE curves as a function of the magnetic field are displayed. The lower limits of the curves are the most important for estimating magnet stability. For turn 40, the lower limits are defined by cases 1, 2 and 3. As expected, the lower limits are completely defined by heated volumes located at the thin edge.

The shape of the curves in figure 7.2 for the different cases is discussed:

- **Cases 1 to 4**
  Calculations for cases 1 to 4 comprise heat depositions at the thin edge of the cable, see figure 7.2a. At 9.2 T the stepwise change from 200 to 8 μJ indicates the transition to the single strand stability regime for case I. In analogy to i_{kink} we can define $B_{a,kink}$ at the intersection between APC I and APC II.
  In figure 7.2d, the MQE per unit volume is plotted. At high B_a, the MQE/V is independent of the heated volume, indicating that APC I applies for all cases, and the thin edge has the lowest MQE. For case 4, no kink is visible, since all the strands in the cable are heated and current distribution can play no role. For cases 1 to 3 curves deviate from case 4 at $B_{a,kink}$. Therefore the impact of $B_{a,kink}$ can be described as: for $B_a < B_{akink}$ current redistribution improves the cable stability; for $B_a > B_{akink}$ the enthalpy margin is decisive for quench. Above $B_{a,kink}$ of case 1, the cases 2, 3 and 4 exhibit a higher MQE due to the larger volume, but MQE/V is similar for all cases.

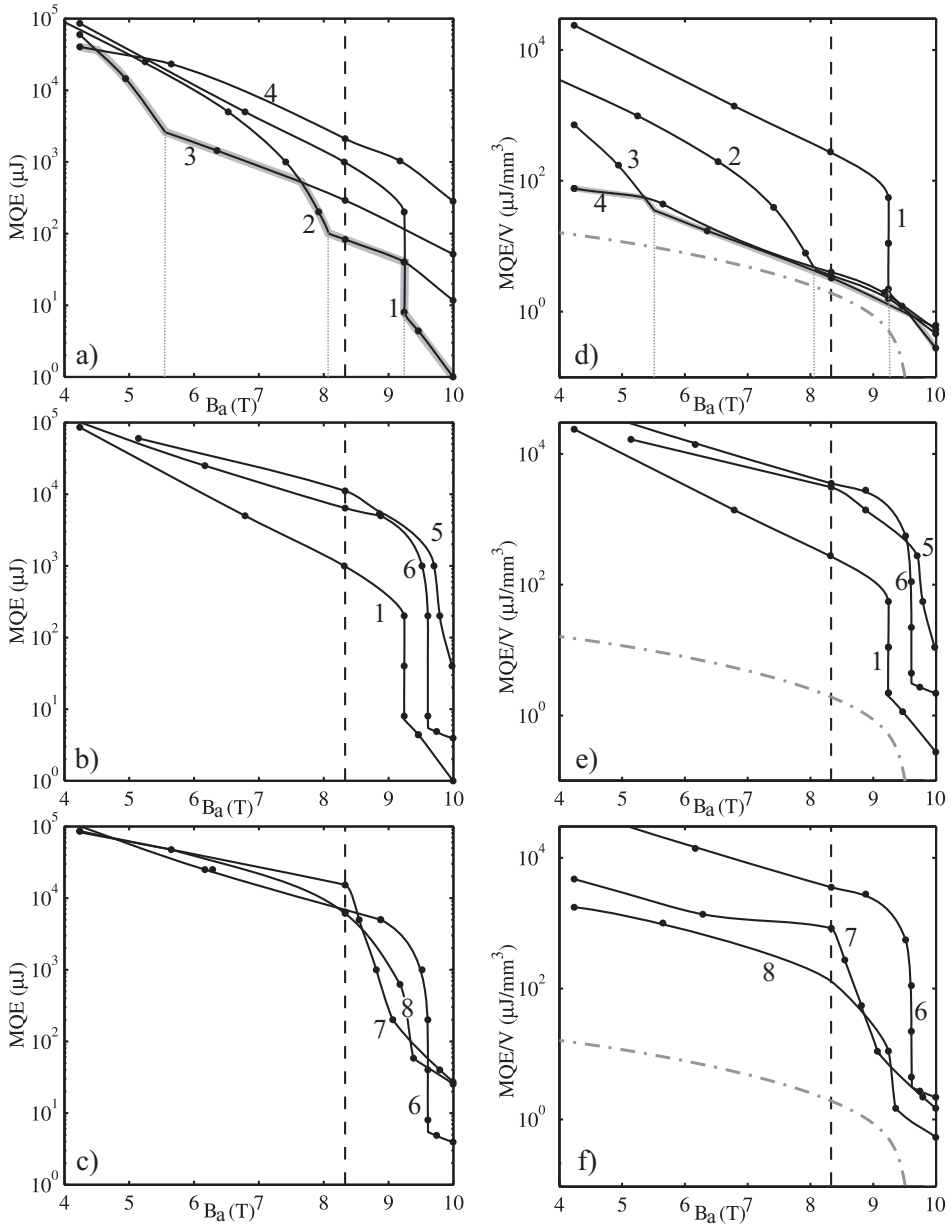

Figure 7.2: In a), b) and c) MQE and in d), e) and f) MQE per unit volume as a function of B_a in LHC turn 40 for the eight cases defined in section 7.1.1. B_a/I = 0.706 T/kA, T = 1.9 K. The design operation field is at 8.33 T. The dash-dotted line in d), e) and f) shows the enthalpy margin of the conductor at peak magnetic field [107].

$B_{a,kink}$ is at 9.2, 8.1 and 5.6 T for cases 1, 2 and 3, respectively. The lowest MQE as a function of B_a is defined by all four cases, see the thick gray line in figure 7.2a.
Case 4 shows a higher MQE/V than the shown enthalpy margin of the conductor, since helium cooling increase MQE.
Case 2 is the worst case for LHC dipole magnets at the operation magnetic field of 8.33 T. Since a realistic heat deposition from beam loss may cover more than one strand at the edge, case 2 is a realistic case, showing an MQE of only 90 μJ, with MQE/V of about 4 μJ/mm^3.

- **Cases 1, 5 and 6**
  MQE and MQE/V as function of B_a for the smallest heated volumes, cases 1, 5 and 6, show a very steep curve between 9 and 10 T, see figures 7.2b and e. $B_{a,kink}$ is lowest for case 1, since it is located in the highest magnetic field position of the magnet. Case 5, at the thick edge, has a slightly higher $B_{a,kink}$, compared to the center position, although B is much less. Since the volumes are only slightly different, the MQE/V curves look very similar.
- **Cases 6 to 8**
  The MQE for cases 6, 7 and 8 are almost the same below 8.33 T, and with rather high values between 10^4 to 10^5 μJ, see figure 7.2c. The value of $B_{a,kink}$ is 9.1, 9.4 and 9.6 T for cases 7, 8 and 6, respectively. The reason for the higher value of $B_{a,kink}$ for case 8 compared to case 7 is the fast redistribution of current due to the instant appearance of a normal zone in the strand over half a twist pitch.
  In figure 7.2f the MQE/V curves show the highest value for case 6. Case 8 exhibits the lowest value of MQE for most of the range of B_a, since the volume comprises a section close to the thin edge in the high-field region.

At low magnetic field and therefore low current, the curves merge to a narrow band of MQE. The QDM is relatively high and the heat from the heat pulse spreads over the cable width. Joule heating is reduced compared to higher cable currents, while the input pulse energy is increased. The stability mechanism is therefore dominated by the thermal input of the heat pulse.

In general cases 1 and 2 define most of the lower limits of MQE. Therefore the most susceptible point in the straight section of a dipole magnet is the thin edge.

In a similar approach the MQE curves for LHC dipole turns 25 and 26 are calculated. The analyzed cases can be compiled by drawing the enclosed area of all MQE curves, see figure 7.3. The lower boundary of the areas show the minimum of MQE for all cases in all magnet turns. The lower boundary is generally defined by cases 1, 2 and 3 for each turn. The upper boundary provides the quench energy that is sufficient to quench the cable, and therefore the magnet, for all heat deposition cases.

The enthalpy margin of the conductor, defined by $\int_{T_{bath}}^{T_c} C_p dT$, is a widely used measure for stability. The enthalpy margin and the MQE/V in case 4 for turn 40 are multiplied by the heated volume of case 1 with a length of 3.9 mm and added to figure 7.3. The MQE/V in case 4 can be regarded as the enthalpy margin including

the helium cooling.

At $B_a = 8.33$ T, the lowest MQE is 20 μJ calculated with the enthalpy margin including helium and 90 μJ calculated with CUDI. The detailed analysis with CUDI reveals a 4 times higher MQE. At B_a is 4, the difference increases to a factor of more than 100. Therefore the enthalpy margin is not suitable for calculating MQE, but a detailed analysis, including current redistribution calculations, gives a satisfactory estimate of cable stability.

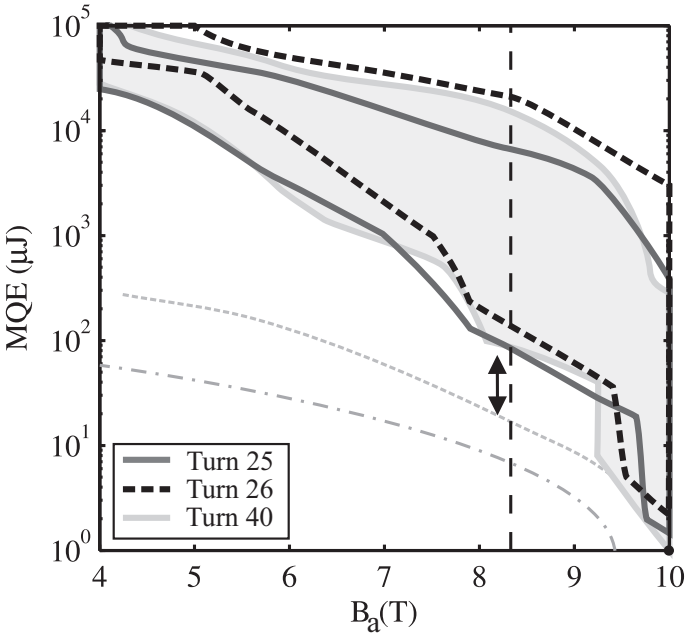

Figure 7.3: Area encompassing the MQE curves for all eight heated volume cases defined in section 7.1.1 for LHC main dipole magnets in turns 25, 26 and 40. The dash-dotted line and the dashed line indicate the enthalpy margin (no He included) of the conductor [107] and the MQE/V in case 4 multiplied by the heated volume in case 1 (with He in voids), respectively.

The areas encompassing the MQE per unit volume for the LHC dipole magnet turns 25, 26 and 40 are shown in figure 7.4. The lower limitations of the areas show the enthalpy margin given by case 4 in each magnet turn.

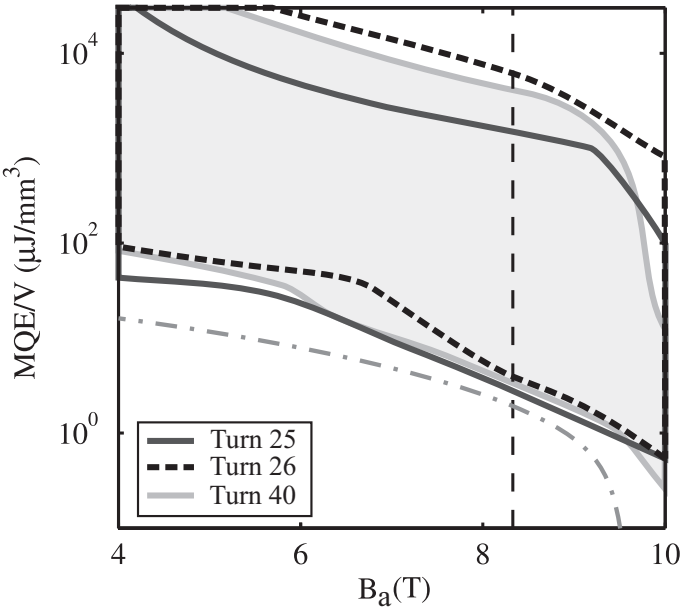

Figure 7.4: Area encompassing the MQE per unit volume curves of all eight heated volume cases defined in section 7.1.1 for LHC main dipole magnets in turn 25, 26 and 40. The dash-dotted line indicates the enthalpy margin of turn 40 at peak magnetic field [107].

Turns 27 to 39 will exhibit MQE values between the curves calculated for the turn with minimum and maximum magnetic field, turns 26 and 40, respectively. Turns 1 to 24 will exhibit higher MQE and enthalpy margincompared to turn 25, as they are positioned in a lower overall magnetic field.

The training quenches in LHC dipole magnets below 8.33 T can only be triggered by local energy depositions larger than about 90 μJ. The estimated energy release in figure 2.2 shows an energy density of up to 20 μJ/mm^3. Comparing this level with figure 7.4, training quenches can be expected at fields above $\approx$ 6.5 T. However, this value can only be used as a rough estimate. With the mild slope of the calculated curve in figure 7.4 the error margin in field is more than 10 %.

The training quenches in one of the LHC octants comprising 154 dipole magnets, see figure 1.7, started above 7 T and the number of training quenches rapidly increased above 7.5 T. It shows that the estimate is useful for prediction of the probability of training quench.

7.1.3 Quench energy levels in SIS 300 quadrupole magnets

The design of the concept cable for the SIS 300 quadrupole magnets is recently agreed upon [108]. The cable with 19 LHC 02 strands with a diameter of 0.825 mm

has stainless steel core to increase R_c to the desired level > 10 mΩ. Due to the requirements of CUDI the cable is scaled in simulations to an even number of 18 strands. The width, the current, the number of strands and the thickness at the thick edge of the cable are reduced by a factor of 18/19. The strand parameters and the thickness of the cable at the thin edge are not changed. The design magnetic gradient of the aperture is 45 T/m, at a cable current of 6220 A. Turn 20, see figure 1.3b, is exposed to the highest magnetic field of 3.6 T at the thin edge and 3 T at the thick edge at the design magnetic gradient.

The main characteristics of the cable are listed in table 7.2.

Table 7.2: Characteristics of the cable in a SIS 300 quadrupole magnet as used in simulations

Parameter	Unit	Value
N_s	-	18
d_s	mm	0.825
R_c	$\mu\Omega$	10000
R_a	$\mu\Omega$	200
RRR	-	200
Cu/SC ratio	-	1.95
Cooling	-	Supercritical helium
$(dB_a/dx)/I$	$\mathrm{Tm^{-1}kA^{-1}}$	7.64

To characterize the stability of the SIS 300 quadrupoles, a similar approach as for the LHC dipoles is taken. With CUDI the MQE is determined for the eight cases as described and depicted in section 7.1.1. In figure 7.5 the MQE curves are displayed.

The variations between the different cases is in general qualitatively similar to the variation for the LHC dipole cable, see figure 7.2.

Above $dB_{a,kink}/dx$ of 47 T/m, case 1 shows the lowest MQE, similar to the LHC dipole cable. With a design operation gradient of 45 T/m, $dB_{a,kink}/dx$ is only a few percent higher than the operation gradient. The MQE above $dB_{a,kink}/dx$ suddenly decreases by a factor of about 8. Therefore it is likely that many magnets at operating gradient are in stability regime I, the single wire stability regime.

Above $dB_{a,kink}/dx$ a temperature increase in one strand over a length of a mm to above T_c would lead to a quench of the magnet. Therefore the magnet is very vulnerable to a heat deposition of any volume.

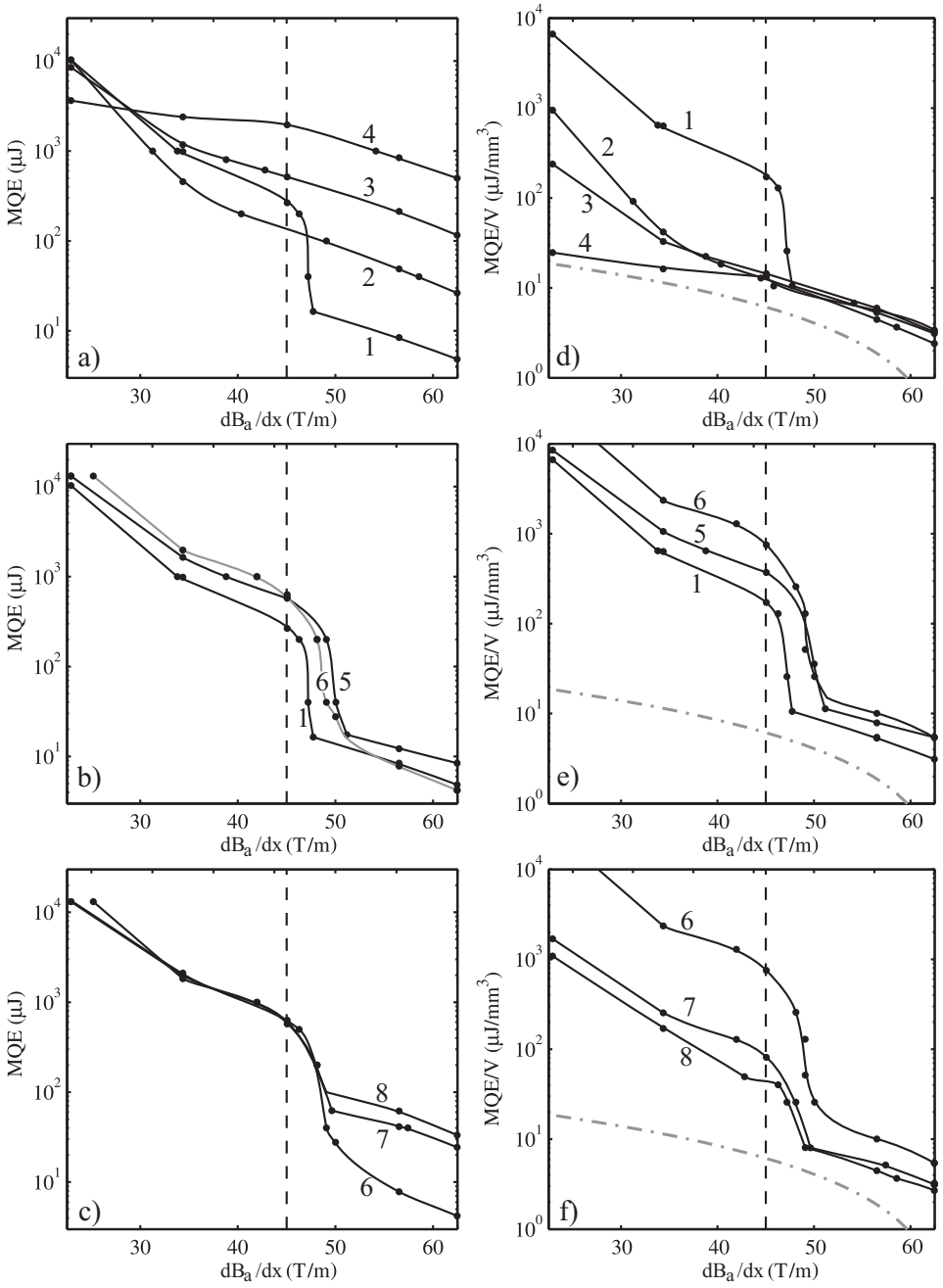

Figure 7.5: In a), b) and c) MQE and in d), e) and f) MQE per unit volume as a function of dB_a/dx in SIS quadrupole turn 20 for the eight cases. The dash-dotted line in d), e) and f) shows the enthalpy margin of the conductor at peak magnetic field [107].

7.2 Effect of non-uniform current distribution on stability

A superconducting cable is usually connected to current leads or other magnets in series by a soldered connection. A fast current ramp in a fully transposed cable forces the current to spread uniform over the strands. However, current redistributes to a condition with minimum voltage across the cable depending on the total resistance of each current path. For superconducting cables the resistance is dominated by the cable joint, thus a non-uniform joint causes non-uniform current distribution in the cable. Measurements of the self field along sample LHC 01 - C with a non-uniform joint shows a non-uniform current distribution, see section 3.4.3.

The MQE of this sample is measured at the center position in stability regime I. With a know I_c as a function of MQE the current in each strand is deduced. In figure 7.6 the current in each strand is shown and the average current per strand is 570 A. The maximum current in a strand is about 760 and the minimum current is about 190.

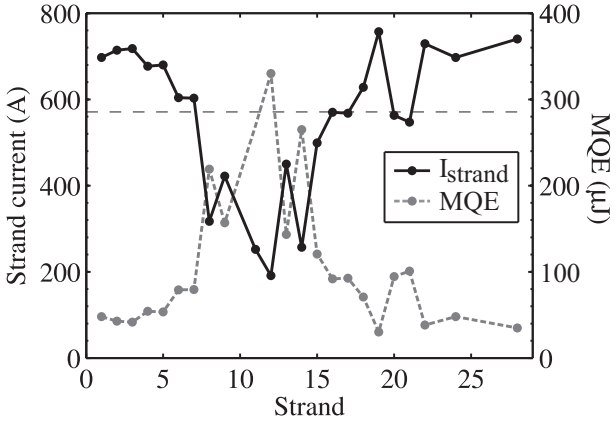

Figure 7.6: Measured MQE and deduced current for the 28 strands of sample LHC 01 - C for a total current of 16 kA. The dashed line indicates the average current per strand. For 5 strands the MQE was not measured.

The MQE curves are measured for the strands with a low and a high current, strands 3 and 12 in both normal liquid and superfluid helium, see figure 7.7. It shows a large overall reduction of MQE for the strands with the high current. The reduction of I_{kink} is not only due to the increased current in the heated strand, but as well due to the high current in the neighboring strands 2 and 4.

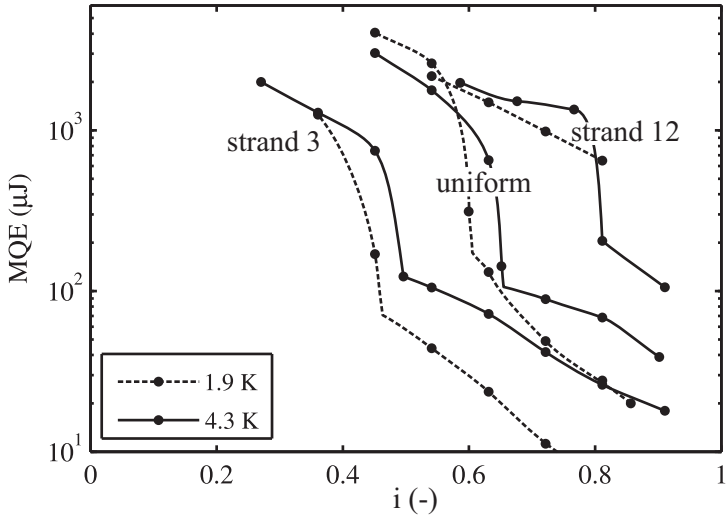

Figure 7.7: Measured MQE as a function of i for strand 3 with high current and strand 12 with low current at 1.9 K at 9 K and 4.3 K at 6 T. The measured MQE for the same sample with uniform current distribution is obtained after improving the joint.

To investigate the effect of current distribution on MQE by means of simulations, the following well-defined case is assumed:
The soldered joint has a high resistance and the contact length with the current lead $\neq nl_p/2$. The resistance between the current lead and each strand depends on the contact length of the strand. The strand contact length has a triangular pattern, therefore the current distribution is triangular. A sinusoidal pattern of current with a normalized amplitude of 0.1 is assumed, thus the highest strand current is 10 % higher than the average strand current. Using CUDI the MQE is calculated for the eight cases as described in section 7.1.1. The center of the heated volume is always located at the strand with the highest current to find the lowest MQE value. The simulations are performed for the LHC dipole turn 40 and the SIS 300 quadrupole turn 20.

In figure 7.8 the areas encompassing the MQE curves for the LHC dipole turn 40 are shown for both the uniform and non-uniform current distribution. Above 7 T, the main difference is a reduction of B_{kink} by 0.3 T. For fields below 7 T, the curves for non-uniform and uniform current distribution are rather similar, as heat flow to neighboring strands is more important than current redistribution.

Small non-uniformity of the current ($\pm$ 10 %) is still acceptable for LHC dipoles, since $B_{a,kink}$ is larger than the operating magnetic field. Large non-uniformity ($>\pm$ 30 %) means a reduction of $B_{a,kink}$ below operating magnetic field and the magnet is more sensitive to small heat depositions from beam loss an strand movement.

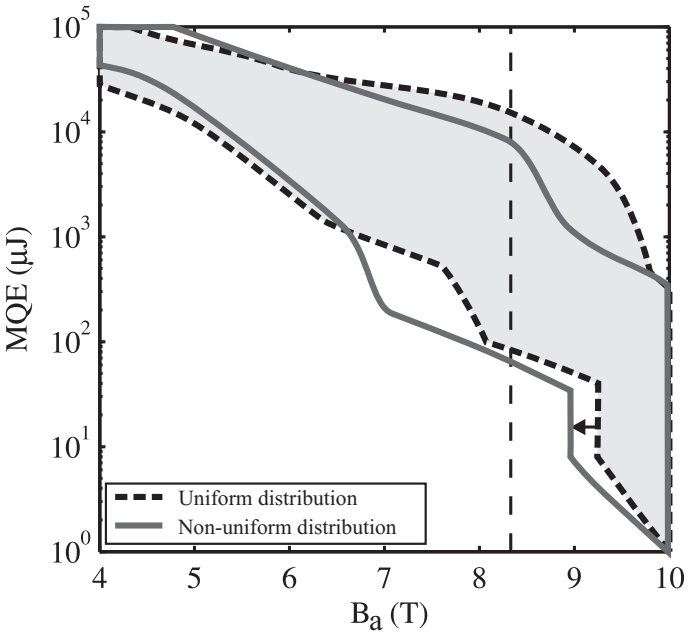

Figure 7.8: Area encompassing the MQE curves of the eight cases for the LHC dipole magnet turn 40 for a uniform and a ± 10 % non-uniform current distribution. For the non-uniform distribution, the MQE is determined for the location with the highest current.

In figure 7.8 the area encompassing the MQE curves for the SIS dipole turn 20 is shown for both the uniform and non-uniform current distribution. The most important difference between the uniform and non-uniform current distribution is the decrease in $dB_{a,kink}/dx$ of 3 T/m. The variation is significant, since $dB_{a,kink}/dx$ is reduced below the operation magnetic field gradient for case 1. With a small normal zone at the thin edge in only one strand, the magnet will quench at operation magnetic field, posing a large risk of multiple quenches during operation with a high energy beam. The example is a nice demonstration that a magnet, relatively safe for a uniform current distribution, can become unsafe in the case of ± 10 % current deviation per strand. Bad splices and other reasons of non-uniformities have to be considered and a proper margin needs be respected.

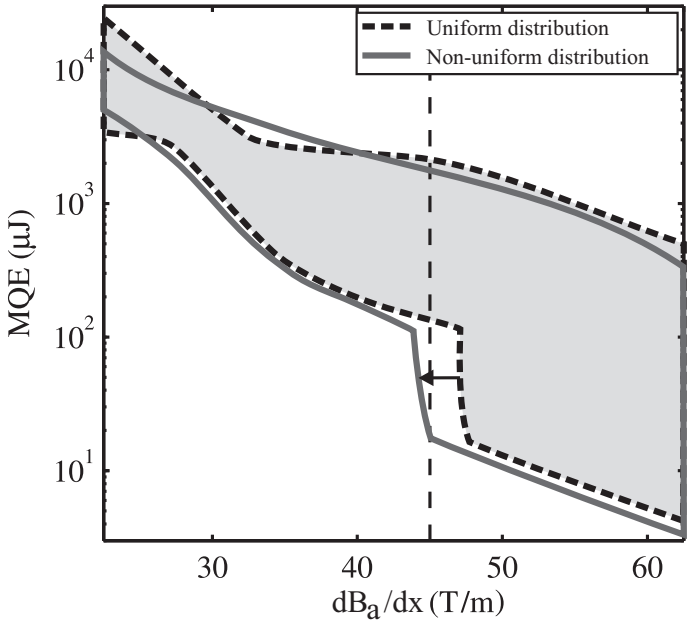

Figure 7.9: Area encompassing the MQE curves for the eight heated volume cases defined in section 7.1.1 for the SIS quadrupole turn 20 with a uniform and a ± 10 % non-uniform current distribution.

7.3 Core versus highly resistive coating

In the design of cables for fast ramping magnets the limitation of AC loss requires a relatively high R_c, while R_a can be much lower. A high R_c is obtained either with a highly resistive coating or by applying a highly resistive core between the layers of the cable. An important difference between these solutions is the control of R_a. For a non-cored cable R_a is related to R_c and typically higher than R_c. In a cored cable on the contrary, the value of R_a can be controlled separately from R_c by the strand coating. In the design of the cables for the SIS 300 quadrupoles both the cored as the non-cored cables were considered. In 2008 a decision is made to choose the cored cable design based on the simulation results as shown in this chapter.

In this section the effect on stability of two specific designs of the cables for SIS 300 quadrupole magnets is investigated. The minimum required values for R_a and R_c are 200 and 10000 $\mu\Omega$, respectively. For the non-cored cable a high resistive coating is necessary, like Ni of Cr [109], R_a and R_c are assumed to be equal to 10 mΩ. For the cored cable R_a and R_c are taken 200 $\mu\Omega$ and 10 mΩ, respectively.

In section 4.2 the characteristic current redistribution patterns are discussed. It was shown that the current redistribution is faster for both a reduced R_a and R_c. Therefore in the non-cored cable with a highly resistive coating the expected

current redistribution is much less, due to the high R_a and high R_c. For the cored cable a much faster current redistribution is expected due to the reduction of R_a by a factor of 50. Since fast current redistribution is the main mechanism for improving cable stability, it is expected that a cored cable provides better stability compared to a non-cored cable.

The case of a cable in the highest field position of the SIS 300 quadrupole is described as accurately as possible. In the most recent design the cable consists of 19 strands of the type SIS 300, specified in table 1.2. The main cable specifications are found in table 1.4. CUDI requires an even number of strands, therefore the cable is scaled to 18 strands, as discussed in 7.1.3.

The cable is cooled with supercritical helium at a temperature of 4.5 K. Helium is present in the inner voids, whereas the outer voids and the thick and thin edges are assumed to be covered with insulation material.

In the cored cable, part of the voids is occupied by the 25 μm thick core and the helium volume is reduced. The reduction in volume is about equally distributed over the outer and inner voids. A 25 μm core encompasses about 2 % of the total envelope volume. With an inner free volume of about 5 % of the total envelope volume, the actual helium volume in the cable is 20 % less in the cored cable compared to the non-cored cable. The variation in A_{He} is difficult to estimate. To approximate the effect of a core a correction factor of 0.8 is applied, similar to V_{He}.

The interstrand thermal conductance in the adjacent direction varies between the cored and non-cored cables due to surface contact variations. However, the thermal resistance of the proposed Ni coating is not known and its influence is therefore neglected in this simulation. The value of $F_{int,a}$ is set to 400 $\mathrm{WK^{-1}m^{-(1+b)}}$. In the cored cable, the heat transfer between the crossing strands is reduced, due to the core. As discussed in section 4.1 the compensation factor $F_{int,c}$ for the cored cable is taken a factor of 5 lower than $F_{int,a}$.

The cases defined in section 7.1.1 are analyzed. In figure 7.10 the calculated MQE for non-cored cable design for the eight cases is shown. The simulation results for the cored cable, as is the design choice, are already shown in section 7.1.3.

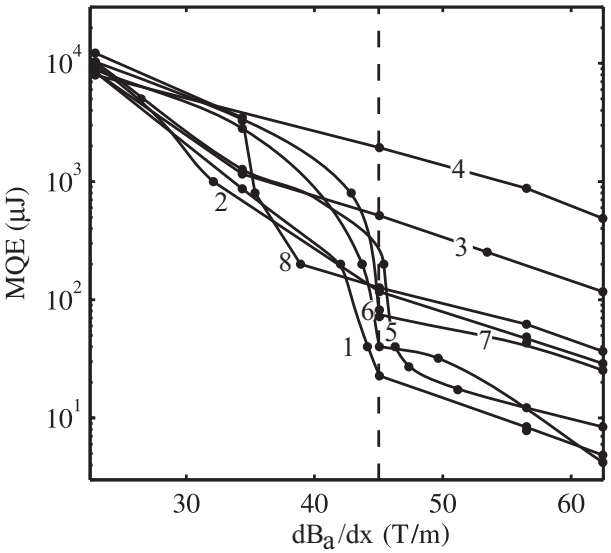

Figure 7.10: MQE as a function of dB_a/dx in SIS 300 quadrupole turn 20 for the cable design with a highly resistive coating. The numbers indicate the eight cases defined in section 7.1.1.

The most important characteristic of case 1, $dB_{a,kink}/dx$ is about 45 T/m. With a normal zone in one of the strands for a short length of about 2.8 mm at the edge section, the quench of the magnet is unavoidable. For cases 5 and 6, $dB_{a,kink}/dx$ is at almost the same value. Operation at 45 T/m would jeopardize quench-free operation of the magnet, and therefore the stable operation of the entire accelerator. A maximum stable operation of the magnet is expected from the presented curves at about 35 to 40 T/m.

The choice for a cored cable in SIS 300 quadrupoles shows the impact and necessity of stability analysis with CUDI.

In figure 7.11 the area encompassing the MQE data for the cored cable is compared with the area encompassing the data for the non-cored cable. It shows clearly that in the cable design with highly resistive coating $dB_{a,kink}/dx$, indicated by the arrow, shifts down by about 3 T/m or 6 % of operation field.

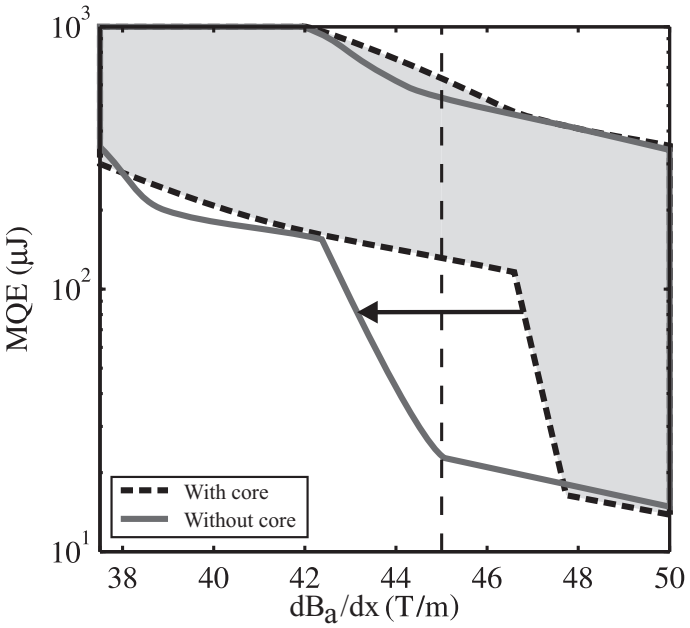

Figure 7.11: Area encompassing the MQE curves of the eight cases for SIS 300 quadrupole turn 20 for the cable design with a core and without a core. The arrow indicates the reduction $dB_{a,kink}/dx$ for the cable design without core.

At 45 T/m a strong increase in MQE by a factor of 6 is obtained by applying a core. The comparison between the MQE data as shown in this section has dominated the decision to adopt the cored cable design for the SIS 300 quadrupole magnets in November 2008.

7.4 Improvement of edge stability

The measurements shown in chapter 6 reveal a lower MQE in both edges for a homogeneous magnetic field distribution. Simulations performed for cables applied in the LHC and SIS 300 magnets, show the lowest MQE at the thin edge, due to higher local field, see section 7.1. From a stability point of view, the thin edge is therefore the weakest spot in the magnet.

Multiple causes contribute to the reduced stability at the thin edge:

- The magnetic field is highest at the thin edge, so that both the temperature margin and the critical current are reduced, see figure 2.13.
- The interstrand thermal conductance is higher at the edges of the cable, see chapter 4, causing more heating of initially cold strands next to the heated sections. Therefore in regime II and higher, the transverse normal zone propagation increases, resulting in a lower MQE, see section 4.4.

- The helium volume and the helium wetted surface are smallest at the thin edge, see section 2.5, reducing the cooling and hence MQE, see chapter 5.

Since the magnetic field pattern cannot be changed, two engineering options to improve the cable stability at the thin edge are: 1) Local reduction of the interstrand thermal conductance by applying a coating layer between the strands at the thin edge position and 2) the increase of the local helium contact at the thin edge by removing the Kapton layer. The LHC dipole turn 40 represents samples cooled with superfluid helium and the SIS 300 quadrupole turn 20 represent samples cooled with supercritical helium. Heated volume cases 1 to 4 are located directly at the thin edge and exhibit the lowest MQE and are therefore only taken into account.

7.4.1 Local reduction of the interstrand thermal conductance

A reduction of the interstrand thermal conductance reduces the transverse normal zone propagation, therefore improving the chances for recovery of normal strands. Reduction of the local interstrand thermal contact in a Rutherford cable is difficult to achieve. There are no examples yet of reducing the local interstrand thermal contact in a Rutherford cable. However, several options might be feasible without increasing the thickness of the cable too much at the thin edge. After cabling, the cable can be opened by a continuous process [84] and a thin, low conductive non-metallic coating may be applied. However, this concept needs further investigation since the space is limited and the coating needs to withstand high pressure. Local variation of the metallic coating might be insufficient for a proper decrease of the thermal conductance.

Simulations with CUDI are performed to reveal the maximum influence of a local coating on MQE by reducing the thermal conductance in the edge to 1 % of the original value. A local increase by a factor of 100 of R_a is a side effect. In figure 7.12 the position of the highly resistive coating is visualized. Simulations are performed for a superfluid helium cooled LHC 01 cable in turn 40 of the LHC dipole magnet for comparison with the simulation results in section 7.1.2 and for a supercritical helium cooled cored SIS 300 cable in the SIS 300 quadrupole magnet for comparison with the simulation results in section 7.1.3.

Figure 7.12: The black lines and black surface visualize the location of a highly resistive coating at the thin edge of the cable.

In figure 7.13 the areas enclosing the simulated MQE values for cases 1 to 4 are shown for LHC turn 40 in the normal condition, as described in section 7.1.2, and the case with the locally reduced interstrand thermal contact conductance F_{int}.

$B_{a,kink}$ is slightly increased by 0.15 T %. At operating field no significant variation in MQE is observed.

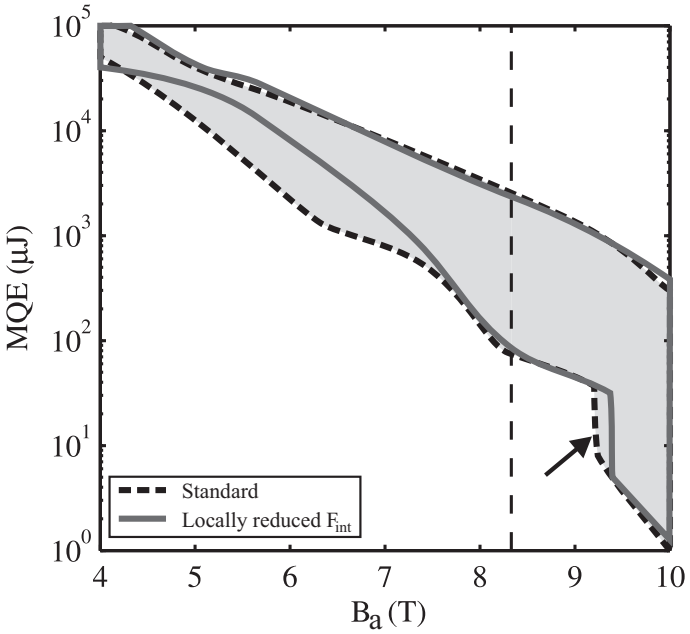

Figure 7.13: Area encompassing the MQE curves of for cases 1 to 4 for LHC dipole turn 40 for the standard cable design and the adapted design with local decrease of $F_{int,a}$ at the thin edge.

In figure 7.14 the area enclosing the simulated MQE values for cases 1 to 4 are shown for SIS 300 quadrupole turn 20 in the normal condition, as described in section 7.1.3, and the case with the locally reduced interstrand thermal contact conductance $F_{int,a}$. $B_{a,kink}$ is increased significantly by 4 T/m. Due to the local reduction of $F_{int,a}$ at the edge, the margin of $B_{a,kink}$ is strongly reduced. Therefore the research to implement low thermal conductance at the thin edge is promising and worthwhile to investigate further.

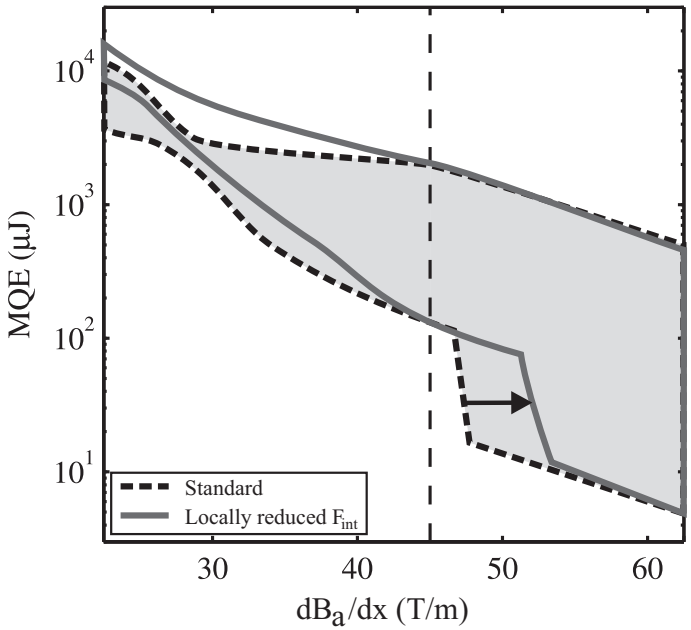

Figure 7.14: Area encompassing the MQE curves for cases 1 to 4 for SIS quadrupole turn 20 for the standard cable design and the adapted design with the local decrease of $F_{int,a}$ at the thin edge.

7.4.2 Local removal of the insulation at the thin edge

For the purpose of steady-state cooling some designs incorporate helium channels in the insulation covering the thin edge, see figure 7.15 [110]. The increased helium surface combined with the enhanced flow of supercritical helium improves the overall cooling of the cable. Since helium cooling improves also the transient stability, the effect of helium slots is investigated.

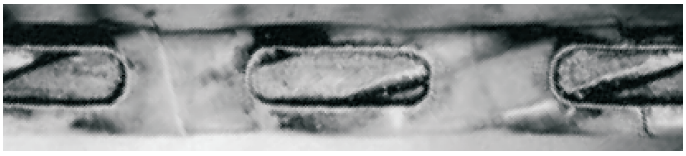

Figure 7.15: Photograph of helium slots at the thin edge of a cable from [110].

The maximum thin edge surface per strand is roughly determined by the cable thickness at the edge multiplied by l_p/Ns. The maximum additional cooled surface is 6.2 mm^2 for an LHC 01 cable and 4.0 mm^2 for a SIS 300 quadrupole cable, respectively. By adding this surface to the inner surface found in figure 2.32, the

local value for A_{He} increases by a factor of about 10 for the LHC 01 cable and SIS 300 quadrupole cable. Therefore, the local cooling can be improved by a factor of 10, resulting in a cooling at the thin edge, which is up to three times higher compared to the center of the cable.

A second advantage of removing the insulation is the large volume of helium that can be addressed for cooling. In superfluid helium, the cooling might resemble open bath conditions and in a forced flow of supercritical helium, the helium may be refreshed constantly, thus improving the effective volume of helium strongly. For the simulations a fixed volume of helium is chosen with a thickness of 0.5 mm, increasing the total volume of helium by a factor of 2.

Even when the impact on MQE is small, the impact on magnet stability can be significant, since the additional steady state cooling by helium channels ensures a more stable and reduced temperature of the cable at the thin edge.

The simulation results for the cable in LHC dipole turn 40 are shown for the standard design, as discussed in section 7.1.2, and the sample with additional helium cooling at the thin edge. The increase in MQE at 6 T is a factor of 5 and the shift in $B_{a,kink}$ is about 0.3 T. At the operation field of 8.33 T, the difference in MQE is not significant.

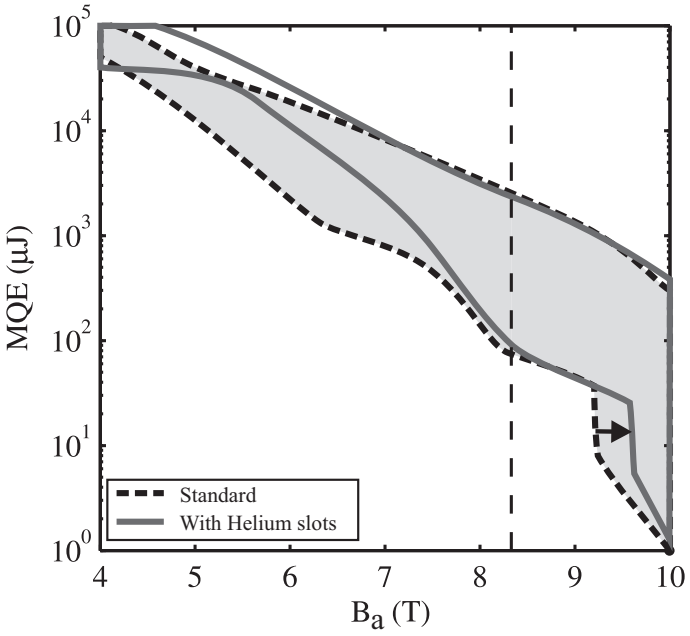

Figure 7.16: Area encompassing the MQE curves of for cases 1 to 4 for LHC dipole turn 40 for the standard cable design and the adapted design with helium slot at the thin edge of the cable.

The simulation results for turn 20 in the SIS quadrupole are shown for the standard sample, as discussed in section 7.1.3, and the sample with additional helium cooling at the thin edge. The increase for $B_{a,kink}$ is less than 1 T/m. At the operation magnetic field gradient of 45 T/m, the difference in MQE is not significant.

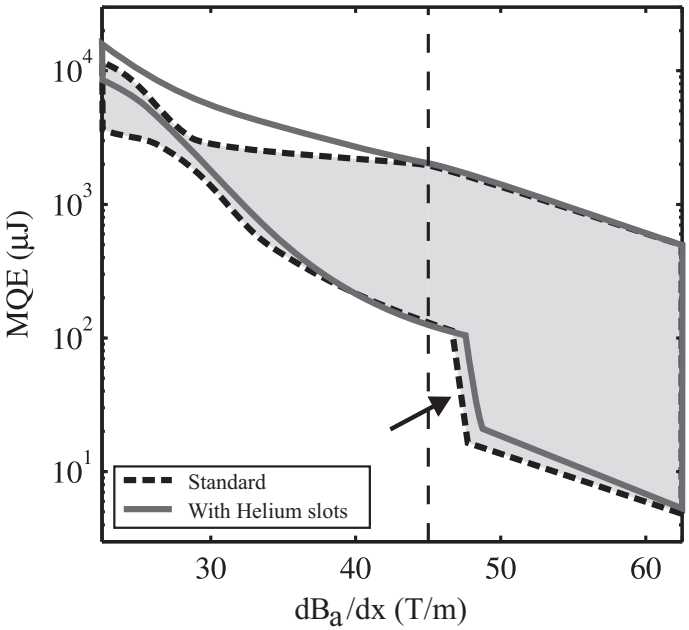

Figure 7.17: Area encompassing the MQE curves for cases 1 to 4 for SIS 300 quadrupole turn 20 for the standard cable design and the adapted design with helium slot at the thin edge of the cable.

The impact of the improved helium cooling on MQE is significant for cables in LHC dipole turn 40. Supercritical helium exhibits much lower heat capacity and therefore the impact of helium channels on MQE for turn 20 in the SIS 300 quadrupole.

7.5 Stability of mixed strand cables

For several reasons superconducting cables are designed with mixed strands, in which the superconducting strands are alternated with normal conducting (Cu) strands. For the three samples, the critical current of the cable is kept constant. Typical configurations comprise of 1 Cu strand per 2 or 3 strands. Specifically in Nb_3Sn cables the mixed design is applied since minimizing the amount of Cu that is co-processed with the superconductor reduces the overall production cost [111].

Furthermore, the quench propagation velocity increases drastically up to an order of magnitude, which simplifies the detection of a magnet quench.

In this thesis the research is limited NbTi cables, whereas mixed strand cables are designed mainly for Nb_3Sn applications. However, even though the results with NbTi cables are not quantitatively representative for the Nb_3Sn cables, the qualitative behavior will be the same. The CUDI simulations are performed with the supercritical helium cooled SIS 300 quadrupole cable with a constant field of 3.6 T across the cable width. The total Cu/SC ratio of the cable is set to 3.4, therefore the Cu/SC ratio of the superconducting strands varies between the cables, see table 7.3. The RRR is set to 200 for both the superconducting and the Cu strands.

Three cable configurations with 18 strands are investigated, see figure 7.18: a) Cable 1/1 consist of 18 superconducting strands, b) cable 2/3 consist of 12 superconducting and 6 normal conducting strands and c) cable 1/2 consists of 9 superconducting and 9 normal conducting strands. The strands in cable 2/3 have similar specifications as the SIS 300 quadrupole strand, as used in section 7.1.3.

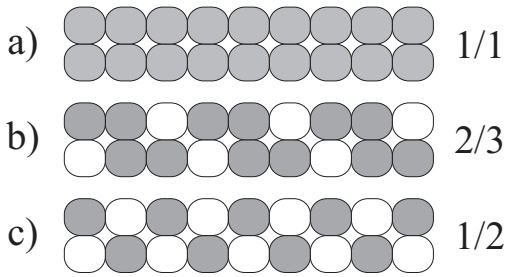

Figure 7.18: Illustration of the three cable layouts. The gray strands are superconducting, the white strands are made of Cu and carry no current. a) All strands are superconducting. b) 2 out of 3 strands are superconducting. c) 1 out of 3 strands are superconducting.

Table 7.3: Specification of the superconducting strands.

Cable	Cu/SC ratio	I_c
	-	A
1/1	3.43	426
2/3	1.95	639
1/2	1.21	851

MQE is calculated as a function of i for the eight cases described in section 7.1.1 for the three layouts and the areas encompassing the MQE curves are determined, see figure 7.19.

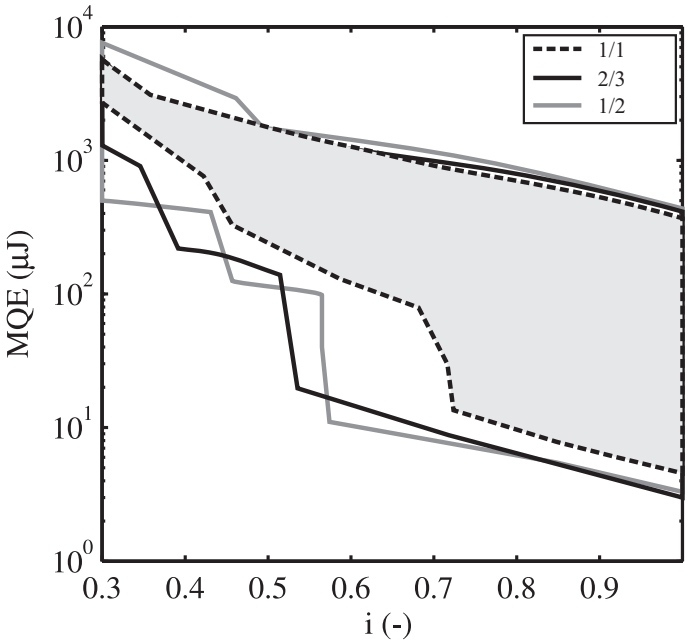

Figure 7.19: Area encompassing the calculated MQE as a function of i for the eight cases. The cable consists of 18 strand of which 18, 12 and 9 strands are superconducting. $I_c = 7.7$ kA.

The main characteristic of the curves, i_{kink} is 0.72, 0.54 and 0.57 for configuration 1/1, 2/3 and 1/2, respectively. Clearly configuration 1/1 is advantageous, having the highest MQE.

The variations in MQE are explained by the primary current redistribution paths and the thermal behavior for the three configurations, see figure 7.20:

- In configuration 1/1 a superconducting strand has two superconducting neighbors.
- In configuration each superconducting strand has one normal conducting and one superconducting neighbor. Current decrease in the heated strand is therefore slower and Joule heating and normal zone propagation is increased. The current in the superconducting neighbor increases more due to redistribution, since it is the only strand acting as primary current redistribution path. Therefore the adjacent propagation increases and stability decreases compared to configuration 1/1.

- In configuration 1/2 the superconducting strands have only normal conducting neighbors. The primary current redistribution is into the second adjacent strands. With higher inductance involved, current decrease in the heated strand is slower. However, the nearest neighboring strands act as a strong thermal barrier between the heated strand and the next neighboring strands that carry high currents, therefore improving stability.

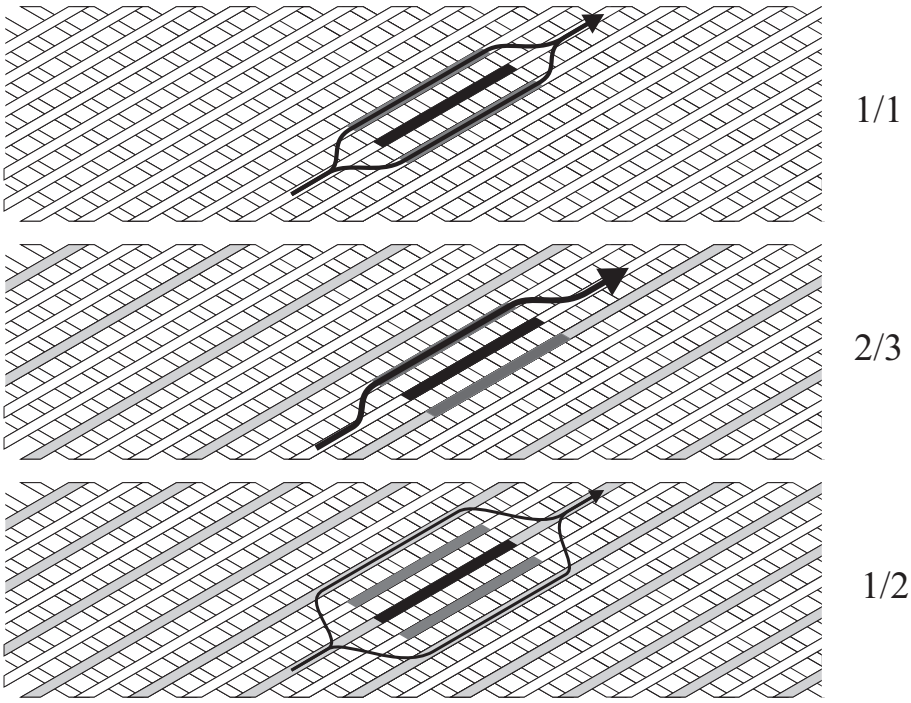

Figure 7.20: Illustration of the primary current distribution and heat flows after a transients local heat deposition for the three cable layouts. The light gray strands indicate the normal conducting strands, the black strand sections are heated superconducting strands and the dark gray sections show the neighboring strands impacted by heat flow. The arrows indicate the primary current redistribution paths for each sample.

In general a uniform distribution of superconductor in the cable shows the highest MQE and the highest i_{kink}. Configuration 2/3 strand exhibits a lower MQE and i_{kink} compared to 1/2, although the superconductor is distributed more uniformly in the cable. For configuration 1/2, the current redistribution path is into the second neighboring strands and heat exchange is mainly with the first neighboring strands. Therefore, configuration 1/2 performs better in terms of stability compared to configuration 2/3.

Cables with mixed strands are cheaper to produce, compared to fully super-

conducting cable. However, calculations show that from a stability point of view cables with mixed strands perform much worse and stable operation can be at a 30 % lower i of about 0.5 in the presented case.

7.6 Conclusion

To describe the stability of a cable in magnet operation conditions a representative set of heated volumes is defined. The MQE for all cases is calculated as a function of B_a for LHC dipole magnets and as a function of dB_a/dx for SIS 300 quadrupole magnets for the turn subject to the highest magnetic field.

One possibility to prevent a magnet from quenching is to maintain locally $T < T_c$ at all times, the single wire stability criterion. However, the energy needed to raise the temperature of a short length of a strand to T_c is small, in the order of 2 to 20 μJ. An event with the deposition of such an energy is likely to occur during magnet operation.

A second possibility is the recovery of a locally normal strand due to current redistribution. In simulations with heated volumes in one strand, the MQE increases strongly by a factor of 10 to 100 compared to the single wire stability. Cable design improvements aim at increasing $B_{a,kink}$ or $dB_{a,kink}/dx$. The start of regime II at $B_{a,kink}$ or $dB_{a,kink}/dx$ is therefore the most important design characteristic.

In LHC dipole magnets $B_{a,kink}$ is minimum in the turn exposed to the highest magnetic field. The design operation field of 8.33 T is significantly lower than $B_{a,kink}$ of 9.2 T. At 8.33 T, the lowest MQE is larger 90 μJ, for a heated volume in multiple strands at the thin edge.

For the SIS 300 quadrupole magnets the calculated $dB_{a,kink}/dx$ is 47 T/m, which is only 4% above the design operation field gradient of 45 T/m. Since the accuracy of calculations is limited and local variations in the cable occur, the margin is too small to guarantee improved stability due to current redistribution.

Non-uniform current distribution

Non-uniform current distribution is a realistic problem for superconducting accelerator magnets. The stability against short and local heat deposition deteriorates. A sinusoidal pattern of current distribution with an amplitude of ± 10 % of the current reduces $B_{a,kink}$ for turn 40 in the LHC dipole magnet from 9.2 to 8.9 T.

For turn 20 in the SIS 300 quadrupole magnet the simulations show a less dramatic reduction, but with a higher consequence in $dB_{a,kink}/dx$ from 47 to 45 T/m. Therefore at the operation field of the SIS 300 quadrupole magnet, a normal zone in a short section of a single strand would lead to a quench of the entire magnet. Uniform current distribution is therefore of high importance.

Core versus high resistive coating

Fast ramping magnets require high R_c and medium R_a to limit AC loss to the required level. By implementing a highly resistive stainless steel core between

the layers of the cable, R_c can be increased to the required level. The value of R_a is controlled separately by the coating and R_a can be more than an order of magnitude smaller than R_c. A highly resistive coating affects both R_c and R_a.

Simulations performed on two cable designs for the SIS 300 quadrupole magnets show a clear advantage in cable stability for the cored cable. In the cable with the highly resistive coating $dB_{a,kink}/dx$ is reduced by 8% compared to the cored cable. The main mechanism for reduced stability is the slower current redistribution process, due to higher R_a. A secondary effect is the reduced thermal exchange between the crossing strands, reducing the cross propagation velocity.

In general the reduction of R_c and R_a improve the stability of superconducting cables. Roughly estimated, if $R_c > 1$ mΩ, it is advantageous to implement a core in the cable. For $R_c < 100$ $\mu\Omega$, the advantage is less and the more difficult fabrication process and the reduced helium content in the voids make a core redundant.

Improvements of cable stability

Since the thin edge exhibits the lowest levels of MQE it makes sense to improve the stability of the cable at this position.

Removal of the insulation from the cable at the thin edge exposes the strand surface to helium and the cooling improves. Calculations for the LHC dipole magnet show that for cables cooled with superfluid helium the removal of insulation at the thin edge improves the stability significantly. For SIS 300 quadrupole magnets, cooled with supercritical helium, the improvement is much less significant.

Reduction of the interstrand thermal conductance at the thin edge promises a dramatic increase in $dB_{a,kink}/dx$ of 10 % for SIS 300 quadrupole magnets. Due to a reduced interstrand thermal contact, the transverse normal zone propagation at the thin edge is reduced. Calculations for LHC dipole magnets show a much smaller improvement.

Mixed strands

The effects of alternation of copper strands with superconducting strands in a cable is strongly dependent on the cable configuration. Non-uniform distribution of superconductor among the strands reduces i_{kink}, since the reduction of the number of superconducting neighbors reduces the number of primary current redistribution paths.

However, the configuration with 1/2 superconducting strands shows an improved stability compared to the configuration with 2/3 superconducting strands. The improvement is explained by the low temperature of the current redistribution paths, since the normal conducting strands provide a thermal barrier between the hot strand and current redistribution paths.

Chapter 8

Conclusion and recommendations

The focus of this thesis has been on the understanding of cable stability mechanisms, the Minimum Quench Energy (MQE) of the cable and the options for improvement of cable stability in real accelerator magnets. The main conclusion is summarized and recommendations are made for further research.

8.1 Cable stability mechanisms

Stability of superconducting cables against local transient heat depositions is described by two main physics mechanisms: thermodynamics and electrodynamics.

The main characteristic of cable stability is the strong coupling between these to mechanisms: a small raise in temperature of 1 to 3 K in the conductor to above T_c implies a strong increase in resistivity, leading to Joule heating.
The recovery of a cable from a local normal zone introduced by a heat deposition can be described as follows:

- The longitudinal normal zone propagation velocity reduces due to current redistribution. The ratio of Joule heating and cooling reduces and finally the normal zone propagation velocity turns negative and recovery commences.
- Meanwhile the temperature and current in the adjacent strands and the temperature in the crossing strands rise. If the initially heated strand recovers before the normal zone expands into too many neighbors, the cable recovers.

For the first time the criteria for cable quench are defined accurately and in detail. It is shown that the transversal propagation is characterized by well defined criteria for the stepwise expansion of the normal zone into one of neighboring strands. Transversal propagation criteria are distinguished in two types: Adjacent Propagation Criteria (APC) and Cross Propagation Criteria (CPC), see figure 8.1.

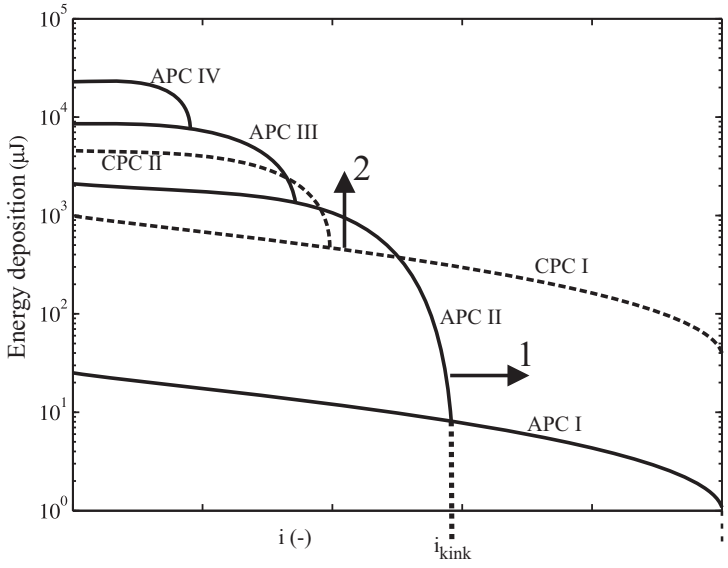

Figure 8.1: Energy deposition versus normalized current showing the limiting criteria for Adjacent Propagation and Cross Propagation.

The MQE curve for a cable as a function of the normalized current i is composed of multiple criteria and the sharp kinks in the curve originate from the intersection

of two criteria. The most important characteristic of an MQE curve is the intersection of criterion APC I with criterion APC II at the normalized current i_{kink}. It separates stability regime I, where APC I is decisive from stability regime II, where APC II is decisive. For dipole and quadrupole magnets, the MQE can be illustrated as a function of B_a and dB_a/dx, respectively.
For the first time, the cable stability mechanisms are now fully understood and validated by measurements.

In regime I, a small local heat deposition just exceeding the enthalpy margin unavoidably causes a quench of the cable and therefore the entire magnet. In regime II, a normal zone can recover and the permissible heat deposition is increased by a factor of up to 100.

The MQE change is so strong, that the statistical chance of a magnet to quench is dramatically reduced for currents below i_{kink}. Therefore a logical upper limit for reliable and stable magnet operation is i_{kink} in general, and in terms of magnetic field the corresponding $B_{a,kink}$ for a dipole magnet and $dB_{a,kink}/dx$ for a quadrupole magnet.

The research for improvement of cable stability is focused on two main questions:

1. How to increase i_{kink}?

2. How to increase the MQE for $i < i_{kink}$?

8.2 Measuring cable stability

The FRESCA cable test facility provides a unique test environment for investigating cable stability. With a wide variety of measurement instruments and methods, the mechanisms of cable stability can be investigated.

The transient heat depositions induced by conductor movement and beam loss in accelerator magnets are simulated in the experiments by heat pulses generated by local spot heaters on a strand. The graphite paste heater represents transient local heat depositions very well and i_{kink} and the MQE in stability regimes II and higher have been determined accurately.

By step-wise increasing the pulse heater energy the cable quench point can be probed and the MQE accurately determined within $\pm$ 5 %. Most of the MQE curves show the sharp transitions between the propagation criteria as shown in figure 8.1.

Voltage taps, locally applied on a short section of a strand, provide important information about the normal zone development in the strands and the sequence and timing of transverse normal zone propagation. Local voltage measurements provide a strong support for the cable stability regimes description.

An array of Hall probes measuring the self-field profile when placed along the cable thin edge provides indirect information about current distribution and the changes therein. It enables the identification of the stability regimes in cables with low and high resistance between adjacent strands R_a and between crossing strands R_c.

Through the combination of MQE, voltage and self-field measurements, the existence of different stability regimes are experimentally validated.

Measurements show a large difference in MQE across the cable width in all cables. The i_{kink} and MQE are reduced drastically at both the thin and thick edges. It shows that the variation in local conditions, such as cooling and interstrand contacts, have a strong influence on stability.

The reduced MQE and the lower i_{kink} are mainly attributed to two causes: the reduced cooling at the cable edge and the increased interstrand thermal conduction at the edge. Both causes originate from geometric variations in the cable due to the compression during cable production:

1. The neighboring strands at the edge are strongly compressed and highly compacted, thus reducing the void volume and the helium contact surface.
2. The contact surface between the adjacent strands is enlarged. Due to the almost perpendicular pressure on the contact surface the interstrand thermal conductance is improved.

Since the thin edge of the cable is always exposed to the highest field in the magnet, it has the lowest stability.

8.3 Modeling cable stability

The cable is modeled with a 3-dimensional network of nodes interconnected by strand sections and contact resistances. CUDI is a very advanced cable simulation code and it provides valuable insight in the cable stability mechanisms.

The network model CUDI is a powerful tool to simulate the processes in a cable following a local thermal heat pulse. The thermal and electrical processes are numerically described and the currents, temperatures and resistances are iteratively calculated. The possible variation in input parameters is very large, enabling a detailed description of all locally varying parameters and the magnetic field profiles as present in the cable test facility and in any magnet. Therefore, CUDI stability analysis can be validated by comparison with well-defined experiments and then be used to simulate cable stability in magnet applications.

Input parameters for the cooling of the cable are obtained from literature for superfluid, normal liquid and supercritical helium. The geometry of the cable voids is difficult to describe and the accuracy of the model is limited by the discretization. The helium filled voids are separated into volumes assigned to one strand section.

The literature values for several situations of helium cooling and thermal contact conductance are used to fit CUDI simulation results to the measured MQE, local

voltages and self-fields. It is shown that the MQE curve calculated with CUDI can fit accurately to the measured curves, for both the center as well as the edge heater and in superfluid as well as normal liquid helium. The sharp transitions in the MQE curve between the different normal zone propagation criteria clearly identifies the separation of the decisive criterion for quench.

The agreement between the accurate calculation and the measured MQE, local voltages and local self-field has validated CUDI for calculations of the stability of Rutherford cables against transient heat disturbances.

8.4 Improving cable stability

Since the first superconducting accelerator magnets started operation in 1983, only Rutherford type cables are used in the design of all superconducting accelerators, except for the SIS 100 magnets. Rutherford cables feature an overall high current density due to an almost 100 % compaction factor and good stacking possibilities.

Constraints in cable design are enforced by magnet design, forces on the conductor, AC loss, magnet field errors, conductor cooling, steady state stability, etc. Many constraints are dictated by budget limitations, others by technical or physical limitations. Cable geometry variations are limited by the need for a very high current density in the windings and a specific shape for stacking the cables into a configuration that warrants an accurate magnetic field profile.

The stability of a cable can be influenced as follows:

- The small volume fraction of voids in the cable, filled with helium, has a strong influence on the stability of the conductor against transient heat depositions. Reducing the compaction of the cable, which increases the void volume with helium, cause a reduction in longitudinal and transversal normal zone propagation. The large heat capacity of helium provides a large heat sink for cooling of the cable. Superfluid He II and liquid He I exhibit very high transient heat flux, thus limiting the temperature raise of the conductor and limiting the longitudinal normal zone propagation velocity. In supercritical helium the heat diffusion is much less, but still significant.
- An increase of the wetted perimeter of the strand by helium reduces longitudinal and transversal normal zone propagation.
- Reducing R_c in a non-cored cable and reducing R_a in a cored cable will speed up current redistribution and cause a reduction of the longitudinal normal zone propagation. However, the minimum values of R_c and R_a are strictly enforced by other constraints as AC loss and field errors. Therefore the minimum value of R_c and R_a need to be calculated accurately such that an optimum R_c and R_a value can be implemented.
  The electric resistance is dominated by the resistance of the metal-oxide layer grown on top of the coating. The influence of strand coatings, coating treatments and applying a core or full soldering are well-known.

- Reducing the thermal conductance between crossing and adjacent strands leads to a reduced transversal normal zone propagation in the crossing and adjacent direction, respectively. In practice the interstrand thermal contact conductance is mainly limited by the surface to surface contact.
  With a core present, the cross propagation is reduced significantly.
- An increase of the RRR of the matrix cause a slight reduction of the longitudinal normal zone propagation.
- Also an increase of the copper-to-superconductor ratio leads to a reduction of the longitudinal normal zone propagation. Since the overall current density reduces as well this is normally not desirable.

Therefore, the electrical and thermal conductances are dominated by different mechanisms and can possibly be optimized for a certain superconducting cable. A reduction of the interstrand contact area is possible by a lower compaction factor, but is accompanied by an increase in the interstrand electrical resistance, void volume and wetted strand surface.

However, a reduction in the compaction loosens the strands and training quenches are more likely in magnets, initiated by strand movement. The wetted perimeter is strongly coupled to the compaction factor and the interstrand contact area.

Current redistribution around a normal zone takes place over a much longer strand section, compared to the very local heat exchange. Therefore, local variations in resistance have only a minor influence on stability and the local variations in heat exchange at the edges have a significant influence on the stability.

8.5 Cable stability in a magnet

Until now, the magnet and cable designs have mainly focused on high critical current, low AC loss and limited field errors. The investigation of the stability of a cable design is important to add as design criterion to construct a safer magnet that is less susceptible for transients that may lead to magnet training.

A good evaluation of the stability of a specific cable design can be made by a combination of experiments and simulations. The following steps should be followed:

1. If the cable is made, perform MQE measurements.
2. Collect all the input parameters.
3. Perform CUDI simulations and validate the input parameters by a comparison of measured and calculated MQE.
4. Perform CUDI simulations to determine the MQE for the cable in magnet conditions.

If a cable sample is not available, calculations by CUDI can still be performed for an evaluation of cable stability, without experimental validation of the input parameters. After examination of the cable stability performance, weak spots in a cable can be identified and possibly improved. For two cases the stability in the highest field turns in a magnet is presented.

For the LHC main dipoles, the key condition for improved stability due to current redistribution is satisfied. $B_{a,kink}$ is about 9.2 T, thus significantly higher than the operating field of 8.33 T. At operating field the cable is most vulnerable to heat depositions in a few neighboring strands. The calculated MQE at operating field is 4 times higher than the single strand MQE.

In SIS 300 main quadrupoles, the key condition for improved stability due to current redistribution is just satisfied, leaving no margin. However, $dB_{a,kink}/dx$ of heaters on a single strand is about 47 T/m, thus only a few percent higher than the nominal magnetic gradient of 45 T/m. A small reduction of $dB_{a,kink}$ due to current non-uniformity or local imperfections would reduce MQE by a factor of 7.

The choice for a cored over a non-cored cable design for SIS 300 main quadrupoles is based on the calculations in this thesis. For fast-ramping magnets with the requirement of $R_c > 1$ mΩ, it is essential to keep R_a as low as possible. The only possibility to provide high R_c with low R_a is by applying a high resistive core in the median plane of the cable. The use of highly resistive coating prevents the separate control of R_a and R_c and is therefore not suitable for obtaining the best possible stability. If the non-cored cable design would be used, the stable operating magnetic gradient would be reduced significantly.

The negative effect of non-uniform current distribution on cable stability is strong. A 10 % non-uniform current distribution cause a 7 % reduction in $dB_{a,kink}/dx$ in SIS 300 quadrupoles and a 3 % reduction in $B_{a,kink}$ in the LHC dipole. Therefore non-uniformity of current can jeopardize quench free operation of accelerator systems.

Two possibilities of increasing stability at the most vulnerable part of the cable, the thin edge, are investigated:

- The removal of insulation material at the thin edge of the cable causes an increase of the helium cooled surface area and the available helium volume. The transient cooling at the edge of cable is improved as well as the steady state cooling, providing a lower operation temperature. For the superfluid helium cooled LHC dipole magnets the calculated improvement is significant, whereas the improvement for the SIS 300 quadrupole magnets is only small. The removal of insulation at the cable edge is already applied in some cable designs and is therefore feasible.
- The application of a coating or insulation between the strands at the thin edge decreases the interstrand thermal conduction locally. Simulations show that a significant improvement of stability can be obtained for the SIS 300 quadrupole magnets with an increase in $dB_{a,kink}/dx$ of more than 4 T/m. The improvement for LHC cables is less significant. However, the technical feasibility still requires a more thorough investigation.

So-called mixed cables with a non-uniform distribution of superconductor over the strands are less expensive compared to cables with all strands superconducting. However, the stability of a mixed cable is much worse and the maximum attainable

magnetic field or field gradient in a magnet is significantly less than for a design with all strands superconducting.

8.6 Recommendations

The relation between the heat leading to training quenches and the effect on the quench behavior is largely unknown. This research provides the theory of mechanisms preventing the cable to quench and the tools for describing cable stability. Further research is needed to identify and quantify the disturbances that lead to training quenches.

Investigation of the cable stability of current accelerator magnets and their quench behavior could provide further insight. Especially the relation between $B_{a,kink}$ or $dB_{a,kink}/dx$ and the quench probability for the different magnets is worth to evaluate.

The interstrand thermal conduction is largely unknown and unspecified, contrary to the electrical interstrand resistance. For AgSn coated strands, the thermal conduction is estimated by fitting simulation results to experimental data. With a database combining the thermal conduction, electrical conduction and mechanical properties of a number of coating materials progress can be made in optimizing both cable stability as well as other design properties of the cable.

Stability of a cable within the coil end turns of dipole and quadrupole magnets are not included in this thesis as cable geometry is badly defined in these regions and the contacts between adjacent strands are locally interrupted. The helium volume is also hard to define. The magnetic field varies strongly not only across the cable width, but also along the cable length. Since part of the quenches in accelerator magnets occur in the coil ends it is recommended to characterize the geometry in the coil ends and investigate the local cable stability.

The focus of this research was on NbTi superconducting cables, the material of choice for the main magnets of present accelerators. Research programs to future magnets focus on the application of Nb_3Sn and BiSrCaCuO based cables. Many Nb_3Sn conductors show flux-jump instabilities and are normally impregnated, therefore local helium cooling is not an option. The specifications of Nb_3Sn cables results for CUDI calculations need to be obtained and validated with experiments. Quantification of MQE levels is needed to optimize the stability of future magnets.

Bibliography

[1] *LHC design report, CERN, Geneve, Switzerland, EDMS 445830 and 445839.*

[2] E. Fischer, H. G. Khodzhibagiyan, and A.D. Kovalenko. Full size model magnets for the FAIR SIS 100 synchrotron. *IEEE Trans. Appl. Supercond.*, 18:260 – 263, 2008.

[3] G. Moritz. Rapidly-cycling superconducting accelerator magnets for FAIR at GSI. In *Proceedings of PAC07, Albuquerque, USA*, 2007.

[4] M.N. Wilson. Superconductivity and accelerators: the good companions. *IEEE Trans. Appl. Supercond.*, 9:111–121, 1999.

[5] J. Kaugerts, G. Moritz, M.N. Wilson, A.K Ghosh, A. den Ouden, I. Bogdanov, S. Kozub, P. Shcherbakov, L. Shirshov, L. Tkachenko, D. Richter, A.P. Verweij, G.P. Willering, P. Fabbricatore, and G. Volpini. Cable design for FAIR SIS 300. *IEEE Trans. Appl. Supercond.*, 17:1477 – 1480, 2007.

[6] O. Tsukamoto. Mechanical disturbances in Rutherford-type and braid conductors. *IEEE Trans. Magn.*, 19:443–445, 1983.

[7] W. Goldacker, A. Frank, R. Heller, S.I. Schlachter, B. Ringsdorf, K.P. Weiss, C. Schmidt, and S. Schuller. Roebel assembled coated conductors (RACC): preparation, properties and progress. *IEEE Trans. Appl. Supercond.*, 17:3398–3401, 2007.

[8] M.N. Wilson. *Superconducting Magnets.* Clarendon Press, Oxford, 1983.

[9] R.B. Palmer. Superconducting accelerator magnets: A review of their design and training. In *ICHEP conference, Texas*, 1992.

[10] P. Pugnat and A. Siemko. Review of quench performance of LHC main superconducting magnets. *IEEE Trans. Appl. Supercond.*, 17:1091 – 1096, 2007.

[11] http://hcc.web.cern.ch/hcc/. LHC hardware commissioning website. June 2008.

[12] Y. Iwasa. Stability and protection of superconducting magnets - a discussion. *IEEE Trans. Appl. Supercond.*, 15:1615 – 1620, 2005.

[13] C. Meuris, B. Baudouy, D. Leroy, and B. Szeless. Heat transfer in electrical insulation of LHC cables cooled with superfluid helium. *Cryogenics*, 39:921–931, 1999.

[14] R.S. Kensley and Y. Iwasa. Frictional properties of metal insulator surfaces at cryogenic temperatures. *Cryogenics*, 20:25 – 36, 1980.

[15] H. Maeda, O. Tsukamoto, and Y. Iwasa. The mechanism of friction motion and its effect at 4.2 K in superconducting magnet winding models. *Cryogenics*, 22:287 – 295, 1982.

[16] P.F. Smith and B. Colyer. A solution to the training problem in superconducting magnets. *Cryogenics*, 15:201–207, 1975.

[17] A.K Ghosh, M. Garber, K.E. Robins, and W.B. Sampson. Training in test samples of superconducting cables for accelerator magnets. *IEEE Trans. Magn.*, 25:1831–1834, 1989.

[18] P. Pugnat, B. Khomenko, A. Rijllart, S. Sanfilippo, and A. Siemko. Statistical diagnosis method of conductor motions in superconducting magnets to predict their quench performance. *IEEE Trans. Appl. Supercond.*, 11:1705 – 1708, 2001.

[19] M.N. Wilson. Calculation of minimum quench energies in Rutherford cables. *IEEE Trans. Appl. Supercond.*, 7:950–953, 1997.

[20] E.S. Bobrov, J.E.C. Williams, and Y. Iwasa. Mechanical disturbances in superconducting coils. *Cryogenics*, 25:307 – 316, 1985.

[21] Y. Iwasa. Mechanical disturbances in superconducting magnets - a review. *IEEE Trans. Magn.*, 28:113 – 120, 1992.

[22] B. Jeanneret and H. Burkhardt. On the measurement of the beam losses in the LHC rings. Technical report, CERN, LHC project report, EDMS 328146, 2004.

[23] J.B. Jeanneret, D. Leroy, L.R. Oberli, and T. Trenkler. Quench levels and transient beam losses in LHC magnets. Technical report, LHC project report 44, 1996.

[24] R.W. Arenz, C. F. Clark, and W.N. Lawless. Thermal conductivity and electrical resistivity of copper in intense magnetic fields at low temperatures. *Physical review B*, 26:2728–2732, 1982.

[25] A.P. Martinelli and S.L. Wipf. Investigation of cryogenic stability. In *Appl. Superc. Conf. New York, 1972, IEEE*, 1972.

[26] P. Bauer. *Stability of superconducting strands for accelerator magnets.* PhD thesis, Technical University Vienna, Austria, 1998.

[27] E. Gmelin, M. Asen-Palmer, M. Reuther, and R. Villar. Thermal boundary resistance of mechanical contacts between solids at sub-ambient temperatures. *J. Phys. D: Appl. Phys.*, 32:19–43, 1999.

[28] B. Baudouy, M.X. Francois, F.P. Juster, and C. Meuris. He II heat transfer through superconducting cables electrical insulation. *Cryogenics*, 40:127 – 136, 2000.

[29] A.P. Verweij. *Electrodynamics of superconducting cables in accelerator magnets.* PhD thesis, University of Twente, The Netherlands, 1995.

[30] B. Turck. Influence of a transverse conductance on current sharing in a two-layer superconducting cable. *Cryogenics*, 14:448–454, 1974.

[31] G. Ries. Stability in superconducting multistrand cables. *Cryogenics*, 20:513–519, 1980.

[32] G.B.J. Mulder, L.J.M. van de Klundert, and V.S. Vysotsky. Quench development in superconducting cable having insulated strands with high resistive matrix (part 2, analysis). *IEEE Trans. Magnetics*, 28:739–742, 1992.

[33] T. Yoshino, M. Tsuda, and A. Ishiyama. Improvement of transient stability of non-insulated AC multi-strand superconducting cables. *IEEE Trans. Appl. Supercond.*, 7:231–234, 1997.

[34] S.W. Kim and R. Wolf. Stability of superconducting cable with multiple strands. Technical report, Fermilab TD-note 00-014, 2000.

[35] L. Bottura, C. Rosso, and M. Breschi. A general model for thermal, hydraulic and electrical analysis for superconducting cables. *Cryogenics*, 40:617–626, 2000.

[36] N. Mitchell. Modeling of non-uniform current diffusion coupled with thermo-hydraulic effects in superconducting cables. *Cryogenics*, 40:637–653, 2000.

[37] Y. Lei, Y. Yu, H. Nan, Y. Dai, and Q. Wang. Influence of inter-strand electrical and thermal conductivity on stability of Rutherford cables in accelerator magnets. *IEEE Trans. Appl. Supercond.*, 14:1338–1342, 2004.

[38] N. Amemiya, K. Ryu, T. Kikuch, and O. Tsukamoto. Influence of current re-distribution and thermal diffusion among strands on stability of superconducting cable against local disturbances. *IEEE Trans. Magnetics*, 30:2281–2284, 1994.

[39] A.K. Ghosh, W.B. Sampson, and M.N. Wilson. Minimum quench energies of Rutherford cables and single wires. *IEEE Trans. Appl. Supercond.*, 7:954–957, 1997.

[40] M. Breschi, P. Granieri, M. Calvi, M. Coccoli, and L. Bottura. Quench propagation and stability analysis of Rutherford resistive core cables. *Cryogenics*, 46:606–614, 2006.

[41] L. Bottura, M. Calvi, and A. Siemko. Stability analysis of the LHC cables. *Cryogenics*, 46:481–493, 2006.

[42] G.H. Morgan. Eddy currents in flat metal-filled superconducting braids. *J. Appl. Phys.*, 44:3319–3322, 1973.

[43] V.E. Sytnikov, G.G. Svalov, S.G. Akopov, and I.B. Peshkov. Coupling losses in superconducting transposed conductors located in changing magnetic fields. *Cryogenics*, 29:926 – 930, 1989.

[44] E.M.J Niessen, D. ter Avest, and L.J.M. van de Klundert. Application of the network method to superconducting cables. *Proc. LTEC 90*, page p 5.4, 1990.

[45] M. Tsuda, N. Toyoda, M. Matsui, and A. Ishiyama. Stability of non-insulated AC multistrand superconducting cables. *IEEE Trans. Magnetics*, 32:2854–2857, 1996.

[46] A.P. Verweij. CUDI: A model for calculation of electrodynamic and thermal behavior of superconducting cables. *Cryogenics*, 46:619–626, 2006.

[47] M.S. Lubell. Empirical scaling formulas for critical current and critical field for commercial NbTi. *IEEE Trans. Magn.*, 19:754–757, 1983.

[48] A. Bejan. *Heat transfer*. Wiley, New York, 1993.

[49] M.N. Wilson, W.B. Sampson, and A.K Ghosh. Experimentally measured minimum quench energies of LHC cables. Technical report, CERN, Geneva, Switzerland, LHC project report 86, 1997.

[50] S.W. Kim, D. Leroy, M.N. Wilson, A.K Ghosh, and W.B. Sampson. Stability measurements of Rutherford cables with various treatments. Technical report, CERN, Geneva, Switzerland, LHC project report 250, 1998.

[51] A.K Ghosh, A. Prodell, W.B. Sampson, R.M. Scanlan, D. Leroy, and L.R. Oberli. Minimum quench energy measurements on prototype LHC inner cables in normal helium at 4.4 K and in superfluid helium at 1.9 K. *IEEE Trans. Appl. Supercond.*, 9:257–260, 1999.

[52] N. Amemiya, H. Yonekawat, T. Ogitsu, E. Kobayashi, K. Sasaki, K. Ohuchi, K. Tsuchiya, and K. Miyashita. Influence of current re-distribution on minimum quench energy of superconducting triplex cable against local disturbance. *Cryogenics*, 38:559–568, 1998.

[53] N. Hirano, T. Mito, A. Takahata, A. Iwamoto, R. Maekawa, Y. Yamamoto, B. Ikeda, Y. Kubo, M. Morita, O. Taguchi, and R. Saito. Effects of the current redistribution within Nb_3Sn compacted-strand cable on its stability. *IEEE Trans. Appl. Supercond.*, 7:770 – 773, 1997.

[54] A.K Ghosh, W.B. Sampson, S.W. Kim, D. Leroy, L.R. Oberli, and M.N. Wilson. Stability measurements on cored cables in normal and superfluid helium. *Physica C.*, 310:335 – 339, 1998.

[55] A. Kawagoe, K. Yoshikawa, F. Sumiyoshi, T. Kawashima, and T. Mito. Minimum quench energy of new type Rutherford cable with both high stability and low losses. *Physica C.*, 378-381:1154 – 1157, 2002.

[56] N. Amemiya, H. Yonekawa, E. Kobayashi, T. Ogitsu, K. Sasaki, K. Ohuchi, K. Tsuchiya, and T. Shintomi. Current redistribution and stability of superconducting triplex cable without electrical insulation carrying non-uniform current. *Cryogenics*, 43:249–254, 2003.

[57] G.P. Willering, A.P. Verweij, C. Scheuerlein, A. den Ouden, and H.H.J. ten Kate. Difference in stability between edge and center in a Rutherford cable. *IEEE Trans. Appl. Supercond.*, 18:1253 – 1256, 2008.

[58] T. Shimada, M. Sugimoto, Y. Nagasu, A. Takagi, K. Wada, H. Shimizu, A. Kimura, and S. Meguro. Manufacturing of superconducting cable for the LHC - key technology and statistical analysis. *IEEE Trans. Appl. Supercond.*, 12:1075–1078, 2002.

[59] J. Depond, D. Leroy, and L.R. Oberli. Superconducting cable topology. Technical report, LHC - AT/MMS internal note 97-09, 1997.

[60] C. Scheuerlein, G.P. Willering, A.P. Verweij, A. Bonasia, L.R. Oberli, M. Taborelli, and D. Richter. Aluminum strand coating for increasing the interstrand contact resistance in Rutherford type superconducting cables. ASC conference, Chicago, 2008. To be published.

[61] G. Frei, S. Hartmann, G. Kuhne, C. Scheuerlein, and G.P. Willering. Void fraction, interstrand contact area and free strand surface area in an LHC Rutherford cable. In *presented at ASC conference, Chicago, USA*, 2008.

[62] A.P. Verweij, J. Genest, A. Knezovic, D.F. Leroy, J.-P. Marzolf, and L.R. Oberli. 1.9 K test facility for the reception of the superconducting cables for the LHC. *IEEE Trans. Appl. Supercond.*, 9:153–156, 1999.

[63] O. Vincent-Viry. Longitudinal field variation MFRESCA. Technical report, Fresca internal note, 2004-01.

[64] P. Bauer, J. Donnier, and L.R. Oberli. Tip heater for minimum quench energy measurements on superconducting strands. *IEEE Trans. Appl. Supercond.*, 9:1141 – 1144, 1999.

[65] F. Trillaud, F. Ayela, A. Devred, M. Fratini, D. Leboeuf, and P. Tixador. Quench propagation ignition using single-mode diode laser. *IEEE Trans. Appl. Supercond.*, 15:3648 – 3651, 2005.

[66] F. Trillaud, F. Ayela, A. Devred, M. Fratini, D. Leboeuf, and P. Tixador. A novel technique for minimum quench energy measurements in superconductors using a single-mode diode laser. *Cryogenics*, 45:585 – 588, 2005.

[67] G.P. Willering, Denari C., S. Geminian, and A.P. Verweij. New FRESCA sample holder for cable stability experiments. Technical report, CERN - AT/MCS internal note 2005-11, EDMS 691690, 2005.

[68] K. Seo, M. Morita, S. Nakamura, T. Yamada, and Y. Jizo. Minimum Quench Energy measurement for superconducting wires. *IEEE Trans. Magn.*, 32:3089 – 3093, 1996.

[69] S.W. Kim, T. Shintomi, N. Kimura, Y. Makida, H. Hirabayashi, T. Mito, A. Iwamoto, and Y. Yamamoto. Experimental studies on stabilities of Rutherford cables for superconducting accelerator magnets. *IEEE Trans. Magn.*, 32:2784 – 2787, 1996.

[70] G.P. Willering and A.P. Verweij. Modeling the heat flow from a graphite paste heater used for cable stability measurements. Technical report, CERN - AT/MCS Internal Note 2007-12, EDMS 882131, 2007.

[71] A.P. Verweij, M.P. Oomen, and H.H.J. ten Kate. Boundary-Induced Coupling Currents in a 1.3 m Rutherford-type cable due to a locally applied field change. *IEEE Trans. Appl. Supercond.*, 7:270 – 273, 1997.

[72] A.P. Verweij. Current redistribution in the cables of LHC magnets. Technical report, CERN, LHC-project-note-90, 1997.

[73] G.P. Willering, A.P. Verweij, and H.H.J. ten Kate. Current redistribution around the superconducting-to-normal transition in superconducting Nb-Ti Rutherford cables. *Journ. of Physics: Conference Series*, 97:012119, 2008.

[74] M.D. Sumption, W.W. Collings, R.M. Scanlan, A. Nijhuis, H.H.J. ten Kate, S.W. Kim, M. Wake, and T. Shintomi. Influence of strand surface condition on interstrand contact resistance and coupling loss in NbTi-wound Rutherford cables. *Cryogenics*, 39:197 – 208, 1999.

[75] M. Lenglet, K. Kartouni, J. Machefert, J.M. Claude, P. Steinmetz, E. Beauprez, J. Heinrich, and N. Celati. Low temperature oxidation of copper: the formation of CuO. *Materials research bull.*, 30:393 – 403, 1995.

[76] D. Richter, J.D. Adam, J. Depond, D. Leroy, and L.R. Oberli. DC measurement of electrical contacts between strands in superconducting cables for the LHC main magnets. *IEEE Trans. Appl. Supercond.*, 7:786–792, 1997.

[77] C. Scheuerlein, M. Taborelli, and M. Cantoni. Oxidation and contact resistance of Sn-Ag coated superconducting strands for the Large Hadron Collider (LHC). *Appl. Surface Science*, 253:1393 – 1398, 2006.

[78] M.J Nilles and S.W. Sciver. Effects of oxidation and roughness on Cu contact resistance from 4 K to 290 K. *Adv. Cryog. Engin.*, 34:443 – 450, 1988.

[79] Y. Lei, Y. Yu, Y. Dai, and H. Nan. Measurements of interstrand thermal and electrical conductance in multistrand superconducting cables. *IEEE Trans. Appl. Supercond.*, 12:1052 – 1055, 2002.

[80] Y. Zhang, N.P. Ong, Z.A. Xu, K. Krishana, R. Gagnon, and L. Taillefer. Determining the Wiedemann-Franz ratio from the thermal hall conductivity: application to Cu and YBaCuO. *Phys. Rev. Lett.*, 84:p 2219 – 2222, 2000.

[81] R. Otmani, A. Devred, and P. Tixador. Interstrand and AC-loss measurements on Rutherford-type cable for accelerator magnet applications. *IEEE Trans. Appl. Supercond.*, 11:2760–2763, 2001.

[82] J.E. Jensen, W.A. Tuttle, and R.B. Stewart. BNL - selected cryogenic data notebook. Technical report, Brookhaven Nat. Lab., USA, BNL 10200-R, 1980.

[83] P. Bauer, H. Rajainmaki, and E. Salpietro. EFDA material data compilation for superconductor simulation. Technical report, EFDA, Germany, 2007.

[84] J.D. Adam, D. Leroy, L.R. Oberli, D. Richter, M.N. Wilson, R. Wolf, H. Higley, A.D. McInturff, R.M. Scanlan, A. Nijhuis, H.H.J. ten Kate, and S. Wessel. Rutherford cables with anisotropic transverse resistance. *IEEE Trans. Appl. Supercond.*, 7:958 – 961, 1997.

[85] A.K Ghosh and J. D'Ambra. Interstrand resistance of prototype SIS 300 dipole cable. Technical report, BNL, AM-MD-343, 2005.

[86] G.P. Willering, A.P. Verweij, J. Kaugerts, and H.H.J. ten Kate. Stability of Nb-Ti Rutherford cables exhibiting different contact resistances. *IEEE Trans. Appl. Supercond.*, 18:1263 – 1266, 2008.

[87] R. Soika, M. D. Anerella, A.K Ghosh, P. Wanderer, M.N. Wilson, W.V. Hassenzahl, J. Kaugerts, and G. Moritz. Interstrand resistance measurements in cored Nb-Ti Rutherford cables. *IEEE Trans. Appl. Supercond.*, 13:2380 – 2383, 2003.

[88] R. Soika and A.K Ghosh. Interstrand resistances in cored Rutherford-type superconducting cables. *Cryogenics*, 45:149 – 154, 2005.

[89] W.B. Bloem. *Transient heat transfer to supercritical helium at low temperatures.* PhD thesis, University of Twente, Enschede, The Netherlands, 1986.

[90] Cryodata, inc., p.o. box 558, niwot co, 80544.

[91] S.W. van Sciver. *Helium cryogenics.* Plenum Press, New York, 1986.

[92] P. Seyfert, J. Lafferranderie, and G. Claudet. Time dependent heat transport in subcooled superfluid helium. *Cryogenics*, 22:401 – 408, 1982.

[93] A. Kashani and S.W. van Sciver. High heat flux Kapitza conductance of technical copper with several different surface preparations. *Cryogenics*, 25:238 – 242, 1985.

[94] R. Xu Cheng, B., N. Borca, A. Solokov, C.S. Yang, L. Yuan, and S.H. Liou. Characterization of the native Cr_2O_3 oxide surface of CrO_2. *Appl. Phys. Letters*, 79:p 3122 – 3124, 2001.

[95] O. Madelung, U. Rssler, and M. Schulz. *Non-Tetrahedrally bonded elements and binary compounds I.* Springer-Verlag, 1998.

[96] R. Freer. Debye characteristic temperatures of some crystals with NaCl structure. *Journ. Mater. Sc.*, 16:p 3225 – 3227, 1981.

[97] G.S. Collins, T. Kachnowski, and N. Benczer-Koller. Application of the Mossbauer effect to the characterization of an amorphous tin-oxide system. *Physical review B*, 19:1369 – 1373, 1979.

[98] G. Claudet and P. Seyfert. Bath cooling with subcooled superfluid helium. *Adv. Cryog. Engin.*, 27:375, 1981.

[99] A. Iwamoto, R. Maekawa, and T. Mito. Kapitza conductance of an oxidized copper surface in saturated He II. *Cryogenics*, 41:367 – 371, 2001.

[100] R. Wang. Criterion for quantum turbulence onset after rectangular heat pulse in superfluid helium. *Cryogenics*, 35:883 – 886, 1995.

[101] C.E. Chase. Thermal conduction in liquid helium II. Effects of channel geometry. *Physical review*, 131:1898 – 1903, 1963.

[102] W.G. Steward. Transient helium heat transfer phase I - Static coolant. *Int. J. Heat Mass Transfer*, 21:863–874, 1978.

[103] C. Schmidt. Transient heat transfer into a closed small volume of liquid or supercritical helium. *Cryogenics*, 28:585 – 598, 1988.

[104] C. Schmidt. Transient heat transfer to a closed volume of He I and its influence on superconductor stability. *Cryogenics*, 31:618 – 623, 1991.

[105] D. Richter, J.D. Adam, D. Leroy, and L.R. Oberli. Strand coating for the superconducting cables of the LHC main magnets. *IEEE Trans. Appl. Supercond.*, 9:735 – 741, 1999.

[106] L. Bottura, G. D'Angelo, M. Gateau, P. Legrand, M. Modena, K. Naoui, D. Perini, P. Pugnat, S. Sanfilippo, F. Savary, W. Scandale, A. Siemko, P. Sievers, G. Spigo, J. Vlogaert, and C. Wyss. Performance of the LHC final prototype and first pre-series superconducting dipole magnets. *IEEE Trans. Appl. Supercond.*, 12:211 – 214, 2002.

[107] A.P. Verweij. Private communication. 2009.

[108] H. Mueller. Private communication, 2008.

[109] A. Ageyev, N. Andreev, I. Bogdanov, S. Kozub, K. Myznikov, A. Olyunin, A. Orlov, P. Shcherbakov, V. Sytnik, L. Tkachenko, and A. Zlobin. Performance of UNK dipoles with natural oxide coating of strands. *IEEE Trans. Appl. Supercond.*, 14:263 – 266, 2004.

[110] M.N. Wilson, G. Moritz, M. D. Anerella, G. Ganetis, A.K Ghosh, W.V. Hassenzahl, A. Jain, P. Joshi, J. Kaugerts, C. Muehle, J. Muratore, R. Thomas, G. Walter, and P. Wanderer. Design studies on superconducting Cosθ magnets for a fast pulsed synchrotron. *IEEE Trans. Appl. Supercond.*, 12:p 313 – 316, 2002.

[111] M. Coccoli, R.M. Scanlan, M. Calvi, S. Caspi, L. Chiesa, R. Hafalia, H.C. Higley, D.R. Dietderich, S.A. Gourlay, A. Lietzke, A.D. McInturff, and G. Sabbi. Fabrication and performance of Nb_3Sn Rutherford-type cable with Cu added as a separate component. *IEEE Trans. Appl. Supercond.*, 14:p 971 – 974, 2004.

Nomenclature

Symbol	Meaning	Unit
$a_{f,I}$	Heat transfer coefficient of film boiling to He I	$\mathrm{WK^{-1}m^{-2}}$
$a_{f,II}$	Heat transfer coefficient of film boiling to He II	$\mathrm{WK^{-1}m^{-2}}$
a_K	Kapitza conductance parameter	$\mathrm{WK^{-n}m^{-2}}$
$a_{sc,c}$	Correction factor for heat transfer to supercritical He	-
$a_{sc,ss}$	Steady state heat transfer to supercritical He	$\mathrm{WK^{-1}m^{-2}}$
A	Area	$\mathrm{m^2}$
A_a	Contact area between adjacent strands	$\mathrm{m^2}$
A_c	Contact area between crossing strands	$\mathrm{m^2}$
A_{He}	Area of the strand wetted by helium	$\mathrm{m^2}$
A_m	Cross section area of the matrix	$\mathrm{m^2}$
A_s	Cross section area of the strand	$\mathrm{m^2}$
B	Magnetic field	T
B_a	Central field in the aperture of a magnet	T
$B_{a,kink}$	Magnetic field at the intersection of APC I and APC II	T
B_{sf}	Self-field	T
c_{cu}	Heat capacity of copper	$\mathrm{JK^{-1}kg^{-1}}$
c_{sc}	Heat capacity of the superconductor	$\mathrm{JK^{-1}kg^{-1}}$
C_1, C_2	Constants for characterization of I_c	A, $\mathrm{AT^{-1}}$
d_f	Filament diameter	m
d_s	Strand diameter	m
E_p	Pulse energy	J
E_0	Enthalpy limit of a helium volume	J
f_w	Wetted surface fraction	-
f_c	Compaction factor	-
f_{corr}	Correction factor for the pulse energy	-
$F_{int,a}$	Thermal conductance between adjacent strands	$\mathrm{WK^{-(1+b)}m^{-2}}$
$F_{int,c}$	Thermal conductance between crossing strands	$\mathrm{WK^{-(1+b)}m^{-2}}$
F_L	Lorentz force	N

Symbol	Meaning	Unit
h_{He}	Heat transfer coefficient for helium cooling	$\mathrm{WK^{-1}m^{-2}}$
h_K^p	Theoretical Kapitza heat flux by phonon conduction	$\mathrm{WK^{-1}m^{-2}}$
h_K	Practical Kapitza heat flux	$\mathrm{WK^{-1}m^{-2}}$
i	Normalized current	-
i_{kink}	Normalized current at the intersection of APC I and APC II	-
I	Current	A
I_c	Critical current density	A
I_{kink}	Current at the intersection of APC I and APC II	A
I_q	Quench current	A
I_t	Transition current	A
J	Current density	$\mathrm{Am^{-2}}$
J_c	Critical current density	$\mathrm{Am^{-2}}$
J_m	Current density in the matrix	$\mathrm{Am^{-2}}$
k_B	Boltzmann constant	$\mathrm{JK^{-1}}$
l_{MPZ}	Length of MPZ	m
l_{nz}	Normal zone length	m
l_p	Twist pitch of the strands	m
L	Inductance	H
L_0	Lorentz number	$\mathrm{W\Omega K^{-2}}$
M	Magnetization	$\mathrm{Am^{-1}}$
n_K	n-power in the Kapitza conductance formula	-
N_b	Number of calculation bands	-
N_s	Number of strands	-
p_{diss}	Heat dissipation	$\mathrm{Wm^{-3}}$
p_{ext}	Heat flux from an external source	$\mathrm{Wm^{-3}}$
p_{He}	Heat flux to helium	$\mathrm{Wm^{-3}}$
p_{is}	Interstrand heat flux	$\mathrm{Wm^{-3}}$
pd	Pulse duration	s
P	Wetted perimeter by helium	$\mathrm{m^2}$
P_p	Pulse power	W
q	Heat flux	$\mathrm{Wm^{-2}}$
$q_{f,II}$	Film boiling limit for He II	$\mathrm{Wm^{-2}}$
$Q_{f,I}$	Film boiling limit for He I	$\mathrm{Jm^{-2}}$
$Q_{p,I}$	Energy to reach the critical pressure	$\mathrm{Jm^{-3}}$
r	Radius	m
R	Resistance	Ω
R_a	Resistance between adjacent strands	Ω
R_c	Resistance between crossing strands	Ω
$R_{coating}$	Resistance of the strand coating	Ω
$R_{contact}$	Contact resistance	Ω
R_{oxide}	Resistance of the metal-oxide layer on a strand	Ω
S	Electrical conductance	Ω^{-1}

Symbol	Meaning	Unit
$t_{f,I}$	Start time of film boiling for He I	s
$t_{f,II}$	Start time of film boiling for He II	s
t_{nz}	Start time of a normal zone	s
T	Temperature	K
T_c	Critical temperature	K
T_λ	Transition temperature between superfluid and liquid helium	K
T_{He}	Helium bath temperature	K
T_m	Temperature margin	K
T_{room}	Room temperature	K
$v_{q,long}$	Longitudinal normal zone propagation velocity	ms^{-1}
$v_{q,trans}$	Transversal normal zone propagation velocity	ms^{-1}
V_{emf}	Voltage induced by electro-magnetic force	V
V_{He}	Helium volume	m^3
x, y, z	Cartesian coordinates	m
Greek symbols		
α	Angle between the strand and the cable	deg
γ	Proportionality factor supercritical helium	-
Θ_D	Debye temperature	K
κ_{cu}	Thermal conductivity of copper	$\mathrm{WK}^{-1}\mathrm{m}^{-2}$
λ	Copper to superconductor ratio (Cu/SC)	-
λ_e	Electron conduction	$\mathrm{WK}^{-1}\mathrm{m}^{-1}$
λ_p	Phonon conduction	$\mathrm{WK}^{-1}\mathrm{m}^{-1}$
μ_0	Permeability of vacuum	Hm^{-1}
ρ_{cu}	Resistivity of copper	Ωm
ρ_{sc}	Resistivity of the superconductor	Ωm
$\tau_{\theta,f}$	Thermal diffusion time in the filament	s
$\tau_{m,c}$	Magnetic diffusion time of the matrix	s

Common subscripts

a	Adjacent
c	Critical or Cross
cu	Copper
$diss$	Dissipation
eff	Effective
ext	External
He	Helium
$init$	Initial
int	Interstrand
$j, j+1, j+2, ...$	Numbering of subsequent strands, with j the heated strand.
$kink$	Intersection of APC I and APC II
m	Matrix or margin
max	Maximum
min	Minimum
sc	Superconductor

Abbreviations

APC	Adjacent Propagation Criterion
CPC	Cross Propagation Criterion
CUDI	Calculation code "Current Distribution"
LHC	Large Hadron Collider
MPZ	Minimum Propagation Zone
MQE	Minimum Quench Energy
QDM	Quench Decision Moment
RRR	Residual Resistance Ratio
SIS	Schwer-Ionen (Heavy Ion) Synchrotron

Samenvatting (Summary in Dutch)

Supergeleiders
Supergeleidende kabels zijn uitermate geschikt om compacte hoogveld magneten mee te wikkelen, vanwege de hoge limiet in stroomdichtheid in combinatie met de afwezigheid van elektrische weerstand. Het meest gangbare type kabel voor deeltjesversnellers is de Rutherford kabel, bestaande uit getwiste draden (of strands). De strands zijn opgebouwd uit getwiste supergeleidende filamenten, ingebed in een koperen matrix. Iedere strand heeft een raakvlak met naastgelegen parallelle strands en een raakvlak met alle strands in de andere laag van de kabel, de kruisende strands.

In een supergeleider bestaat de kans op een abrupte overgang van de supergeleidende toestand naar de normaal geleidende toestand. Deze overgang wordt bepaald door het kritieke vlak, gevormd door magneetveld, temperatuur en stroom. Het werkgebied van de meeste supergeleidende magneten ligt ongeveer tussen 50 en 70% van de kritieke stroom en ongeveer 1 tot 2 K onder de kritieke temperatuur. Bij het overschrijden van het kritieke vlak, in het algemeen door een kleine temperatuurtoename in de geleider tot boven de kritieke temperatuur, vindt er warmteontwikkeling plaats in de geleider. De warme zone breidt zich uit en een "quench" kan zich voordoen, een irreversibele overgang naar de normaal geleidende toestand. De enige manier om te herstellen van een lokale normale zone is een goede koeling of een drastische afname van de stroom.

Dit proefschrift behandelt de stabiliteit van supergeleidende Rutherford kabels en in het bijzonder de effecten van stroomherverdeling op de stabiliteit tegen lokale energie deposities.

Onderzoekmethoden
Met behulp van experimenten aan kabels is de stroomherverdeling en de minimale quench energie (de minimale energie die nodig is om een quench te veroorzaken ofwel MQE) bestudeerd. Veranderingen in de stroomverdeling zorgt voor een door Hall probes meetbare verandering van het lokale magneetveld. De lokale spanning over strands wordt gemeten waaruit de start en de lengte van een normale zone en

de verandering in de stroom per strand kunnen worden afgeleid.

Het numerieke computermodel CUDI beschrijft alle thermische en elektrische processen in een kabel. CUDI simulaties geven een nog duidelijker inzicht in de processen van stroomverdeling vergeleken met metingen en is onmisbaar in het accuraat beschrijven van de processen die de stabiliteit van een kabel bepalen. Door het vergelijken van de meetresultaten met resultaten van simulaties is CUDI gevalideerd.

Stabiliteitscriteria

De stabiliteit van losse supergeleidende strands is in het verleden uitgebreid onderzocht en wordt accuraat beschreven door de theorie, waarbij alleen longitudinale propagatie van de normale zone (in de lengterichting van de strand) beschreven wordt bij constante stroom. In kabels is het proces meer gecompliceerd vanwege longitudinale normale zone propagatie en transversale normale zone propagatie (tussen verschillende strands). Deze propagatie wordt beïnvloed door zowel temperatuur als stroomverdeling, waarbij een koppeling bestaat tussen beide verdelingen. De volgende begrippen en processen worden geïntroduceerd in hoofdstuk 2:

- **Stroomherverdeling.** Rond een normale zone zal de stroom gaan herverdelen. Het vernieuwde stroompad heeft naast weerstand ook een inductieve component. Gezien de herverdelingstijden in de ordegrootte van microseconden zal de stroom zich voornamelijk gaan herverdelen naar het stroompad met de minste inductie, ofwel de naastgelegen parallelle strands.
- **Longitudinale normale zone propagatie.** De initiële snelheid van longitudinale propagatie in de strand is in de ordegrootte van 1 - 10 meters per seconde, maar die snelheid neemt snel af vanwege de verminderde stroom in de strand zolang de naastliggende strands supergeleidend zijn. Een lage elektrische interstrand weerstand zorgt voor een snelle afname van de stroom in de strand.
- **Transversale normale zone propagatie.** De normale zone kan propageren naar de parallelle strands door een verhoogde stroom en temperatuur en naar de kruisende strands alleen door een verhoogde temperatuur. Het is zaak om de naburige strands koel te houden en de interstrand thermische weerstand zo hoog mogelijk te houden.
- **Beslissend moment voor quench.** De start van een normale zone in de strand waarin een normale zone irreversibel leidt tot een quench wordt het "Quench Decision Moment" genoemd. De scherp afgetekende overgang maakt het mogelijk om goed gedefinieerde stabiliteits criteria te ontwikkelen.

De criteria worden in twee hoofdtypes ingedeeld: propagatie tussen de parallelle strands en tussen de kruisende strands. Het belangrijkste criterium is de propagatie tussen parallelle strands die de stabiliteit van een losse strand onderscheidt van de stabiliteit van een strand in de kabel. De stroom waarbij deze overgang plaatsvindt wordt I_{kink} genoemd en kan worden gebruikt als natuurlijke bovengrens voor het werkgebied van een kabel in specifieke condities.

Invloed van verschillende kabel parameters op stabiliteit

De invloed van de drie belangrijkste kabel parameters wordt uitvoerig beschreven:

interstrand elektrische weerstand, interstrand thermische geleiding en koeling door helium.

De oxide laag die groeit op de strand of strand coating bepaalt in hoge mate de elektrische weerstand. De elektrische weerstand is voor versnellermagneten gespecificeerd door de eisen voor de veldkwaliteit en koppelstroom verliezen, waarbij een hogere weerstand een betere magneet oplevert. Gelet op de stabiliteit levert juist een lagere weerstand een betere magneet op.

Thermische geleiding wordt grotendeels bepaald door de microscopische contactpunten tussen de strands. Een lagere thermische geleiding zorgt voor een vermindering van de transversale propagatie, terwijl de longitudinale propagatie weinig gevoelig is voor veranderingen.

De koeling van een kabel door helium, opgesloten in de openingen tussen de strands, hangt af van de warmtecapaciteit van het helium en de warmte-uitwisseling tussen strand en helium. De koelende eigenschappen van supervloeibaar en vloeibaar helium dragen sterk bij aan een vertraging van de normale zone propagatie en een verhoging van de minimum quench energie. In mindere mate geldt dit ook voor superkritisch helium. In veel gevallen is het contactoppervlak van de strand met het helium de belangrijkste grootheid om verbeteringen te bewerkstelligen.

Versnellermagneten

In deeltjesversnellers wordt de interactie tussen de elementaire bouwstenen van materie bestudeerd door botsingen tussen hoogenergetische deeltjes te analyseren. De meest krachtige versnellers zijn circulair en bevatten dipoolmagneten die deeltjes in een circulaire baan houden, terwijl in iedere omloop energie aan de bundels wordt toegevoegd door een oscillerend elektrisch veld. Quadrupoolmagneten worden gebruikt om de bundel te focussen en een hoge botsingsdichtheid mogelijk te maken. De sterkte van het dipoolveld bepaalt de energie van de deeltjes, terwijl de kwaliteit van het magneetveld en de sterkte van de quadrupoolgradient de hoeveelheid botsingen bepaalt.

Twee versnellers worden behandeld in dit proefschrift: de Large Hadron Collider (LHC) te Genève en de Schwer-Ionen-Synchrotron (SIS) 300 te Darmstadt. De LHC is de grootste deeltjesversneller en is operationeel sinds 2008. De LHC-magneten worden gekoeld door supervloeibaar helium bij 1.9 K, waarbij het dipoolveld 8.3 T kan bereiken. De energie van de deeltjes wordt langzaam opgevoerd tot 7 TeV in ongeveer 20 minuten. De SIS 300 is nog in de ontwerp fase met de volgende parameters: de magneten worden gekoeld met superkritisch helium bij 4.5 K, waarbij het dipoolveld 4.5 T kan bereiken.

De minimum quench energie van de kabel voor verschillende volumes van de warmtepuls is berekend. Deze is meer dan een ordegrootte hoger dan de huidige geschatte waarde voor de LHC dipolen aan de hand van de stabiliteit van losse strands.

Twee ontwerpen van de SIS 300 kabel zijn doorgerekend: een kabel met een roestvrijstalen strip tussen de kruisende strands en een kabel met een coating met een hoge weerstand, waardoor ook de weerstand tussen de parallelle strands wordt

verhoogd. De berekeningen wijzen duidelijk het voordeel van een kabel met een roestvrijstalen strip aan voor verbeterde stabiliteit.

In een magneet zijn verschillende oorzaken mogelijk voor een niet-homogene stroomverdeling in de kabel, zoals koppelstromen en een niet-homogene soldeerverbinding. Niet-homogene stroomverdeling zorgt voor een significante vermindering van I_{kink} en daarmee het operationele magneetveld.

Het meest gevoelige deel van de kabel voor een warmte-puls is de dunne kant, die tevens blootgesteld is aan het hoogste magneetveld. De thermische propagatie van de normale zone tussen strands is zeer lokaal, terwijl de stroomherverdelingsprocessen over een grotere lengte plaatsvinden. Een lokale verbetering van stabiliteit is berekend met twee methoden gebaseerd op verbeterde koeling en verminderde warmte-uitwisseling: het vergroten van het gekoelde oppervlak van de strand aan de rand van de kabel en een coating tussen strands die laag geleidend is.

Met het definiëren van de processen die een rol spelen in de stabiliteit van de kabel en de kwantificering van kabelstabiliteit in magneet toepassingen is het quenchgedrag van magneten beter te voorspellen en kan het ontwerp van toekomstige magneten worden geoptimaliseerd.

Dankwoord - Acknowledgements

Het werk dat voor u ligt is de afsluiting van een promotietraject en het einde van een mooie periode. Het was een tijd waarin ik veel heb geleerd; over mijn vak en over mijzelf. Het onderzoek was als het maken van een grote puzzel waarbij de stukjes met elkaar verbonden zijn. Bij het op zijn plaats leggen van een stukje verschuift het andere weer. Bij het schrijven van dit proefschrift vielen alle stukjes netjes op hun plaats, zodat het grote geheel duidelijk werd. Met enige trots presenteer ik dan ook dit boekwerk en ik hoop dat het van waarde mag zijn voor het begrip en verbetering van de stabiliteit van supergeleidende kabels en magneten.

Terugkijkend besef ik ook hoeveel dank ik ben verschuldigd aan veel personen die hebben bijgedragen aan dit proefschrift op een directe of indirecte manier.

Prof. Herman ten Kate dank ik voor het in mij gestelde vertrouwen toen hij mij een promotieplaats aanbood. De inhoudelijke discussies en je inzet voor het neerzetten van een kwalitatief goed proefschrift zijn heel waardevol geweest. Tijdens de drie jaar dat ik op het CERN mijn onderzoek heb gedaan heeft Arjan Verweij mij op allerlei manieren bijgestaan, interesse getoond, mij gemotiveerd en daarnaast een grote bijdrage geleverd aan het onderzoek door het schrijven en op verzoek aanpassen van het simulatie programma CUDI. Arjan, naast het hebben van een belangrijke aandeel in het slagen van dit onderzoek heb je je ook een goede vriend betoond, ook al heb je mij nooit heb gegund als eerste op de top van een berg aan te komen, hetzij op de fiets, hetzij lopend.

The team consisting of Charles-Henri Denari, Remi Rota and, last but not least, Stefano Geminian has proven very valuable in the technical support of the experiments in the test station FRESCA. Thanks a lot for the effort and the many coffee breaks. Christian Scheuerlein has been very helpful with his knowledge of surface materials of strands and he has been a pleasant office mate. The discussions with and work of Jonas Lantz on helium cooling were helpful. Other persons at CERN I want to acknowledge for their interest and collegiality are: Alejandro, Angelo, David, Giuseppe, Luc, Luca, Lucio, Nikolai and Stephen.

The collaboration with GSI has been very useful: Juris Kaugerts provided me with important cable samples. The decision for the cable design of SIS 300 magnets is based on this research and I thank Hans Müller for sharing information and for the pleasant and interesting cooperation.

Ik zal goede herinneringen blijven houden aan de leden van de vakgroep Lage Temperaturen op de Universiteit Twente, die discussies nuttig en het verblijf aangenaam maakten. Met name wil ik noemen Andries, Arend, Arnold, Erik, Wouter, Marc, Matthijs, Sander, Wouter en Yasuyuki.

Ook mijn kamergenoten Margriet, Martijn, Martin, Pierre Emanuel, Robert-Paul, Steven en Tim droegen daaraan bij en hoewel zij tot een andere groep behoren voelde ik mij er helemaal geaccepteerd.

Mijn familie en vrienden zijn mij erg dierbaar en ik dank hen voor hun onvoorwaardelijke vriendschap en interesse, wetende dat zij mij mede hebben gevormd. In het bijzonder wil ik mijn ouders danken voor hun voortdurende steun en meelevendheid. De door jullie gegeven stimulans, maar ook de vrijheid om mijn eigen weg te gaan heb ik altijd erg gewaardeerd.
Annalies, mijn geliefde vrouw, ik bewonder je geduld, steun en aanpassingsvermogen. Je hebt met mij zelfs 3 jaar in Frankrijk willen wonen en je zou het zo weer doen. Met veel plezier zie ik de komende tijd tegemoet, zelfs nu de aanstaande gezinsuitbreiding ons leven grotendeels lijkt te gaan beheersen.

Enschede, mei 2009 Gerard Willering